Chemoselectivity of Immobilized Transition Metal Catalysts

Filipe Teixeira

2014

Agradecimentos

No man is an island.
No man stands alone.

D. Brown

O trabalho aqui apresentado não teria sido possível sem a ajuda de algumas pessoas e instituições, às quais dirijo o meu sincero agradecimento.

Em primeiro lugar gostaria de agradecer à minha orientadora Professora Drª Natália Cordeiro pela forma como acolheu as minhas ideias ao longo destes últimos anos, e pelas várias oportunidades que me ofereceu para aprender muito mais sobre ciência do que aquilo que poderei escrever ou ler em qualquer artigo científico. O mesmo agradecimento extende-se à Professora Drª Cristina Freire pela forma pronta como, no papel de co-orientadora, contribuiu para aprofundar as discussões dos resultados. O sentido de pragmatismo de ambas será certamente algo que irei tomar como exemplo no meu futuro.

Gostaria também de agradecer ao Professor Dr. André Melo pelo apoio dado dado desde o primeiro momento, as discussões interessantes e o rigor que emprestou a muitos dos meus manuscritos originais.

Uma boa parte do trabalho contido nesta tese não teria sido possível sem a ajuda do Professor Ricardo Mosquera, da Universidade de Vigo. Para além das suas contribuições para a aplicação da Teoria AIM nos complexos metálicos estudados, não poderia deixar de mencionar a forma calorosa como me recebeu no seu grupo de investigação, ao longo das minhas estadias e visitas a Vigo. De igual forma, agradeço ao seu grupo de investigação, em particular ao David Ferro, Nicolás Otero, Nicolás Berdullas, Marta Sánchez e ao Marcos Mandado pela forma como me acolheram, e ajudaram a fazer de Vigo a minha cidade fora do Porto.

A nível pessoal, não poderia deixar de agradecer à Manuela Moreira e à Cristina Neves pela amizade constante com que marcaram presença na minha vida ao longo deste projecto. Os momentos que partilhamos ao longo dos últimos quatro anos são memórias que irei sempre prezar na esperança de novos reencontros.

Uma palavra de agradecimento também é devida ao Alexandre Ferreira pela motivação dada para que eu retomasse os trabalhos de investigação, assim como pelo

apoio, companheirismo e humor que emprestou a esta fase. De igual forma gostaria de agradecer ao Ricardo Rodrigues pela amizade e humanidade que demonstrou ao longo de períodos bastante delicados e a todo um grande grupo de “malucos” que partilha comigo a minha paixão pelo fitness e pela dança, e cuja amizade e energia muitas vezes afugentaram as nuvens negras do pessimismo.

Por fim, este trabalho não teria sido possível sem o apoio financeiro da Fundação para a Ciência e Tecnologia, através da Bolsa de Doutoramento SFRH/BD/64314/2009, assim como financiamento ao REQUIMTE - Laboratório Associado através dos projetos Pest-C/EQB/LA0006/2013 e NORTE-07-0124-FEDER-000067.

Resumo

Novos nano-catalisadores híbridos têm sido desenvolvidos nos últimos anos baseados na ideia de imobilizar num material de suporte complexos de metais de transição com reconhecida atividade catalítica. Estes novos catalisadores poderão providenciar abordagens mais económicas e amigas do ambiente na produção de químicos de elevado valor acrescentado. Em muitos desses novos materiais, o centro metálico encontra-se ligado a um ligando modificado, ou a uma molécula de ligação (linker) ou a um grupo funcional à superfície do material de suporte. Isto corresponde a uma mudança no ambiente químico em torno do centro metálico. Neste trabalho, os efeitos da imobilização de complexos de metais de transição são estudados recorrendo a diversos modelos computacionais. O trabalho é especialmente votado ao estudo da epoxidação de alcenos e alcoóis alílicos catalizada por complexos de manganês-salen, Mn(salen), e di(acetilacetonato) de vanadilo (IV), $VO(acac)_2$, respectivamente. De forma a entender melhor os efeitos da ancoragem à superfície de um material de suporte, desenvolveram-se diversos modelos computacionais para estes complexos de metais de transição nos quais o ambiente em torno do átomo metálico mimetiza aquele que é encontrado em diferentes complexos imobilizados.

Na primeira parte do trabalho de investigação examinaram-se vários modelos computacionais. Em particular, o uso de factores de escala vibracionais universais foi reexaminado à luz de novas técnicas para a avaliação das incertezas associadas. Calcularam-se novos factores de escala, e as suas incertezas associadas, para cálculos de Hartree-Fock assim como usando a Teoria dos Funcionais de Densidade (DFT), usando um conjunto de calibração anteriormente concebido. Os resultados demonstraram que um fator de escala universal para a previsão de frequências fundamentais de vibração teria, no melhor dos cenários possíveis, apenas dois algarismos significativos. O uso de tais factores de escala foi portanto desencorajado na maioria das aplicações computacionais em química.

O nível de teoria usado no estudo dos complexos de metal de transição foi estudado a partir das energias relativas dos diferentes estados de spin de complexos de Mn(salen) e oxo-Mn(salen). Os resultados desse estudo permitiram o uso do funcional X3LYP com uma base de qualidade triplo-ζ. Diversos métodos de análise populacional foram também estudados para estes complexos, chegando-se à conclusão que a Análise

de População Natural (NPA) e a análise de Átomos em Moléculas (AIM) têm um desempenho superior aos demais métodos testados. Como tal, estes dois métodos foram usados em trabalhos posteriores.

Na segunda parte deste trabalho analizaram-se diferentes modelos de complexos de Mn(salen) numa comparação com os modelos simplificados usados em estudos teóricos anteriores. Para esse fim, dados sobre a geometria e estrutura electrónica de diversos complexos de Mn(salen) e Mn(acacen') (acacen' = 3,3'-(etano-1,2-diilbis(azanililideno))bis(prop-1-en-olato)) foram estudados usando DFT e NPA. Os resultados foram seguidamente estudados usando a Análise de Componentes Principais (PCA), tendo-se chegado à conclusão que os complexos Mn(acacen') não são representativos das propriedades de complexos de Mn(salen). Por outro lado, demonstrou-se que o complexo Mn(salen) é representativo da estrutura encontrada em torno do átomo central de manganês em complexos mais elaborados, tal como é o caso do catalisador de Jacobsen.

Tendo em conta os resultados anteriores, foram estudados diversos complexos de Mn(salen) com diferentes ligandos axiais, escolhidos de forma a simular o ambiente químico em torno do átomo de manganês nos seus análogos imobilizados. Os resultados obtidos sugerem que a imobiliazação levada a cabo com linkers análogos dos grupos fenilcarboxilo e fenilsulfito induz menores alterações nas propriedades estudadas para estes complexos. Para além disso verificou-se a existência de uma relação entre a carga do ligando salen e a quantidade de carga transferida do ligando axial (linker) para o centro metálico.

Na terceira parte deste trabalho estudou-se o mecanismo das epoxidações catalizadas por $VO(acac)_2$. Considerações energéticas permitiram a formulação de um modelo para o ciclo catalítico deste complexo de metal de transição. Este modelo contempla a existência de uma espécia ativa de alquilperoxo-vanádio (V) enquanto responsável pela epoxidação do substrato uma vez atingido o equilíbrio químico. Para além disso, os resultados sugerem que tal intermediário poderá libertar-se do seu linker num processo energeticamente favorável. Este cenário é mais viável durante a epoxidação de álcoois alílicos do que na epoxidação de alcenos. Finalmente, o estudo da reação elementar de transferência de oxigénio para o substrato foi estudada em mais detalhe. Os resultados deste último estudo foram conjugados com os dados da análise AIM dos reagentes envolvidos em cada reação de forma a criar um modelo linear para a a barreira energética aparente respectiva. O modelo linear resultante obteve um desempenho satisfatório e permitiu a racionalização das barreiras de activação deste tipo de reacções.

Palavras-chave: Catálise; Complexos de Metais de Transição; Catalizadores Imobilizados; Teoria dos Funcionais de Densidade (DFT); Teoria dos Átomos nas Moléculas (AIM); Propriedades Moleculares; Manganês; Vanádio

Abstract

Recent years have witnessed the development of novel hybrid nano-catalysts in which a transition metal complex with known catalytic activity is anchored onto a supporting material. These novel catalysts may find their usefulness in the production of fine chemicals, providing economical and environmental benefits relative to the use of older technology. In many of these novel catalysts the transition metal is attached to a modified ligand, a linker molecule or to a functional group in the surface of the supporting material. This situation changes the chemical environment of the metal center. In this work, the effects of immobilization of different transition metal complexes are studied using different computational approaches. The work focus in the epoxidation of alkenes and allylic alcohols catalyzed by manganese-salen, Mn(salen), and vanadium (IV) acetylacetonate, $VO(acac)_2$, respectively. In order to better understand the effects of anchoring onto a supporting surface, several computational models for these transition metal complexes were considered as possible mimics for the chemical environment of the metal center in different immobilization scenarios.

In the first part of the research work, different computational methods were examined. In particular, the use of universal vibrational scaling factors is re-examined by applying new guidelines to express their uncertainty. New vibrational scaling factors for first principles calculations were calculated, as well as their respective uncertainties, using a standard calibration set. The results shown that an universal vibrational scaling factor may have at best only two significant digits, and its use is therefore discouraged for most chemical applications.

The level of theory used in the study of the transition metal complexes was studied by observing the ordering of the different spin states in Mn(salen) and oxo-Mn(salen) catalysts. The results favored the use of the X3LYP functional with a triple-ζ quality basis set. Furthermore, different methods for the computation of effective atomic charges and spin densities in Mn(salen) complexes were examined. Natural Population Analysis (NPA) or Atom in Molecules (AIM) performed noticeably better than other methods, and were used in subsequent work.

In the second part of this work, different models for Mn(salen) complexes were compared with the simplified models used in previous theoretical studies. For this purpose, data on the geometry and electronic structure of different Mn(salen) and Mn(acacen')

complexes (acacen' = 3,3'-(ethane-1,2-diylbis(azanylylidene))bis(prop-1-en-olate)) were gathered from DFT and NPA calculations. These were subjected to a Principal Component Analysys (PCA), showing that Mn(acacen') complexes are not proper surrogates for the larger Mn(salen) catalysts. On the other hand, the geometry and electronic structure around the metal center in Mn(salen) is an accurate representation of what is found in larger complexes, such as the Jacobsen catalysts.

With these results in mind, the consequences of anchoring Mn(salen) catalysts using one of the vacant positions in the metal center's coordination sphere was studied by considering the coordination of different ligands that mimic the chemical environment of manganese in the immobilized versions of these catalysts. The results suggest that immobilization with phenylcarboxyl of phenylsulfide linkers carries the least changes in the properties of the Mn(salen) catalysts, in terms of the ordering of the different spin states and the energy involved in their oxidation to oxo-Mn(salen) species. Moreover, a relationship was found between the charge of the salen ligand and the amount of charge transferred from the axial ligand to the metal center.

In the third part of the work, is devoted to the study of $VO(acac)_2$ catalyzed epoxidations. Energetic considerations allowed the formulation of a model for the catalytic cycle of this complex. This model contemplates the formation of alkylperoxo-vanadium (V) species as the main epoxidizing agents in the steady state phase of the reaction. Moreover, the results concluded that these intermediates may loose their linker ligand in energetically favored reactions, and that this scenario is more likely to occur when the substrate is an allylic alcohols instead of an unfunctionalized alkene. Finally, the oxygen transfer step between an active vanadium complex and an olefinic substrate was study in more detail. The results from this study were confronted with the AIM analysis of the electronic structure of the reactants in these reactions and a linear model for the apparent energetic barrier of epoxidation reactions using vanadium alkylperoxo complexes was developed and examined.

Keywords: Catalysis; Transition Metal Complexes; Immobilized Transition Metal Catalysts; Density Functional Theory (DFT); Theory of Atoms in Molecules (AIM); Molecular Properties; Manganese; Vanadium

Scope of the Thesis

The main purpose of this research was to evaluate the consequences of immobilization in transition metal complexes. In particular, immobilization techniques in which the procedure directly affects the coordination sphere of the metal center received considerable attention. Moreover, this work focuses on the chemistry of Mn(salen) complexes and $VO(acac)_2$ towards the epoxidation of alkenes and allylic alcohols, respectively. The energetics of the immobilized complexes and their most significant intermediates are investigated using DFT calculations at the X3LYP/triple-ζ level of theory, and the properties of each system at their equilibrium geometries are rationalized using different computational approaches. To achieve this main goal, some specific aims of this thesis were:

1. To establish theoretical methodologies for the evaluation of the energy (electronic and also zero point vibrational corrections) of transition metal catalysts (Chapters 3 and 4)

2. To explore different computational methods for the recovery of information on the electronic structure of transition metal catalysts, in particular effective atomic charges and spin densities (Chapter 4).

3. To investigate the differences between different Mn(salen) and Mn(acacen') complexes in diverse chemical environments that mimic both the homogeneous state as well as their anchored derivatives (Chapter 5).

4. To investigate the effect of different axial ligands on the properties of Mn(salen) complexes and their oxo-derivatives, and infer the potential effect of using different linker molecules in the immobilization procedure (Chapter 6).

5. To explore the mechanism of $VO(acac)_2$ towards the epoxidation of alkenes and allylic alcohols (Chapters 7 and 8).

6. To investigate the effects of immobilization of $VO(acac)_2$ via Schiff base condensation in $VO(acac)_2$/TBHP epoxidations (Chapter 7).

Author publications

Articles published or submitted to peer-reviewed journals containing work related to this thesis:

F. Teixeira, A. Melo and M. Natália D. S. Cordeiro, "Calibration sets and the accuracy of vibrational scaling factors: A case study with the X3LYP hybrid functional", *Journal of Chemical Physics*, **133** (2010), 114109

F. Teixeira, R. Mosquera, A. Melo, C. Freire and M. Natália D. S. Cordeiro, "Charge Distribution in Mn(salen) Complexes", *International Journal of Quantum Chemistry*, **114** (2014), 525–533

F. Teixeira, R. A. Mosquera, A. Melo, C. Freire and M. Natália D. S. Cordeiro, "Principal Component Analysis of Mn(salen) Complexes", *Physical Chemistry Chemical Physics*, Submitted on February 18, 2014

F. Teixeira, R. Mosquera, A. Melo, C. Freire and M. Natália D. S. Cordeiro, "Effects of Axial Coordination on Immobilized Mn(salen) Catalysts", *Journal of Physical Chemistry A*, Submitted on June 24, 2014

F. Teixeira, A. Melo, C. Freire and M. Natália D. S. Cordeiro, "Energetics of Vanadyl (IV) Acetylacetonate/TBHP Epoxidations", *Journal of Molecular Catalysis A: Chemical*, Submitted on June 19, 2014

Manuscripts containing work related to this thesis:

F. Teixeira, R. Mosquera, A. Melo, C. Freire and M. Natália D. S. Cordeiro, "Reactivity of Alkylperoxo-vanadium Complexes Towards the Epoxidation of Alkenes and Allylic Alcohols: An Atoms in Molecules Approach", Manuscript in preparation to be submitted to *International Journal of Quantum Chemistry*.

Articles in peer-reviewed journals not included in this dissertation, but published in the course of the doctoral work:

F. Teixeira, A. Melo and M. Natália D. S. Cordeiro, "Response to "Comment on 'Uncertainties in scaling factors for ab initio vibrational zero-point energies' and 'Calibration sets and the accuracy of vibrational scaling factors: A case study with the X3LYP hybrid functional'", *Journal of Chemical Physics*, **134** (2011), 167103

A. Gaspar, F. Teixeira, E. Uriarte, N. Milhazes, A. Melo, M. Natália D. S. Cordeiro, F. Ortuso, S. Alcaro and F. Borges, "Towards the Discovery of a Novel Class of Monoamine Oxidase Inhibitors: Structure-Property-Activity and Docking Studies on Chromone Amides", *ChemMedChem*, **6** (2011), 628–632

A. Almeida, J. A. Ferreira, F. Teixeira, C. Gomes, M. Natália D. S. Cordeiro, H. Osório, L. L. Santos, C. A. Reis. R. Vitorino and F. Amado, “Challenging the limits of detection of sialylated Thomsen-Friedenreich antigens by in-gel deglycosylation and nano-LC-MALDI-TOF-MS”, *Electrophoresis*, **34** (2013), 2337–2341

F. Teixeira, A. Melo and M. Natália D. S. Cordeiro, “Aza-Diels-Alder addition of cyclopentadiene to propynyliminoglyoxylates”, *Computational and Theoretical Chemistry*, **1012** (2013), 54–59

Contents

List of Figures

List of Tables

Abbreviations and Symbols

6-CN-DMC	2,2-dimethyl-6-cyanochromene
AC	Active Complex
acac	Acetylacetonate
acacen'	3,3'-(ethane-1,2-diylbis(azanylylidene))bis(prop-1-en-olate))
AcO	Acetate
AcOH	Acetic Acid
AIM	Quantum Theory of Atoms in Molecules
APTES	(3-Aminopropyl)triethoxysilane
BCP	Bond Critical Point
CASSCF	Complete active space self-consistent field
CC	Coupled Cluster
CCD	Coupled Cluster with Doubles
CCM	Continuous Chirality Measurement
CCP	Cage Critical Point
CCSD	Coupled Cluster with Singles and Doubles
CI	Configuration Interaction
CISD	Configuration interaction with singles and doubles
CP	Critical Point
CSF	Configuration State Function
CSM	Continuous Symmetry Measurements
DFT	Density Functional Theory

ECP	Effective Core Potential
GGA	Generalized Gradient Approximation
Hacac	Acetylacetone
HF	Hartree-Fock method
IC	Inactive Complex
IRC	Intrinsic Reaction Coordinate
KS	Kohn-Sham formalism
LCAO	Linear Combination of Atomic Orbitals
LDA	Local Density Approximation
LSD	Local Spin Density Approximation
MCSCF	Multi-configuration space self-consistent field
MD	Molecular Dynamics
MM	Molecular Mechanics
MP2	Møller-Plesset second order perturbation theory
NAO	Natural Atomic Orbital
NBO	Natural Bond Orbital Theory
NCP	Nuclear Critical Point
NPA	Natural Population Analysis
OLS	Ordinary Linear Regression
PC	Principal Component
PCA	Principal Component Analysis
PES	Potential Energy Surface
QTAIM	Quantum Theory of Atoms in Molecules
RCP	Ring Critical Point
RHF	Restricted Hartree-Fock
rms	Root mean-square error

ROHF	Restricted Open-shell Hartree-Fock
rPCA	Principal Component Analysis with orthogonal rotation of the Principal Components
salen	*N*,*N*-ethylenebis(salicyldeneaminato)
TBHP	*tert*-butylhydroperoxide
TBP	tert-butylperoxy
UHF	Unrestricted Hartree-Fock
ZPVE	Zero-Point Vibrational Energy
E_{el}	Electronic energy
ϵ_0	Electic vacuum permittivity
$\gamma_1(\mathbf{r}, \mathbf{r}')$	First order density matrix
$\hbar$	Reduced Plank constant ($\frac{h}{2\pi}$)
h	Plank constant
$\hat{H}$	Hamiltonian operator
k_B	Boltzman constant
$n(\mathbf{r})$	Electron probability density
PCA	Principal Component Analysis
R	Ideal gas constant
$\rho(\mathbf{r})$	Electron density
SCF	Self-consistent field
$\hat{T}$	Kinetic energy operator
$^{\text{t}}$BuOH	*tert*-butanol
$\hat{V}_{\text{ee}}$	Electron-electron interaction operator
$\hat{V}_{\text{ne}}$	Nucleus-electron interaction operator
Φ	Wave function, as a solution to the electronic Hamiltonian
r^2	Coefficient of determination
σ_x	Standard deviation of x
$\bar{x}$	Mean, or average, value of x

Chapter 1

Overview

The need to manufacture chiral compounds for industrial applications has increased significantly over the past three decades [1]. Most of this development has been driven by the pharmaceutical industry, as the commercialization of a single enantiomer over racemic drugs maximizes patient benefit and better complies with the demands from regulatory agencies. Further demands on asymmetric synthesis have been put forward by the flavoring, fragrance and agrochemicals industry, as well as by recent developments in the field of material sciences [1, 2]. At the same time, an increased in the awareness of the impact of chemistry-based industries in the environment at the local, regional and global scale gave rise to the aspiration for safer and more environmentally benign chemicals and processes [2].

The concerns for the use of safer chemicals and processes condensed around the concept of "Green Chemistry". Green Chemistry is a philosophy described by Anastas and others which seeks to minimize the impact of chemical activities on the environment [3–6]. Two of the 12 Principles of Green Chemistry encourage the development of processes with an emphasis on atom economy (*i.e.* attempt to incorporate all the atoms of the initial reagents into the final product) and avoidance of derivatives such as protecting groups and chiral auxiliaries [4, 7]. Another Principle of Green Chemistry advocates the use of catalysis instead of stoichiometric reagents [2, 6, 8].

Different paths are available in order to obtain single-enantiomer compounds. Examples of which include physical separation of the enantiomers, kinetic resolution, and asymmetric synthesis. However, separations and resolutions are disfavored from the point of view of Green Chemistry, as half of the product of a non-asymmetrical synthesis is wasted [2]. Instead, Green Chemistry advocates the production of chiral, non racemic compounds using asymmetric synthesis techniques in general, and from the arsenal of asymmetric synthesis techniques available to the chemical industry, the use of enantioselective catalysts is strongly encouraged [8–13].

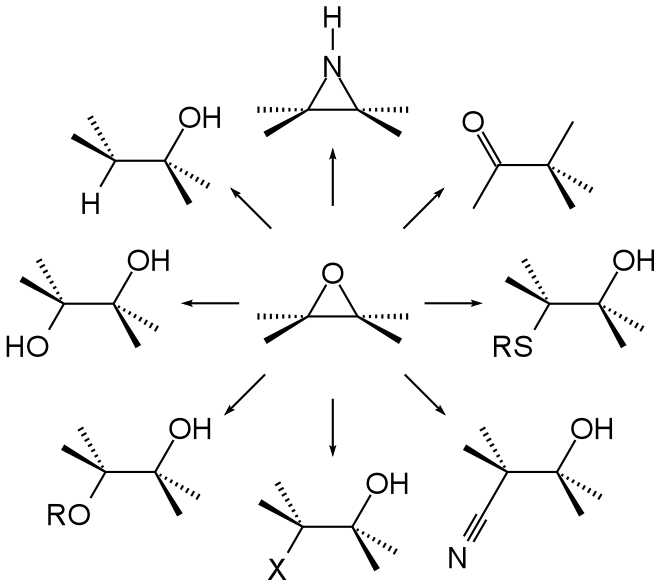

Figure 1.1: Possible outcomes from common reactions of epoxides.

1.1 Evolution of epoxidation processes

Epoxides are cyclic ethers in which one oxygen atom and two carbon atoms are arranged approximately as an equilateral triangle [14]. A significant amount of strain energy emerges from this particular arrangement of atoms, making any ring-opening reaction highly exothermic [15]. As exemplified in Figure 1.1, these highly reactive, yet apparently simple structures may take part in a number of different reactions. Moreover, up to two chiral carbon atoms may form upon ring-opening. Because of this, epoxides are well established intermediates in asymmetric synthesis, being important intermediates in the synthesis of more complex chemical structures such as medicines, fragrances and polymers [16].

Different synthetic routes are available for the formation of epoxides [17]. The most simple epoxides, such as oxacyclopropane (also known as ethylene oxide, or oxirane), were originally produced by treating 2-chloroethanol with a base (Wurtz's method) [15]. This was the main preparative procedure for the production of oxirane until the 1930's, when it was supplanted by the direct reaction between ethene (ethylene) and molecular oxygen, using silver as a catalyst. However, this process requires high temperatures and a precise control of the oxygen intake. It also raises safety concerns as O_2/organic mixtures can sometimes spontaneously ignite. More complex epoxides can be produced by oxidation of alkenes using organic epoxidizing agents such as organic peracids (or peroxyacids) [18, 19], oxone (potassium peroxymonosulfate) [20–24], dioxiranes [25–27] or oxaziridines [28]. However, the use of organic epoxidizing agents is hindered by the high cost of these compounds, their relatively low active oxygen content (worst atom

economy) and their potentially harmful by-products. Because of this, their use as been mostly restricted to the production of fine chemicals on a limited scale [17].

Peroxides, in particular hydrogen peroxide, H_2O_2 , offer viable alternatives to the use of molecular oxygen. As an oxidant, hydrogen peroxide offers the largest atom economy after O_2. Moreover, its by-product is environmentally harmless (water) and, being a liquid, is easier to transport, storage and manipulate than O_2 [29]. Also, H_2O_2/organic mixtures are much safer to handle than those with O_2 and the use of more efficient catalysts such as zeolites, metal oxides and transition metal complexes allows for milder reaction conditions [30, 31]. These aspects further allow the techniques developed around this framework to be applied in the synthesis of more structurally complex epoxides [17].

In certain cases, H_2O_2 is too reactive, leading to side reactions such as such as lactonization, ketonization, oxidative cleavage and, eventually, catalyst poisoning [32]. In those cases, the use of a less reactive organic peroxide is prescribed. *Tert*-butylhydroperoxide (TBHP) has been particularly popular, partially due to its relative low cost, moderate active oxygen content, moderate reactivity (compared to H_2O_2) and the high stability of TBHP/organic mixtures. Furthermore, the main waste product that comes from using TBHP is *tert*-butanol (^{t}BuOH), which can be recycled into the production of THBP [29].

Transition metal complexes are important catalysts in the industrial epoxidation of simple alkenes and other olefinic materials such as allylic alcohols, allowing the production of more complex epoxides, as well as the regioselective epoxidation of polyunsaturated compounds or the stereoselective formation of chiral epoxides. The field of alkene epoxidation catalyzed by transition metal complexes is remarkably diverse, with a multitude of metal/ligand combinations being available [17, 32–35]. Some of the most remarkable success stories are those of chromium- and manganese-salen complexes [36], metalloporphyrins [37–41], as well as different titanium, vanadium or molybdenum complexes [42–44].

Industrial epoxidation processes, based on solid phase catalysts such as zeolites and insoluble metal oxides, can be implemented without many technical difficulties [1, 2, 13, 45, 46]. On the other hand, the catalytic efficiency of transition metal complexes is yet to be fully harnessed, due to their high cost, low stability and difficult recovery. Meeting these challenges, several strategies have been devised for better harnessing the catalytic efficiency and chemoselectivity of these homogeneous catalysts. Such strategies have been focus on improving the recovery of the catalysts, with both economical and environmental advantages [47, 48].

This is usually accomplished by immobilizing transition metal complexes onto a solid supporting material. In general, immobilized homogeneous catalysts tend to have reduced activities compared to their homogeneous analogues. However, this drawback can be offset by the advantages of easy catalyst recovery and reduction of trace metal contamination [30]. Moreover, the immobilization procedure may also alter the catalyst

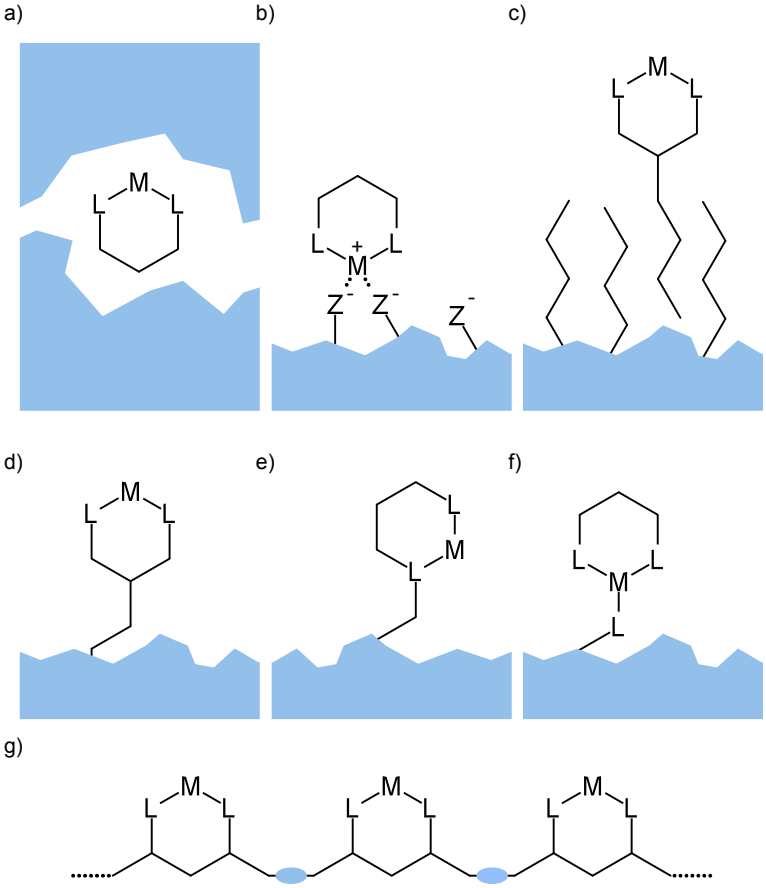

Figure 1.2: Methods for the immobilization of transition metal complexes onto solid supports: encapsulation (a); electrostatic interaction (b); van der Waals interaction (c); covalent bonding (d, e and f) and using a coordination polymer (g) , represented as an one-dimensional polymer, for simplicity. Adapted from Ref. [50].

selectivity, and thus provide more opportunities to fine tune the catalyst to the production of the desired product with minimal waste of reactants in side reactions [49]. The ultimate goal in this line of research is to minimized the cost, and environmental safety concerns involved in the use of homogeneous transition metal catalysts by combining their catalytic efficiency and selectivity with the ease of recovery of a heterogeneous catalyst [50]. The evolution of this concept is testified by the type of supporting material used, starting from bulk solid supports such as activated carbon, mesoporous silicas, clays and zeolites, to nanostructured materials such as carbon nanotubes, silica nanoparticles and magnetic nanoparticles, yielding the so-called hybrid nanocatalysts [50–54].

The strategies available for the immobilization process are illustrated in Figure 1.2, showing that these can be classified according to the type of interaction between the complex and its support: covalent bonding (usually involving a linker molecule that binds to both catalyst and support), non-covalent interactions (either by $\pi - \pi$, van der Waals or electrostatic interactions, or through hydrogen bonding), encapsulation or by using a porous coordination polymers [47, 48].

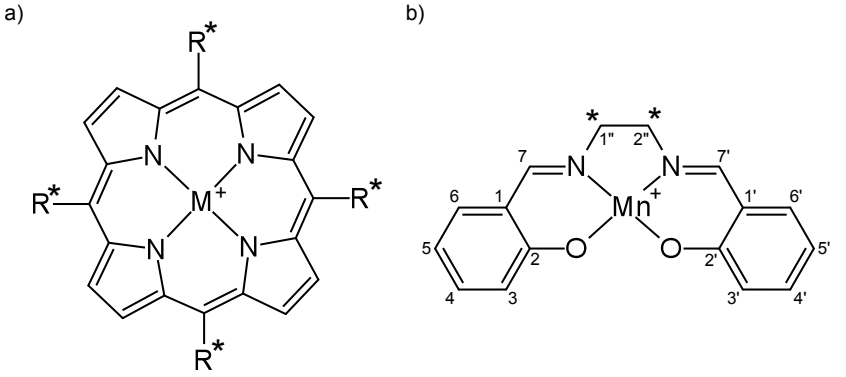

Figure 1.3: General structures of a chiral metalloporphyrin (a) and of a chiral Mn(salen) complex with the IUPAC numbering scheme (b).

The strategies involving covalent bonding between the linker and the transition metal atom (Figures 1.2e and 1.2f) are particularly interesting, as the moiety around the metal center may differ significantly from that found in their homogeneous analogues. This work is focused on the use of axial coordination with linker molecules as an immobilization strategy for manganese-salen complexes, as well as the anchoring of vanadyl (IV) acetylacetonate by Schiff condensation. This is done in the hope of shedding some light on the consequences of using such immobilization strategies.

1.2 Manganese-salen Catalysts

The most successful approach for achieving high stereoselectivity in the epoxidation of unfunctionalized olefins, evolved from a biomimetic strategy. Oxidation is among the most important reactions in the metabolism of nutrients, toxins and medicines, and many enzymes are effective catalysts in different oxidation reactions [37]. Cytochrome P-450 enzymes are a family of porphyrin-bearing proteins involved in xenobiotic metabolism, biosynthesis of steroids, lipids, vitamins and other natural products [55]. Synthetic metalloporphyrins were originally developed by Groves, Guilmet, Meunier and respective co-workers in the early 1980's as models for investigating the reactivity of P-450 [56–58]. Many of these compounds have been reported to catalyze the epoxidation of unfunctionalized olefins. By altering the substituents in the *meso* positions chiral metalloporphyrins may be produced (Figure 1.3a). These chiral metalloporphyrins are known catalysts in the asymmetric epoxidation of olefins [59–61].

At the same time, the N,N-ethylenebis(salicyldeneaminato) ligand (hence forward referred to as salen) aroused the interest of synthetic chemists as an alternative model compound for the active site of P-450 [62]. Many of these complexes bear catalytic activity towards the epoxidation of unfunctionalized olefins, and over 2500 transition metal complexes based on the salen scaffold have been described and characterized [63]. Chromium-salen, nickel-salen and manganese-salen complexes are good catalysts for

this type of reaction [64–66]. However, manganese-salen (Mn(salen)) complexes are considered as being the most efficient catalysts that include the salen ligand [65]. This lead to the establishment of the Mn(salen) catalyzed epoxidation of olefins, also known as the Jacobsen-Katsuki epoxidation, to become one of the most important preparative epoxidation techniques [17, 67–69].

1.2.1 General Characteristics

The salen ligand forms kinetically non-labile and sterically well defined complexes with manganese (III), in which the four binding sites of the ligand are usually arranged around the manganese atom in a square planar geometry. Unlike porphyrins, salen complexes have two potentially stereogenic sp^3-hybridized carbon atoms in the vicinity of the metal center (see Figure 1.3b). The proximity of these stereogenic centers to the metal binding site allows for better stereochemical control of the epoxidation step than what is observed for chiral metalloporphyrins [67]. The catalytic ability of Mn(salen) complexes towards the epoxidation of unfunctionalized olefins was first reported by Srinivasan *et al.* in 1986 [65]. More recently, Mn(salen) complexes have received considerable interest as possible mimics of catalase and peroxidase [70, 71] and radical scavengers in biological media [72], leading to possible future medical applications in the mitigation of cellular injury caused by radiation in cancer patients [73].

A variety of oxidants are effective for Mn(salen) catalyzed epoxidations, the most popular being iodosylbenzene (PhIO), sodium hypochlorite (NaClO), H_2O_2, TBHP, organic peracids, oxone, dimethyldioxirane and molecular oxygen in conjunction with a sacrificial reductant. While iodosylbenzene and sodium hypochlorite were the preferred oxidants in the first works on Mn(salen) catalyzed epoxidations [65, 74–78], molecular oxygen and H_2O_2 provide interesting alternatives due to their high active oxygen content, low price, high availability and low environmental risk. Their use, however, is hindered because of competing side reactions [30]. On the other hand, TBHP offers a viable environmentally friendly alternative as a terminal oxidant for this class of reactions [79]. The choice of terminal oxidant may have a moderate effect on the yield and stereoselectivity of Mn(salen) epoxidations either due to possible side reactions or because they may form alternative reactive intermediates with the Mn(salen) catalyst [80, 81].

In the early 1990's, Jacobsen, Katsuki and their respective co-workers independently developed the first chiral complexes based on the Mn(salen) scaffold [74–78], arriving at the Jacobsen and Katsuki catalysts shown in Figure 1.4.

The diimine part of the salen ligand (also called diimine bridge) plays a fundamental role in the stereoselectivity of the catalyst. Despite common sense, Jacobsen and co-workers shown that increasing the steric bulk of the diimine bridge beyond what is depicted in Figure 1.4a decreases both reactivity and enantioselectivity. The bulkiness of the substituents at the 3,3' and 5,5' positions increase the enantioselectivity of the

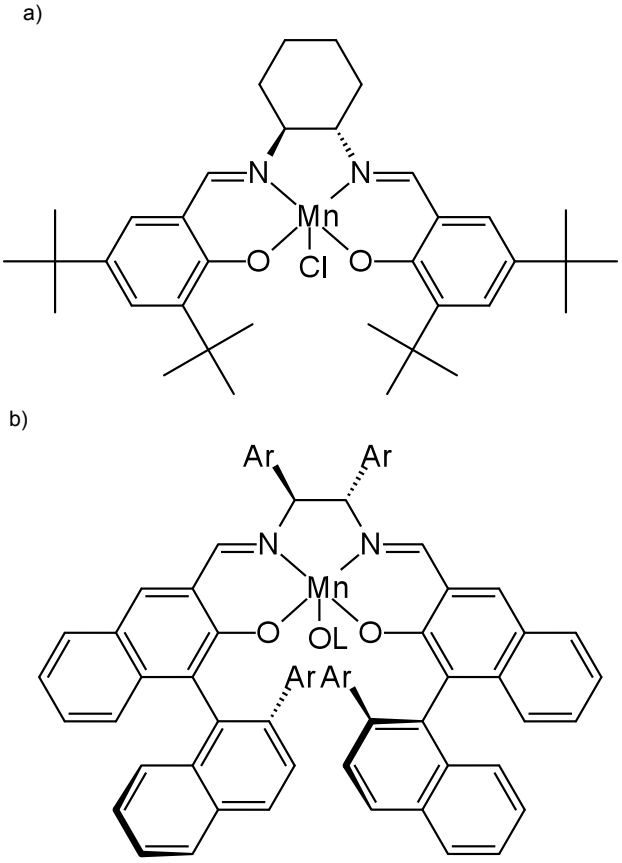

Figure 1.4: Structural formulas of the Jacobsen (a) and Katsuki (b) catalysts. In (b), Ar=3,5-dimtehylphenyl and OL = AcO.

catalyst, although only marginal improvements are noticeable for substituents larger than *tert*-butyl. Furthermore, the presence of electron-withdrawing groups at the 5,5' positions usually enhances the catalytic activity of the complex, while complexes with electron-donating groups at the 5,5' positions show higher enantioselectivity [36, 75, 82]. However, Katsuky and co-workers have noted some exceptions to these observations [62, 78].

Nitrogen heterocycle additives such as pyridine *N*-oxides, pyridines or imidazoles bear a strong influence over the rate, yield and selectivity of Mn(salen) catalysts. These observations have been explained by considering the effect coordination of such bases may impart on the electronic structure of the manganese atom. It was postulated by Kochi that the presence of a donor ligand at the axial position would stabilize intermediate species in the course of the catalytic cycle, thus increasing the rate and yield of the reaction [36, 83]. Moreover, Katsuki and co-workers reported a number of chiral amines or pyridine *N*-oxides that induce enantioselectivity in epoxidations catalyzed by achiral Mn(salen) complexes [84]. These observations have been rationalized by postulating that the salen ligand assumes a stable chiral conformation due to the presence of the chiral donor ligand, thus making the approach of the substrate to the active site of the catalyst more likely to occur under specific orientations.

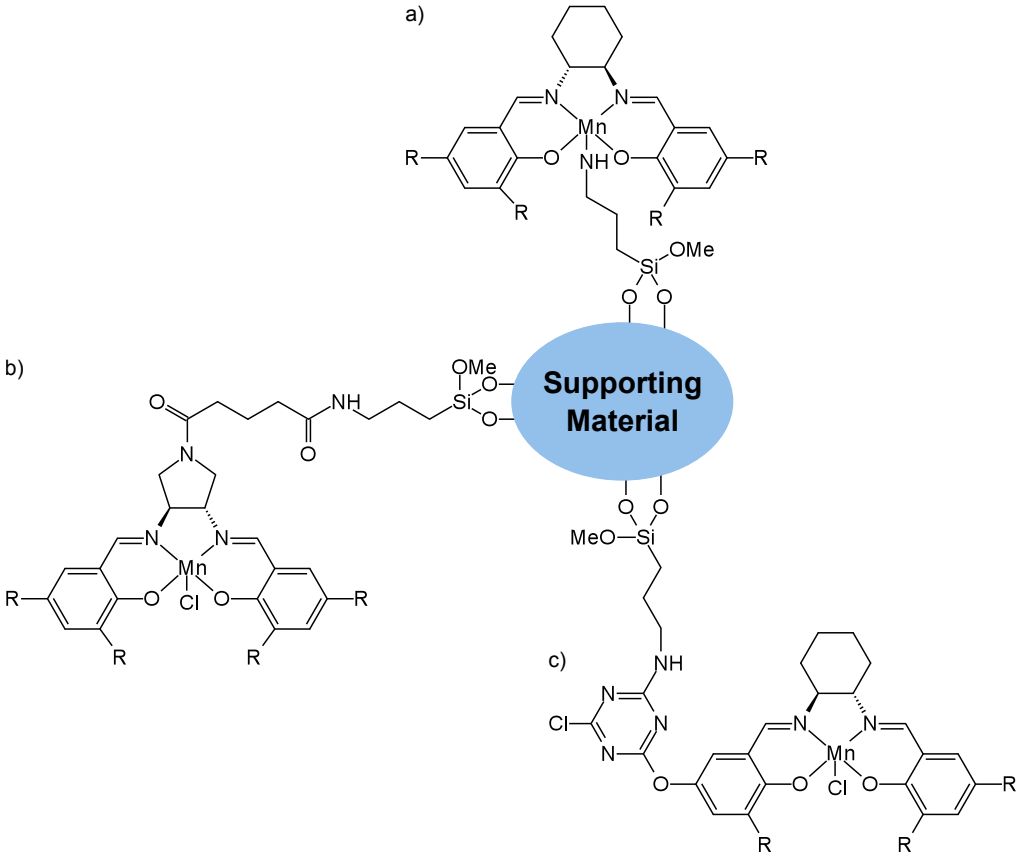

Figure 1.5: Examples of immobilization of Mn(salen) catalysts using covalent attachment: a) Axial coordination to the manganese atom; b) anchoring *via* functionalization of the diimine bridge; c) anchoring *via* functionalization of the salen aromatic moiety. In all cases, R=*tert*-butyl.

The remarkable rates, yields and stereoselectivities achieved by Mn(salen) catalysts in homogeneous media aroused the interest on the development of novel materials with similar catalytic activity towards the epoxidation of unfunctionalized olefins [85, 86]. The supporting materials used in this endeavor range from zeolites [87], pillared clays [88,89], meso and microporous silicas [49,90] to membranes [79,91], and carbon nanostructured materials [92, 93]. Also, the reactivity and structure of Mn(salen) complexes allow the covalent attachment onto the supporting material to be done either by using one of the vacant axial positions in the coordination sphere of Mn (Figure 1.5a) [92, 94, 95], or by functionalization of the salen moiety. In the latter case, the functionalization of the salen ligand can occur either at the diimine bridge (Figure 1.5b) [90] or at the outer aromatic rings of salen (Figure 1.5c), in which case the positions 5,5' and 4,4' are usually preferred [89, 90, 94, 96].

Covalent binding of Mn(salen) complexes onto their supporting material allows for materials with good stability and moderate catalytic efficiency, when compared to encapsulation, for example [50, 86]. On the other hand, the structure of the homogeneous catalyst is inevitably altered. As stated, the catalytic efficiency and selectivity of these catalyst depends on both the presence (and type) of substituents in the aromatic rings of

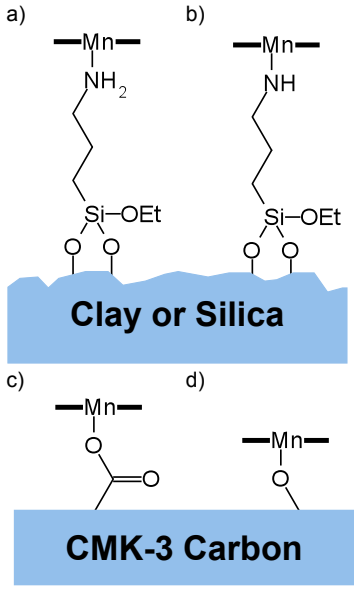

Figure 1.6: Examples of immobilization by axial coordination to the metal center of the Jacobsen catalyst: a) and b) Immobilization onto amine-functionalized supports [94]; c) and d) Immobilization onto nanostructured carbon materials [92]. In all cases, the salen moiety is represented by bold lines, for simplicity.

salen as well as the possible attachment of a donor ligand to one of the vacant positions in the coordination sphere of the manganese atom. It is therefore plausible that some of the differences observed between these new catalysts and their homogeneous counterparts are due to the changes in the moiety around the metal center. This work explores such questions, particularly those related to the problem of axial coordination of the linker molecule to the manganese atom, paying special consideration to the works conducted by Freire and co-workers [92, 94] (Figure 1.6).

In 2009, Das *et al.* [94] reported the immobilization the Jacobsen catalyst onto functionalized silicas (MCM-41 and FSM-16) as well as Laponite. The functionalization of the supporting materials was achieved using (3-aminopropyl)triethoxysilane (APTES) and the immobilization step was performed both directly onto the functionalized material (Figure 1.6a), or after treating the support with $NaCH_3CH_2O$ (Figure 1.6b). Five of the six possible materials were successfully obtained, and tested towards the epoxidation of styrene, α-methyl-styrene and 2,2-dimethyl-6-cyanochromene (6-CN-DMC). In the first catalytic run, the synthesized materials achieved conversion and enantiomeric excess ratings similar to those of the homogeneous phase catalyst, but required more time in order to achieve the same conversion ratings. In all cases, there is a reduction of catalytic efficiency in subsequent runs. This effect was attributed to the leaching of the immobilized complex [94].

More recently, Gaspar *et al.* [92] reported the immobilization of the Jacobsen catalyst onto nanostructured carbon CMK-3 with different surface treatments, yielding the immobilization schemes depicted in Figures 1.6c and 1.6d. The resulting materials were tested in towards the epoxidation of 6-CN-DMC. The immobilized catalysts achieved similar con-

version rates and enantiomeric excesses to those measured on their homogeneous counterparts. Furthermore, in the first catalytic run, the selectivity towards epoxidation was greatly improved. However, in order to obtain such performance, the reaction time had to be greatly increased. In subsequent runs, the catalytic efficiency slowly declined, possibly due to the leaching of the immobilized complex. Nevertheless, the materials produced in this work proved to be much less prone to the leaching than those presented by Das *et al.* [94]. Moreover, the behavior of the immobilization schemes depicted in Figures 1.6c and 1.6d apparently lead to catalysts that behave closer to those in the homogeneous media, a fact that may also be due to the nature of the supporting material [92].

1.2.2 Catalytic Cycle

Knowledge about the catalytic cycle of Mn(salen) complexes towards the epoxidation of alkenes is an important tool towards the fine tunning of novel catalysts. In addition to this, it may also allow the rationalization of the behavior of their immobilized counterparts and help designing new strategies for the development of novel nano-structured catalysts [47, 48, 97–99]. In a first stage, such knowledge has been obtained by analogy to the catalytic cycle of similar transition metal complexes such as metalloporphyrins [57, 59, 100–105], and the much less reactive Cr(salen) complexes [36]. At a later stage, experimental evidence relative to the intermediate species in Mn(salen) catalyzed epoxidations became available, confirming the relationship between Mn(salen) and the two families of complexes previously mentioned. Also, several theoretical chemists made their contributions to the field, exploring details of the reaction mechanism not easily surveyable using experimental techniques and also posing new questions on the subject. Part of this work relates to the effort made by previous theoreticians, and their findings will be discussed in more detail in Section 1.2.3.

The epoxidation of alkenes with Mn(salen) complexes usually takes place in an oxygen-rebound mechanism similar to the one outlined in Figure 1.7. In the first stage of the catalytic cycle, manganese(III)-salen reacts with a terminal oxidant that must be present at stoichiometric amounts in order to form an oxo-manganese(V)-salen intermediate (henceforward, oxo-Mn(salen)). The second stage of the reaction consists in the transfer of the oxygen atom from the oxo-Mn(salen) intermediate to the alkene. In this stage, oxo-Mn(salen) reacts with the olefin, yielding the epoxide and the Mn(salen) catalyst in its original (reduced) form [67].

This mechanism was originally proposed by Groves, Collman and respective coworkers for metalloporphyrin catalyzed oxidations [100–103]. However, the oxo-Mn(salen) intermediates are much more reactive than, for example, their chromium analogues, and were only identified in the late 1990's using mass spectrometry techniques [106].

It is believed that the enantioselectivity of Mn(salen) catalysts is defined early in the second stage, when the alkene approaches the oxo ligand. The pathway and orientation

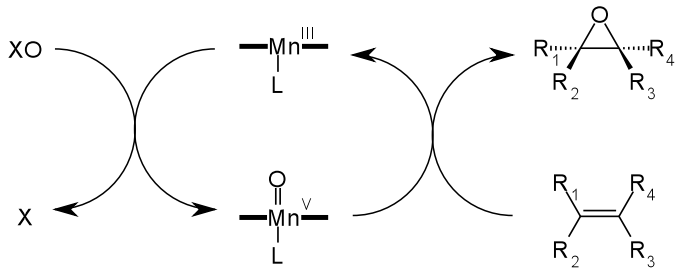

Figure 1.7: Oxygen-rebound mechanism for the Mn(salen) catalyzed epoxidation of alkenes. The structure of the salen catalyst is simplified by a horizontal bar around the Mn atom, XO represents the terminal oxidant, and L is a generic axial ligand.

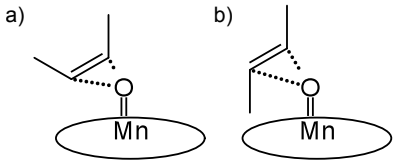

Figure 1.8: The side-on approach model for oxygen transfer showing the less hindered approach for the Z-alkene (a) than for a E-alkene (b).

of the approaching olefin to the catalyst are crucial factors for obtaining high enantioselectivity. This factor strongly depends on the steric and electronic properties of the substituents in the salen complex, as well as on the presence of a chiral diimine moiety [62]. Moreover, it is considered that the olefin approaches the active site of the catalyst in a side-on manner, as exemplified in Figure 1.8. This assumption satisfies the experimental observations that most Mn(salen) catalysts (as well as other salen complexes, and metalloporphyrins) are much more effective in the epoxidation of *Z*-alkenes than of *E*-alkenes [63]. Furthermore, Jacobsen observed that the incorporation of *tert*-butyl substituents at the 3,3' positions of the salen ligand is important for obtaining high enantioselectivity. Without such bulky substituents, the olefin can presumably approach the metal center from the sterically less hindered sites, away from the stereogenic carbon atoms depicted in Figure 1.3b. On the other hand, their incorporation would direct the approach of the olefin to the vicinity of the chiral diimine bridge [74].

While the side-on approach model has received wide acceptance, the mechanism of oxygen transfer from the oxo-Mn(salen) intermediate to the olefin remains controversial. Different reaction paths have been proposed for this step, the most relevant of which involve either a concerted transition state; the formation of a carbon radical intermediate; or the formation of a metallaoxethane intermediate (Figure 1.9) [36, 62, 63].

Kinetic experiments performed by Katsuky and co-workers shown a non-linear relationship between enantioselectivity and temperature, pointing to the existence of a reversibly formed intermediate. Katsuzy and co-workers postulated such intermediate to be a metallaoxethane (Figure 1.9c). The claims by Katsuky were further accompanied by postulating that oxo-Mn(salen) complexes would have a non-planar geometry, showing

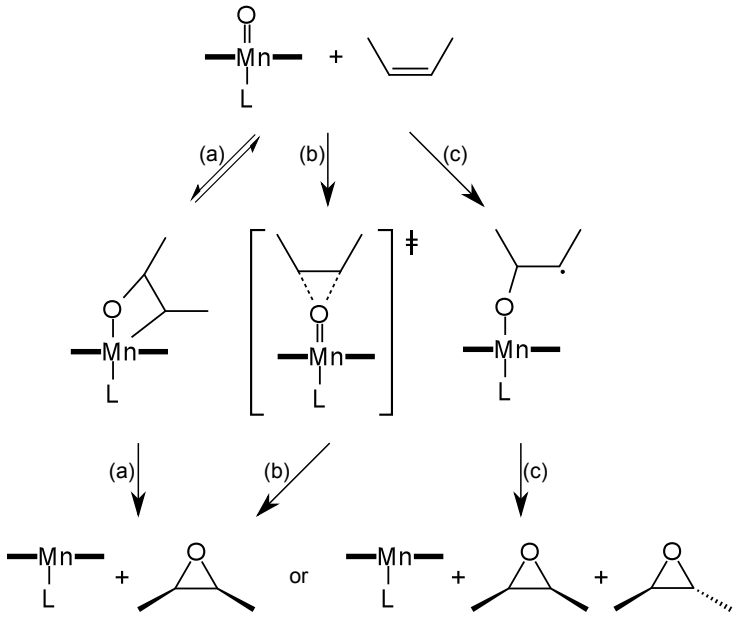

Figure 1.9: Proposed reaction paths for the oxygen atom transfer between oxo-Mn(salen) and an alkene:metallaoxethane intermediate (a); concerted transition state (b); and carbon radical (c).

highly bent, twisted, folded or stepped conformations [36,62]. Indeed, due to sterical constrains, the claims for the existence of a metallaoxethane intermediate may require the salen moiety in the oxo-Mn(salen) intermediate to lie in a non-planar conformation [36].

The kinetic studies conducted by Katsuki were criticized by Jacobsen and co-workers, who found the relationship between enantioselectivity and temperature to be linear over a wider range of temperatures than those tested by Katsuky and co-workers. Also, the use of a *N*-oxide axial ligand strapped to the salen scaffold further allowed Jacobsen and co-workers to contest the hypothesis of a metallaoxethane intermediate, on the grounds of the sterical repulsions that would exist for such an intermediate [107]. Furthermore, several studies advocate that the salen ligand in oxo-Mn(salen) intermediates lays in an approximately planar conformation [74,108], and the synthesis and X-ray diffraction study of a chiral nitrido-Mn-salen complex (a nitrogen analogue of oxo-Mn(salen) species) by Jepsen and co-workers revealed no severe deviations from near-planarity for the salen moiety [109].

The stereoselectivity of Mn(salen) complexes provides further insights into the oxygen transfer mechanism. As shown in Figure 1.9, reaction paths (a) and (b) should, in principle, lead exclusively to the epoxide that reflects the *E/Z* arrangement of the parent alkene (*syn* addition of the oxygen atom), whereas the product of an *anti* addition is better accounted for by postulating the existence of a radical intermediate. The nature of the alkene substrate appears to have a strong influence on the outcome of Mn(salen) catalyzed epoxidations: alkyl-substituted *Z*-alkenes usually attain high yields and stereoselectivities, leading to the hypothesis that such epoxidations may take place under a concerted mechanism (Figure 1.9b) [62,67]. On the other hand, the epoxidation of conju-

gated Z-alkenes produces mixtures of *cis*- and *trans*- epoxides, with the *cis*/*trans* ratio of the resulting epoxides depending on the nature of the substrate. Proponents of the metallaoxethane intermediate had argued that this decrease in stereoselectivity could emerge from the energy difference between two competing intermediates of that kind [110]. On the other hand, Jacobsen and co-workers proposed a carbon radical intermediate as a plausible intermediate in the epoxidation process (Figure 1.9b), yielding a simpler reaction model for this class of reactions [36, 74, 75].

Despite explaining the lack of stereospecificity in the epoxidation of conjugated Z-alkenes, the carbon radical pathway has met some criticism. In the late 1990's, Linde and co-workers used Mn(salen) complexes as catalysts in the epoxidation of phenyl-substituted vinylcyclopropanes, which serve as "radical clocks". These experiments allowed the rejection of a possible carbon radical, because no epimerization or cleavage of the cyclopropane was observed [111]. However, further kinetic studies made by the same authors allowed them to reconsider the possible formation of radical intermediates. According to Linde and co-workers, the product of a *syn* addition is justified by a concerted, although possibly asynchronous, reaction mechanism. On the other hand, a radical intermediate may be the cause for the incomplete stereoselectivity of these catalysts.

More recently, Kürti and co-workers rationalized the experimental data available at the time in order to propose an alternative model for this type of epoxidation reactions, mostly based on steric considerations. According to Kürti, electrostatic, van der Waals and $\pi - \pi$ interactions govern the stereoselectivity of Mn(salen) catalysts. Also, the oxygen-transfer step from the active oxo-Mn(salen) intermediate to the alkene could occur either in a concerted manner or via a carbocation intermediate, similar to the radical intermediate depicted in Figure 1.9, path (c). These two possibilities would be extreme idealized cases, and the stereospecificity for a particular substrate would be dictated by how close to either of these two extremes the actual reaction would occur [112].

1.2.3 Theoretical Studies

Because of its practical importance and the challenges raising from the uncertainties about its reaction mechanism, Mn(salen) catalyzed epoxidations have received considerable attention form the theoretical chemistry community. The application of theoretical methodologies to Mn(salen) complexes and their role as catalysts has been traditionally devoted to two questions: the characterization of the ground state of Mn(salen) species, and the characterization of the reactive intermediates (if any) in the oxygen-transfer step. Moreover, the applications of theoretical methods to the study of Mn(salen) species raised novel questions, such as the determination of the spin multiplicity of the ground state of each of those species; the approximations assumed when constructing a theoretical model for these reactions; and the choice of theoretical methods [36]. These questions will be briefly addressed here before exposing the findings from such studies.

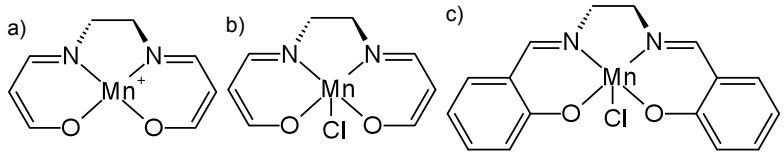

Figure 1.10: Models used in the theoretical studies of Mn(salen) complexes: a) Mn(3,3'-(ethane-1,2-diylbis-(azanylulidene))-bis(prop-1-en-olate), commonly referred as Mn(acacen')$^+$; b) [Mn(acacen')]Cl, and; c) [Mn(salen)]Cl.

The manganese (III) atom in Mn(salen) complexes has a $3d^4$ configuration. It has been suggested that the most stable electronic configuration of Mn(III) would involve having all four *d* electrons unpaired, yielding a quintuplet state. However, the fact that the salen ligand assumes a slightly bent conformation [74, 108] and the effect of axial coordination by a donor ligand may alter this outcome. A triplet (two unpaired *d* electrons) or a singlet (no unpaired electrons) ground state may therefore be viable hypotheses [113, 114]. At the same time, the manganese (V) atom in oxo-Mn(salen) species has a $3d^2$ configuration that allows one to postulate either a triplet or a singlet ground state. Again, the electronic structure of the Mn(V) atom will be influenced by the non-planarity of the salen ligand, the presence of the oxo- ligand and also the eventual presence of an axial ligand [36, 115].

Despite the technological improvements witnessed in recent years, the application of first principles calculations to Mn(salen) catalysts remains a costly procedure, in terms of computational effort. The evaluation of the total energy for a system as large as the Jacobsen catalyst at a fixed geometry is currently feasible under certain levels of theory. However, optimizing the geometry of such complexes is still a lengthy procedure. The search for transition states and the confirmation of their nature usually requires at least two computations of the nuclear Hessian matrix (Section 2.4.1) and the search for a saddle point in the Potential Energy Surface (PES) of the nuclear coordinates. These procedures become more complex as the number of degrees of freedom in the conformational space increases. The use of truncated models (Figure 1.10) as been advocated as a mean to achieve some knowledge on the electronic structure and reaction mechanisms of Mn(salen) complexes at a reasonable computational cost.

One popular simplified model for salen is the ligand usually abbreviated by the symbol acacen' (acacen' = $^-O(CH)_3N-C_2H_4-N(CH)_3O^-$, 3,3'-(ethane-1,2-diylbis(azanylylidene))-bis(prop-1-en-olate))). Mn(acacen') complexes such as those depicted in Figures 1.10a and 1.10b have been the most popular choice for characterizing the ground state of Mn(salen) complexes, and also to study their reactivity [116–120]. One of such models (Figure 1.10a) was first used as a surrogate for a proper Mn(salen) complex (Figure 1.10b) by Linde and co-workers in 1999 [121]. This practice was later followed by Jacobsen and Cavallo, who sought validation for this procedure in a QM/MM study of the reactivity of Mn(salen) catalysts. Under this approximation, the Mn(acacen') system was treated under a first principles quantum mechanical approach, while the atoms belonging

to the outer aromatic rings of salen and their respective substituents were treated using classical mechanics [122]. In a later work, the same authors asserted the validity of using Mn(acacen') as a model for Mn(salen) based on the relative energies of the different states associated with the manganese complexes [123]. Indeed, only a handful of works present results from theoretical calculations performed using a proper Mn(salen) system (Figure 1.10b) [123–125]. The use of truncated models has met some criticism from McGarrigle and Gilheany, due to an inappropriate representation of the conjugated π system associated with the salen ligand [36]. Moreover, recent works have attributed the discrepancies between different theoretical studies to the use of truncations [112, 126, 127]. The question of whether the truncated models Mn(acacen') and Mn(salen) are appropriate representations for larger catalysts, such as the Jacobsen catalyst (Figure 1.4a), was investigated in this work (see Chapter 5). This is the first known contribution in this field since the early works of Jacobsen and Cavallo [122, 123].

Density Functional Theory (DFT) has been the preferred theoretical approach for the study of the electronic structure and reactivity of Mn(salen) catalysts, as it offers reasonable approximations to the energy involved in electron correlation at a reasonable computational cost. The rudiments, advantages and drawbacks of DFT are discussed in Section 2.3. Abashkin *et al.* [115] confronted the results obtained from DFT with those obtained from Coupled Cluster (CC) theory, at the CCSD(T) level of approximation. The DFT calculations were performed using two different functionals, with a pure density functional (BP [128, 129]) predicting a singlet ground state and a hybrid-GGA functional (B3LYP [130]) predicting a quintuplet ground state. The results from CC calculations suggested a singlet ground state being preferred over states of higher spin multiplicity. However, the high cost of CC calculations forced Abashkin and co-workers to use Mn(acacen') (Figure 1.10b) as a model for Mn(salen). In this particular case, the use of truncated models may be regarded as a question of lesser importance, as both theoretical methods were applied to the same model compound. On the other hand, the chosen basis set (Section 2.1) and criterion used to limit the active space in CC calculations may have influenced their results. While DFT calculations were performed using a Split Valence (SV) basis set with some polarization, CC calculations were performed either using the same SV basis set or by applying a triple-ζbasis set for some atoms and restricting the active space of the CC procedure to only the most energetic occupied orbitals. Both procedures translate into additional truncations to the systems. Furthermore, neither the accuracy of DFT is fully explored using such limited basis set, nor the CC method can assure reliable results with so many restrictions [131]. Moreover, the energy of the different states changes significantly when changing basis sets, indicating that the CC results are not converged with respect to the basis set [127].

Complete Active Space Self-Consistent Field (CASSCF) calculations on Mn(acacen') models were performed independently by Ivanic, Sears and their respective teams, starting in 2004 and arriving at different conclusions [116, 117]. According to Ivanic *et al.*,

oxo-Mn(salen) complexes have a triplet ground state, with the first excited singlet state lying about 10 $kJ \cdot mol^{-1}$above it [116]. On the other hand, the calculations performed by Sears and Sherril in 2006 [117] arrived at a singlet ground state with two nearly degenerated triplet states lying approximately 12 $kJ \cdot mol^{-1}$above the ground state. In the same work, Sears and Sherril also compared the results obtained using several density functionals to the results of their CASSCF calculations, and although they pointed out that non-hybrid functionals gave results in qualitative agreement to CASSCF, they were unable to conclude on the overall quality of DFT calculations . Both works rely on SV basis sets with minimal polarization; Ivanic further resorted to Effective Core Potentials (ECP) in order to allow more polarization to be used in the description of the manganese and chlorine atoms. This latter strategy was used in 2009 by Takatani, Sears and Sherril [119, 120] in the benchmark of several density functionals against state averaged CASSCF using the cationic model in Figure 1.10a. These authors concluded that, in principle, DFT (particularly using hybrid density functionals) should provide reliable results [119, 120]. However, their work also relies on SV basis sets with minimal polarization, and moreover, the cationic model they use had already been considered unfit to give a meaningful representation of either Mn(acacen')Cl or proper Mn(salen) complexes. As a result, the calculations by Sears and Sherril in 2009 [119] (cationic model) invert the ordering of the spin states found years earlier by the same authors, on the neutral model in Figure 1.10b. A definitive comparison between DFT and post-Hartree-Fock methods, for treating systems as large as Mn(salen), has not been fully reached due to the limitations of the computational resources. For next times, it is also plausible that this question will remain confined to the realm of pure computational chemistry. In this work, DFT calculations were used as an useful tool for modeling the properties and reactivity of these compounds. From this perspective, the present work shares the general philosophy portrayed in the works of Cavallo and Jacobsen [132].

Despite their shortcomings, several theoretical studies have provided interesting insights on the mechanism of Mn(salen) epoxidation. The reaction between Mn(salen) catalysts and terminal oxidants — the first stage of the catalytic cycle as depicted in Figure 1.7— has received limited attention from the theoretical chemistry community. The reaction of H_2O_2 with Mn(salen) complexes was studied by Abashkin and Burt [70, 125] in order to access the catalase mimetic activity of Mn(salen) complexes. Their DFT calculations suggest that H_2O_2 disproportionation may occur in the presence of Mn(salen) yielding two water molecules and oxygen with an activation barrier of less than 10 $kJ \cdot mol^{-1}$.

On the other hand, the oxygen transfer step in Mn(salen) catalyzed epoxidation has received considerable attention. As stated, most studies have been performed using DFT and Mn(acacen')Cl (Figure 1.10b) as a surrogate model for Mn(salen). However minor differences in the computational procedures led to diverse results.

The first theoretical study on Mn(salen) catalyzed epoxidations was reported by Linde *et al.* in 1999 [121]. This work was performed using the $Mn(acacen')^+$ model (Figure

1.10a). Their findings allowed them to associate the reaction in the quintuplet surface to that of a concerted mechanism (path (b) in Figure 1.9). In the triplet surface, however, the reaction mechanism would follow a radical intermediate (path (c) in Figure 1.9). The authors then concluded that the reaction would begin by alkene attack on the triplet surface, followed by spin crossing to the quintuplet state. The stereospecificity of the reaction would be dictated by the amount of time the system was allowed to stay in the triplet state, due to the radical character of the first transition state in the triplet surface and the fact that formation of the epoxide is concerted and almost spontaneous in the quintuplet surface [121].

The work by Linde and co-workers was criticized by Cavallo and Jacobsen and also by Abashkin and co-workers. By performing similar calculations at the same level of theory as Linde and co-workers, Cavallo and Jacobsen were able to devise a mechanism in which the oxygen transfer step occurs in the triplet surface, without the need for a spin-crossing path [133]. According to Cavallo and Jacobsen, the imperfect stereoselectivity is justified by the formation of a carbon radical species. In this carbon radical, the groups bonded to one of the carbons participating in the olefinic bond would be free to rotate, and the more stable the carbon radical would be, the less stereospecificity would be observed [133].

In their turn, Abashkin and co-workers argued that the controversial spin crossing mechanism, as well as the ordering of the spin states obtained by Linde and co-workers were the result of using Mn(acacen′)$^+$ instead of Mn(acacen′)Cl [115]. In an early stage, Abashkin and co-workers favored the competing reaction channels scheme (originally proposed by Linde and co-workers, in their kinetic studies [111]) as an explanatory model for the stereoselectivity of Mn(salen) catalyzed epoxidations [115]. Their position was latter revised after performing DFT calculations on a full Mn(salen) complex (Figure 1.10c). In this latter work, the authors revisit the spin crossing mechanism, stating that the oxygen transfer step would start at the singlet ground state of the oxo-Mn(salen) complex leading to a concerted mechanism (path (b) in Figure 1.9). However, because the activation energy in the singlet surface is too high, a spin crossing to the triplet surface was plausible. In the triplet surface, the oxygen transfer step occurs *via* a radical intermediate. Thus the stereoselectivity of the reaction would depend on the likelihood of this spin crossing process, which in turn would be affected by the nature of the substrate and changes in the catalyst [125].

Cavallo and Jacobsen have consistently championed the idea of a radical intermediate in the oxygen-transfer step of Mn(salen) epoxidations (path (c) in Figure 1.9) [123, 132–137]. Cavallo and Jacobsen explored the three basic mechanisms depicted in Figure 1.9 using different density functionals, and concluded that pure functionals, specially BP86 [128, 129], were best suited for the development of reaction models that conformed with the experimental observations. On the other hand, the popular hybrid density functional B3LYP [130] tends to stabilize the states with higher multiplicity. This deviation was

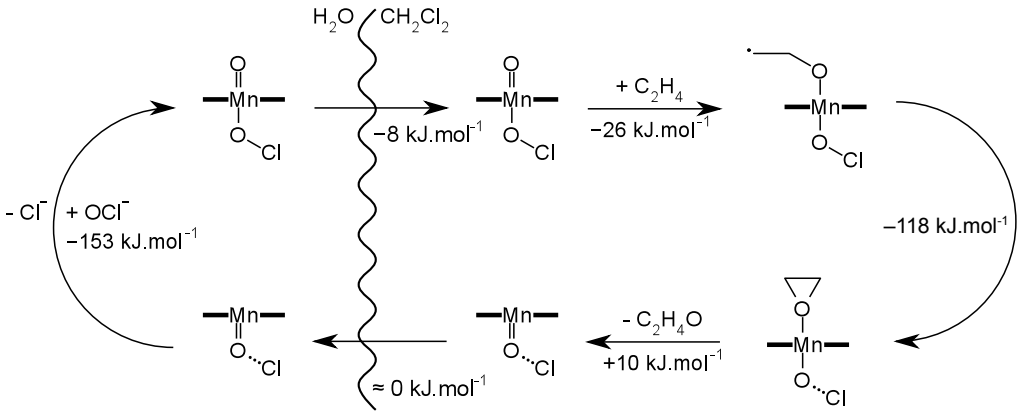

Figure 1.11: Catalytic cycle of Mn(acacen')ClO in a biphasic water/dichloromethane medium. The structure of the acacen' moiety is represented in a simplified fashion, using black bars around the manganese atom.

partially corrected, obtaining a better qualitative agreement with the pure density functionals [136], by the modified functional B3LYP* [138, 139] that uses a smaller weight of the Hartree-Fock exchange.

Using a combined QM/MM technique, Cavallo and Jacobsen not only stated the adequacy of Mn(acacen') complexes as surrogates of Mn(salen), but were also able to probe the different paths of approximation between oxo-Mn(salen) complexes and their substrate. They concluded on the importance of the bulky substituents on the diimine bridge and the 3,3' positions of the salen ligand, while stating the very limited steric effect of large substituents at the 5,5' positions, in accordance with the experimental observations by Jacobsen, Katsuky and their respective co-workers [122]. According to the model prosed by Cavallo and Jacobsen, the stereospecificity observed in this reaction derives from the relative stability of the radical intermediate: an unstable radical intermediate would promptly collapse in order to form the epoxide, whereas more stable intermediates would allow rotation of the substituents in one of the olefinic carbon atoms before the formation of the second C−O bond [122, 132–134]. Spin crossing situations are discarded, together with the possible existence a metallaoxethane intermediate, on energetic grounds [122, 132, 134, 137]. The crowning achievement of Cavallo and Jacobsen was the proposal of a model for the catalyzed ethylene epoxidation, arriving at the complete catalytic cycle depicted in Figure 1.11 that develops exclusively on the triplet surface [135]. In this work, they used Mn(acacen') as a model for Mn(salen) in a biphasic (water/dichloromethane) medium and ClO^- as both terminal oxidant and axial ligand. However, the approach taken by Cavallo and Jacobsen to model Mn(salen) catalyzed epoxidations did not prove satisfactory for explaining the effect axial coordination to the manganese atom over the development of the reaction course [137]. Results in this work (specially Chapters 5 and 6) may shed some light on this inconsistency found in the model by Cavallo and Jacobsen.

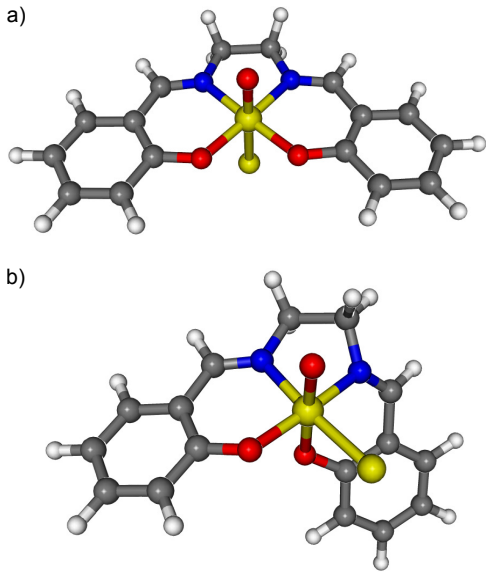

Figure 1.12: *Cis* (a) and *trans* (b) isomers of oxo-Mn(salen)Cl.

Both the teams of Abashkin and Cavallo followed the ideas of Kochi and Jacobsen, using a planar model for Mn(salen). On the other hand Khavrutskii *et al.* [124] pursued the hypothesis of a non-planar, highly bent, conformation of the salen moiety in oxo-Mn(salen) complexes proposed by Katsuki in the 1990's [62, 78]. In particular, Khavrutskii *et al.* [124] studied the epoxidation of ethylene using a proper Mn(salen) model (Figure 1.10c) and a peroxyacid (CH_3COOOH) as terminal oxidant. Their work is singular as it considers the oxygen transfer step from either *cis*-oxo-Mn(salen) and *trans*-oxo-Mn(salen), depicted in Figure 1.12. Moreover, in this work the energies of the molecular geometries at each stationary point (product, reactant or transition state) were refined using a basis set of triple-ζ at a standard B3LYP level of theory. Their results suggest that, starting from *cis*-oxo-Mn(salen) the oxygen transfer step may occur solely on the triplet surface, via a radical intermediate. Indeed, a similar radical intermediate was identified also in the quintuplet surface. The same is also the general case for the reaction path starting from *trans*-oxo-Mn(salen). Despite this, in the particular case of imidazole-coordinated complexes a concerted mechanism was observed in the quintuplet surface. Also, these authors confirmed the *cis* form of oxo-Mn(salen) complexes as being more stable than their *trans* isomers [124].

The behavior of immobilized Mn(salen) complexes was probed by Malek and co-workers [126, 140] in two different studies. In the first study, Molecular Dynamics (MD) simulations were performed in which the movement of all atoms was treated using classical mechanics. Because bond-forming and bond-breaking situations cannot be accounted for in classical mechanics, the study focused on the minima found in the triplet surface by Cavallo and Jacobsen [134, 135]. As MD is much less demanding than DFT and other first principles calculations (in terms of computational effort), the authors

were able to explore the conformational space of these minima for the epoxidation of *Z*-β-methylstyrene and *E*-β-methylstyrene catalyzed by the Jacobsen catalyst. Moreover, the catalyst was immobilized in a nanopore of silica MCM-41 using a phenoxyl group as linker. Both outcomes of the epoxidation reaction (preservation or inversion of the arrangement of the methyl and phenyl groups of the alkene) were considered and the chirality content at each of the different minima was evaluated using the continuous chirality measurements devised by Avnir [141–143] (Section 2.4.4). Their main finding was that immobilization improved the chiral recognition of the catalyst, and that the use of an *E*-alkene imparts greater asymmetric induction onto the immobilized catalyst [126].

In a second study by the same authors, the reaction mechanism for the systems described above was probed using hybrid QM/MM calculations, in which part of the system was treated using DFT with a SV basis set with little polarization (except Mn, that was treated using a triple-ζ, the quality of which cannot be evaluated, as no polarization is mentioned in the published work). In order to accommodate the linker and the substrate in the DFT part of the system, an extreme truncation of the salen ligand was made, with only the nitrogen and oxygen atoms being treated under DFT, together with the two carbon atoms in the diimine bridge. The remainder of the system (*i. e.* most of the Jacobsen catalyst and the silica MCM-41 pore) were treated classically, using Molecular Mechanics (MM). Their results suggest that the silica pore has an important effect in the orientation of the substrate towards the catalysts. More importantly, the linker ligand bears a strong effect on the geometry of the active oxo-Mn(salen) complex, forcing the metal center to lay in the plane of the salen moiety and lengthening the bond between manganese and its oxo ligand [140].

1.3 Vanadyl (IV) acetylacetonate

The epoxidation of allylic alcohols, such as geraniol, plays a role in the production of fragrances and flavoring agents [144]. This can be easily achieved using TBHP or H_2O_2 as oxidants in the presence of catalytic amounts of molybdenum or vanadium complexes, this being the basic idea behind the Halcon process [68, 145]. The final part of this work probes the epoxidation of allylic alcohols using vanadyl (IV) acetylacetonate as catalyst (Chapters 7 and 8).

1.3.1 General Characteristics

Oxobis(2,4-pentanedionato)vanadium (IV), $VO(acac)_2$ (see Figure 1.13), commonly known as vanadyl (IV) acetylacetonate is a yellow solid at room temperature, easily soluble in both polar and non-polar organic solvents. In aqueous solution, one water molecule attaches to the vacant position of $VO(acac)_2$, giving rise to aquo-oxobis(2,4-pentanedionato)vanadium(IV), which may generate oligo- and polymeric vanadium(IV) species, or undergo oxidation, yielding vanadium (V) species [146]. The scope of applicability of

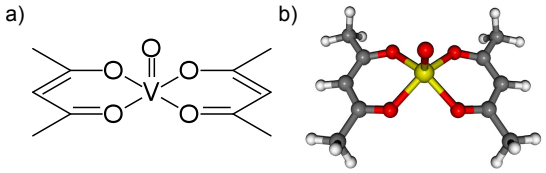

Figure 1.13: Structural formula (a) and ball-and-stick model (b) of vanadyl (IV) acetylacetonate ($VO(acac)_2$).

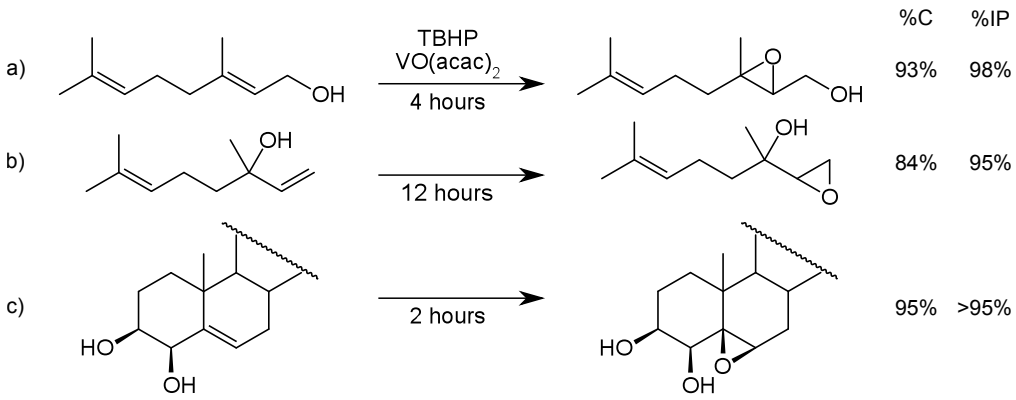

Figure 1.14: Examples of the $VO(acac)_2$ catalyzed regioselective epoxidation of allylic alcohols: %C represents the yield of the reaction, and %IP the isomeric purity of the main product.

$VO(acac)_2$ extends beyond its use as a catalyst in the epoxidation of allylic alcohols, being also used in the oxidation of alkenes to ketones [147], as a peroxide activator in the osmium catalyzed hydroxylation of alkenes [148], the oxidation of thiols to disulfides [149], or as an insulin mimetic [146].

In 1973, Sharpless and Michaelson [150] studied the epoxidation of olefinic alcohols by TBHP in the presence of $VO(acac)_2$. Their results are summarized in Figure 1.14 and show that $VO(acac)_2$ is a remarkable catalyst for the epoxidation of olefinic alcohols in general. Moreover, the epoxidation of polyunsaturated olefinic alcohols occurs regioselectively at the C=C bond that lies closer to the hydroxyl group. This latter observation is particularly true for allylic alcohols such as geraniol and linalool (Figures 1.14a 1.14b, respectively) [150]. Paying homage to their pioneering work, the $VO(acac)_2$ catalyzed epoxidation of allylic alcohols depicted is commonly called the Sharpless epoxidation process [43]. Furthermore, the epoxidation of 4β-hidroxylcholesterol presented some remarkable stereoselectivity, possibly due to the chiral induction by the two chiral centers in the vicinity of the targeted double bond (Figure 1.14c). This latter result allowed Sharpless to postulate that the substrate is somehow coordinated to the vanadium atom in the oxygen-transfer step of the catalytic cycle [150].

Experiments performed by Michaelson [151] suggested that the acetylacetonate ligands (acac) are promptly replaced by other donors. Thus, $VO(acac)_2$ is more accurately described as a catalyst precursor. A practical application of this is the addition of chiral hydroxamic acids or terpenoids to the $VO(acac)_2$/TBHP system, which resulted in enantiomeric excesses for the epoxidation of geraniol and linalool [152, 153].

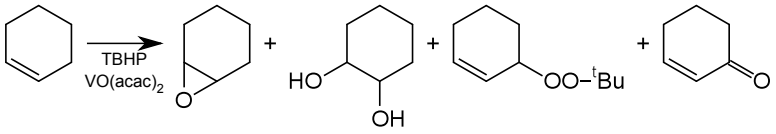

Figure 1.15: Possible reaction products formed during the oxidation of cyclohexene with the $VO(acac)_2$/TBHP system.

Moreover, the epoxidation of unfunctionalized alkenes using the $VO(acac)_2$/TBHP system is also possible, although the epoxidation process of an alkene such as cyclohexene may result in a number of side products such as cyclohexane-1,2-diol, *tert*-butyl-2-cyclohexenyl-1-peroxide, and 2-cyclohexene-1-one, beside the intended cyclohexene oxide (Figure 1.15), as noted by Leus *et al.* [154].

The development of heterogeneous and hybrid catalysts based on the $VO(acac)_2$ motif, although not as matured as the case of Mn(salen) catalysts, has been the stage for some interesting new strategies, with varying degrees of success. In 1996, Voort *et al.* [155] reported the thermal decomposition of $VO(acac)_2$ adsorbed on a silica surface, coating silica with a layer of vanadium oxide. This strategy was later adapted to an alumina surface, as reported by Baltes *et al.* [156], who also characterized the materials obtained before thermolysis took place. Their results showed that the outcome of the reaction of $VO(acac)_2$ with alumina prior to thermolysis varies as a function of the surface loading. Small surface loadings promote ligand exchange reactions that lead to the formation of vanadyl-alumina adducts, while at greater surface loadings the neutral and acidic hydroxyl groups of the alumina support become involved in hydrogen bond and ionic interactions with $VO(acac)_2$ or $VO(acac)^+$, respectively [156]. These bonded vanadium adducts decompose above 150° C forming vanadium oxide structures similar to those found in Voort's work [155]. In 2001 Baltes and co-workers [157] studied the reaction of $VO(acac)_2$ and mesoporous silica, achieving similar results to those found using alumina [156]. Both works concluded that the supporting material becomes covered with tetrahedral $(SiO)_3V{=}O$ monomers and that, with increasing surface loadings, polymeric chains of tetrahedral VO_x formed upon oxidation [157].

In 1997, Kumar and co-workers [158] bounded $VO(acac)_2$ to a polymer (chloromethylated macroporous divinylbenzene cross-linked polystyrene beads), as depicted in Figure 1.16a. The procedure was fairly simple, and the immobilized complex was tested as a catalyst in the hydroxylation of benzene. Despite some initial success, the formation of acetic acid was evident, and accounted for a loss of about 25% of the vanadium content of the material after four runs. After the catalyst was used for 6 times, the material became too brittle to be used. Further evidence was collected to ensure that the catalytic properties of the system were due to the immobilized catalyst and not to the vanadium metal that leached during the experiments . This strategy was latter adapted by Maurya and co-workers [159,160] in the immobilization of more involved vanadium (IV) and vanadium (V) complexes onto different polymeric materials, which were tested in the oxidation of

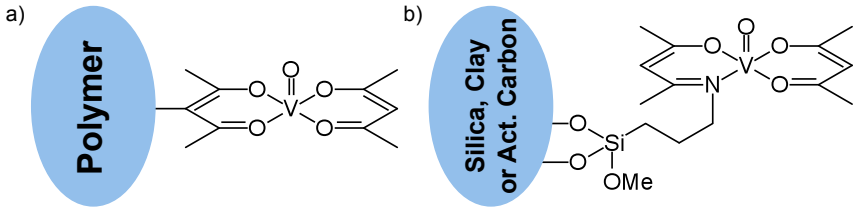

Figure 1.16: Examples of hybrid nanocatalysts obtained by immobilization of $VO(acac)_2$ onto different supporting materials: a) chrolomethylated polymer [158]; Schiff base condensation onto silica, clays or activated carbons [161–163].

cyclohexene. However, the major product was cyclohexene-1-ol, instead of cyclohexene oxide.

Schiff base condensation provides an alternative approach to the anchoring of $VO(acac)_2$, allowing it to be immobilized by reacting with a surface coated with amine groups. The functionalization of the supporting material is usually carried out using a bifunctional molecule which is able to react with the supporting material on one side and $VO(acac)_2$ on the other. Aminosilanes, particularly APTES, have been successfully used to anchor $VO(acac)_2$ to activated carbons [93, 162], clays [163], and silica [161, 164] (Figure 1.16b).

The catalytic activity of $VO(acac)_2$ anchored onto activated carbons is similar to that homogeneous $VO(acac)_2$ [162]. Similar results are obtained when using silica as the support material [161]. However, the presence of unprotected hydroxyl groups in the silica surface compromises the chemical stability of these hybrid materials [161]. The catalytic activity of $VO(acac)_2$ anchored onto a clay surface varies according to the support material and immobilization strategy. For example, $VO(acac)_2$ anchored to an APTES functionalized K10-montmorillonite achieves the same conversion rates as the homogeneous catalyst, with excellent chemical stability between run cycles. By comparison, $VO(acac)_2$ directly immobilized onto the surface of K10-montmorillonite rapidly loses activity between cycles, possibly due to leaching [163]. On the other hand, anchoring $VO(acac)_2$ to an APTES functionalized laponite results in a poor performing material which achieves less than 30% of the conversion rate of the free catalyst. However, direct immobilization of $VO(acac)_2$ to laponite allows for conversion rates of over 50% of the homogeneous catalyst, with relative stability against leaching of the catalyst [50, 163].

1.3.2 Catalytic Cycle

Taking into account its behavior in the reaction medium, $VO(acac)_2$ is more accurately described as a catalyst precursor. Because of this, a plethora of reactions are possible for the $VO(acac)_2$/TBHP system. The most comprehensive overview of the catalytic cycle of $VO(acac)_2$ is provided by Vandichel and co-workers [165] and consists in the principle of two main reaction families: activation of vanadium (IV) and vanadium (V) complexes and epoxidations, in which the active complexes are rendered inactive again (Figure 1.17). Radical decomposition reactions allow the modification of the oxidation state of vanadium from IV to V and vice-versa, and several ligand exchange reactions are possible.

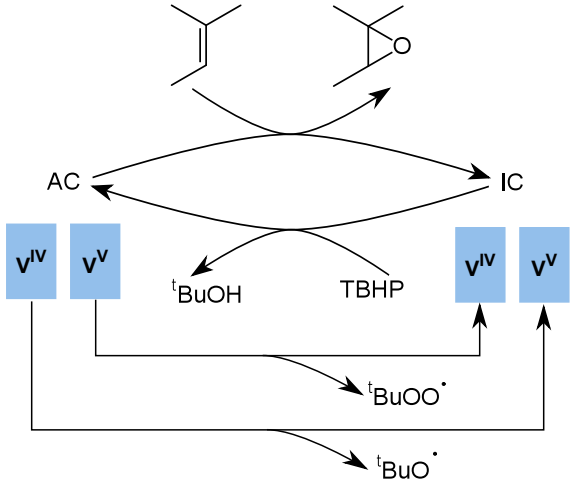

Figure 1.17: General overview of the reaction families involved in the $VO(acac)_2$/TBHP epoxidations, showing the transformation between active complexes (AC) and inactive complexes (IC). The scheme considers *tert*-butanol as the main by-product of TBHP in the activation step and also the possible side reactions that allow the transition between the two oxidation states of vanadium.

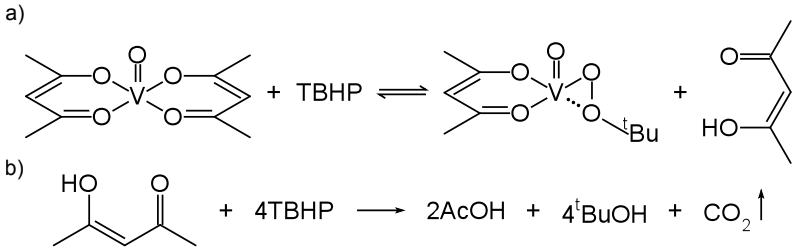

Figure 1.18: Ligand exchange reaction in the initial stages of the catalytic cycle (a), and oxidation of acetylacetone(b).

Moreover, the acetylacetonate ligands are likely to to undergo irreversible oxidation to acetic acid (AcOH) and CO_2 in the early stages of the reaction [166, 167].

A key factor in the complexity of the reaction mechanism is the number of potential ligands in the reaction media. Considering the $VO(acac)_2$ catalyzed epoxidation of an unfunctionalized alkene, at the beginning of the reaction, the system is most likely to form adducts between $VO(acac)_2$ and TBHP [168–170]. Is has been proposed that $VO(acac)_2$ looses at least one of its acetylacetonate ligands in the initial stages of the catalytic cycle, with formation of acetylacetone (Hacac). Acetylacetone may in turn be oxidized to acetic acid (AcOH). Due to the irreversibility of the oxidation process of Hacac, this species will become less abundant as the system evolves in time. This process was originally proposed by Stepovic and co-workers and accounts for the presence of AcOH in the reaction mixture [166, 167], as depicted in Figure 1.18. The development of AcOH during the course of the reaction further increases the complexity of the catalytic cycle, as it may participate in ligand-exchange reactions with several vanadium species.

As the reaction develops, more potential ligands become available, such as $^tBuO^-$, AcO^- and OH^-. These species are respectively originated from the use of TBHP in the epoxidation reaction, the oxidation of acac, and from proton transfers to the oxo moiety

of the vanadyl group [165]. The different active complexes (AC) were classified by Vandicel *et al.* [165] in eight families, seven of which originate from four families of inactive complexes (IC), as depicted in Figure 1.19. Several equilibria are established between IC's and AC's with the same oxidation state of the metal center, as depicted in Figure 1.20. The eighth family of active complexes, AC8, may be the result of either from a rearrangement of AC5 or the abstraction of one of the ligands in a AC6 complex, as shown in Figure 1.20. Furthermore, the oxidation of vanadium (IV) to vanadium (V) is accounted for *via* radical decomposition of an active vanadium (IV) complex, with release of $^{t}BuO^{\cdot}$. In a similar manner, reduction from vanadium (IV) to vanadium (V) may occur via the homolytic cleavage of the O−O bond in an active vanadium (V) complex, as exemplified in Figure 1.21. However, it should be noted that an overwhelming amount of experimental observations suggest that the reduction of vanadium (V) to vanadium (IV) is highly unlikely [153, 168–171].

As to the oxygen transfer step, experimental evidence suggests that the oxygen atom distal to the *tert*-butyl group is responsible for the epoxidation of the substrate's C=C double bond [150, 169, 172, 173]. In the 1970's, Mimoun and co-workers [32, 33] postulated that the π system of the olefin would coordinate to the vanadium atom, forming a five member ring intermediate that would resolve in the formation of the epoxide. Later, Sharpless and co-workers [42] proposed a three membered ring intermediate as an alternative hypothesis. According to Sharpless, the Mimoun mechanism is incompatible to the relative rate constants measured in kinetic experiments [42, 174]. On the other hand, the Sharpless mechanism correctly explains the high regio- and stereoselectivity in the epoxidation of allylic alcohols [150], the isotopic labeling experiments reported by Chong and Sharpless in 1977 [44], and the observations of Itoh *et al.* [172] on the epoxidation of cyclic allylic alcohols.

More recently, different theoretical groups studied the mechanism of several vanadium-catalyzed epoxidations using different ligands at the DFT/triple-ζ level of theory. In their quests, they were unable to find stable π-complexes between vanadium and the C=C double bond, which is required for a Mimouin-type transition state to develop [165]. By contrast, all transition states found in these calculations correspond to the general model predicted by Sharpless, with a slightly asynchronous concerted mechanism, and a three-membered ring-like structure at the transition state geometry [165, 175–178].

Under the Sharpless model, the eight families of active complexes depicted in Figure 1.19 can be classified into four major groups, according to the possible outcome of the epoxidation step: active complexes which are adducts of TBHP (AC1 and AC4), (*tert*-butylperoxo)vanadium complexes (AC2, AC3, AC5 and AC6), (*tert*-butylperoxo)(hydroxo)vanadium complexes(certain members of the previous group) and (peroxo)vanadium complexes (AC8). It is unlikely that AC7 complexes would participate in the epoxidation step, due to the steric hindrances between the five groups coordinated to the metal center. According to Vandichel *et al.* [165], the most likely fate of AC7 complexes would be dis-

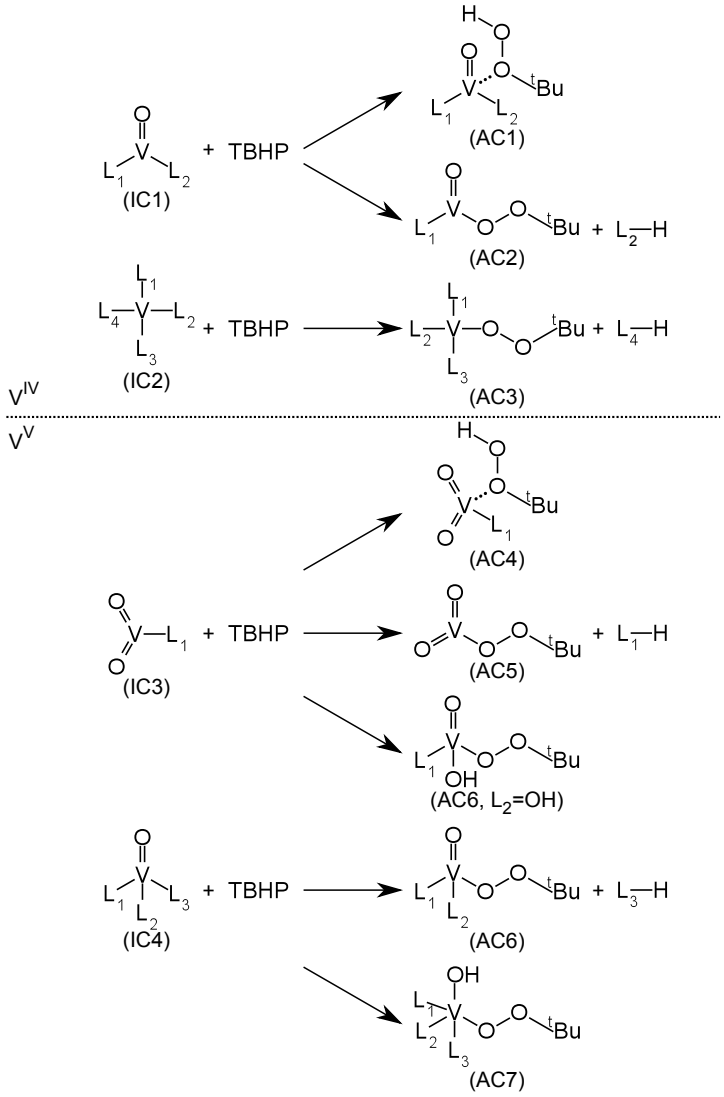

Figure 1.19: Generic structures for the inactive and active complexes in the catalytic cycle of the $VO(acac)_2$/TBHP system, and plausible activation reactions that link families of active and inactive complexes.

proportionation into an AC6 complex, with lost of one of its ligands (Figure 1.20), or loss of $^{t}BuOO^{\cdot}$, yielding an inactive complex of the IC2 family.

Figure 1.22 exemplifies the different fates of the four groups of active complexes mentioned above. For the adducts of TBHP (AC1 and AC4), the oxygen transfer step is coordinated to the transfer of a proton from TBHP to one of the ligands in the complex. Different outcomes are possible, depending on whether or not the proton is captured by the oxo ligand (Figure 1.22a). As shown in Figure 1.22b, (*tert*-butylperoxo)vanadium complexes AC2, AC3, AC5 and AC6 react in a more straight forward fashion, yielding the epoxide and returning to one specific type of inactive complex. This picture is more involved, should a hydroxo group be present in one of the previously mentioned complexes (Figure 1.22c). In that case, one additional reaction path is possible, as the hydroxo group may act as a proton donor, facilitating the release of $^{t}BuOH$ and restoring the vanadyl moiety. Finally,

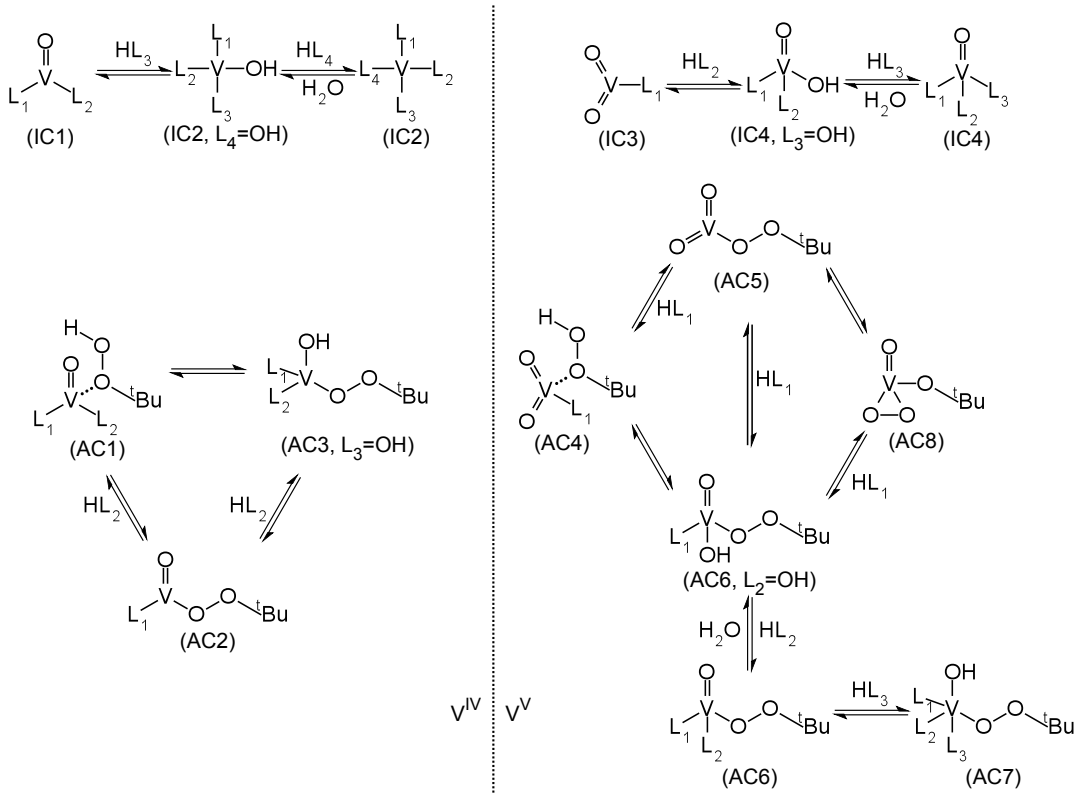

Figure 1.20: Equilibrium relationships between inactive complexes (IC) and active complexes (AC) with the same oxidation state of vanadium.

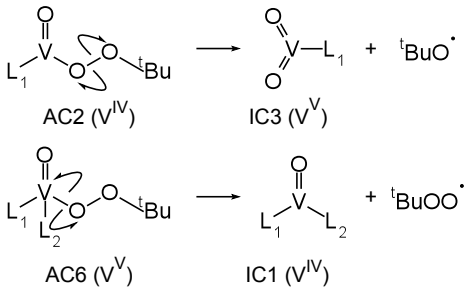

Figure 1.21: Examples of radical decomposition reactions that allow the oxidation of vanadium (IV) to vanadium (V), and vice-versa.

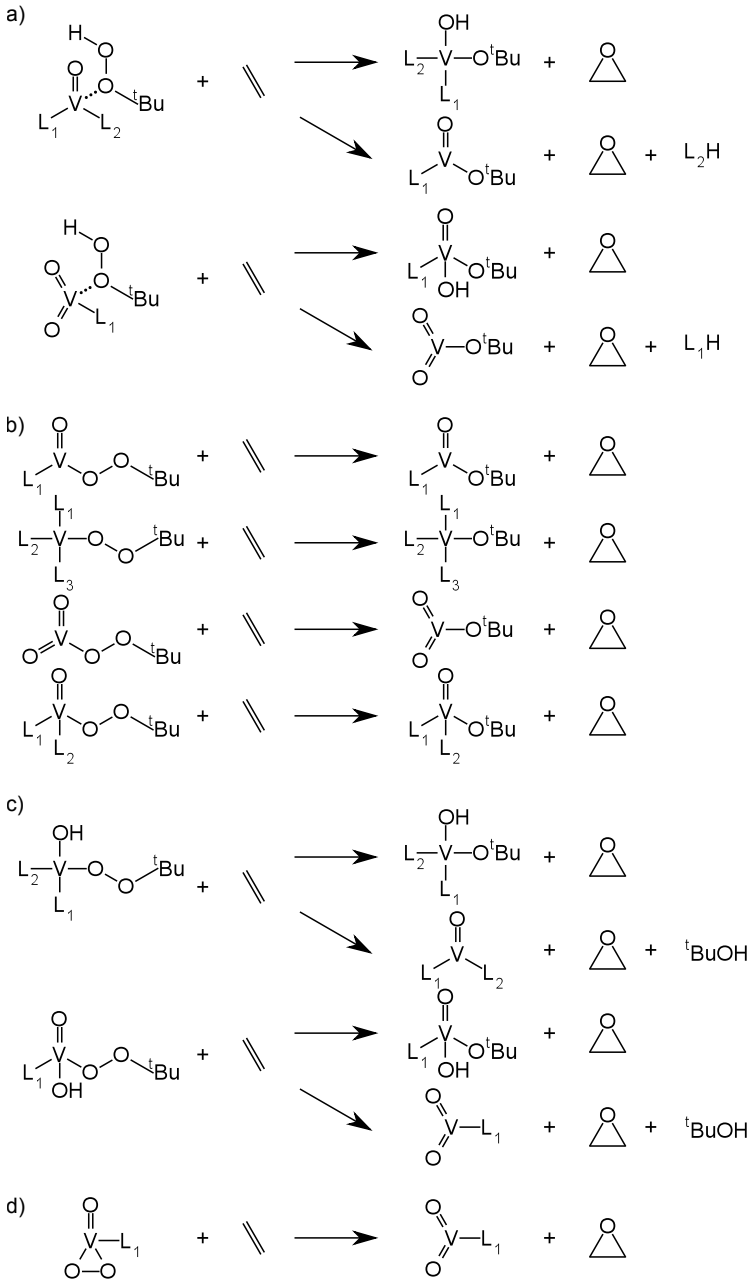

Figure 1.22: Examples of deactivation of the active vanadium (IV) and vanadium (V) complexes upon epoxidation of ethylene: a) possible outcomes for complexes AC1 or AC7; b) possible outcomes for ordinary (*tert*-butylperoxo)vanadium complexes; c) possible outcomes for (*tert*-butylperoxo)vanadium with a hydroxo group; and d) possible outcome for AC8 complexes.

AC8 complexes are likely to react in a manner similar to the ordinary (*tert*-butylperoxo)vanadium complexes. Nevertheless, previous studies, particularly that of Vandichel, report that the reaction energetics for AC8 is quite different from that of other active complexes, presenting a lower energy barrier towards epoxidation [165].

A few caveats need to be addressed when translating Vandichel's model for the $VO(acac)_2$/TBHP epoxidation of alkenes to the epoxidation of allylic alcohols. Both al-

lylic alcohols and their epoxides are possible ligands to vanadium, forming either alcohol-vanadium adducts, or alkyloxo complexes. Epoxidation of an alkyloxo ligand with a C=C double bond is not only possible, but the key factor for explaining the regioselectivity reported for the Sharpless epoxidation. Moreover, the coordination of the allylic alkyloxo to vanadium (V) may activate the double bond, due to the inductive effect of the metal center [44, 151]. In the particular case of geraniol as substrate, the coordination of the allylic alcohol to vanadium places the $C_{(3)}=C_{(4)}$ double bond in close proximity to the distal oxygen of the alkylperoxo ligand. This opens new possibilities for the epoxidation of the $C_{(3)}=C_{(4)}$ double bond, while the approach of the $C_{(6)}=C_{(7)}$ double bond to the alkylperoxo ligand is sterically hindered. However, both double bonds of geraniol may react with any of the active complexes in Figure 1.19 in the same fashion as an unfunctionalized olefin (*i. e.* with the substrate not coordinated to the metal center). This justifies the small percentage of $C_{(6)}-C_{(7)}$ epoxide formed in this reaction [31, 150, 153, 172].

In this work, the model for $VO(acac)_2$/TBHP epoxidations derived by Vandichel and co-workers [165] is expanded in order to include the specifics of the Sharpless epoxidation of allylic alcohols. Also, the development of novel hybrid nanocatalysts derived from $VO(acac)_2$ by Schiff condensation raises new interesting questions [161–163]. For example, according to the model presented above, the acac ligands are promptly displaced and irreversibly oxidized to AcOH and CO_2. However, it is not clear what is the role of the ligand that links the metal atom to the supporting material. Several hypotheses may be suggested, such as a similar fate to that of acac; a possible displacement from the coordination sphere of vanadium remaining available to recapture the metal at a later stage; or a stable binding to the metal center during the whole catalytic cycle should the N−V and O−V bonds that hold the vanadium atom to its support be strong enough. Some contributions to answer these questions are made in the second part of this work (see Chapter 7).

Chapter 2

Theoretical Methods

It is often said that the purpose of computing is insight, not numbers. In order to gain insight on the phenomena described in Chapter 1, different computational methodologies were employed. For example, the electronic structure of the relevant molecular species was evaluated using Density Functional Theory (DFT), which belongs to the arsenal of theoretical methods based in quantum mechanics. Because of this, this chapter starts by providing some elementary information on the principles of quantum mechanics, and some of the most relevant methodologies used in the study of chemical systems (Sections 2.1 and 2.2). Having this background in mind, we introduce DFT, with special emphasis on the Kohn-Sham formalism, which dominates the applications of DFT used in this work. Section 2.4 provides information on different methods employed to interpret the results from DFT calculations. This includes the determination of thermodynamic properties, effective atomic charges, analysis of the topology of the electron density and the treatment of chirality. Finally, Section 2.5 addresses some of the statistical procedures used, with particular focus on multivariate analysis methods such as Principal Component Analysis (PCA).

2.1 Principles of Quantum Chemistry

Quantum mechanics was developed in the first half of the 20th century in order to accommodate the experimental evidence that, at the atomic scale, matter does not behave in a manner similar to what is observed at the macroscopic scale [179]. The foundation of quantum mechanics is attributed to the work of Max Plank in 1900, in which the spectrum of the black body radiation is explained by postulating that the energy should be exchanged in discrete quantities [180]. Quantum chemistry may be defined as the branch of chemistry specialized in the development of explanatory models for the chemical and physical properties on matter though the application of quantum mechanics.

The central quest of quantum chemistry is to solve the time-independent Schrödinger equation [181]

$$\hat{H}|\Phi\rangle = E|\Phi\rangle \tag{2.1}$$

where $\hat{H}$ is the time-independent Hamiltonian, which is the operator associated to the total energy of the system. In Equation 2.1 Φ is an eigenfunction of $\hat{H}$ and E is the correspondent eigenvalue. Each state of the system is described by an eigenfunction of this type and its total energy corresponds to the associated eigenvalue. The molecular Hamiltonian is the sum of the operators for the kinetic energy of the nuclei, the kinetic energy of the electrons and the electrostatic interactions between all charged particles. The Born-Oppenheimer approximation assumes that electrons can adjust instantaneously their positions, for any modification of nuclear coordinates. In this context, for determining the electronic structure, Equation 2.1 can be reorganized by considering the nuclear coordinates as fixed parameters. This approximation is valid in most chemical applications of quantum mechanics and will be assumed throughout this work. Under the Born-Oppenheimer approximation, $\hat{H}$ only accounts for the kinetic energy of the electrons and the electrostatic interactions they experience. Within this framework,

$$\hat{H}|\Psi\rangle = \left(\hat{T} + \hat{V}_{\text{ee}} + \hat{V}_{\text{ne}}\right)|\Phi\rangle = E_{\text{el}}|\Phi\rangle, \tag{2.2}$$

where $\hat{T}$ is the kinetic energy operator, $\hat{V}_{\text{ee}}$ is the electron-electron interaction term, and $\hat{V}_{\text{ne}}$ represents the interaction between electrons and nuclei. For a system of N electrons and M nuclei these operators take the form (in atomic units[1]) [182, 183]

$$\hat{T} = -\frac{1}{2}\sum_{i}^{N}\nabla_i^2 \tag{2.3}$$

$$\hat{V}_{\text{ee}} = \sum_{i}^{N}\sum_{j>i}^{N}\frac{1}{|\mathbf{r}_i - \mathbf{r}_j|} \tag{2.4}$$

$$\hat{V}_{\text{ne}} = \sum_{i}^{N}\sum_{k}^{M} -\frac{Z_k}{|\mathbf{r}_i - \mathbf{r}_k|} \tag{2.5}$$

where Z_k is the nuclear charge of atom k. The total energy of the system is given by adding the potential energy due to the nuclear repulsions to E_{el}

$$E = E_{\text{el}} + \sum_{k}^{M}\sum_{l>k}^{M}\frac{Z_k Z_l}{|\mathbf{r}_k - \mathbf{r}_l|} \tag{2.6}$$

According to the laws of quantum mechanics, the set of eigenfunctions of the Hamiltonian, $\{\Phi\}$ defines the maximum amount of information that can be gained about the

[1] Atomic units will be extensively used in this chapter, as they render simpler expressions for the quantum mechanical operators. One atomic unit of energy (1 E_{h}) is equivalent to approximately 627 kcal.mol^{-1}, or 2526 kJ $\cdot$ mol^{-1}, and the atomic unit of length is equivalent to 0.529Å. In these units, the numerical values of $\hbar$ and $4\pi\epsilon_0$ are unity.

system. Because Schrödinger derived Equation 2.1 by adapting the classical wave mechanics to the principles of quantum mechanics) [181], each of these functions is commonly called a wavefunction. The wavefunction associated to the lowest energy is of primary concern to quantum chemistry, as it contains all the information on the system at its ground state. All other wavefunctions and their corresponding energies describe excited states [183]. Unless stated otherwise, the following discussion will refer to the ground state of chemical systems and their corresponding energies.

Without the use of special relativity, and the consequent use of the Dirac equation instead of Equation 2.1, the electron spin must be accounted as an *ad hoc* quantum effect. Each electron has a spin quantum number. The correspondent magnetic spin number (m_s) can have two possible values ($1/2$ or $-1/2$) These two states are translated into two spin functions α and β, which account for one additional degree of freedom for each electron [182].

The Pauli principle requires the wavefunction to be anti-symmetric with respect to the exchange between any two electrons. In fulfillment of this principle the wavefunction for a polyelectronic system is better represented as the determinant of one-electron functions (Slater determinant) [184]. Each one-electron function in the Slater determinant is called a spin-orbital function. Furthermore, Ψ must be univocal, continuous and square-integrable, this last requisite not being applicable when dealing with free particles [185].

Each one-electron spin orbital is usually expressed as a linear combination of atomic orbitals (LCAO). In all first principles calculation in this work, the atomic orbitals, ϕ_μ, are expressed in the form of Gaussian basis sets. These basis sets contain linear combinations of simple three dimensional Gaussian functions, $\chi_{\gamma,\mu}$, called primitives. Each atomic orbital, ϕ_μ, is in itself a linear combination of P primitives

$$\phi_\mu(\mathbf{r}_i) = Y_{l,m} \times \sum_{\gamma=1}^{P} d_{\gamma,\mu}\chi_{\gamma,\mu}(\mathbf{r}_i) \tag{2.7}$$

where $Y_{l.m}$ is the angular component of the orbital, and each function ϕ_μ is called a contracted Gaussian, in basis set nomenclature [186].

A minimal basis set must contain at least one contracted Gaussian with an adequate angular component for each occupied atomic orbital. These basis sets however are too rigid and have fallen out of use with the advent of the digital computer as a tool for quantum chemistry. A better description of the radial behavior of the electron density can be achieved by increasing the number of primitives used in each contracted Gaussian. Furthermore, the use of two contracted Gaussians to describe each atomic valence orbital allows for a better description of chemical bonding [187]. Basis sets constructed using this scheme are denoted split-valence (SV) of double-ζ valence (DZV) basis sets. Further flexibility may be obtained by using three contracted Gaussians per valence orbital, giving rise to triple-ζ valence (TZV) basis sets [182].

Additional flexibility of the basis set may be achieved by adding contracted Gaussians with the same radial distribution of the valence-shell functions, but higher angular momentum. These additional contracted Gaussians are called polarization functions, and a basis set that includes such functions is said to be a polarized basis set. Polarization plays a major role in giving the basis set the necessary flexibility to give accurate energies and wavefunction properties. Moreover, the correct description of anions usually requires the use of additional contracted Gaussians of lower angular momentum in the valence shell. Basis sets that include such functions are denoted augmented basis sets [182].

The basis set for an atom can be expressed by its contraction pattern, which denotes the number of orbital functions with a given angular momentum (*s*, *p*, *d*, *f*, etc) as well as the number of primitives in each orbital function. For example, the typical basis set used in this work to describe manganese atoms has the contraction pattern $\{842111/63111/411/1\}$, meaning that it has six orbital functions of type *s*, five orbital functions of type *p*, three of type *d*, and one of type *f*. Furthermore, the orbital function of type *f* has only one primitive, as do two of the *d*-type orbitals, while the other *d*-type function is a contraction of four primitives, with more complex contraction pattern in the *p* and *s*-type functions [182].

The spin multiplicity, given by $2S + 1$ with S being the total spin quantum number, is an important property of a chemical system. This property corresponds to the number of combinations for the electronic spin, compatible with the symmetry of the respective ground state wavefunction. The spin multiplicity can be also assumed as an indirect evaluation of the amount of the unpaired electronic spin in the same state. While a closed shell system is characterized for having all their electrons paired ($S = 0$) yielding a spin multiplicity of 1 (singlet), an open-shell systems may have any spin multiplicity. The most common open-shell systems have one to five unpaired electrons giving spin multiplicities of 2 (doublet), 3 (triplet), etc. The concept of spin multiplicity is specially important in transition metal complexes in which the metal's *d* orbitals are partially filled, allowing states with different spin multiplicities to lie close in energy [188]. Because the electron spin acts as a fourth degree of freedom for electrons, defining the spin multiplicity for a given wavefunction acts as a symmetry constrain on the wavefunction [189, 190].

The central problem in quantum chemistry is to determine the ground state wavefunction. Because $\hat{V}_{ee}$ operates on the coordinates of each possible pair of electrons the application of Equation 2.2 to a polyelectronic system results in a system of second-order differential equations with non-separable variables, which is impossible to solve analytically. The next few sections of this Chapter are an overview of the most relevant numerical techniques used to obtain approximated solutions for this equation. These include Hartree-Fock (HF), approach, post-Hartree-Fock methods and the DFT formalism.

2.2 Wavefunction Methods

Wavefunction methods aim to achieve numerical solutions to the application of Schrödinger equation to polyelectronic systems. In its broadest sense, this is a huge family of methods with very different accuracies, ranging from very crude to very-high-level approximations of Ψ. The cornerstone of wavefunction methods is the Hartree-Fock approximation. Empirical parameters can be used to simplify the Hartree-Fock equations, giving rise to semi-empirical methods, which are not covered in this work. On the other hand, the Hartree-Fock wavefunction is usually the starting point for more advanced techniques [182].

2.2.1 The Hartree-Fock Approximation

The first successful approach to obtain approximate solutions to Equation 2.2 was developed by Hartree and Fock in the late 1920's. The fundamental idea behind the Hartree-Fock (HF) approximation is the possibility of approximating $\hat{V}_{ee}$ by a mean-field potential, yielding an independent-particle model for the electrons [191, 192]. Assuming that the wavefunction can be expressed as a single Slater determinant (Equation **??**) the independent particle model allows each spin-orbital to be treated by a (quasi-independent) equation similar to Equation 2.1

$$\hat{H}_{HF}\phi_i = \epsilon_i\phi_i \tag{2.8}$$

forming a system of K equations (one for each spin-orbital) that is known as the Hartree-Fock equations in which ψ_i is one of the set of K spin-orbitals and ϵ_i represents its energy. Because HF is an independent-particle model, the total electronic energy is the sum of the energies of all occupied spin-orbitals. However, for correcting the effect of double counting, the average interaction energy between the electrons has to be subtracted to this quantity. The Hartree-Fock Hamiltonian, also known as the Fock operator, is defined as

$$\hat{H}_{HF} = \hat{H}_{\text{core}} + \sum_{i}^{N_{occ}}\sum_{j>i}^{N_{occ}}\left(\hat{J}_{ij} - \hat{K}_{ij}\right) \tag{2.9}$$

where $\hat{H}_{\text{core}}$ is the one-electron Hamiltonian of a single electron under the potential of the nuclei; i. e. the sum of the one-electron operators $\hat{T}$ and $\hat{V}_{ne}$ (Equations 2.3 and 2.5). The remaining terms in Equation 2.9 are shorthand for the two-electron operators dealing with the coulombic interaction between the electrons ($\hat{J}$) and the exchange interaction ($\hat{K}$), the latter of which represents a purely quantum effect that derives from Pauli's principle [183]. These operators take the form

$$\hat{J}_{ij} = \langle\phi_i|\phi_j\rangle\frac{1}{r_{1,2}}\langle\phi_i|\phi_j\rangle \tag{2.10}$$

and

$$\hat{K}_{ij} = \langle\phi_i|\phi_j\rangle\frac{1}{r_{1,2}}\langle\phi_j|\phi_i\rangle \tag{2.11}$$

The Hartree-Fock Hamiltonian contains the spin orbitals that it is trying to determine. This implies that the coefficients $C_{\mu,i}$ in Equation **??** must be given from educated guesses of from the results of simpler calculations. At the same time, the variational principle assures that, for any trial wavefunction Ψ_{trial} [184, 193, 194]

$$E_{\text{GS}} \leq \frac{\langle \Psi_{\text{trial}} | \hat{H} | \Psi_{\text{trial}} \rangle}{\langle \Psi_{\text{trial}} | \Psi_{\text{trial}} \rangle} \tag{2.12}$$

where E_{GS} is the ground state energy. The purpose of the Hartree-Fock method is to find the set of coefficients $C_{\mu i}$ that minimize the total energy of the system [195]. This is accomplished by solving the determinantal equation known as the Roothann equation [194]

$$\mathbf{FC} = \mathbf{SC}\epsilon \tag{2.13}$$

where **C** is a $K \times K$ matrix with the coefficients from the LCAO expansion, ϵ is a diagonal matrix with the orbital energies, **S** is the overlap matrix between the different atomic spin orbitals and **F** is the Fock matrix, whose elements are the the sums of one- and two-electron integrals in Equation 2.9 [182, 186]. The resulting coefficients in **C** are used to generate a new Slater determinant which can be used in the following iteration of this process. The better the Slater determinant approaches the real wavefunction for the system, the lower its energy is. This minimization is carried on under the restrain that the spin orbitals must be orthogonal

$$\langle \phi_i | \phi_j \rangle = \delta_{ij} \tag{2.14}$$

in which $\delta_{i,j}$ is Dirac's delta function. When successive solutions for the wave equation are equal (within the desired numerical accuracy), the solutions are called 'self-consistent'. In his original work, Hartree actually refers to the field generated by the charge density, thus coining the term Self-Consistent Field (SCF) when referring to the solutions obtained using this method [192].

The HF method simplifies the exact treatment of a system of N electrons by introducing the mean field approximation. This implies that the coulombic interaction between electrons is given by integrating the repulsion term in Equation 2.4. Such an approximation gives the average effect of the electron-electron interaction, but not the explicit (instantaneous) interaction between electrons. Because of the mean-field approximation, HF energies are always greater than the exact energy. On the other hand, HF is a variational method, meaning that the approximate energies are always upper bounds of the exact energy [196].

The HF method requires the computation of several integrals spreading over the position of two electrons. The computation of these two-electron integrals is the most time-consuming part of the Hartree-Fock procedure. Formally, for a system with M_{basis} basis functions the computational cost of a Hartree-Fock iteration scales as M_{basis}^4. However, this cost can be greatly reduced by taking advantage of the symmetry of the wavefunction

and further developments in integral evaluation software allows for nearly linear scaling to be achieved in some cases [182].

Closed shell systems (singlets) may be treated under the Restricted Hartree-Fock (RHF) approximation, in which spin orbitals which differ only in their spin coordinate share the same LCAO coefficients. This approximation brings a significant cost reduction in computational effort when calculating the two electron integrals mentioned above [182].

The application of HF to open-shell systems may be carried under different formalisms, the most famous being the Restricted Open-shell Hartree-Fock (ROHF) and the Unrestricted Hartree-Fock (UHF) methods. In both cases, the number of α and β electrons is deduced from the spin multiplicity of the system, which is supplied as a parameter for the calculations.

Under the ROHF formalism, the energy and spatial distribution of the α spin orbitals is coupled to those of the β spin orbitals [197]. This coupling however is not clearly defined and different coupling schemes are available, giving rise to different energies for the virtual orbitals [198].

On the other hand, UHF treats α and β spin orbitals independently, using two coupled Roothaan equations (one for each set of electrons) and yielding two different sets of orbitals [199]. This causes the α and β spin orbitals to be different in shape and energy, and the application of the spin momentum operator, $\hat{S}^2$, gives expectation values for the spin multiplicity which are usually greater than the value supplied. This phenomenon is called spin contamination and can be portrayed as the inclusion of states of higher spin multiplicity into the UHF wavefunction. This effect is called spin contamination, and may be interpreted as the UHF wavefunction including contributions from states with higher spin multiplicity. Because the α and β spin orbitals from the ROHF wavefunction are coupled, the expectation value for the spin multiplicity is always the one supplied to the calculation, yielding no spin contamination [194, 197]. On the other hand, the properties of spin dictate that the pairing of α and β spin orbitals in the ROHF approximation is an additional constrain on the system. Because of this, the energy of an UHF wavefunction is always lower than that of the ROHF equivalent for the same system [182].

2.2.2 Electron Correlation Methods

The Hartree-Fock method provides an approximation of the state of lowest energy for a given symmetry (usually the ground state) of a polyelectronic system. This may be improved by using more flexible basis sets to express the wavefunction. However, even with an infinite basis set, the HF energy will tend to a value (the so called Hartree-Fock limit) higher than that experimentally observed. This is a consequence of the mean field approximation. The difference between the total electronic energy of a system and its Hartree-Fock energy is called the correlation energy. Several methods are available to improve HF, recovering at least part of the correlation energy. Two such methods (config-

uration interaction and coupled cluster theory) have been applied to the transition metal systems studied in this work. A brief discussion on such methods is therefore in order. Despite having different origins and theoretical support, the implementation of both method reflects the idea that (within the LCAO formalism) the true wavefunction is better approximated as a linear combination of Slater determinants [189].

Configuration interaction (CI) methods are multi determinant methods in which the wavefunction can be written as

$$\Psi_{CI} = a_0\Psi_{HF} + \sum_{i=1} a_i\Psi_i \tag{2.15}$$

where Ψ_{HF} is the Hartree-Fock solution for the system at hand, Ψ_i denotes a Slater determinant constructed by the excitation of one or more electrons from the Hartree-Fock solution, while a_0 and a_i are numerical coefficients that are variationally optimized; each Ψ_i is called Configuration State Function (CSF) in CI nomenclature [200]. CI methods mainly differ on the subject of which excitations Ψ_i are considered and whether the orbital coefficients for the excited CSFs are optimized [182].

Multi-Configuration Self-Consistent Field techniques (MCSCF) are a class of CI methods that not only determine the coefficients a_i (including a_0) in equation 2.15 but also allow the orbital coefficients for each excited CSF to be optimized. This additional optimization requirement not only increases the computational cost of the procedure, but also raises convergence issues that generally require the use of more sophisticated optimization techniques than those usually employed in the case of HF or simpler CI methods [182]. Despite these difficulties, Complete Active Space Self-Consistent Field (CASSCF) is a MCSCF technique that has become popular in the scientific literature [200]. In CASSCF calcuations, the orbitals are divided into three categories: inactive inner orbitals, which are always doubly occupied; inactive external orbitals, which are always unoccupied; and a set of active orbitals, within which all possible electron configurations are considered [200]. The nomenclature for CASSCF calculations involves stating the number of electrons, n, and orbitals, m, in the active space in the form CASSCF(n,m) [182]. CASSCF is a valuable tool for studying phenomena in which only a limited number of molecular orbitals are modified while preserving the overall electronic structure of the inactive orbitals. Results from CASSCF calculations strongly depend on a proper choice of the active orbitals. When studying chemical reactivity, the active space must contain all orbitals which are modified in the course of the reaction. The process of selecting the active space when it comes to surveying the electronic structure of a given molecule is however less straightforward. Ideally, the active space should contain all valence electrons, and also an adequate number of virtual orbitals. Hückel diagrams, natural occupations, spectroscopic data and the analysis of general valence-bond calculations usually help designing the active space [182, 200]. Moreover, the correlation energy associated with the electrons in the inactive orbitals may be estimated using perturbation theory, in order to improve accuracy [200].

Coupled Cluster (CC) methods are usually regarded giving as the most exact (and expensive) approximations to the analytical solution of the time-independent Schrödinger equation for a given basis set when the full CI method is not applicable. The CC corrections to the Hartree-Fock solution, Ψ_{HF} are given by

$$\begin{aligned} \Psi_{CC} &= e^{T}\Psi_{HF} \\ e^{T} &= 1 + T + \frac{1}{2}T^{2} + \frac{1}{6}T^{3} + ... = \sum_{k=0}^{\infty}\frac{1}{k!}T^{k} \end{aligned} \tag{2.16}$$

where T^n is an operator that generates all n^{th} excited states when acting on the Hartree-Fock reference function. The lowest levels of CC theory are Coupled Cluster with Doubles (CCD) and Coupled Cluster with Singles and Doubles (CCSD). The computational demands of either methods formally scale with M^6_{basis}. Although this is the same scaling factor as CISD, CC calculations involve the computation of two-electron integrals over molecular orbitals, making the computations more demanding [182].

CC methods are usually considered to be more robust towards a poorly constructed HF Salter determinant than other wavefunction correlation methods, such as CI and perturbation methods. However, CC methods are not variational, in contrast to CI. This means that the energy resulting from a CC calculation may lie bellow the exact energy of the system. On the other hand CC methods are size consistent, a feature missed by all truncated forms of CI theory [182].

In general, the application of wavefunction methods to the study transition metal complexes has been hindered by their computational cost. Hartree-Fock is prone to give qualitatively incorrect approximations to the ground state of transition metal complexes, and the use of wavefunction methods for electron correlation usually require the use of truncated models in order to cope with their computational cost. Also, the remarkable accuracy these methods can produce is only achievable when using very flexible and well balanced basis sets, at least at the level of a triple-ζ with enough polarization functions [131,201]. This has not been accomplished in most cases, where the use of smaller basis sets is used as a secondary truncation of the model in order to accomplish the computations within a reasonable computational cost [115, 117–120].

2.3 Density Functional Theory

Density Functional Theory (DFT) approaches the problem of achieving a numerical solution for the time-independent, non-relativistic, Schrödinger equation in a radically different manner than what is prescribed by wavefunction methods. The foundations of DFT can be traced back to the thermodynamics of ideal gases [202] and, in its quantum mechanical version, points towards a central idea that the energy of a system of N electrons under the potential of M nuclei is a functional of the electron density. The term functional refers to a mathematical procedure that maps functions to real numbers. Also, since DFT is

usually applied within the Born-Oppenheimer approximation, the potential generated by the nuclei is usually considered an external potential.

Whereas wavefunction methods attempt to approximate Ψ, DFT methods focus on the probability density, $n(\mathbf{r})$, of finding any of the N electrons at the position $\mathbf{r}$. This function is obtained from the N-electron wavefunction by integrating $|\Psi|^2 = \Psi^*\Psi$ over the first $N-1$ electrons. The Hohenberg-Kohn theorem assures that the relation between $n(\mathbf{r})$ and Ψ is bijective [203], allowing for the calculation of the ground state wavefunction associated with a given probability density. The ground state energy of the system can therefore be expressed as a functional of $n(\mathbf{r})$

$$E[n(\mathbf{r})] = T[n(\mathbf{r})] + \int v_e(\mathbf{r})n(\mathbf{r})d\mathbf{r} + \frac{1}{2}\int\int \frac{n(\mathbf{r})n(\mathbf{r}')}{|\mathbf{r}-\mathbf{r}'|}d\mathbf{r}d\mathbf{r}' + E_{xc}[n(\mathbf{r})] \tag{2.17}$$

where $T[n(\mathbf{r})]$ is the kinetic energy functional, $v_e(\mathbf{r})$ represents the external potential felt by the electrons, and $E_{xc}[n(\mathbf{r})]$ is the exchange and correlation functional of a system of interacting electrons. While $v_e(\mathbf{r})$ is calculated from the information supplied to the calculation procedure, $T[n(\mathbf{r})]$ and $E_{xc}[n(\mathbf{r})]$ must be deduced from first principles [131].

For $T[n(\mathbf{r})]$, this is achieved under the Kohn-Sham (KS) formalism by mapping the behavior of the N interacting electrons in the system to that of an auxiliary system of N non-interacting electrons, both systems sharing the same probability density. The time independent Schrödinger equation (Equation 2.1) for the auxiliary system of non-interacting electrons, can be easily solved and used to recover (at least part of) the kinetic energy. This effectively re-introduces the molecular orbital framework into DFT, and the eigenfunctions found for the auxiliary system are called the Kohn-Sham orbitals. The kinetic energy functional can be calculated from the Kohn-Sham orbitals [204]

$$T_s[n(\mathbf{r})] = -\frac{1}{2}\sum_{i}^{N_{occ}}\langle\psi_i|\nabla^2|\psi\rangle \tag{2.18}$$

Therefore $T_s[n(\mathbf{r})]$ is a functional of the density, since the Kohn-Sham orbitals are themselves functionals of the density [131]. Furthermore, since the auxiliary system shares the same density as that of the interacting electrons, the shape and properties of the KS orbitals already include the effects of electron correlation [131].

The exchange-correlation functional, $E_{xc}[n(\mathbf{r})]$ may be regarded as a necessary correction to the independent particle model that includes electron correlation, the purely quantum mechanic effect of electron exchange, and also correct for the fact that the coulombic repulsion, as expressed in Equation 2.17, allows for an electron to interact with itself (self-interaction) [189]. Although there is no simple exact expression for $E_{xc}[n(\mathbf{r})]$, the fact that it will depend solely on the local evaluation of $n(\mathbf{r})$ ensures that a self-consistent field approach may be used for solving the KS equations. Indeed, DFT is formally an independent-particle model like Hartree-Fock, although providing better approximations to the ground state energy and properties of a multi-electron system [182]. Furthermore,

much of the same computational techniques used to improve the SCF convergence of the HF equations may be employed for solving the Kohn-Sham equations [131].

The most basic approach to the exchange-correlation functional is the Local Density Approximation (LDA) in which E_{xc} depends solely on the local value of the electron density, following original ideas by J. C. Slater that predate the development of Kohn-Sham's DFT [193]. The Local Spin Density Approximation (LSDA, or LSD) is a straightforward generalization of LDA in order to include electron spin into the functionals [205]. This is done by accounting the exchange and correlation interactions among the densities of α and β electrons, and also the interaction between these two densities. Furthermore, the exchange and correlation part of E_{xc} may be separated. One of the earliest exchange-correlation functionals based on LSDA is SVWN, in which the exchange part follows the ideas developed by Slater [205] and the correlation part was devised by Vosko, Wilk and Nusair [206] from the data on several simulations of the non-homogeneous electron gas performed by Ceperley and Alder [207].

A better approximation to E_{xc} is provided by including not only information on the local density, but also the gradient of the density, in order to account for the non-homogeneity of the electron density in real systems: this is called the Generalized Gradient Approximation (GGA). Several GGA functionals have been developed in the 1980's and 1990's, including some popular functionals to date such as Perdew-Wang 91 (PW91 [208]) and Becke exchange with Lee-Wang-Parr correlation (BLYP [128, 209]).

The inclusion of the second derivatives of the electronic density into E_{xc} not only provides further information on the local non-homogeneity of the electron density, but also allows for an explicit determination of the kinetic energy density

$$T(\mathbf{r}) = \frac{1}{2}\sum_{i}^{N_{occ}} |\nabla\psi_i(\mathbf{r})|^2 \tag{2.19}$$

Functionals like TPSS [210] and M06-L [211] provide the most popular examples for this approach, commonly called "meta-GGA".

One of the most severe limitations of DFT is its dependence on the local description of $n(\mathbf{r})$, afflicting the accurate representation of the exchange energy. This results in errors when dealing with medium and long range effects such as the ones found in the study of certain isomerizations. The inclusion of the exact (non-local) Hartree-Fock exchange into the expression for $E_{xc}[n(\mathbf{r})]$ is the central feature of hybrid-GGA and meta-hybrid-GGA functionals, mixing HF exchange with GGA and meta-GGA functionals, respectively. Some of the most popular functionals in current use at the time of writing belong to these two categories, including B3LYP [130], X3LYP [212, 213], and most members of the M06 suite (with the exception of M06-L) [211]. Because the meaning of exchange and correlation energies differs between DFT and wave-function theory, what is called the correlation part of E_{xc} actually recovers some of the exchange energy given by Hartree-Fock. In the same manner, part of the energy recovered from the exchange parcel of E_{xc} corresponds

to what is considered correlation energy, in wavefunction terminology [214]. These conceptual differences between DFT and wavefunction theory force the introduction of a local exchange functional in the formulation of hybrid-GGA and meta-hybrid-GGA functionals. For example, most hybrid-GGA functionals are defined using the formula

$$E_{xc} = aE^x_{HF} + (1-a)E^x_{LSD} + bE^x_{GGA} + (1-c)E^c_{LSD} + cE^c_{GGA} \tag{2.20}$$

where E^x_{HF} is the Hartree-Fock exchange, E^x_{LSD} is the local (Slater) exchange, E^x_{GGA} is a GGA exchange functional, E^c_{LSD} is a local correlation functional and E^c_{GGA} is a GGA correlation functional. The coefficients a, b and c are determined in order to reproduce either the properties of the non-homogeneous electron gas determined by high level simulations, the energies and geometries provided by high level wavefunction calculations on a set of molecules or reference experimental data. For the functional X3LYP, which is extensively used in this work, E^x_{GGA} is a correction of the GGA exchange energy based on the B88 exchange functional [128] and the exchange part of PW91, while E^c_{GGA} is the GGA correlation functional derived by Lee, Yang and Parr (LYP) [209], with $a = 0.218$, $b = 0.709$ and $c = 0.129$ [213, 215].

A more recent development was the introduction of double-hybrid-GGA functionals pioneered by Grimme and co-workers [216]. These functionals further include exact partial correlation, in the form of a perturbative treatment of the Kohn-Sham orbitals based on Møller-Plesset second order perturbation theory (MP2).

Non-hybrid density functionals formally scale as M^3_{basis}, while hybrid functionals formally scale as M^4_{basis} because of their Hartree-Fock component [182]. On their turn, double-hybrid functionals may scale formally as M^5_{basis}, considering the computational cost of the MP2 procedure. Contrary to wave-function methods, the integrals in DFT are evaluated by numerical integration. This results in the fact that DFT calculations are generally slower than Hartree-Fock, for the same system and basis set. On the other hand, new software technology has lowered the computational cost of DFT to the point where linear scaling (scaling with M^1_{basis}) is attained without significant loss of accuracy [131].

All implementations of DFT allow the use of the restricted KS formalism for treating closed-shell systems, in which the probability densities of the α and β ($n^\alpha(\mathbf{r})$ and $n^\beta(\mathbf{r})$) electrons are the same. When dealing with open-shell systems, the unrestricted KS formalism is recommended (despite the existence of a restricted open-shell KS formalism which is akin to ROHF), giving different probability densities for the α and β electrons. In the DFT formalism, the spin expectation values are obtained by applying $\hat{S}^2$ to an approximate wavefunction which is the Slater determinant of the occupied KS orbitals. As in the case of UHF this expectation value is usually greater than the spin multiplicity supplied to the calculation. Nevertheless the unrestricted Kohn-Sham method (analogous to UHF) is less prone to spin contamination than UHF, meaning that $\langle S^2 \rangle$ is usually close to $S(S+1)$. This is due to the fact that electron correlation is already included in the shape of the orbitals, something that common wavefunction methods can only account

for by considering Slater determinants that correspond to excited states [182]. It has also been argued that spin contamination is not well defined in DFT, as real systems may display "spin polarization" (i.e. regions with a predominance of α electrons over β electrons). Furthermore, because the expectation value of S comes from the KS orbitals and not from $n^{\alpha}(\mathbf{r})$ and $n^{\beta}(\mathbf{r})$ it is generally not possible to exactly formulate a given spin state within density functional theory, with the exception of the highest spin state [217]. Because of this, several authors prefer referring to different spin states by their total spin density $S = |n^{\alpha}(\mathbf{r}) - n^{\beta}(\mathbf{r})|$ [135][2]. This convention is followed in this work, with the symbols *S0*, *S1*, *S2*, etc referring to total spin densities of zero (singlet), one (doublet), two (triplet), etc, respectively.

The accuracy of DFT methods varies significantly with respect to the functional used and the problem being treated. In general, LSD performs better than Hartree-Fock, but considerably worse than GGA, meta-GGA and hybrid-GGA. On the other hand, hybrid methods tend to out perform other forms of DFT when benchmarking against experimental data [218–220]. Moreover, the accuracy of DFT calculations depends heavily on the basis set used. For example, the high accuracy claimed by B3LYP is only observed at the basis set limit and does not reflect the accuracy obtained with the split-valence basis sets that are popularly used as a way to model large molecules at a reasonable computational cost [131].

Several chemical problems provide difficult challenges to DFT: van der Waals type interactions are usually poorly characterized; bonds are usually too stable, giving rise to an overestimation of the activation energies. Excited states that are not orthogonal to the ground state can not be easily accounted for. Energy differences between states of different multiplicities can also be poorly described, particularly in the case of non-hybrid functionals [182]. As stated by Kohn in his Nobel Lecture [221]: *"DFT has found many useful applications when moderate accuracies are required. It is not a precision method which, in principle, can be pushed to arbitrary accuracy"*. Despite its shortcomings, DFT is has been the workhorse of computational chemistry since the early 1990's and will probably continue to be the weapon of choice when addressing problems involving computations over large systems or a large number of medium size systems.

2.4 Molecular Properties

Obtaining the total energy and some approximation to a system's wavefunction is but a step in the theoretical study of the chemical properties of a given system. Geometry optimization techniques are used to find the position of the nuclei at their most stable conformations. More involved optimization allow the search for transition state structures, further enhancing one's capability to study and predict the behavior of a chemical sys-

[2] An equivalent formulation of the total spin density can be made from the charge densities of the α and β electrons: $S = |\rho_{\alpha} - \rho_{\beta}|$.

tem. From these optimized geometries, the prediction of vibrational spectra, under the harmonic oscillator approximation, and thermodynamic properties follow naturally. On the other hand, many chemical and physical properties may be rationalized in terms of the charge distribution. Bader's Quantum Theory of Atoms in Molecules (QTAIM, or AIM) and Weinhold's Natural Bond Orbital Theory(NBO)/Natural Population Analysis (NPA) are robust techniques that translate much of the information contained in a system's wavefunction into concepts which are familiar to most chemists. Because chirality is an important question in this work, the Continuous Chirality Measurement (CCM) is presented as a tool for extract a quantitative description of a system's chiral content from their equilibrium geometry.

2.4.1 Geometry Optimization, Vibrational Analysis and Thermodynamic Properties

Under the Born-Oppenheimer approximation, the electronic wavefunction does not account for the movement of the nuclei. Despite this, the energy of a chemical system is a function of the nuclear positions, defining a Potential Energy Surface (PES). For a system with N nuclei, the PES is a function in $3N-6$ variables ($3N-5$, for linear systems). The purpose of geometry optimization techniques is to find the position of the nuclei that correspond to stationary points of the PES. From the chemical point of view, minima and first order saddle points are the most interesting points in the PES as they correspond to equilibrium geometries of stable species, and transition states between two stable species, respectively [196].

Geometry optimization techniques usually require the computation of the partial first derivative of the energy with respect to each of the nuclear coordinates: the gradient of the energy [189]. Well established techniques for finding the minimum in the PES that lies closer to an initial guess geometry are iterative procedures based on Newton's method (gradient following) [222]. Most techniques further benefit from having some knowledge on the second derivatives of the energy with respect to the nuclear coordinates. These derivatives are collectively manipulated in the form of a $3N \times 3N$ matrix, called the Hessian matrix, H. For the purpose of finding minima in the PES, the nuclear Hessian may be supplied by a low level theory, such as the rules published by Schlegel [223], with considerable savings in computational effort.

Finding a minimum in the PES is a routine procedure, since there are tabled values for bond lengths and angles that allow one to provide the software with a good initial guess geometry and there are well established algorithms that minimize the number of iterations needed [222, 224–226]. On the other hand, the search for a transition state requires a good initial guess to the transition state geometry that is usually the result from more advanced techniques such as surface scans and gradient following, together with some chemical intuition [196]. Moreover, the search for a transition state requires an initial

Hessian matrix computed at an appropriate level of theory, increasing the computational cost of finding such structures [227–231].

Once the geometry of the desired stationary point is reached, a new computation of the Hessian is done, and transformed into mass-weighted coordinates. Under the harmonic oscillator approximation, the eigenvalues of the mass-weighted nuclear Hessian are related to the fundamental frequencies in the vibrational spectrum of the system being treated, and the corresponding eigenvectors provide the normal modes of vibration [182]. A minimum in the PES corresponds to a system with all positive vibrational frequencies[3] whereas a transition state has all positive frequencies, except for one, which is imaginary. The reaction coordinate associated with each transition state is described by the normal mode with the imaginary vibrational frequency. A constraint descend along this normal mode allows the identification of the minima in the PES on either side of the transition state, thus allowing the characterization of an elemental step in a reaction mechanism. In order to do so, different Intrinsic Reaction Coordinate (IRC) methods have been developed and applied [232–236].

The knowledge of the fundamental vibrational frequencies also allows for the calculation of thermodynamic quantities [183]. According to statistical thermodynamics, most of the aggregate thermodynamic variables of the system, such as the total energy, free energy, entropy, and pressure, can be expressed in terms of the partition function or its derivatives. For each degree of freedom, the partition function of a system with definite composition, at constant temperature, T, and volume (canonical ensemble) is given by

$$Q(T) = \sum_i e^{-\frac{E_i}{k_B T}} \tag{2.21}$$

where the summation extends to all energy levels, E_i, and k_B is the Boltzmann constant. The different degrees of freedom of a molecular system are usually divided into electronic, translational, rotational and vibrational components, and the total energy is expressed as their sum

$$E(T) = E_{elec}(T) + E_{trans}(T) + E_{rot}(T) + E_{vib}(T) \tag{2.22}$$

In the calculation of each component of $E(T)$, two extreme situations appear: either T is so small that only the state of least energy is occupied, or T is sufficiently large for the classical approximation to hold. For each degree of freedom, a critical temperature Θ_c is defined; if Θ_c/T is small, then the energy levels are closely spaced compared with $k_B T$, and the classical approximation holds [237]. When dealing with the electronic component of the energy, one assumes that the electronic excited states are not thermally accessible, and $E_{elec}(T)$ is given by the ground state energy given by wavefunction of DFT calculations [183]. On the other hand, the classical (continuous) approximation may be used for determining the translational and rotational contributions to the energy [237].

[3] Six (five for linear systems) eigenvectors of the mass-weighted nuclear Hessian correspond to translational and rotational degrees of freedom, and have their associated eigenvalues should be zero, within the numerical accuracy of the computational procedure.

The other hand the vibrational partition function retains its quantized structure on the range of temperatures and fundamental vibrational frequencies usually found in chemistry (with the possible exception of very low vibrational frequencies [238–241]). One of the components of $E_{vib}(T)$ is the zero-point vibrational energy (ZPVE), which arises from the fact that at 0 K the position of the nuclei can not be fully determined, under the Heisenberg principle. This is a temperature-independent term that may be approximated as [242]

$$\text{ZPVE} \simeq \frac{1}{2}\sum_{i}^{N_{vib}} \nu_i \tag{2.23}$$

where the sum extends to all vibrational frequencies ($N_{vib} = 3N - 6$, or $3N - 5$ for linear molecules) and ν_i are the fundamental vibrational frequencies. Because ZPVE is present even at 0 K, this is an important correction to the energy of the system, and its inclusion is highly recommended [243]. The temperature-dependent component of E_{vib} is given by

$$E_{vib}(T) = R\sum_{i}^{N_{vib}} \Theta_{\nu,i}\left(\frac{1}{2} + \frac{1}{e^{\Theta_{\nu,i}/T} - 1}\right) \tag{2.24}$$

where R is the gas constant and $\Theta_{\nu,i}$ is the characteristic vibrational temperature $\Theta_{\nu,i} = {}^{h\nu_i}/_{k_B}$, where h is Plank's constant. Once the all the contributions to the total energy are known, the absolute enthalpy is given by [244]

$$H(T) = E(T) + RT \tag{2.25}$$

The entropy of the system may also be partitioned into electronic, translational, rotational and vibrational contributions. By the same arguments, the electronic component of the entropy is null for singlet ground-states and constant for non-singlet ground-states. Also the translational and rotational components of this property are calculated using classical statistical mechanics. The vibrational component of the entropy, is given by

$$S_{vib}(T) = R\sum_{i}^{N_{vib}} \left(\frac{{}^{\Theta_{v,i}}/_{T}}{e^{\Theta_{v,i}/T} - 1} - \ln\left(1 - e^{-\Theta_{v,i}/T}\right)\right) \tag{2.26}$$

The calculation of the Gibbs energy is done in a trivial manner ($G = H - TS$). Once these quantities are known, reaction energetics can be studied by using the adequate energy balance. Furthermore, activation energies, enthalpies and Gibbs energies for elementary steps can also be estimated by comparing the thermodynamic functions for reactants and the transition state [237].

It is known that the theoretical prediction of vibrational frequencies tends to over estimate the experimentally observed ones, affecting the accuracy of the calculated thermodynamic properties. During the 1980's and the 1990's, several authors advocated the use of empirical scale factors for correcting this systematic trend [245–247]. This approach culminated in the reference work by Scott and and Radom [242]. In recent years Irikura *et al.* [248, 249] have questioned the accuracy of such universal scale factors. Some contributions to this questions are made in this work (see Chapter 3).

2.4.2 Natural Population and Natural Bond Order Analysis

From the chemical point of view, a molecule's reactivity can be rationalized in terms of concepts such as chemical bonds, non-bonding electron pairs and atomic charges. However, these concepts do not correspond to physical observables and therefore there is no unique and definite way of obtaining such information from the wavefunction [250]. This becomes ever more troublesome when dealing with the complicated structure of multi-determinant wavefunctions, such as those obtained from MP2, CI or CC techniques. The first order density matrix, $\gamma_1(\mathbf{q},\mathbf{q}')$ is particularly interesting for simplifying the information in the wavefunction:

$$\gamma_1(\mathbf{q}_1,\mathbf{q}_1') = N\int \Psi^*(\mathbf{q}_1',\mathbf{q}_2,\ldots,\mathbf{q}_N)\Psi(\mathbf{q}_1,\mathbf{q}_2,\ldots,\mathbf{q}_N)d\mathbf{q}_2 d\mathbf{q}_3\ldots d\mathbf{q}_N \qquad (2.27)$$

where N is the number of electrons in the system, and the product $\Psi^*\Psi$ is integrated to $N-1$ electrons, each of each being described using three spacial dimensions and one spin degree of freedom. In the same manner, the reduced density matrix, γ_1^{red}, is defined in terms of the spacial coordinates of the electrons

$$\gamma_1^{\text{red}}(\mathbf{x}_1,\mathbf{x}_1') = N\int \Psi^*(\mathbf{x}_1',\mathbf{x}_2,\ldots,\mathbf{x}_N)\Psi(\mathbf{x}_1,\mathbf{x}_2,\ldots,\mathbf{x}_N)d\mathbf{x}_2 d\mathbf{x}_3\ldots d\mathbf{x}_N \qquad (2.28)$$

In the 1950's, Löwdin defined the Natural Orbitals as the eigenvectors of $\gamma_1(\mathbf{q},\mathbf{q}')$ and their associated eigenvalues as their Natural Occupation Numbers [251]. Despite its simple structure, many properties of chemical systems can be inferred from $\gamma_1(\mathbf{r},\mathbf{r}')$, as exemplified by Löwdin [251, 252] and latter revised by Davidson [253]. Furthermore, because Equation 2.27 refers to the wavefunction and its complex conjugate in an abstract manner, Natural Orbitals reflect the electron density of any wavefunction, irrespective of the number of determinants used in its expression [254]. Therefore throughout this and the following section, the term wavefunction will be use in a broad sense, signifying either the single determinant wavefunction resulting from a Hartree-Fock calculation, a single determinant containing the Kohn-Sham orbitals from a DFT calculation or the natural orbitals from a correlated wavefunction calculation.

Although Natural Orbitals may in some cases be easier to interpret than those obtained at the end of a first principles calculation, their interpretation in terms of the chemical concepts mentioned above can still be cumbersome [253]. This is illustrated by the fact that natural occupation numbers may differ significantly from the integers 0, 1 or 2. The Natural Bond Orbitals (NBO) were developed as a localization scheme that is applied to $\gamma_1(\mathbf{r},\mathbf{r}')$ while preserving the orthogonality of the resulting orbitals. This is done in two stages: first $\gamma_1(\mathbf{r},\mathbf{r}')$ is partitioned into atomic sub-blocks. The eigenvectors of each atomic sub-block define the Natural Atomic Orbitals (NAO), with eigenvalues of 2 for doubly occupied non-bonding pairs and eigenvalues of 1 for each half filled orbital available for covalent bonding. In the second step, two-atom sub-blocks are considered and the covalent bonds emerge as eigenvectors of the two-atomic sub-blocks with associated

eigenvalues of 2 (in addition to the already known atomic non-bonding pairs). Because these orbitals are not orthogonal, an orthogonalization step is required at the end of the procedure [255, 256]. This method was later expanded in order to include open-shell systems, which take into account two different first order density matrices: one for α and other for β electrons [257].

The occupied NBOs are therefore localized eigenvectors of one- and two-center blocks of $\gamma_1(\mathbf{r}, \mathbf{r}')$ which describe one-center core and non-bonding orbitals, as well as two-center bonds and anti-bonds, reproducing the Lewis structure of the molecule [257]. The remaining orbitals represent one-center Rydberg and two-center unoccupied anti-bonds, with only residual occupancies. From the NBOs, the hybridization of each atom can be calculated, further allowing the chemical rationalization of the results obtained in first principles calculations. Furthermore, the effective atomic charges of each atom can be calculated from the nuclear charge and the sum of the eigenvectors associated with its NAOs. This population analysis technique is called Natural Population Analysis (NPA) and the effective atomic charges are commonly known as natural charges [258].

NBO and NPA are popular for the rationalization of physical and chemical properties since they provide a bridge between the results of quantum mechanical computations and the classical concepts of chemistry in a definite and economic manner (in terms of computational cost) [259].

2.4.3 Atoms In Molecules

Bader's theory of Atoms in Molecules (AIM) recovers some of the principles of chemistry from the topological properties of the electron density, $\rho(\mathbf{r})$, which is the trace of $\gamma_1(\mathbf{r}, \mathbf{r}')$ and is also related to the probability density, $n(\mathbf{r})$, used in DFT (see Section 2.3)

$$\rho(\mathbf{r}) = \mathrm{tr}(\gamma_1(\mathbf{r}, \mathbf{r}')) = \sum_{i}^{N_{occ}} |\nabla \psi_i(\mathbf{r})|^2 = q \times n(\mathbf{r}) \tag{2.29}$$

where the sum is done across all N_{occ} occupied orbitals and q is the charge of the electron (which is -1, in atomic units). Because $\rho(\mathbf{r})$ is a function in three dimensional space, it may present maxima, minima and saddle points along its domain. These stationary points are characterized by the vanishing of the gradient (or directional first derivatives) of $\rho(\mathbf{r})$, $\nabla\rho(\mathbf{r})$

$$\nabla\rho(\mathbf{r}) = \frac{d\rho}{dx}\vec{e}_x + \frac{d\rho}{dy}\vec{e}_y + \frac{d\rho}{dz}\vec{e}_z \rightarrow \begin{cases} = \vec{0} & \text{(A)} \\ \neq \vec{0} & \text{(B)} \end{cases} \tag{2.30}$$

where case (A) is observed at stationary points (and at infinity) and (B) is the general case. In AIM terminology, stationary points of $\rho(\mathbf{r})$ are called critical points (CP). Critical points are characterized by their rank (ω) and signature (σ) and are symbolized by (ω, σ). The rank is the number of non-zero curvatures of $\rho(\mathbf{r})$, being that points with $\omega < 3$ correspond to mathematically unstable structures [260]. The curvatures are given by the

eigenvalues of the Hessian matrix of $\rho(\mathbf{r})$. Four types of stable critical points are possible, each type being associated with an element of chemical structure:

$(3, -3)$ Three negative curvatures: nuclear critical point (NCP) $\rho(\mathbf{r})$ is a local maximum.

$(3, -1)$ Two negative curvatures: bond critical point (BCP); $\rho(\mathbf{r})$ is a maximum in the plane defined by the two negative curvatures and a minimum along the third direction.

$(3, +1)$ Two positive curvatures: ring critical point (RCP); $\rho(\mathbf{r})$ is a minimum in the plane defined by the two positive curvatures and a maximum along the third direction.

$(3 + 3)$ Three positive curvatures: cage critical point (CCP); $\rho(\mathbf{r})$ is a local minimum.

Bond critical points are particularly interesting features of $\rho(\mathbf{r})$ since the properties of $\rho(\mathbf{r}_{BCP})$ can be correlated to the properties of the chemical bond between two atoms. The value of $\rho(\mathbf{r}_{BCP})$ itself is related to the order (single, double of triple) of the covalent bond between the two adjacent nuclei [261]. This is, however, not a linear relationship, as exposed by Bader in his book: the increase in the bond order attained by adding one electron to an empty π molecular orbital will bear little effect on the value of the electron density at the BCP, since it lays in the nodal plane of the π orbital occupied by the additional electron [262]. The ellipticity of the electron density at the BCP is given by

$$\epsilon = \frac{\lambda_1}{\lambda_2} - 1 \tag{2.31}$$

where λ_1 and λ_2 are the two negative curvatures (by convention, $|\lambda_1| \geq |\lambda_2|$) of the electron density at the BCP, as given by the eigenvalues of the Hessian matrix of $\rho(\mathbf{r}_{BCP})$. Furthermore, the existence of a BCP is a necessary but not sufficient condition for the existence of a covalent bond. The ellipticity is a measure of the symmetry of $\rho(\mathbf{r}_{BCP})$: a simple bond is cylindrically symmetrical, having $\epsilon = 0$, as the π character increases so does ϵ, reaching a maximum in the case of double bonds, such as the C=C bond in ethene. Further increase in the bond order reduces the value of ϵ until the cylindrically symmetrical shape of a triple bond is reached.

In addition to the topology of $\rho(\mathbf{r})$, the Laplacian of the electron density, $\nabla^2\rho(\mathbf{r})$, also contains valuable information on the electronic structure of the molecule and the atoms within it. This is defined as the sum of three curvatures of the density at any given point [263, 264]

$$\nabla^2\rho(\mathbf{r}) = \nabla \cdot \nabla\rho(\mathbf{r}) = \frac{\partial^2\rho(\mathbf{r})}{\partial x^2} + \frac{\partial^2\rho(\mathbf{r})}{\partial y^2} + \frac{\partial^2\rho(\mathbf{r})}{\partial z^2} \tag{2.32}$$

Negative values of $\nabla^2\rho(\mathbf{r})$ indicate regions where the electron population is locally concentrated, and vice versa. Critical points of $\nabla^2\rho(\mathbf{r})$, in particular local minima, can be used in order to locate features normally associated with highly localized electrons, such as bonds and lone pairs [265].

The Laplacian of the electron density at the BCP also allows for a more concise discernment of the nature of the bond. The local statement of the virial theorem relates $\nabla^2\rho(\mathbf{r})$ and the potential energy density, $\mathcal{V}(\mathbf{r})$, in the following manner

$$\left(\frac{\hbar^2}{4m_e}\right)\nabla^2\rho(\mathbf{r}) = 2G(\mathbf{r}) + \mathcal{V}(\mathbf{r}) \tag{2.33}$$

where $G(\mathbf{r})$ is the gradient kinetic energy density, which is given by the numerical expression

$$G(\mathbf{r}) = \frac{\hbar^2}{2m_e}N_e\sum_{i=1}^{N_{orb}}\left(n_i\cdot\nabla\psi_i^2(\mathbf{r})\right) = \frac{\hbar^2}{2m_e}\nabla^2\mathrm{tr}(\gamma_1(\mathbf{r},\mathbf{r}')) \tag{2.34}$$

where N_e is the number of electrons, N_{orb} is the number of occupied orbitals, n_i is the occupation of the orbital ψ_i. In the 1980's Cremer and Kraka [266] developed an interpretation of chemical bonding around the total electronic energy density, $H(\mathbf{r})$ defined as

$$H(\mathbf{r}) = G(\mathbf{r}) + \mathcal{V}(\mathbf{r}) \tag{2.35}$$

a negative value of $H(\mathbf{r}_{\mathrm{BCP}})$ is a clear indicator of a covalent bond, while hydrogen bonds and van der Waals interactions are characterized by BCPs with positive $H(\mathbf{r}_{\mathrm{BCP}})$ [267].

The topology of the electron density defines three-dimensional basins, each encompassing one nucleus. This allows the partition of the molecular electron density into atomic basins, thus defining the shape of each atom within the molecule. Population analysis is possible in AIM through the integration of $\rho(\mathbf{r})$ over each atomic basin. Furthermore, a local expression for any one-electron operator can be devised from the first-order density matrix allowing for the calculation of local densities, such as the ones used in the derivation of Equation 2.34. This further allows the partition of other molecular properties such as the kinetic, potential and total energies [268, 269]. At the same time, the major problem with AIM lays with the integration within the atomic basins, which must be carried on using numerical integration techniques. This issue makes AIM population analysis computationally more expensive than, for example, NBO [182].

AIM has been successfully applied in the study of several important subjects in chemistry, such as the description of chemical bonding [270], the definition of transferable groups and their properties [271], the study of strain energy [272], the description of metal-ligand bonding [273–275] and the development of quantum chemical descriptors for Quantitative Structure-Activity Relationship (QSAR) and Quantitative Structure-Property Relationship (QSPR) studies [276].

2.4.4 Continuous Chirality Measurement

The concept of chirality has been traditionally linked to the existence of objects which are non-superimposable mirror images of each other. An object, such as a molecule or crystal is said to be chiral if it is not identical to its mirror image. By contrast, achiral (commonly said symmetrical) molecules are identical to their mirror image [14]. This definition

of chirality as a binary property (i.e. one that is either present or absent for a given object) was been upgraded by the pioneering work of Avnir and co-workers. In the 1990's, Avnir and co-workers [141–143, 277, 278] realized that for many questions regarding symmetry in chemistry, the traditional definition of chirality was not adequate. As a solution, different Continuous Symmetry Measurements (CSM) were proposed, from which the Continuous Chirality Measurement (CCM) is a particular case. These measurements are tools that allow one to calculate the distance between an object and the closest G-symmetric object, defined as

$$S(G) = \frac{1}{N \cdot d} \sum_{i=1}^{N} (p_i - \hat{p}_i)^2 \tag{2.36}$$

where $\{p_i\}_{i=1}^{N}$ is the set of N points that define the object (position of each nuclei, in th case of chemical systems), G is a specified symmetry group (usually C_s or C_2) and d is the root mean square (rms) distance of p_i from the center of mass [279]. For convenience, the set $\{p_i\}_{i=1}^{N}$ is normalized, such that

$$\frac{1}{N} \sum p_i^2 = 1 \tag{2.37}$$

The set of points $\{\hat{p}_i\}_{i=1}^{N}$ defines the closest G-symmetric object. A procedure for determining this object was elaborated by Zabrosky and Avnir and is commonly called the "fold and unfold" method [141–143]. This procedure is outlined in Figure 2.1 and consists in the following steps:

1. **Set-up**: the original configuration points $p_1, p_2, \ldots, p_N$ are organized into pairs $\{p_i, p_j\}$ of points that are mirror images of each other. Points that are unique towards reflection (i.e. do not have a mirror image correspondent or lay at the reflection plane) are paired up with themselves $\{p_i, p_i\}$.

2. **Folding**: each pair of points is folded by applying the identity transformation to one point and by reflecting the other point across a mirror plane. The folded points are represented by $\tilde{p}_i$.

3. **Averaging**: Each pair of folded points $\{\tilde{p}_i, \tilde{p}_j\}$ is averaged, obtaining a single averaged point, $\hat{p}_i$.

4. **Unfolding**: each averaged point is unfolded by reflecting back across the mirror plane, the object defined by the set of points $\{\hat{p}_i\}_{i=1}^{N}$ is mirror symmetric.

The mirror symmetric object is then rotated in order to find the best possible way of superimpose it to the original object. Equation 2.36 can then be applied [141, 279].

CCM has been successfully applied to a number of problems in organic and inorganic chemistry, including transition metal catalysis [280–282]. In this work, CCM is applied as a descriptor for the overall geometry of Mn(salen) and Mn(acacen') complexes in Chapter 5. Figure 2.2 illustrates such a application, depicting the geometry of an Mn(salen) complex, and its closest mirror symmetric structure.

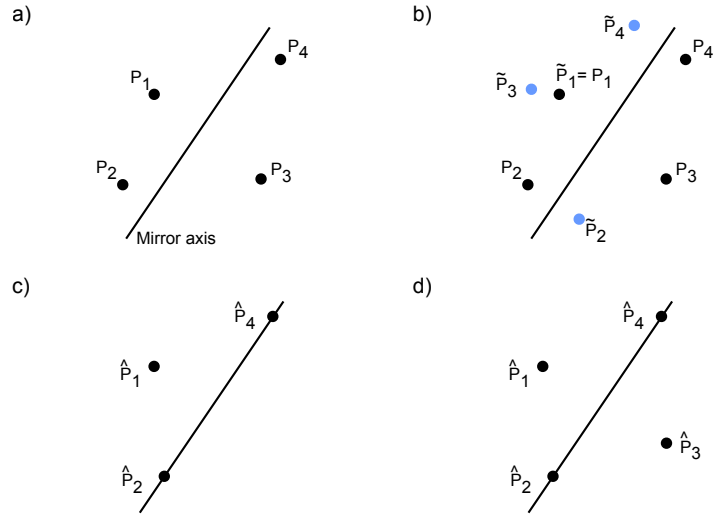

Figure 2.1: An illustration of the fold and unfold algorithm. a) Set-up: the points are divided into sets $\{P_1, P_3\}$, $\{P_2, P_2\}$ and $\{P_4, P_4\}$; b) Folding: the folded points ($\tilde{P}_i$) are represented as blue dots, in this process, the identity operation was applied to P_1; c) Averaging; and d) Unfolding back the set of averaged points defines the closest set of points $\{\hat{P}_i\}$ that is mirror symmetric.

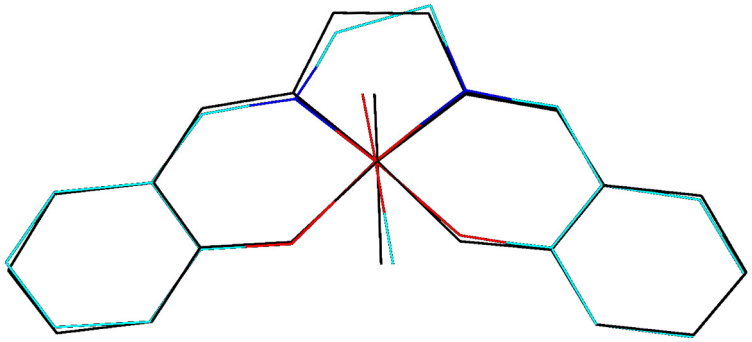

Figure 2.2: Superimposed image of the non-hydrogen atoms of Oxo-Mn(salen)Cl (colored lines) with that of the nearest mirror symmetric structure (grey lines).

2.5 Statistical Methods

Statistics is an important mathematical tool for condensing sparse information into a condensed form that is easier to interpret. Some of the most rudimentary concepts in statistics, such as mean (or average) value, $\bar{x}$, variance and standard deviation, σ_x, are well known concepts that convey information about the mean value of any given property and how the different measurements of such properties spread around their expectation values. More advanced concepts such as skewness and kurtosis allow for a deeper understanding on how these values are distributed [283,284], although a graphical representation of the distribution of the data using a histogram or a density graph may at times provide a more intuitive way of conveying such information [285]. Principal Component Analysis (PCA) and linear regression are two statistical methods that played important

roles in the research work reported in this thesis, and are exposed in the following sections.

2.5.1 Linear Regression

Linear regression lays at the heart of statistics, as it is an assortment of techniques capable of predicting a response variable from one or more predictor (independent) variables. Ordinary Linear Regression (OLS) is an extension of the minimum least squares method fits to multiple independent variables. In OLS the response variable, $\hat{Y}$, as a linear combination of k independent variables X_i, assuming n observations

$$\hat{Y}_i = \hat{\beta}_o + \hat{\beta}_1 X_{1,i} + \hat{\beta}_2 X_{2,i} + ... + \hat{\beta}_k X_{k,i} \qquad i = 1, ..., n \tag{2.38}$$

where $\hat{Y}_i$ is the predicted value of the dependent variable for observation i, $X_{j,i}$ is the jth predictor variable for the ith observation, $\hat{\beta}_0$ is the intercept and $\hat{\beta}_j$ is the regression coefficient for the jth predictor. The goal of OLS is to devise a set of intercepts and coefficients that minimize the sum of square residuals, E, from a set of observations of Y

$$E = \sum_{i=1}^{n} \epsilon_i^2 = \sum_{i=1}^{n} \left(Y_i - \hat{Y}_i \right)^2 = \sum_{i=1}^{n} \left(Y_i - \hat{\beta}_o + \hat{\beta}_1 X_{1,i} + ... + \hat{\beta}_k X_{k,i} \right)^2 \tag{2.39}$$

a number of techniques are used for this purpose [286]. The magnitude of each regression coefficient $\hat{\beta}_j$ is an indicator of how strongly Y varies with the corresponding predictor X_j. If Y and X_j appear to bear a non-linear relationship, linearization techniques allow the application of one or more functions to any of the involved variables in order to obtain a set of transformed variables that bear linear relationship with each other. The most common functions used in linearization are the quadratic and the square root, as well as the natural and decimal logarithms. Furthermore, the dependent variable may be fitted to the interaction (product) of two predictor variables [286].

The quality of the fitting procedure is traditionally measured by the square of the correlation coefficient or coefficient of determination, r^2, which reflects the proportion of the variance in Y that is explained by the linear model, $\hat{Y}$

$$r^2 = \frac{\sum_i^n \left(\hat{Y}_i - \bar{Y} \right)^2}{\sum_i^n \left(Y_i - \bar{Y} \right)^2} \tag{2.40}$$

where $\bar{Y}$ is the average of the dependent variable Y [287]. In general, r^2 increases with the number of predictor variables, as more and more variables will explain more and more of the variance in Y, however, many variables may affect r^2 only due to chance correlation. In order to correct this property, the adjusted r^2 is usually preferred in multivariate regression

$$r^2_{adj} = \frac{n-1}{n-k-1} r^2 \tag{2.41}$$

where n is the number of observations and k is the number of predictors [288].

As with every other statistically inferred quantity, the coefficients $\hat{\beta}_j$ in Equation 2.38 lay within a confidence interval. Assuming that the errors in the regression (residuals) are normally distributed and that there is a sufficiently large number of observations, each coefficient follows a t distribution with $n-2$ degrees of freedom from which its confidence interval can be obtained [287].

Permutation tests provide an alternative estimation of the confidence intervals at the expense of higher computational cost. The basic idea behind permutation tests is to calculate the confidence intervals by estimating the distribution of $\hat{\beta}_j$ taking into account all the possible permutations in the observations instead of relying on a theoretical distribution. Because of this, permutation tests do not require the two assumptions mentioned earlier to be true. Permutation tests not only allow the determination of a confidence interval for each $\hat{\beta}_j$ but also return a F-statistic here the null hypothesis is $\hat{\beta}_j = 0$, thus allowing one to infer the statistical significance of each $\hat{\beta}_j$. Since the computational cost of an exact permutation analysis increases as $n!$, most software implementations rely on a probabilistic sampling of the permutations in which sampling continues until the estimated standard deviation of $\hat{\beta}_j$ falls below a given fraction (usually 10%) of the estimated p-value [286].

2.5.2 Principal Component Analysis

Principal Component Analysis (PCA) is a data reduction technique that transforms a large amount of variables into a much smaller set of uncorrelated variables called principal components (PC). The goals of PCA are simplification, through data reduction, in order to allow variable selection, outlier detection, as well as classification and modeling of the information contained in a data matrix [289]. Considering a data matrix $\mathbf{X}$ with n observations of k variables, the kernel of PCA is to find the eigenvectors and eigenvalues of $\mathbf{X}^T\mathbf{X}$. Each PC is associated with an eigenvalue of $\mathbf{X}^T\mathbf{X}$ and its corresponding eigenvector [182]. An alternative formulation of PCA allows the same information to be recovered from the correlation, or the covariance matrix. The eigenvalues are related to the percentage of variance explained by their corresponding PC, whereas the eigenvectors contain the coefficients for the expression of each PC as a linear combination of the k variables in $\mathbf{X}$. The matrix containing the eigenvectors of $\mathbf{X}^T\mathbf{X}$ is called the *loadings*, $\mathbf{M}_L$. The product $\mathbf{X}\mathbf{M}_L$ corresponds to a change in coordinates, yielding the *scores* matrix,$\mathbf{M}_S$. Each column of $\mathbf{M}_S$ contains the n values that would be observed should the corresponding PC be measured directly [288].

Data matrices with a large number of (possibly redundant) variables pose the important question on the number of components to be extracted from PCA, *i.e.* the number of components that actually contain information. One popular method is to recover all principal components (PCs) until a certain cumulative amount of variance is explained.

Depending on the structure of the data, too many or too few components may be extracted, leading to difficulties in the interpretation of the lesser PCs, or to the discardment of relevant information, respectively. The Kaiser-Harris criterion suggests discarding components with an associated eigenvalue less than 1.0, as they explain less variance than that contained in a single variable of the original data. The Cattell-Scree test plots the eigenvalues against their component numbers. Scree plots show an elbow or bend, and the components above this feature are retained. A more robust test is to extract eigenvalues from random data matrices of the same size as the data matrix. If an eigenvalue based on real data is greater than the average corresponding eigenvalue from a set of random data matrices, that component is retained [286]. This approach is called the parallel analysis and is used in Chapter 5 to determine the number of principal components to extract from a large data matrix containing information on the geometry and electronic structure of several Mn(salen) complexes.

While the loadings contain information on how the data is structured, the scores allow relationships between observations in the data matrix to become evident. Because the PCs form an orthogonal basis, each PC describes different parts of the variation in the original data matrix. The identification of clusters in the scatter plots of the scores for each PC (or pairs of PCs) allows the classification of the observations in the data matrix into categories, or the association of each PC to pre-existing categorical variables that are associated with the observations in $\mathbf{X}$. As a technique, PCA is blind to any *a priori* categorization of the observations contained in the data matrix. This is in contrast to other techniques such as classification trees, and Linear Discriminant Analysis, in which the classification of the observations in the data matrix plays an important role in the analysis of the numerical data [288].

Beside its use as a classification tool in multivariate analysis, PCA also provides a solution to one of the most common problems in linear regression. Situations were the number of descriptors is large (in particular when the number of descriptors exceeds the number of observations) or when the descriptors are strongly correlated, linear regression techniques tend to give poor results. The scores obtained from the most significant PCs may be used as compound orthogonal descriptors, thus facilitating the linear regression. Furthermore, should each PC be linked to particular categorical descriptors of the observations in the data matrix, a semi-quantitative analysis of how those categorical variables affect the outcome of the dependent variable may be obtained [182].

Despite having been invented as a tool for psychometric research [290, 291], PCA is an important tool in chemistry with applications ranging from analytical and food chemistry [289], to the prediction of chemical properties through data mining [292, 293] and the prediction of reaction paths [227].

Chapter 3

Calibration sets and the Accuracy of Vibrational Scaling Factors: A Case Study with the X3LYP Hybrid Functional[1]

Abstract

A linear least squares methodology was used to determine the vibrational scaling factors for the X3LYP density functional. Uncertainties for these scaling factors were calculated according to the method devised by Irikura and co-workers (*J. Phys. Chem. A*, **2005**, *109*, 8430–8437). The calibration set was systematically partitioned according to several of its descriptors and the scaling factors for X3LYP were recalculated for each subset. Results show that the scaling factors are only significant up to the second digit, irrespective of the calibration set used. Furthermore, multivariate statistical analysis allowed us to conclude that the scaling factors and associated uncertainties are independent of the size of the calibration set and strongly suggest the practical impossibility of obtaining vibrational scaling factors with more than two significant digits.

3.1 Introduction

The prediction of vibrational frequencies using first principles methods is possibly one of the main applications of theoretical and computational chemistry nowadays. These calculated vibrational frequencies find usefulness in the identification of experimentally observed reactive intermediates and the elucidation of structural features [294–297]. The calculations involved usually rely on the harmonic oscillator model, the limitations

[1] Adapted from F. Teixeira, A. Melo and M. Natália D. S. Cordeiro, *J. Chem. Phys.* **2010**, 133, 114109
The contributions of F. Teixeira to this work were the following: Running the first principle computations, performing the multivariate data analysis and writing the first draft of the manuscript.

of which had been extensively exposed in previous works [239, 298]. Despite its limitations, the harmonic oscillator model is able to give fairly accurate predictions of vibrational frequencies, although calculated vibrational wave numbers are usually higher than their corresponding experimental counterparts. A bias b_i can therefore be defined as

$$b_i = \frac{\omega_i}{\tilde{\nu}_i} \tag{3.1}$$

where ω_i is the calculated harmonic wave number and $\tilde{\nu}_i$ is the experimentally observed vibrational wave number. Pople and co-workers first observed in 1981 that the harmonic vibrational wave numbers calculated at the HF/6-21G level of theory have a mean bias, b_{av} of 1.123 [299]. From these results, a scaling factor $s = b_{\text{av}}^{-1}$ of 0.89 was proposed for this method. In 1985, Defrees and McLean published the scaling factors for HF and MP2 based on the average bias for wave number predictions for 30 molecular ions [245]. Also, estimations of vibrational scaling factors using larger calibration sets and based on a least-squares approach were published since the 1990's [242, 247, 300–307].

In the least-squares theory, the scaling factor s is the value that minimizes the least-square objective function

$$\Delta^2 = \sum_i (s\,\omega_i - \tilde{\nu}_i)^2 \tag{3.2}$$

The solution of which is given by

$$s = \frac{\sum_i \omega_i \tilde{\nu}_i}{\sum_i \omega_i^2} \tag{3.3}$$

Since this method implies the use of experimentally determined fundamental vibrational wave numbers, a survey on the accuracy of the empirical scaling factors is in order. The first approach as to the accuracy of the empirical scaling factors was the calculation of the root mean-square error rms in the form

$$\text{rms} = \sqrt{\frac{\sum_i^N (s\,\omega_i - \tilde{\nu}_i)^2}{N}} \tag{3.4}$$

where N is the number of vibrational modes considered. Root mean-square errors are relatively easy to work with, and the work of Wong [246] allowed a first glimpse on the accuracy of the empirical scale factors. This made rms a surrogate method for estimating uncertainty. Although rms is a valid first approach to the accuracy of the scaling factors, it does not replace the determination of their associated uncertainty. A method to do so was derived by Irikura and coworkers in 2005 [248, 249, 308] in the form

$$u(s) = \sqrt{\frac{\sum_i \omega_i^2 (s_i - s)^2}{\sum_i \omega_i^2}} \tag{3.5}$$

where $u(s)$ is the uncertainty associated with the scaling factor s and $s_i = b_i^{-1}$. According to this approach, the uncertainty associated with s depends heavily on the variance of the bias b_i . Other sources for error contemplated in the work by Irikura *et al.* were the

small variance associated with random error resulting from the calculation of ω_i and the uncertainty in the experimental determination of $\tilde{\nu}_i$. These two factors have been considered negligible in such work [248]. Nevertheless, the availability of a method to calculate $u(s)$ allows us to further explore the variables which may influence the determination of s and $u(s)$, and thus shred some reasoning on the use of such empirical parameters.

The choice of the calibration set is a question that has been unexplored, most papers using only one calibration set and comparing to the results published in other works. As such, the question of which — if any — parameters of the calibration set influence s and $u(s)$ remains unanswered. In this work, empirical scaling factors for Hartree-Fock and density functional methods are calculated, together with their associated uncertainties, using a calibration set similar to that of Radom and Scott [242]. This calibration set is further partitioned according to several parameters which may influence our results. Finally, multivariate statistical analysis will be carried out in order to achieve a better understanding of how changes in the calibration set affect our results.

3.2 Computational Methods

A full data set F of vibrational modes was defined for the present work. The vibrational modes included in this set were obtained from the NIST Webbook [309] and belong to neutral chemical species (either molecules or radicals) that contain no more than four atoms of the second or third row, with no more than 10 atoms in total [242]. Most of the data presented in this set was published by Shimanouchi [310], however for some of the molecules that comply with this criteria the vibrational data has been collected from different sources. This is the case for the following species: BH_3 [311, 312], singlet and triplet CH_2 [313, 314], CH_3 [315–317], H_2O_2 [318, 319], H_2S_2 [320], HClO [321, 322], HCO [323, 324], HNCO [325–327], HOCN [328, 329] and HOF [330, 331]. Additionally, the vibrational data of diatomic neutral species collected from Irikura [332] was included in the F set. The F set therefore contains 1069 vibrational modes collected from 143 chemical species and closely mimics the sets used in previous works [242, 246, 247, 304, 305].

The geometries of the selected molecules were fully optimized at the Hartree-Fock (HF), B3LYP [209, 333] and X3LYP [209, 212, 213] levels of theory using Pople's split valence basis sets (6-31G, 6-31G(d), 6-31+G(d), 6-31G(d,p), 6-31+G(d,p)), Pople's valence triple-ζ basis sets (6-311G(d,p), 6-311G(df,p), 6-311+G(df,p)) and Dunning's correlation-consistent basis sets (cc-pVDZ and aug-cc-pVDZ). Vibrational wavenumbers were subsequently calculated at the corresponding level of theory. All quantum chemistry calculations were performed using the General Atomic and Molecular Electronic Structure System (GAMESS) quantum chemistry package [334]. The aug-cc-pVDZ basis set data for Be was collected from the EMSL Basis Set Exchange database [335, 336]. The resulting vibrational wave numbers were further inspected using the MacMolPlt molecular

Table 3.1: Scaling factors *s* and their respective uncertainties *u*(*s*) , for the prediction of vibrational fundamentals, arranged by theoretical method and basis set, determined using the full set *F* . Quantities are expressed as $s \pm u(s)$ and arranged by theoretical method and basis set.

	HF	B3LYP	X3LYP
6-31G	0.9086 ± 0.0468	0.9723 ± 0.0481	0.9695 ± 0.0483
6-31G(d)	0.8981 ± 0.0334	0.9654 ± 0.0280	0.9626 ± 0.0276
6-31+G(d)	0.9002 ± 0.0320	0.9677 ± 0.0288	0.9648 ± 0.0279
6-31G(d,p)	0.9018 ± 0.0347	0.9666 ± 0.0277	0.9639 ± 0.0272
6-31+G(d,p)	0.9036 ± 0.0330	0.9685 ± 0.0282	0.9660 ± 0.0276
6-311G(d,p)	0.9090 ± 0.0350	0.9729 ± 0.0281	0.9703 ± 0.0270
6-311G(df,p)	0.9079 ± 0.0361	0.9717 ± 0.0270	0.9691 ± 0.0268
6-311+G(df,p)	0.9083 ± 0.0356	0.9721 ± 0.0273	0.9698 ± 0.0302
cc-pVDZ	0.9080 ± 0.0338	0.9746 ± 0.0294	0.9724 ± 0.0323
aug-cc-pVDZ	0.9118 ± 0.0336	0.9747 ± 0.0311	0.9723 ± 0.0338

graphics program [337] in order to ensure the correspondence between experimental attributions and the calculated results.

The complete database of experimentally determined wave numbers and their respective calculated harmonic wavenumbers was further partitioned according to the uncertainty range of the experimentally determined wave numbers, to the type of vibrational mode and to the range of the experimental wave numbers. Statistical characterization of *F* and its subsets as well as the determination of the empirical scaling factors was performed using the R language [338, 339].

3.3 Results and Discussion

HF calculations gave theoretical harmonic vibrational wave numbers ω_i which were on average 140 cm^{-1}higher than their respective experimentally determined wave numbers $\tilde{\nu}_i$. On the other hand, DFT methods allowed for more exact unscaled harmonic vibrational wave numbers, for example, the average errors for B3LYP/6-31G(d) and X3LYP/6-31G(d) were 43.7 $cm^{-1}$and 48.3 cm^{-1}, respectively. Upon inspection, the predicted vibrational modes were in good agreement with the experimental attributions. The major exceptions to this observation were wrongful attributions of symmetrical and anti-symmetrical stretching and deformation modes of methyl, methylene and silyl groups.

The scaling factors and associated uncertainties for HF, X3LYP and B3LYP were calculated using the full set *F* and are displayed in Table 3.1. These results are in good accordance with other previously published results [242, 248]. As expected, the HF level of theory presents the poorest results, not only because of its smaller scaling factors, but also because of the magnitude of their associated uncertainties. On the other hand, B3LYP and X3LYP behaved in a most similar fashion, and the resulting scaling factors are equivalent, within their associated uncertainties.

The 6-31G basis set gave poorer results than the other larger basis sets, proving its inadequacy for this kind of work. In all other cases, an overall invariance of the scaling factors with respect to the basis set was observed for each level of theory. These results allow us to further simplify our accounts on the exploration of the calibration set. As such, we present and discuss the results obtained at the X3LYP/6-31G(d,p) level of theory. Non-conformities with the chosen level of theory will be pointed out in due place in the discussion and the scaling factors for all levels of theory and calibration sets tested are available in the supplementary information[2].

Partition schemes for F When splitting F , we were sensitive to three parameters: experimental error associated with the experimentally determined vibrational frequency, type of vibrational mode and the range of wavenumbers considered.

The uncertainties associated with the experimentally determined vibrational frequencies, $u(\tilde{\nu}_i)$, in the F set range from less than 1 cm^{-1} to about 30 cm^{-1}. Frequencies collected by Schimanouchi [310] have their uncertainties classified in five classes, according to the range of their uncertainties. Frequencies taken from other sources were subject to examination before assigning an uncertainty range. In general, the experimentally determined vibrational frequencies published in the last two decades have uncertainties below 1 cm^{-1}, thus falling into Schimanouchi's A class. It should be noted that according to Irikura [248], the contribution of $u(\tilde{\nu}_i)$ to $u(s)$ is negligible. As such, $u(\tilde{\nu}_i)$ will only be used for the purpose of partitioning F . Five subsets of F (denoted A to E) were defined according to the range for $u(\tilde{\nu}_i)$. Preliminary results shown that the E set, which contains experimental data with associated errors between 15 and 30 cm^{-1}, gives rise to scaling factors with very large associated uncertainties. Therefore experimental data with associated uncertainties above 15 cm^{-1} were excluded in all further partitioning schemes for F . The F set deprived of this experimental data will be denoted in this work as F' .

In order to know how X3LYP together with the harmonic oscillator model behaves for each of the most common vibrational modes, the F' set was partitioned into nine subsets. Eight of these subsets (T_1 to T_8) are comprising vibrations that fit into one of these categories: stretching, bending, torsion, deformation, scissoring, wagging, rocking and twisting, respectively. The ninth subset, T_9 , contains the vibrational modes that do not take part on any of the previously defined subsets. T_9 is therefore composed of ring-specific modes of cyclopropane, C_2H_4O, C_2H_4NH and B_2H_6, as well as out-of-plane (OPLA) vibrations.

Finally, the wave number range was also used as a discriminator in another partitioning scheme for F' . The distribution of $\tilde{\nu}_i$ in the F' set (Figure 3.1) shows that it can be divided into four ranges, each of which containing a non-interrupted highly populated region. This criterion was used when defining sets R_1 , R_2 , R_3 and R_4 . Another conceiv-

[2]The supplementary information is available in digital format in the CD-ROM that accompanies this work.

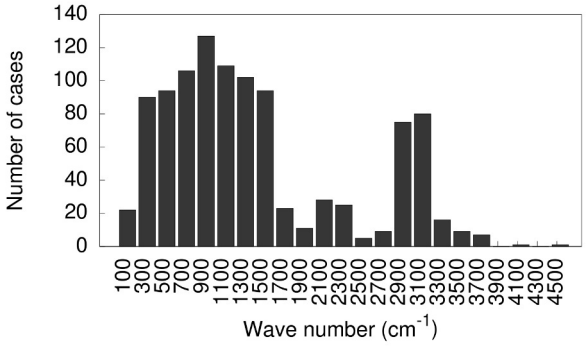

Figure 3.1: Distribution of $\tilde{\nu}_i$ in the F' set.

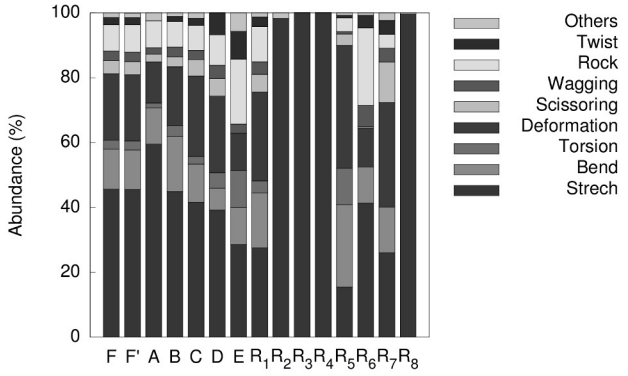

Figure 3.2: Composition of F and its subsets. Subsets of the T_x family are all homogeneous, according to the classification here used, are are therefore omitted.

able partition scheme for F' is to use its quartiles as boundaries between subsets. Sets R_5 , R_6 , R_7 and R_8 were defined in such fashion.

Statistical description of the sets described above is presented in Table 3.2 and the composition of these sets in terms of their vibrational modes content are depicted in figure 3.2.

An overview of Table 3.2 and Figure 3.2 shows that the several subsets of F form a diverse family, not only in terms of their overall statistical description, but also in terms of their composition in terms of vibrational modes. The rest of this work will explore the way such diversity reflects in terms of the resulting scaling factors and their associated uncertainties.

Results The scaling factors for X3LYP/6-31G(d,p) using the calibration sets are presented in Table 3.3. The scaling factors calculated using F and F' are equivalent for the whole range of theoretical methods tested, however, using F' gives rise to smaller uncertainties. This fact can be easily justified by the negative effect of using poor quality experimental data in the calibration. As Table 3.3 shows, the scaling factor using only the E set is most unsatisfying, giving an associated uncertainty which is about 7% in relation

Table 3.2: Statistical description of F and its subsets. Range, Average $u_{max}(\tilde{\nu}_i)$, $\tilde{\nu}_{av}$ and $\sigma(\tilde{\nu}_i)$ are presented in cm^{-1}. The skewness coefficient, G_2 , is defined as $G_2 = (Q_3 + Q_1 - 2Me)/(Q_3 - Q_1)$ and kurtosis, K , is defined as $K = (Q_3 - Q_1)/(2(P_{90} - P_{10}))$, where Q_n , P_n and Me refer to the n^{th} quartile, the n^{th} percentile and the median of the population, respectively.

Set	Range	n	Average $u_{max}(\tilde{\nu}_i)$	$\tilde{\nu}_{av}$	$\sigma(\tilde{\nu}_i)$	G_2	K
F	109.0–4401.2	1069	6.3	1408.0	943.9	0.2866	0.2400
F'	109.0–4401.2	1034	5.5	1410.1	943.6	0.2788	0.2379
A	295.0–4401.2	205	1.0	1727.5	983.6	0.4512	0.3435
B	126.5–3618.8	265	3.0	1304.3	916.4	0.2189	0.1588
C	123.0–3427.0	416	6.0	1263.2	871.9	-0.0702	0.1657
D	109.0–3570.0	148	15.0	1572.8	1005.7	0.5195	0.3835
E	123.0–2967.8	35	30.0	1347.3	964.5	0.6264	0.2469
T_1	351.4–4401.2	472	5.1	2038.6	1001.0	-0.1810	0.4152
T_2	208.0–1594.6	131	4.7	891.4	374.4	0.4506	0.3500
T_3	109.0–656.3	29	6.7	283.8	145.7	0.1960	0.2187
T_4	149.2–1627.4	212	6.2	874.7	489.0	0.0876	0.4213
T_5	188.0–1623.0	42	6.6	1196.7	499.2	-0.8441	0.1244
T_6	460.0–1381.0	30	6.3	1059.2	228.2	0.0390	0.3759
T_7	372.0–1249.1	84	5.7	936.1	200.7	-0.4421	0.2422
T_8	522.2–1419.0	23	9.4	1078.3	237.6	-0.2505	0.2435
T_9	368.0–2110.0	11	3.5	1187.5	491.8	-0.4232	0.1547
R_1	109.0–1885.3	774	5.6	921.2	420.6	0.0266	0.3099
R_2	1928.0–2434.5	58	4.1	2192.7	111.0	0.1424	0.2065
R_3	2528.0–3193.0	168	6.3	2968.6	125.7	-0.2423	0.1537
R_4	3282.7–4401.2	34	3.4	3504.6	242.9	0.2572	0.3256
R_5	109.0–700.0	259	5.8	439.4	159.3	-0.0230	0.3086
R_6	701.4–1151.0	259	5.1	927.5	125.3	0.0854	0.2977
R_7	1151.4–1928.0	257	5.7	1404.3	166.4	-0.2631	0.2205
R_8	1957.0–4401.2	259	5.4	2869.1	423.9	-0.6724	0.1895

to the scaling factor. On the other hand, the use of B , C and D lowered the uncertainty without affecting the scaling factor in a significant fashion. Although this could be interpreted as an effect of the uncertainty of the experimental data on the uncertainty of the scaling factor, results from the A set disprove such conclusion for the moment.

The T_x family of calibration sets allowed us to test the behavior of the theoretical methods used and of the harmonic oscillator model toward each of the most common vibrational modes to be found in chemical systems. Considering that a systematic error is preferable to a large uncertainty, results suggest that the harmonic model works quite well for stretching vibrational modes. While these modes gathered in T_1 give rise to small uncertainties in the scaling factor, torsional modes from T_3 gave, as expected, the highest uncertainties. These results confirm the inadequacy of the harmonic oscillator model to the treatment of torsion modes, and the necessity for other approaches [239, 298]. The T_3 calibration set was also the one on which some sensitivity towards the choice of the basis set was found. In general, the addition of polarization functions to the basis sets decreases the uncertainty, the best results being obtained with the 6-311G(df,p) basis

Table 3.3: Scaling factors for X3LYP/6-31G(d,p) and their respective uncertainties determined using various calibration sets. Quantities are expressed as $s \pm u(s)$.

Set	Scaling Factor	Set	Scaling Factor
F	0.9639 ± 0.0272	T_6	0.9752 ± 0.0222
F'	0.9636 ± 0.0237	T_7	0.9844 ± 0.0398
A	0.9679 ± 0.0270	T_8	0.9858 ± 0.0217
B	0.9617 ± 0.0212	T_9	0.9951 ± 0.0655
C	0.9623 ± 0.0250	R_1	0.9730 ± 0.0372
D	0.9616 ± 0.0172	R_2	0.9632 ± 0.0193
E	0.9764 ± 0.0795	R_3	0.9590 ± 0.0126
T_1	0.9610 ± 0.0189	R_4	0.9626 ± 0.0189
T_2	0.9682 ± 0.0320	R_5	0.9898 ± 0.0712
T_3	0.9740 ± 0.1169	R_6	0.9767 ± 0.0449
T_4	0.9721 ± 0.0286	R_7	0.9695 ± 0.0259
T_5	0.9795 ± 0.0495	R_8	0.9602 ± 0.0151

set, for the three levels of theory considered. Also, the addition of polarization functions lead to a small increase in the uncertainty of the scaling factors, although the addition of diffuse functions decreased the quality of the determined scaling factors. Nevertheless, the value of the scaling factors of the T_3 subset are very close to the values obtained for other "better behaved" vibrational modes such as bending and deformation modes. As such, one may conclude that the bias in the prediction of torsion frequencies is largely due to the nature of the atoms or groups involved and less on the fact that the shape of the potential energy surface (PES) around these type of modes diverges quickly from the shape of the harmonic potential.

Another important question when thinking about the importance of these calibration sets is the almost complete absence of ring-specific vibrational modes in the F set. As such, the T_9 set is essentially composed of OPLA and ring-specific modes. Results obtained with this calibration set show that the scaling factor for these modes is consistently higher and with greater associated uncertainties than with the majority of the other subsets of F . This behavior is consistent across the whole of levels of theory tested and suggests that ring specific modes, as well as, OPLA vibrational modes should be subjected to further study.

The scaling factors determined using the R_x family of sets exhibit a complex behavior that partially reflects the predominance of certain vibrational modes in certain areas of the infrared spectra. As such, the R_1 set gave rise to high scaling factors with large associated uncertainties, the inverse behavior being observed for R_4 and R_8 . In general, both the scaling factors as well as their associated uncertainties decrease regularly with increasing cutoff values for the considered wave numbers. This observation is true when using split valence basis sets, as well as for X3LYP/6-311G(d,p). The use of triple-ζ basis sets with f polarization functions or the use of correlation consistent basis sets lead to more stable scaling factors for the three lower quartiles of F' . In spite of this, the

uncertainty associated with these scaling factors follow the previously described general tendency. This fact is possibly related to the more diverse composition of sets R_5 , R_6 and R_7 , as shown in Figure 3.2, and also to the fact that the bigger triple-ζ and correlation consistent basis set may allow for a marginal increase in the quality of the prediction for low frequency vibrational modes.

Multivariate analysis. Up to this point, we were able to qualitatively observe the behavior of the scaling factors toward the composition and characteristics of the calibration set. In this context, multivariate statistical analysis enables us to confirm our previous observations and also to reveal less obvious effects. In this study, each calibration set is described by the number of experimental vibrational wave numbers included, the average value of their respective maximum uncertainties, $\tilde{\nu}_{\text{av}}$, $\sigma(\tilde{\nu}_i)$, the skewness coefficient G_2 , kurtosis K , as presented in Table 3.2 and also the percentage of each vibrational mode, according to the classes defined earlier in this work and already depicted in Figure 3.2. A preliminary covariance analysis allowed us to remove any further information about the wave number spread of the calibration set, since it is co-variant with $\sigma(\tilde{\nu}_i)$.

Partial least squares (PLS) regression allowed us to establish which of the set descriptors most significantly influence the values of the scaling set and uncertainties. Both the scaling factors s and their associated uncertainty $u(s)$ were also normalized prior to the analysis. PLS analysis was carried on a *per* theoretical method basis, in order not to introduce hidden factors for variance. In all cases, PLS analysis was able to justify over 85% of the variance of s and $u(s)$ using 14 hidden components.

In general, both s and $u(s)$ were revealed to be very sensitive to $\tilde{\nu}_{\text{av}}$, $\sigma(\tilde{\nu}_i)$ and to the percentage of torsion modes in the calibration set. Surprisingly, PLS results show that s is particularly sensitive to the percentage of vibrational modes present in the T_9 subset, although this result may be influenced by the small number of vibrational modes with such classification. On the other hand, the average maximum error of the experimental frequencies in the calibration set strongly influences $u(s)$, but not s itself. As an example, the coefficients of the PLS regression procedure for X3LYP/6-31G(d,p) are shown in Table 3.4.

In general, s and $u(s)$ are quite sensitive to $\tilde{\nu}_{\text{av}}$ and $\sigma(\tilde{\nu}_i)$, both variables giving negative coefficients. This confirms the qualitative analysis of Table 3.3, according to which the higher the wavenumbers considered in the calibration set, the lower are the scaling factors and their respective uncertainties. Results also show that s and $u(s)$ are much less sensitive towards the skewness parameter G_2 , and are virtually insensitive towards kurtosis.

The positive relationships between $u(s)$ and the average $u_{\text{max}}(\tilde{\nu}_i)$ shows that, although the uncertainty in $\tilde{\nu}_i$ has a negligible weight in the expression of $u(s)$ (equation 3.5) [248], the choice of experimental data with high associated uncertainty definitively decreases the quality of the determined scaling factors.

Table 3.4: Coefficients for the PLS regression of s and $u(s)$ towards the descriptors of the calibration set, considering 14 hidden components.

Descriptor	s	$u(s)$
n	−0.048	−0.003
Average $u_{\max}(\tilde{\nu}_i)$	0.123	0.357
$\tilde{\nu}_{\text{av}}$	−0.522	−0.496
$\sigma(\tilde{\nu}_i)$	−0.396	−0.248
G_2	0.126	0.128
K	−0.018	−0.020
%(Stretches)	−0.109	−0.002
%(Bends)	−0.174	−0.116
%(Torsions)	−0.416	0.394
%(Deformations)	−0.070	−0.155
%(Scissoring)	0.189	0.138
%(Wagging)	−0.062	−0.224
%(Rocking)	0.132	−0.045
%(Twisting)	0.154	−0.249
%(Others)	0.458	0.279

The coefficients from the PLS regression also show that $u(s)$ increases with increasing percentage of torsion modes and also with increasing uncertainty in $\tilde{\nu}_i$ and also with the increase in %(Torsions). This confirms the already mentioned ineffectiveness of the harmonic oscillator model when dealing with torsion modes. Despite the small number of ring-specific vibrational modes present in our data set, the very high positive coefficients for %(Others) suggest that the currently used scaling factors may not be proper for use in the study of cyclic structures. This conclusions should, however be subjected to further analysis using a data set with more ring systems. The specific nature of cyclic systems was thoroughly studied by Durig and Laane [340–342], and further discussion in this matter is outside the scope of this work. Although s and $u(s)$ are generally insensitive towards the percentage of most vibrational modes, some levels of theory revealed themselves to be more sensitive to the composition of the calibration set. This is the case of X3LYP/6-311+G(df,p) and X3LYP/cc-pVDZ, which $u(s)$ are sensitive to the percentage of bending, deformation, stretching, twisting and wagging vibrational modes in the calibration set, with coefficients of −0.235, −0.281, 0.298, −0.304 and −0.263 for X3LYP/6-311+G(df,p) and −0.230, −0.285, 0.286, 0.320 and −0.252 for X3LYP/cc-pVDZ, respectively. Additionally, the scaling factors for X3LYP/cc-pVDZ are also sensitive to the percentage of scissoring vibrational modes (coefficient: 0.364). At the X3LYP/aug-cc-pVDZ level of theory, s is strongly dependent on the percentage of stretching modes in the calibration set (coefficient: −0.529), while $u(s)$ shows a significant dependence not only in the percentage of stretching modes in the calibration set, but also of deformation, and twisting modes, with coefficients 0.357, −0.283 and −0.319, respectively.

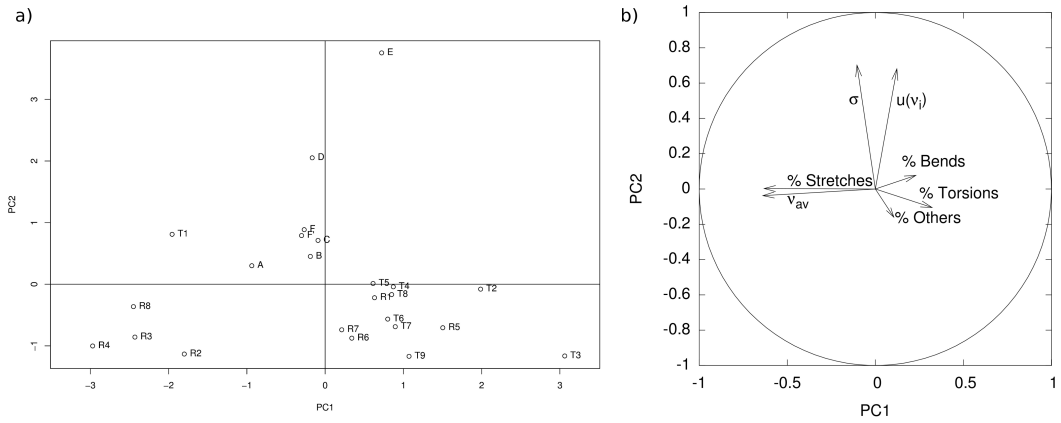

Figure 3.3: Representation of the scores of the PCA analysis for PC1 and PC2 (a) and the correlation circle between their components (b).

From the results in Table 3.4, we conclude that the descriptors that most influence the determined scaling factors and respective uncertainties are the average $u_{\max}(\tilde{\nu}_i)$, $\tilde{\nu}_{\text{av}}$, $\sigma(\tilde{\nu}_i)$, %(Torsions), %(Others), knowing that %(Stretches) and %(Bends) may also play a significant role for some theoretical methods. F , F' and their subsets were analysed using principal component analysis (PCA) using these seven descriptors.

The results from PCA analysis are displayed in Figure 3.3. The first three principal components account for more than 65% of the variance of the system. Figure 3.3 shows that the first two components are able to split the sets used in this work into three groups, with some sets (such as A , E , T_1 and T_3) isolated from the others. On the other hand, the third principal component is particularly sensitive to the percentage of bending and torsion modes and merely separates T_2 and T_3 from the other sets.

PCA analysis confirms that the calibration sets used spread through a wide range of values for the variables which have the most relevant effect in s and $u(s)$. This results provide ground to affirm that the patterns that emerged from PLS regression are valid for any calibration set used to determine s and $u(s)$ using a minimum least-squares regression.

3.4 Conclusions

The vibrational scaling factors for the X3LYP density functional were calculated and were proven to be interchangeable with those here published for B3LYP, within their respective uncertainties. Our results not only confirm Irikura's observation that the scaling factors determined by a least-squares approach are significant only up to two significant digits. Moreover, our results also show that altering the calibration set has little effect in improving the accuracy of the vibrational scaling factors. Being so, the use of scaling factors would lead to corrected vibrational wavenumbers with only two significant digits, which is most unsatisfying for even the most modest applications.

Further work by Irikura [249] shows that the scaling factors for zero-point energy (ZPE) corrections suffer from the same large associated uncertainties. Although the experimental data set for ZPE scaling factors is much too limit for us to conduct a similar analysis of the calibration sets, we believe that our conclusions can be further extended to the scaling factors for ZPE and for the prediction of thermodynamic properties.

The most important conclusion of our work is the inadequacy of the vibrational frequencies calculated using the harmonic oscillator model in even the most modest applications in chemistry. Despite the negative prospective for the use of scaling factors as a mean to bring theoretical calculations closer to experimental results, the present works stresses the importance of the development, implementation and use of more accurate methods for the prediction of vibrational frequencies using first principles methods.

Chapter 4

Charge Distribution in Mn(salen) Complexes[1]

Abstract

The charge and spin distribution in manganese-salen complexes were analyzed using different basis sets and density functionals. Five population analysis methods (Mulliken, Löwdin, NPA, AIM and CHelpG) were used to characterize the charge distribution. Results show that NPA and AIM were the only methods capable of giving charges witht the correct sign for all cases under study. According to the analysis of the natural charge and spin distributions, the salen ligand shows a complex behavior, counteracting the effect of the chloro and oxo ligands on the metal center. Furthermore, the presence of a chloride counter ion increases the oxo-radical character of Oxo-Mn(salen) complexes, which may play an important role in the rationalization of the catalytic properties of Mn(salen) complexes.

4.1 Introduction

Recent years have witnessed the development of novel materials with interesting catalytic activities which are based on the manganese-salen scaffold, henceforward referred to as Mn(salen) [88–92,94,343–346]. Mn(salen) complexes have long been known to efficiently catalyze the epoxidation of unfunctionalized olefins [36, 62], and chiral variations on this scaffold attain remarkable enantioselectivity upon the epoxidation of olefins [75, 78, 112].

Quantum methods, and in particular Density Functional Theory (DFT), allowed very significant insights on the catalytic cycle of Mn(salen) complexes. During the 2000's, theoretical studies on these systems gave a fair description of the catalytic cycle of these systems [135, 136]. Both cationic [Mn(salen)$^+$], **1**, and neutral [Mn(salen)]Cl, **3**, systems

[1] Adapted from F. Teixeira, A. Melo, C. Freire and M. Natália D. S. Cordeiro, *Int. J. Quant. Chem.*, 114, **2014**, 525-533
The contributions of F. Teixeira to this work were the following: Running the first principle computations, performing the multivariate data analysis and writing the first draft of the manuscript.

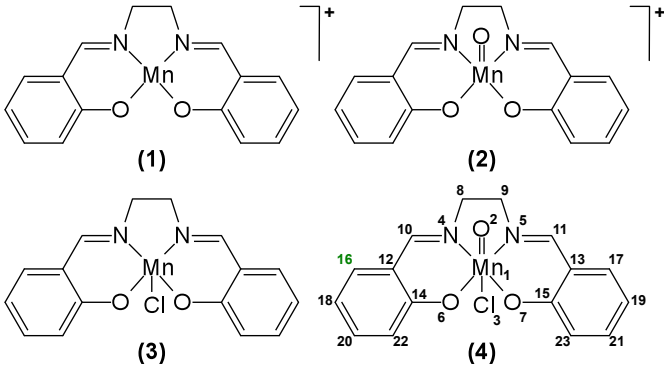

Figure 4.1: Molecular formulas of Mn(salen) and related systems.

(Figure 4.1) have been studied with slightly different results [115, 125, 134, 135, 137]. The catalytic epoxidation of olefins by Mn(salen) is a two stage process: in the first stage, a terminal oxidant reacts with the inactive catalyst to give an oxo-manganese complex ([Oxo − Mn(salen)$^+$], **2**, or [Oxo − Mn(salen)]Cl, **4**, in Figure 4.1); in the following stage, the olefin reacts with the oxo-manganese complex, giving the final epoxide and regenerating the original catalyst [115, 121, 136, 137]. For reasons of simplicity, we shall use the term Mn(salen) as a mean to generically address the four systems under study, and use the numbering scheme presented in Figure 4.1 when referring to each individual complex.

Effective atomic charges are one of the most useful ways to interpret the electronic structure of a chemical system. The ability to localize charges in a chemical system allows for a rationalization of organic and inorganic reactivity, as well as prediction of its physical and chemical properties [347]. Furthermore, effective atomic charges are used as parameters for the computation of electrostatic interactions in several Molecular Mechanics (MM) simulation techniques [182]. The population analysis methods, applied to determinate such type of effective charges, play then an important role for rationalizing the behavior of the Mn(salen) catalyst and derived materials. Because effective atomic charges are not directly associated with a physical observable, different approaches to the determination of such charges have emerged: population analysis based on the basis functions (such as Mulliken and Löwdin population analysis [186]), population analysis based on the electron density (such as the Natural Population Analysis [258], NPA, and the integration of atomic basins defined under the Atoms In Molecules [262], AIM, formalism), fitting of the electrostatic potential (CHelpG [348], being an example of such a procedure), or by fitting spectroscopic and/or empirical data [270]. The performance of these methodologies has been extensively tested in a multitude of different scenarios such as prediction of pK_a values [347], and determination of charge transfer phenomena [349, 350]. In 2004, Martin and Zipse studied the charge distribution on the water molecule using the five aforementioned methods together with both wave mechanics and DFT calculations using different basis sets. This allowed some conclusions on how the effective atomic charges obtained using different partition schemes vary according to the

level of theory used to obtain the wave function or density function they require [250]. In their conclusions, Martin and Zipse point out to the poor results given by Mulliken population analysis and also to the possibility that some methodologies, specially CHelpG and similar techniques, may be unsuitable for larger systems [250]. Despite that, Mulliken and CHelpG charges have been used in some works concerning Mn(salen) complexes [126, 351–353].

In this work, we question whether the capabilities of the five aforementioned population analysis techniques are adequate to represent the charge distribution in Mn(salen) complexes, and also which is the physical picture that arises from such analysis. In order to do so, effective atomic charges for the atoms in the four Mn(salen) systems depicted in Figure 4.1 were calculated using the five aforementioned partition schemes (Mulliken, Löwdin, NPA, AIM and CHelpG). These charges were determined from DFT calculations using functionals that correspond to different approximations of the exchange-correlation energy functional, under the Kohn-Shan formalism [354] and different basis sets. The results are displayed in order to gain some physical insight on how charge is distributed in these complexes, and how that may affect their catalytic efficiency and also their chemical stability.

4.2 Methodology

All DFT calculations, as well as the calculation of Mulliken, Löwdin and CHelpG charges, where performed using the Orca program package, version 2.8 [355]. Natural Population Analysis (NPA) was performed using version 5.2 of the NBO program from the University of Wisconsin [356]. AIM charges were calculated using the AIMPAC package [357] from Prof. R. Bader. A conversion utility (Molden2AIM) from Prof. Wenli Zou at the Southern Methodist University, Dallas [358] was used to generate the input of AIMPAC from the output of Orca.

Throughout this work, we have chosen to follow the nomenclature used by Cavallo and Jacobsen [136]. The relevant electronic states are identified by a notation indicating the respective total spin density $S = |\rho_\alpha(\mathbf{r}) - \rho_\beta(\mathbf{r})|$. So that the symbols *S0*, *S2* and *S4* refer to total spin densities of zero (singlet), two (triplet) and four (quintet) unpaired electrons, respectively.

The geometry of the four Mn(salen) systems (**1**-**4**) were optimized at their singlet, triplet and quintet configurations using the LSD [205], PW91 [208, 359], X3LYP [213] and TPSS [210] functionals together with three basis sets predefined in the software package: DefBas-2, DefBas-3 and DefBas-4, based on Ahlrichs basis sets with additional polarization functions taken from the TurboMole library [360, 361]. For reasons of convenience, the naming scheme for the basis sets will coincide with that found in the software package. Being so, DefBas-2 corresponds to a split valence (SV) basis set with contraction scheme $\{31\}$ for hydrogen and $\{511/31/1\}$ for atoms in the main group, and a triple-

ζ valence (TZV) basis set with contraction pattern $\{842111/6311/411\}$ for manganese; DefBas-3 corresponds to a TZV basis set which is $\{311\}$ for hydrogen, $\{62111/411/1\}$ for atoms in the main group and $\{842111/6311/411/1\}$ for manganese; and DefBas-4 corresponds to a TZV basis set which is $\{311/1\}$ for hydrogen, $\{62111/411/11\}$ for atoms in the main group and $\{842111/63111/411/1\}$ for manganese.

For the *S2* and *S4* states, all calculations were performed under an unrestricted Kohn-Shan scheme, with independent treatment of the electron densities $\rho_\alpha(\mathbf{r})$ and $\rho_\beta(\mathbf{r})$. For *S0* systems, preliminary calculations at the X3LYP/DefBas-3 level of theory were performed using the unrestricted scheme, the restricted scheme and also a broken-symmetry unrestricted scheme. These preliminary calculations allowed us to conclude that the results from the unrestricted and restricted types converged to the same geometry and energy. With these results in mind, a restricted Kohn-Shan formalism was used in the calculations for the *S0* systems.

4.3 Results and Discussion

A large amount of data was collected in this work. In order to streamline this discussion, these results shall be presented in the following manner: first, we shall present the relative ordering of the lowest energy *S0*, *S2* and *S4* states and describe the equilibrium geometries of each complex at the different levels of theory. In a second stage, the five methods for determining effective atomic charges will be evaluated using the manganese and some of its adjoining atoms as a study case. After that, we present a detailed study of the charge distribution on the four Mn(salen) complexes at the X3LYP/DefBas-4 level of theory, these results being representative of those obtained using most density functionals and basis sets tested. Finally, we present the spin distribution for the *S2* and *S4* states of the four Mn(salen) complexes and draw a general picture of the distribution of the electronic density on these complexes.

4.3.1 Energetic and Geometric Considerations

Absolute energies for all systems are given in the supplementary information[2]. The relative energies of the *S0* and *S4* states (taking the *S2* state as the reference) of the four Mn(salen) systems are displayed in Table 4.1. The obainted results suggest that LSD comparatively favors states with the lowest spin multiplicity: lowering the relative energy of the *S0* state by about 20 kJ/mol and consistently increasing that of the *S4*, although in a more diversified manner. All functionals agree on a *S0* ground state for **1**, which is in accordance to the DFT and Coupled Cluster results presented by Abasking and co-workers [115].

[2]The supplementary information is available in digital format in the CD-ROM that accompanies this work.

Table 4.1: Relative energies (in kJ/mol) for the relevant electronic states of the Mn(salen) and Oxo-Mn(salen) complexes. For a given level of theory, the energy of the *S2* state is set to zero.

Level of Theory	**1**		**2**		**3**		**4**	
	S0	*S4*	*S0*	*S4*	*S0*	*S4*	*S0*	*S4*
LSD/DefBas-2	–68.1	102.8	–19.2	94.7	12.2	240.5	–13.5	230.6
LSD/DefBas-3	–66.0	104.6	–16.0	99.2	6.1	242.5	–11.9	232.4
LSD/DefBas-4	–65.5	110.2	–15.7	100.0	6.5	241.6	–13.4	231.0
PW91/DefBas-2	–44.8	72.2	0.4	65.9	24.4	224.0	6.0	246.8
PW91/DefBas-3	–42.7	73.5	2.8	69.6	17.9	225.7	5.8	218.4
PW91/DefBas-4	–42.0	77.9	4.0	70.4	18.8	224.6	5.0	217.1
TPSS/DefBas-2	–44.9	72.0	3.0	58.1	29.1	222.9	7.9	218.6
TPSS/DefBas-3	–43.9	74.0	5.0	62.7	22.7	224.9	7.4	219.9
TPSS/DefBas-4	–44.2	77.5	5.9	63.6	23.8	223.9	6.5	218.5
X3LYP/DefBas-2	–19.5	80.5	21.8	40.4	24.1	236.8	13.5	229.3
X3LYP/DefBas-3	–18.7	82.3	23.5	45.0	16.5	238.6	7.8	232.3
X3LYP/DefBas-4	–21.7	84.1	24.9	46.5	20.0	237.3	7.7	231.4

Despite the aforementioned bias shown by LSD, all other levels of theory agree on a triplet ground state for compounds **2**, **3** and **4**. PW91 and TPSS predict near degeneracy between *S0* and *S2* for species **2** and **4**, whereas X3LYP only reports that possibility for compound **4**. The results for compound **4** are in qualitative accordance to the CASSCF results independently published by Ivanic, Sears and their respective co-workers, using a truncated model for the salen ligand [116,117]. Within each functional, the ordering of the different states is unaltered upon varying the basis set, although the results accomplished using DefBas-3 and DefBas-4 are more similar to each other than to those obtained using the DefBas-2 basis set.

The equilibrium geometries of the four Mn(salen) complexes are given in the supplementary information. All methods predicted a square planar geometry around the metal atom for complex **1**. In complexes **2** and **3**, the pentacoordinated manganese atom is slightly distorted towards a pyramidal-type geometry. Results show that the geometry obtained for complex **2** is close to that of a square pyramid with the $O_{(2)}$ atom occupying the axial position; whereas that of complex **3** appears to be close to an trigonal bipyramidal configuration with the Cl atom at one of the equatorial positions, the other two equatorial positions being occupied by one N and one O atom from the salen ligand. In addition, the results show that, for any given complex, the geometries present little variation for the different spin states and levels of theory. Taking this into account, the average $Mn - O_{(2)}$ bond distance in complexes **2** and **4** is 1.532 Å with a standard deviation of 0.014 Å; similarly, the $Mn - Cl$ bond distance in complexes **3** and **4** is 2.25 ± 0.11 Å. As to the bonds connecting Mn to the salen ligand, the bond length for $Mn - N_{(4,5)}$ is 1.78 ± 0.03 Å, whereas the $Mn - O_{(6,7)}$ is 1.72 ± 0.06 Å.

4.3.2 Charge Distribution

Information on the Mulliken, Löwdin, NPA, AIM and CHelpG effective atomic charges for the four complexes in Figure 4.1 at all spin states and calculated at all levels of theory is available in the supplementary information. Figure 4.2 exemplifies how the five population analysis tested behave when applied to the electronic structure of **3** at the *S2* state calculated at different levels of theory. This compound was chosen as an example since all levels of theory agree on its *S2* ground state. As expected, Mulliken and Löwdin population analysis show a high dependence on the basis set. Unsurprisingly, Mulliken population analysis often results in charges of the wrong sign; the most striking example being the manganese atom in complex **4** bearing a negative charge (for basis sets DefBas-3 and DefBas-4). This worsening in performance when increasing the complexity of the basis set indicates that DefBas-3 and DefBas-4 are probably too big for the Mulliken scheme to be applied [182]. Because large basis sets are invaluable in describing the electronic structure of these transition metal complexes, Mulliken population analysis should be discarded as a plausible method for determining effective atomic charges in such species. Despite also presenting a strong dependence on the basis set, Löwdin charges always bear a positive sign for Mn, although sometimes bearing a positive sign for the chlorine atom in complex **3**, as seen in Figure 4.2b. In conclusion, both methods fail at one time or another, making them unreliable for the subject at hand.

On the other hand, NPA and AIM charges are very stable towards the level of theory chosen, as shown in Figures 4.2c and 4.2d. AIM charges, however tend to be more extreme than their NPA counterparts, usually giving charges with a greater absolute value. This is a well known feature of AIM population analysis that has long diminished its applicability in the development of molecular force fields for MM simulations [362]. The numerical integration of the atomic basins necessary for the determination of AIM charges makes the process much more computationally demanding than the determination of NPA charges. This is particularly important when doing the integration of the basins corresponding to manganese and its adjacent atoms, for which the tightest integration grid allowed by AIMPAC had to be applied in conjunction with the more time consuming PROMEGA algorithm [357, 363]. This practical matter makes NPA more appealing when dealing with chemical systems with the same approximate size and number of electrons as those presented here.

The CHelpG charges behavior with respect to the level of theory used to evaluate the electronic structure of the complexes under study is somewhat of a middle ground between the strong dependence shown by Mulliken and Löwdin and the almost complete stability provided by NPA and AIM. CHelpG charges show some variation with respect to the basis set chosen and, to a lesser extent, to the density functional used in the calculations, as can be seen in Figure 4.2e. Their absolute values are usually smaller than their NPA and AIM counterparts. CHelpgG performed poorly when determining the

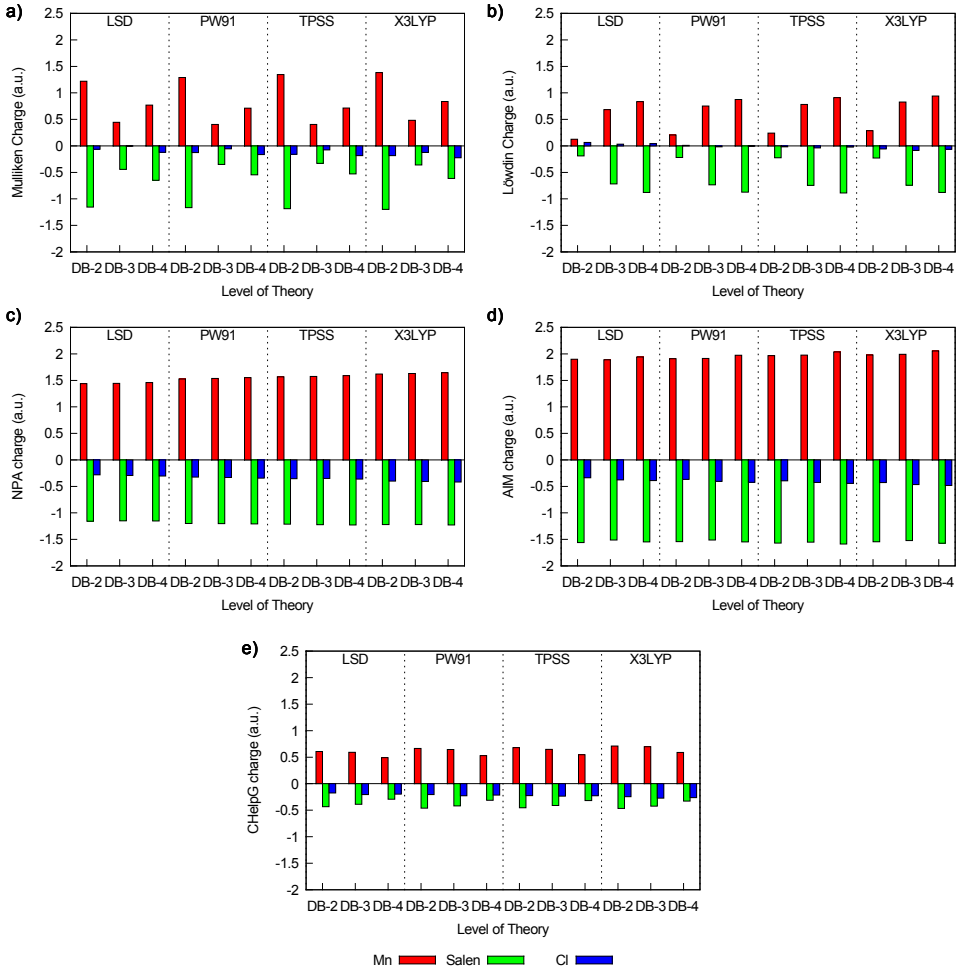

Figure 4.2: Mulliken (a), Löwdin (b), NPA (c), AIM (d), and CHelpG (e) charges for Mn, the salen ligand, and Cl for compound **3** at the *S2* state, calculated at different levels of theory.

charge distribution for states *S0* and *S2* of complex **1**, giving the wrong sign for the charge of Mn and also for the combined charge of the atoms in the salen ligand.

The preliminary analysis allowed us to discard Mulliken and Löwdin charges from further discussion. The distribution of the charges obtained using the three remaining population analysis methods for Mn, $O_{(2)}$ and Cl, as shown in Figure 4.3, suggests that the different methods may give rise to complementary views on the charge distribution on these molecules. The failure of CHelpG in giving charges of the right sign for complex **1** is patent in Figures 4.3a and 4.3b. However, the most interesting feature on Figure 4.3a is the different distributions obtained when evaluating the effective atomic charge of Mn using NPA and AIM. The curve for AIM charges shows that two populations are clearly distinguishable: a population with q(Mn) = 1.92 $\pm$ 0.09 a.u. that corresponds to compounds **1** and **3**, and a second population with q(Mn) = 2.43 $\pm$ 0.08 a.u. corresponding to the oxo-complexes **2** and **4**. On the other hand, NPA does not appear to distinguish between these two populations, distributing the charges for Mn around an average value of

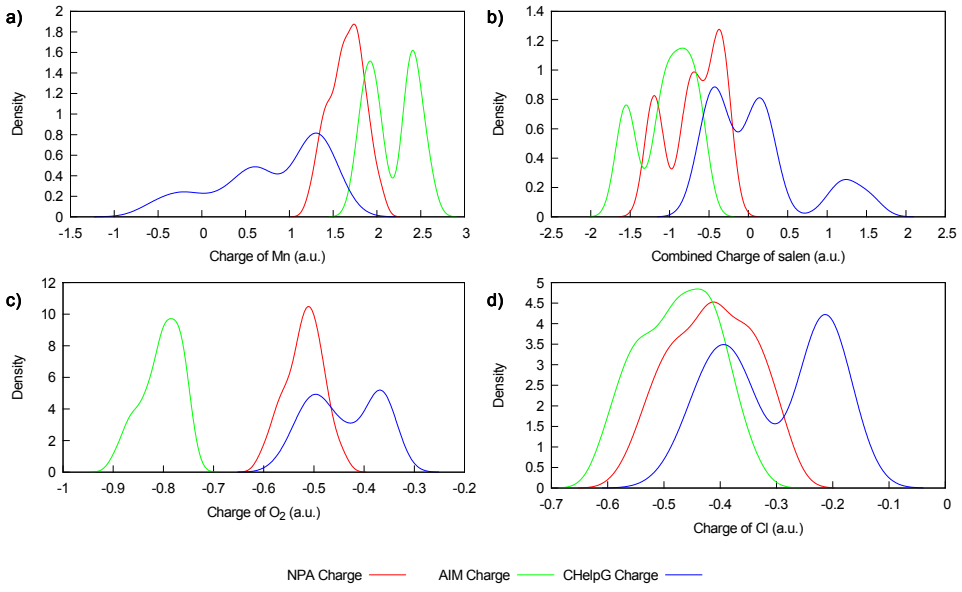

Figure 4.3: Distribution of the values of the charge of Mn (a); salen (b); $O_{(2)}$ (c); and Cl (d) calculated using NPA, AIM and CHelpG.

1.65 ± 0.19 a.u.. Similar results were observed for the distribution of the combined charge of the salen ligand (Figure 4.3b), although in this case both AIM and NPA were capable of discerning two populations. Upon inspection, the lowest charges for salen were observed in complex **3**, with average values of -1.20 ± 0.04 a.u. and -1.55 ± 0.06 a.u. for NPA and AIM, respectively. Thus, both NPA and AIM clearly distinguish the effective charge of the salen ligand in complex **3** from that observed in the remaining complexes.

The distribution of NPA, AIM and CHelpG charges for $O_{(2)}$ is displayed in Figure 4.3c. The results from NPA and AIM suggest that the effective atomic charge of $O_{(2)}$ does not depend on the presence or absence of the chloride counter ion. In contrast to these results, two populations emerge from the distribution of CHelpG charges, centered around the values -0.39 ± 0.03 a.u. and -0.50 ± 0.03 a.u. for complexes **2** and **4**, respectively. A similar scenario emerges from the analysis of the distribution of the effective atomic charges for Cl displayed in Figure 4.3d. While NPA and AIM charges arrange as a single population around an average value of -0.41 ± 0.08 a.u. and -0.48 ± 0.07 a.u., respectively, CHelpG charges divide into two separate populations with average charges of -0.21 ± 0.03 a.u. and -0.40 ± 0.04 a.u. for complexes **3** and **4**, respectively. Despite its shortcomings in the evaluation of effective atomic charges for complex **1**, CHelpG charges provide the interesting results of differentiating the effective charge of the axial ligands $O_{(2)}$ and Cl in complexes **2**, **3** and **4**. This is most likely due to the fact that CHelpG charges are much more sensitive towards polarization effects than NPA or AIM, as described by Rigby and Izgorodina [350].

An overall analysis of Figure 4.3 shows that the variance within the results obtained from NPA, AIM and CHelpG population analysis is more likely to be related to the struc-

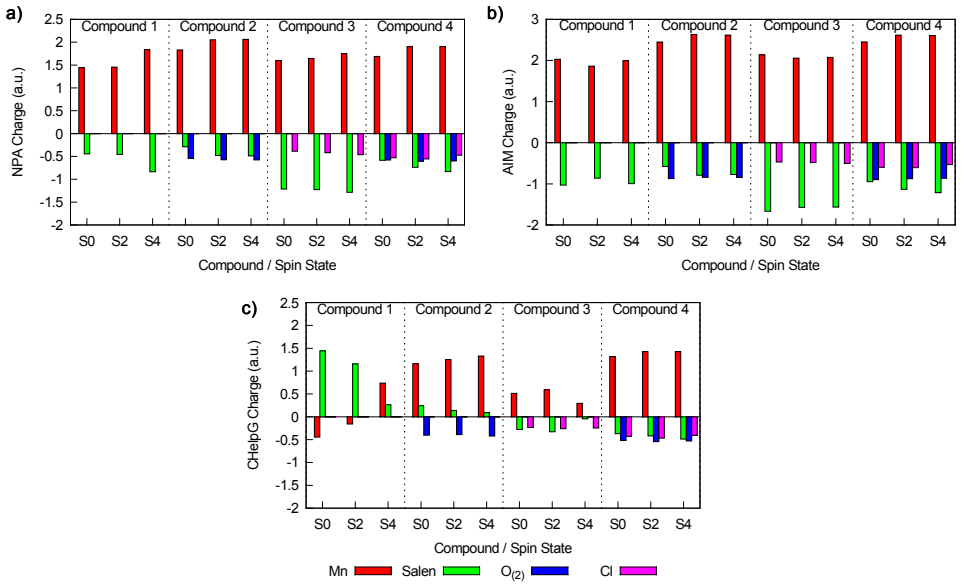

Figure 4.4: NPA (a), AIM (b) and CHelpG (c) charge distribution for the four complexes under study at their *S0*, *S2* and *S4* states at the X3LYP/DefBas-4 level of theory.

tural properties of the system than it is influenced by the choice of basis set or density functional. Being so, for the remainder of this discussion we shall focus on the results obtained at the mboxX3LYP/DefBas-4 level of theory. Such results are depicted in Figure 4.4, showing the NPA, AIM and CHelpG charges of Mn, salen, $O_{(2)}$ and Cl on the four complexes under study at their different spin states. Again, NPA and AIM charges appear to give the same overall picture of the charge distribution for each compound. There are, however, some minor differences between Figures 4.4a and 4.4b which are worth exploring. The *S0* and *S2* states of compound **1** appear to have the same charge distribution, while at *S4* there is a noticeable increase in charge separation in Figure 4.4a. This could be interpreted as the promotion of one electron from one of the metal's 3*d* orbital to one of salen's π^* orbitals. As a complementary hypothesis, the difference between the *S0* to the *S2* states for **1** would lie in the different occupation of the 3*d* orbitals of the manganese atom. Both hypotheses were confirmed by analysis of the frontier molecular orbitals for this compound at the three spin states. Such transitions, however, do not appear to strongly influence the topology of the electron density, thus the AIM charge distribution of **1** remains unaltered throughout the three spin states. For compounds **2** and **4**, similar differences were found between the *S0* state and their *S2* and *S4* states. In both cases the AIM charge distribution is in accordance with that obtained from NPA. However, despite the fact that AIM charges are usually of greater magnitude than NPA ones, the differences on the charge distribution between different states are much less pronounced.

As perceived in Figure 4.4, all methods agree that the main source of variation for the effective atomic charge of Mn is its oxidation state. As for the charge of the salen ligand,

NPA and AIM agree that its magnitude increases upon coordination with chloride. This is particularly obvious when comparing compounds **1** and **3** (Figure 4.4). The charge of salen is less pronounced for the oxo-complexes **2** and **4** when compared to their relative reduced species (**1** and **3**, respectively). These results suggest that salen may act as a charge reservoir that stabilizes the charge of the metal center: it donates some amount of electron density to the metal center upon oxidation, and the opposite transfer of electron density occurs in the presence of a donor ligand.

As stated before, CHelpG failed to give charges of the correct sign for **1**. As shown in Figure 4.4c, the same also happens for the charge of the salen ligand in compound **2**. For compounds **3** and **4**, CHelpG shows a tendency to portrait salen as a ligand bearing little charge; because of this, the changes in the electronic structure of these three complexes are reflected primary on the charges of Mn, $O_{(2)}$ and Cl, thus explaining the behavior observed in Figure 4.3. CHelpG charges seldom allow for the rationalization of reactivity, but are common in the parameterization of molecular force fields, and have been applied to Mn(salen) complexes in recent years [351, 364]. Figure 4.4c, however, suggests that electrostatic interactions involving $O_{(2)}$ and Cl could be overestimated in comparison to those involving the salen ligand, when using such charges. Nevertheless, the consequences of opting for CHelpG charges in detriment of NPA or any other population analysis method in the context of force field parameterization is a complex matter that lies beyond the scope of this work.

Figure 4.5 depicts the charge distribution within the salen ligand for the four Mn(salen) complexes at the *S0* and *S2* spin states; the *S4* state being omitted for the sake of simplicity. The charge distribution in **2**, **3** and **4** is slightly asymmetric, resulting from the twisted conformation of the salen ligand. The *S0* and *S2* states of **1** and **3** show the same charge distribution across the molecule, further assessing the hypothesis that the difference between those two states lies with the different occupation of the metal's 3*d* orbitals. On the other hand, in complexes **2** and **4**, $N_{(4)}$, $N_{(5)}$, $C_{(10)}$ and $C_{(11)}$ appear to have the most noticeable changes in their effective atomic charge when comparing the *S0* and the *S2* state of both molecules. Also, most of the charge in the salen ligand is defined by the atoms in the inner aromatic rings; the carbon atoms in the outer aromatic ring bearing little charge. Upon oxidation, the positive charge of $C_{(10)}$, $C_{(11)}$, $C_{(14)}$ and $C_{(15)}$ increases, while the negative charge of $C_{(12)}$ and $C_{(13)}$ also increase in magnitude. The coordination of chloride to the manganese atom bears a less pronounced effect, affecting only the positive charges in $C_{(10)}$ and $C_{(11)}$, which become smaller. Thus, the formation of oxo-Mn(salen) complexes is accompanied by an increase in the polarization of the $N_{(4)} - C_{(10)}$, $N_{(5)} - C_{(11)}$, $C_{(10)} - C_{(12)}$, and $N_{(11)} - C_{(13)}$bonds, which is moderated by the eventual presence of chloride acting as an axial ligand.

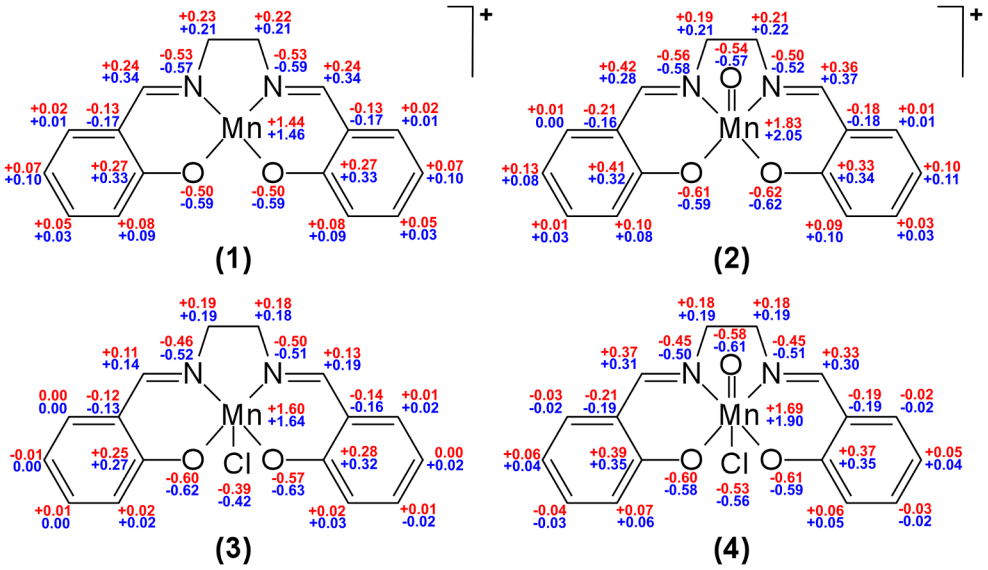

Figure 4.5: Distribution of NPA charges on Mn(salen) complexes, calculated at the X3LYP/DefBas-4 level of theory, for the *S0* (red) and *S2* (blue) spin states. For simplicity, the charge of each hydrogen atom was combined to that of the carbon atom to which it is bonded.

4.3.3 Spin Distribution

Some population analysis methods offer the spin density at each atom as a by-product when supplied with an unrestricted wavefunction. This is not the case of CHelpG, which was design specifically for the calculation of atomic charges. In this work, practical considerations lead us to prefer the input for AIMPAC to be expressed in terms of quasi-restricted orbitals, thus making the AIM spin density also unavailable. Figure 4.6 shows the distribution of the NPA spin density among Mn, salen, $O_{(2)}$, and Cl at the X3LYP/DefBas-4 level of theory. The results shown in Figure 4.6 allow us to further differentiate the behavior of the oxo-Mn(salen) complexes **3** and **4** from that of their reduced counterparts. Not only does the manganese atom retain its spin density (about 1.0 a.u.) at both states, the same appears to be unaffected by the presence or absence of chloride. On the other hand, for complexes **1** and **2**, there is a noticeable increase in the spin density of both Mn and salen. In all cases, $C_{(10)}$ and $C_{(11)}$ bear most of the spin density of salen at the *S2* state, whereas at *S4* the spin density is shared among $C_{(10)}$, $C_{(11)}$, $C_{(14)}$ and $C_{(15)}$. These observations are nicely correlated with the effect $O_{(2)}$ and Cl have on the charge of these four carbon atoms.

Focusing on the *S2* state, the presence of chloride in **2** reduces the spin density at the salen ligand by about half (in comparison to **1**), concentrating the same at the manganese atom. At the same time, the effect of chloride in **4** appears to be the increase in the spin density of the oxo ligand by about 0.05 a.u.. Assuming that the *S2* state is either the ground state or a thermally accessible excited state, these results are significant for explaining how a counter ion or donor ligand might affect the degradation of Mn(salen) and oxo-Mn(salen) compounds. It is known that an increase in the oxo-radical character

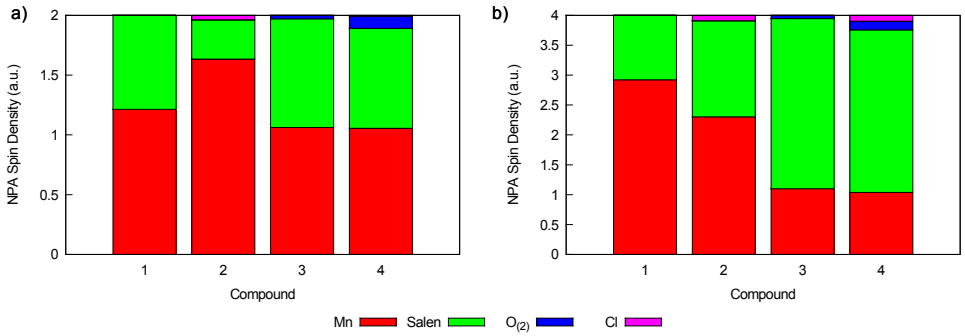

Figure 4.6: NPA spin densities of the Mn, $O_{(2)}$ and Cl atoms, together with the combined spin density of the atoms in the salen ligand, at the *S2* (a) and *S4* (b) states of the four Mn(salen) complexes, at the X3LYP/DefBas-4 level of theory.

of oxo-metalloporphyrins is associated with lower epoxidation activity and increased porphyrin destruction [80]. Should the same effect be true for oxo-(Mn)salen complexes, the presence of chloride as a counter ion would increase the rate of catalyst degradation.

4.4 Conclusions

In this work, five methods for determining effective atomic charges were tested in Mn(salen) complexes. As expected, Mulliken and Löwdin population analysis fail to present a physically sound picture of the charge density for the four complexes studied.

On the other hand, NPA and AIM gave physically sound results, the latter usually giving charges of greater magnitude than the former. These two partitioning schemes gave results much closer to one another than to those obtained using the CHelpG partition scheme. This is in contrast to what was observed by Szefczyk and co-workers when studying intermolecular transfer phenomena [349]. To the best of our knowledge, such difference in the performance between these three partition schemes can only be justified when considering the nature of the metal-salen bond to be more involved than a simple dative bond between salen and the manganese atom. Comparing the NPA charges of each compound at different spin states, it was possible to gain information on the charge transfer mechanism for a conceptual transition between some of those states. Population analysis using NPA allowed further insights into the charge partition between Mn and salen for each complex at different spin states. Some of these comparisons were unnoticeable under AIM. Both NPA and AIM extend beyond the scope of population analysis and their capabilities to rationalize the reactivity of these transition metal complexes remains unexplored.

For the most part, our assertions on the behavior of these five charge partition methods is in good accordance to the conclusions withdrawn by Martin and Zipse [250]. However, some remarks are in order: firstly, AIM charges were not as dependent on the basis set as stated by Martin and Zipse. Such dispersion was mostly observed when using unpolarized basis sets. It is well known that the AIM definition of the atomic basins gives

incorrect results when used in conjunction with unbalanced or underpolarized basis sets, which are corrected upon using more balanced basis sets [262, 365]. In this case, the low dispersion of the AIM charges with respect to basis set and level of theory strongly suggests that the basis sets tested are well balanced and properly polarized. Secondly, CHelpG charges failed to give meaningful results, specially when applied to complexes bearing positive charge (**1** and **2**). On the other hand, for the systems **2**, **3** and **4**, CHelpG charges for Mn, $O_{(2)}$ and Cl were much more sensitive to the composition of the overall system than their NPA and AIM analogues. Such underachievements of the CHelgG scheme was hypothesized by Martin and Zipse [250] and our results confirm that special care must be taken when applying this method to transition metal complexes such as those studied in this work. One might hypothesize that these results from CHelpG could be explained by an improper grid for the determination of the MEP, as suggested by Rigby and Izgorodina [350]. However, this would affect the effective atomic charge of Mn in compound **4** more than in compounds **3**, **2** and **1**. Our results point otherwise, thus discarding the possibility of having used an incorrect grid in the determination of CHelpG charges.

Finally, the results suggest that the charge partition between manganese and the salen ligand reflects not only the oxidation state of the metal and the overall spin density of the complex, but also the presence or absence of an axial ligand such as chloride. Upon oxidation of the metal center, salen may give some of its electron density to manganese. In this process, the charge of salen decreases in magnitude, while the polarization of its inner aromatic rings increases. Chloride appears to moderate this effect. The presence of chloride also carries consequences in terms of the spin distribution (which was analyzed under NPA), the most important being the increase on the oxo-radical character of **4** (in comparison to **3**), which may be important in the rationalization of phenomena such as catalyst destruction and efficiency towards the epoxidation of unfunctionalized olefins.

Chapter 5

Principal Component Analysis of Mn(salen) Catalysts[1]

Abstract

The theoretical study of Mn(salen) catalysts has been traditionally performed under the assumption that the Mn(acacen') (acacen' = 3,3'-(ethane-1,2-diylbis(azanylylidene))bis(prop-1-en-olate)) is an appropriate surrogate for the larger Mn(salen) complexes. In this work, the geometry and the electronic structure of several Mn(salen) and Mn(acacen') model complexes were studied using X3LYP/triple-ζ valence basis set calculations, with the aim of understanding the effects of truncation, metal oxidation, axial coordination, substitution on the aromatic rings of the salen ligand and chirality of the diimine bridge. To achieve this goal, geometric and structural data, obtained from these calculations, were subjected to Principal Component Analysis (PCA) and PCA with orthogonal rotation of the components (rPCA). The results demonstrated that the differences between salen and acacen' complexes account for about 11% of the variance in the data, and are mostly related to the magnitude of the natural charges on the atoms common to both ligands. Variations in the spin state and oxidation state of the metal center account for larger fractions of the total variance (up to 22% and 15%, respectively). Other effects, such as the nature of the diimine bridge or the presence of alkyl substituent in the 3,3' and 5,5' positions of the aldehyde moiety, were found to be less important in terms of explaining the variance within the data set.

A matrix of discriminants was compiled using the loadings of the principal and rotated components that best performed in the classification of the entries in the data. The scores obtained from its application to the data set were used as independent variables for devising linear models of different properties. Predictive linear models, for the energy difference between the singlet and quintuplet states, the energy

[1] Adapted from F. Teixeira, A. Melo, C. Freire and M. Natália D. S. Cordeiro, *Phys. Chem. Chem. Phys* **2014**, (submited)
The contributions of F. Teixeira to this work were the following: Running the first principle computations, performing the multivariate data analysis and writing the first draft of the manuscript.

involved in the oxidation of these complexes to their oxo-derivatives and the spin densities at the oxo ligand of these latter compounds were successfully derived using this approach.

5.1 Introduction

Manganese-salen complexes, hereafter Mn(salen), are well known catalysts in the epoxidation of alkenes and other olefinic materials. Their use in industrial applications has been prompted by their low cost, easy preparation and high activity [86]. The enantioselectivity of Mn(salen) complexes relies not only in the potentially stereogenic sp^3 hybridized carbon atoms of the diimine bridge, but also on both steric and electronic properties of the salen complex [36]. The Jacobsen's catalyst serves as an example of the high levels of catalytic efficiency and stereoselectivity achieved by this class of transition metal complexes. This has triggered further developments in asymmetric catalysis, including the development of novel chiral Mn(salen) complexes [36], the immobilization of such complexes onto different supporting materials [50, 92, 95, 97, 366, 367] and the rationalization of the catalytic cycle of this family of compounds using both theoretical and experimental methods [124, 135, 364, 368].

In the presence of a terminal oxidant, Mn(salen) complexes are typically oxidized to their oxo-Mn(salen) analogues. These oxo-complexes are the active species responsible for the epoxidation of the substrate [36, 106]. In both types of complexes, the salen ligand adopts a nearly planar conformation. In oxo-Mn(salen) complexes, one of the axial positions is occupied by the oxo- ligand, leaving at all times one vacant axial position in the coordination sphere of the manganese atom. The vacant axial position may be occupied by a counter ion such as chloride, or a donor ligand. This possibility provides a valuable route for the anchoring of Mn(salen) complexes onto a supporting material, using a linker molecule. In recent years, this strategy allowed the development of novel materials with interesting catalytic properties [50, 92].

The importance of this catalytic system and the controversies surrounding its catalytic cycle have triggered several theoretical studies. These models rely on Density Functional Theory (DFT) to provide an adequate description of electron correlation at a reasonable cost. The quest for further savings in computational cost has lead to using Mn(acacen') complexes (where acacen' stands for 3,3'-(ethane-1,2-diylbis(azanylylidene))bis(prop-1-en-olate), $^{-}O(CH)_3N-C_2H_4-N(CH)_3O^{-}$) such as **1** (Figure 5.1) as surrogates for the the larger Mn(salen) compounds [36, 135, 136]. More rigorous methods, such as Coupled Cluster (CC) or Complete Active Space Self-Consistent Field (CASSCF), have been sparsely applied to this problem for being too computer-demanding. Moreover, these techniques usually required also further truncation of the molecular models [115, 117, 120].

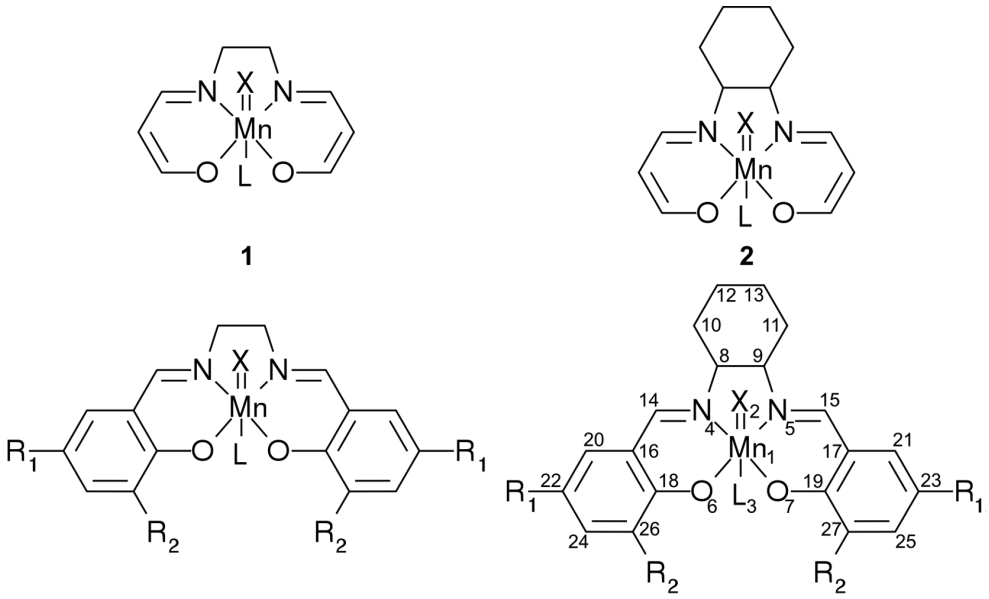

Figure 5.1: Manganese-acacen' (**1** and **2**) and manganese-salen (**3** to **16**) complexes used in this study. The diagram for compounds **4**-**16** further illustrated the numbering scheme used in this work. For each compound, X may either be nothing (re) or O (ox); also, L may either be nothing (null), Cl^- (cl), $CH_3CH_2NH_2$ (amine), or $CH_3CH_2NH^-$ (amide).

With the development of computational technologies and the increased interest in Mn(salen) catalyzed epoxidations, an assessment on how the properties of Mn(acacen') may be translated to those of Mn(salen) complexes is mandatory. The question of whether the conclusions withdrawn from such studies are applicable to the larger Mn(salen) complexes, such as the Jacobsen's catalyst (Figure 5.1, **16**), has been partially addressed by Jacobsen and Cavallo in 2001 [122]. However, this study was only was able to account for the steric effects due to the limitations of the approach assumed. Further insights about this question can only be provided by high-level calculations carried out on the larger Mn(salen) complexes. Despite the initial claims of Jacobsen and Cavallo, some latter studies using different models for Mn(salen) arrived at different conclusions [112, 123, 124], and the use of truncated models has been pointed as one of the possible causes for these disagreements [126].

An in depth survey of the properties of different Mn(salen) complexes requires the use of a data reduction technique, such as Principal Component Analysis (PCA). This technique allows the determination of linear combinations of numerical variables, the principal components (PCs), that explain the maximum amount of variance in the data not already explained by a previous PC, thus simplifying the data analysis [369]. At

the end of the PCA procedure, one obtains a matrix with the coefficients that define each component (the loadings, $\mathbf{M}_L$) and the percentage of variance associated with each PC. The application of the $\mathbf{M}_L$ to the original data matrix corresponds to a change in coordinates, yielding the scores matrix, $\mathbf{M}_S$. Each column of $\mathbf{M}_S$ contains the values that would be observed if the corresponding PC were measured directly. An analysis of the distribution of the scores for each PC allows the association of each PC to categorical variables that are associated with the observations in the original data, this procedure being usually called the supervision step [289, 369]. Throughout this work, the term data set will be used to describe the collection of data available on the systems under study, while the term data matrix will be reserved for the subset of the data set that contains only the numerical variables to be subjected to multivariate analysis.

The primary aim of this work is to assess the implications of using acacen' as a simplified model for salen in manganese complexes. As a secondary objective, the effects of axial coordination are surveyed by comparing models without axial coordination with models coordinated with chloride, which is the traditional counter ion for these complexes. In addition to this, the axial coordination to $CH_3CH_2NH_2$ and $CH_3CH_2NH^-$ was also studied, with the purpose of surveying the effect of anchoring these complexes onto a supporting material using 3-aminopropyltriethoxysilane (APTES) as a linker [94, 366]. For this purpose the geometry and the electronic structure of such type of complexes were analyzed using DFT methods. This study included 112 Mn(salen) and 16 Mn(acacen') molecular models. The variants were generated, by changing the axial ligands and/or the substituents of the aldehyde moiety for the Mn(salen) complexes, according to the notation presented in Figure 5.1. The geometries, for the different molecular models under study, were then optimized using DFT calculations. The properties of the different models were surveyed using PCA in order to better access the impact these variations on the Mn(salen) scaffold. In particular, the results presented here aim at understanding the effect truncation of Mn(salen) complexes to Mn(acacen') may have on the properties extracted from first principles calculations.

5.2 Methodology

DFT Calculations All DFT calculations were performed using the extended hybrid functional X3LYP of Xu and Goddard III [212, 213] as implemented in version 2.8 of the Orca program package [355]. A mixed basis based on the Ahlrichs basis set with additional polarization functions, taken from the TurboMole library [360, 361, 370] was used. This basis set is predefined in the software package under the DefBas-3 keyword and corresponds to a triple-ζ valence basis set with contraction pattern $\{311\}$ for hydrogen, $\{62111/4111/1\}$ for other main group elements and $\{842111/6311/411/1\}$ for manganese.

Throughout this work, we have chosen to follow the nomenclature used by Cavallo and Jacobsen [136] in which the relevant electronic states are identified by a notation indicating the respective total spin density $S = |\rho_\alpha(\mathbf{r}) - \rho_\beta(\mathbf{r})|$. The symbols *S0*, *S2* and *S4* thus refer to total spin densities of zero (singlet), two (triplet) and four (quintet) unpaired electrons, respectively. Additionally, each compound will be named after the categorical variables that describe it, in the form *Model-OxSt-AxLig-SpinSt*, where *Model* is the model number according to Figure 5.1; *OxSt* may take the values "re" or "ox" for the reduced (X=none) and oxidized(X=O) form, respectively; *AxLig* may be "null", "cl", "amine" or "amide" for L= nothing, Cl^-, $CH_3CH_2NH_2$, or $CH_3CH_2NH^-$, respectively; and *SpinSt* is either *S0*, *S2* or *S4*. When dealing with groups of compounds, only the categorical variables common to all elements of the group are given.

For the *S2* and *S4* states, all calculations were performed under an unrestricted Kohn-Shan formalism, with independent treatment of the electron densities $\rho_\alpha(\mathbf{r})$ and $\rho_\beta(\mathbf{r})$. For *S0* systems, the restricted Kohn-Shan formalism was applied in order to lessen the computational effort of such calculations. Preliminary unrestricted and broken symmetry calculations using model **3** have shown that this would be a valid approach.

Geometry optimization on all models was carried out using redundant coordinates. These models were constructed by applying truncations and/or substitutions of the (*S*, *S*)-Jacobsen's catalyst in its oxidized form and with the $CH_3CH_2NH^-$ axial ligand (**16-oxamide**).

The distances between all bonded atoms (except bonds involving hydrogen atoms) at the equilibrium geometry were included in the data set. Following the method established by Cavallo and Jacobsen [134], ligand folding was incorporated in the data set by means of the ligand bent angles, ϕ_e and ϕ_u, as well as the pyramidalization distance (d_P). A bent angle, ϕ, is defined as $\phi = 180^\circ - \angle(X_{NN} - Mn - X_{NO})$ where X_{NN} and X_{NO} refer to the midpoint between the two nitrogen atoms and the midpoint between adjacent N,O atoms, respectively. Following the numbering scheme shown in Figure 5.1, the adjacent N,O atoms considered in ϕ_e are $N_{(4)}$ and $O_{(6)}$, whereas ϕ_u refers to atoms $N_{(5)}$ and $O_{(7)}$. Using the same notation, d_P is defined as the separation between the manganese atom and the $O_{(6)} - X_{N,N} - O_{(7)}$ plane [134]. Information on the chirality content of each structure was provided using Avnir's Continuum Chirality Measurement (CCM) [141,143,277,281]. This measurement was obtained using software developed in-house, based on the methods published by Avnir and Alvarez [279, 281]. For the purpose of this work, the CCM measurements were taken either on atoms 1 and 4 to 15 (*CCMa*) or atoms 1 and 4 to 23 (*CCMs*, is defined only for compounds **3** to **16**).

Natural Population Analysis (NPA) was performed using version 5.9 of the NBO program from the University of Wisconsin [356]. Natural charges and spin densities (for the *S2* and *S4* states) were collected for each atom, except hydrogen atoms, and included in the data set.

Multivariate analysis Multivariate data analysis was carried out using the R language [338] with the Psych package [371] implementation of Principal Component Analysis (PCA) and associated techniques. Moreover, the lmPerm package was used in the development of the linear models.

The original dataset (DB0) consisted of eight categorical variables and 77 numerical variables. The eight categorical variables describe the model identification, *Model*; axial ligand, *AxLig*; spin state, *SpinSt*; metal oxidation state, *OxSt*; structure of the diimine bridge (etildiimine, EDA, or cycloexildiimine, DEDA), *Bridge*; the substituent at R_1, R_1; the substituent at R_2, R_2; and the structure of the equatorial ligand (salen or acacen), *EqLig*. The 75 numerical variables were divided into five groups and include: bond lengths (d) involving Mn and/or atoms 4 to 27 of the salen/acacen ligand (see Figure 5.1); natural charges (q) and spin densities (s) for Mn, $O_{(2)}$ and atoms 4 to 27; global geometric parameters (d_P, ϕ_e, ϕ_u, *CCMa* and *CCMs*), the relative energies of *S2* and *S4* with respect to *S0* ($\Delta E_{0,2}$ and $\Delta E_{0,4}$, respectively), as well as the energetic balance of the oxidation of the reduced species with H_2O_2, assuming spin conservation (ΔE_{ox}). A complete listing of these descriptors is given in the supplementary information[2]. All distances were expressed in angstroms, charges and spin densities were expressed in atomic units, ligand folding angles ϕ_e, and ϕ_u in degrees and energy differences in kJ/mol.

On a first approach, DB0 was pruned out of the following variables: $q(O_{(2)})$, $s(O_{(2)})$, $\Delta E_{0,2}$, $\Delta E_{0,4}$, ΔE_{ox} and also all variables referring carbon atoms $C_{(20)}$ to $C_{(27)}$. This subset of DB0 will be referred to as DB1. The analysis of DB1 allowed the comparison between Mn(salen) and Mn(acacen') complexes, but the effect of the substituents on the aromatic rings of the salen complexes was unnoticeable. In order to compare the features of the different Mn(salen) complexes, another subset of DB0 was used (labeled DB2). The DB2 data set was created from DB0 by pruning $q(O_{(2)})$, $s(O_{(2)})$, $\Delta E_{0,2}$, $\Delta E_{0,4}$ and ΔE_{ox}, as well as all observations regarding models **1** and **2**.

In order to minimize subsequent problems of chance correlation, the protocol for analyzing DB1 and DB2 started by pruning all descriptors for which the coefficient of variance was smaller than 1%. Also, because the numerical values of the remaining descriptors vary significantly, all descriptors were mean centered and scaled to unit variance. Horn's parallel analysis, as implement in the Psych package, was used to determine the number of principal components (PC) or rotated components (RC) considered relevant in PCA, which was performed both without rotation and using the varimax rotation (this latter analysis will henceforth be denoted as rPCA). Because of the large cardinality of DB1 and DB2, the analysis of the scores from PCA and rPCA was performed using density plots (filtered by category), in a manner similar to that presented by H. Attias [372]. This allowed the association of each categorical variable to one or more PCs or RCs in both data sets.

[2]The supplementary information is available in digital format in the CD-ROM that accompanies this work.

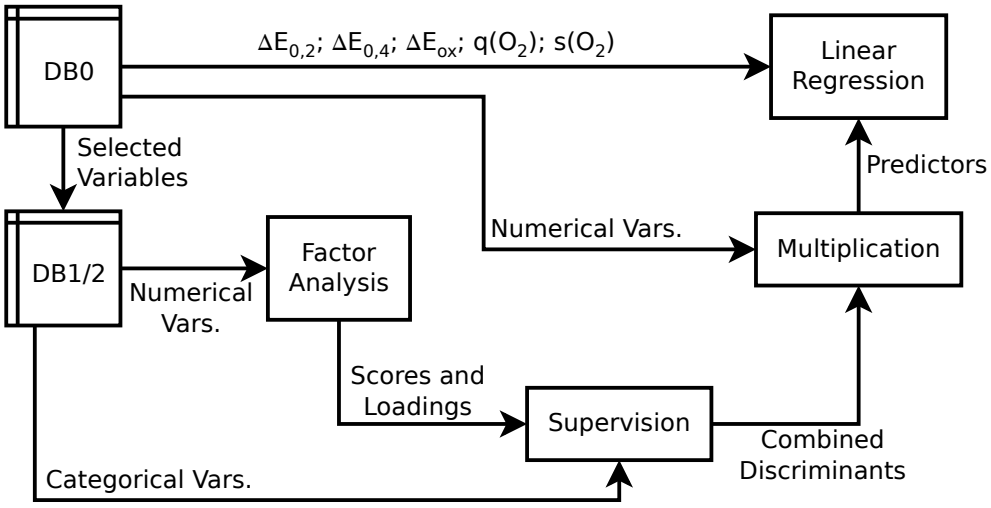

Figure 5.2: Flowchart of the most relevant steps in the multivariate analysis and creation of the linear models.

For the development of the linear models, the best performing PCs or RCs for each of the categorical variables were collected into a matrix of discriminants, or a composite loadings matrix, $\mathbf{M}_{CL}$. Numerical descriptors associated to each categorical variable were obtained by application of $\mathbf{M}_{CL}$ to the data matrix in DB0 (once standardized). These descriptors were then used as independent variables in the development of the linear models for $\Delta E_{0,4}$ and ΔE_{ox}. A diagram containing the most relevant steps of this procedure is given in Figure 5.2.

5.3 Results and Discussion

The results from DFT calculations show that the *S2* state is the preferred ground state, with a low lying *S0* state (about 10 to 40 kJ/mol above the ground state), followed by *S4*, which lies more than 50 kJ/mol above the ground state. The reduced forms of the complexes for which L=none prefer a *S0* ground state with a low lying *S2* state (about 10 to 35 kJ/mol above *S0*), the same being true for **1-re-amide**, **1-ox-null**, **1-ox-amide** and **2-ox-null**. In general, the energy gap between *S2* and *S0* in the oxo-complexes is quite small ($|\Delta E_{0,2}| \leq 10$ kJ/mol) and the two states are quasi-degenerate. These results are in good accordance with published values for the relative energies of the different spin states, considering the compounds for which such data is available [117, 118, 120, 122, 133].

At their equilibrium geometry, tetracoordinate complexes are arranged around Mn in a square planar geometry, while hexacoordinated present the expected octahedral geometry around the metal center. Pentacoordinated species tend to form square pyramidal arrangements around Mn, although with some significant distortion in the case of X=none. In all cases, both salen and acacen' ligands assume a nearly planar conformation around

Table 5.1: Summary of the results from the PCA and rPCA analysis performed on DB1 and DB2, showing the PCs and RCs best associated to each of the categorical variables in the data set. The percentage of variance explained by each PC or RC is given in parenthesis.

Descriptor	DB1				DB2			
	PCA		rPCA		PCA		rPCA	
spinSt	PC1	(22%)	RC1	(15%)	PC1	(24%)	RC1	(15%)
oxSt	PC2	(15%)	RC2	(14%)	PC2	(15%)	RC2	(14%)
eqLig	PC4	(11%)	RC4	(11%)	—		—	
axLig	PC5	(7%)	RC5	(9%)	PC4	(9%)	RC4	(9%)
bridge	PC7	(6%)	RC7	(6%)	PC8	(4%)	RC8	(4%)
R_1	NA[a]		NA[a]		PC9	(3%)	RC10	(3%)
R_2	NA[a]		NA[a]		PC5	(8%)	RC5	(9%)

[a]NA: No clear association was found for this descriptor.

Mn. Absolute energies for all systems, as well as their equilibrium geometries are given in the supplementary information.

5.3.1 Component analysis

The association between each categorical variable (in both DB1 and DB2) and the factors devised from PCA and rPCA was done by examining the distribution of the scores for each component. Table 5.1 shows the links between each categorical variable and a set of principal and rotated components taken from the two subsets of DB0. Moreover, it allows one to estimate the importance of each of these categorical variables in the data set, while details on the distribution of the scores for each component will be given later in this work. As shown in Table 5.1, the application of the varimax rotation to PCA resulted in a decrease of the variance explained by the first few components. PCA also outperformed rPCA in when considering the percentage of variance explained by the components which were associated to the categorical variables (see Table 5.1). The principal components selected during the supervision step account for about 65% of the total variance, whereas the rotated components account for only 55% of the total variance. As shall be shown later, this resulted in poorer classification of the entries on the data set based on the first components. On the other hand, rotation of the principal components allowed a better classification based on the lesser components. In general, PCA performed better at resolving the major sources of variation within each data matrix, while rPCA was able to resolve the more subtle sources of variance.

Both techniques agree that the spin state is the major source of variance in the data, followed by the oxidation state of the metal center, as shown in Table 5.1. The variation in the equatorial ligand (acacen' *versus* salen) accounted for 11% of the variance in DB1, making it the major source of variance. This reveals the magnitude of the impact the use of a truncated model may have in DFT calculations. Furthermore, the large variance

associated with *EqLig* has apparently "muffled" any impact R_1 and R_2 would have on the overall variance of DB1. These observations justified the creation of DB2, in order to better explore the effects of having different substituents in the 3,3' (R_2) and 5,5' (R_1) positions of the salen ligand. As Table 5.1 shows, these variations have a limited effect on the variance of DB2. For completeness, plots of the distributions of all PCs and RCs extracted in these analysis can be found in the supplementary information, as well as a complete description of their respective loadings.

In order to further pursue our objectives, we shall now discuss the links exposed in Table 5.1. In finding the best discriminant for each categorical variable, Table 5.1 gives either two or four candidates. The following discussion compares such candidates on the basis of the distribution of their scores. Furthermore, a rationalization of the physical implications of each source of variance is performed based on the loadings of the best discriminant for each categorical variable.

Spin state (*SpinSt*) The scores of the principal and rotated components of DB1 and DB2 associated with *SpinSt* are distributed as depicted in Figure 5.3. This variable is the main source of variance in both data sets, and PCA was able to achieve a satisfactory separation between entries with different spin state. As can be seen in Figures 5.3a and 5.3c, *S0* species score negative values in the PC1 axis, while *S4* ones occupy the positive domain of PC1. Entries corresponding to compounds at their *S2* state accumulate in the region around the origin. Moreover, rotation of the principal components worsens the pattern found in PCA, as demonstrated in Figures 5.3b and 5.3d. Because PC1 in both data sets gives approximately the same separation among categories of *SpinSt*, PC1 of DB1 was selected to be used as the discriminant associated with this categorical variable, as it renders a simpler expression.

The loadings of PC1 are similar for both DB1 and DB2, with the atomic spin densities and the distances between the nitrogen atoms an their closest sp^2 carbon atom bearing the largest coefficients. The predominance of spin densities in the loadings associated to *SpinSt* is an expected result when taking into consideration the design of the data sets. By definition the spin density in all atoms of the *S0* species is zero. Also, in the *S2* state, most of the spin density is concentrated in the Mn atom, while the *S4* state is characterized by the promotion of at least one unpaired electron to the conjugated π system of the equatorial ligand, in accordance to previous DFT and correlated wave function calculations [117, 118, 120, 373].

Oxidation state of Mn (*OxSt*) The second largest contributor for the variance in both DB1 and DB2 is associated with the oxidation state of the metal center. Again, PCA analysis of both data matrices rendered linear combinations of variables that accomplishes a satisfactory separation between the reduced Mn(salen) complexes and their oxidized oxo-Mn(salen) analogues (Figures 5.4a and 5.4c). As in the case of *SpinSt*, this sepa-

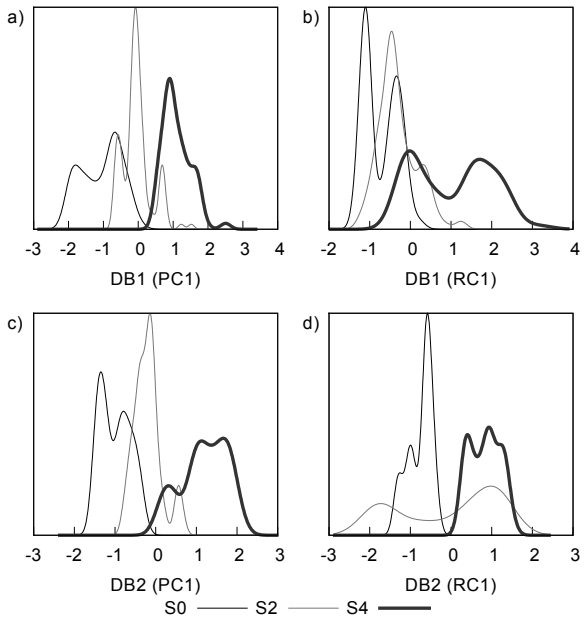

Figure 5.3: Distribution of the scores of the principal and rotated components of DB1 and DB2 best associated with variations in the spin state.

ration becomes less pronounced upon rotation of the principal components, as depicted in Figures 5.4b and 5.4d. The choice of PC2 of DB1 as the discriminant to be associated with *OxSt* yielded the simplest expression for the discriminant, while assuring good separation among its categories.

Inspection of the loadings associated with the principal components of both data matrices reveals a predominance of the natural charges. The sign of the coefficient associated with the natural charges alternates between neighboring atoms in the π system of either salen or acacen'. Both the magnitude of the loadings for the effective atomic charges and their pattern indicate that the charge transfer from salen (or acacen) to Mn is more intense in the oxo-complexes than in their reduced precursors [373]. The distances between Mn and the nitrogen atoms of the equatorial ligand also bear considerable positive coefficients. On the other hand, the loadings suggest a lowering in the chirality measurements upon oxidation of the metal center, which can be rationalized when considering the fact that most species in this study go from a pentacoordinated square planar geometry with some degree of distortion to an octahedral geometry upon oxidation.

Salen/acacen model (*EqLig*) By design, the study of this categorical variable is restricted only to DB1. The variability introduced by this descriptor is best accounted for in PC4 and RC4, both explaining about 11% of the total variance. Excellent separation between entries classified as acacen' and salen was obtained using both PCA and rPCA,

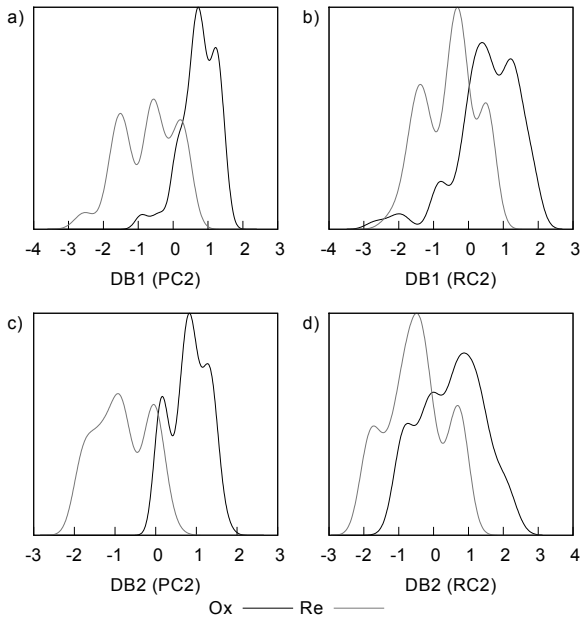

Figure 5.4: Distribution of the scores of the principal and rotated components of DB1 and DB2 best associated with variations in the oxidation state of the manganese atom.

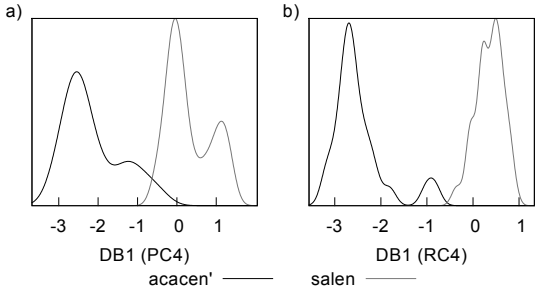

Figure 5.5: Distribution of the scores of the principal and rotated components of DB1 best associated with the variance introduced by the existence of salen and acacen' complexes in the data.

with rPCA performing marginally better, as shown in Figure 5.5. Being so, RC4 was chosen as the discriminant associated with *EqLig*.

The most prominent loadings associated with RC4 are a combination of bond lengths, charges and spin densities for most of the atoms in the aromatic system common to both salen and acacen' ligands. Furthermore, salen complexes score higher values for the chirality measurement (*CCMa*), according to the loadings of RC4. The results further suggest that the salen ligand is capable of more extreme charge separation between $C_{(14)}$, $C_{(15)}$ and their adjacent atoms than that observed for acacen'. Also, the bent conformation of the salen ligand increases the asymmetry of the atoms around the metal center.

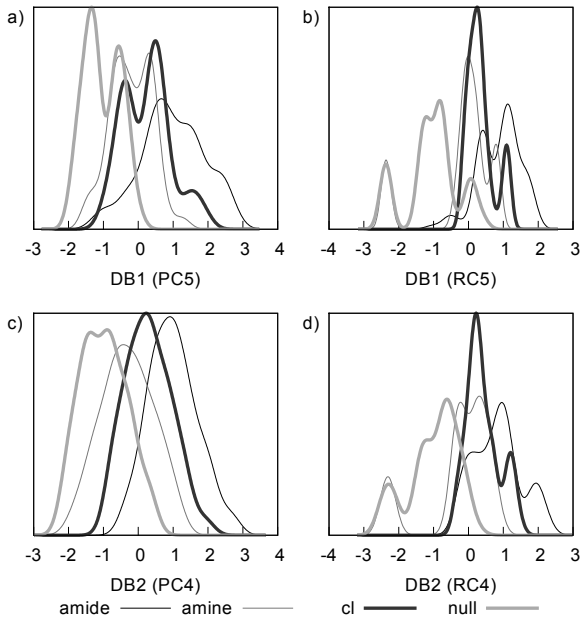

Figure 5.6: Distribution of the scores of the principal and rotated components of DB1 and DB2 best associated with variations in the axial coordination site of Mn(salen) and Mn(acacen') complexes.

In summary, the following properties are likely to be affected by the use of the truncation scheme that motivated this work: increased length of the bonds between Mn and the coordinating atoms of salen/acacen'; higher charge and lower spin density at the Mn atom, accompanied by lower magnitude charges on the oxygen atoms belonging to the ligand; smaller charge separation among the aromatic carbon atoms of the ligand; higher spin density at the ligand and also smaller chirality content around the coordination sphere of the Mn atom.

Axial ligand (*AxLig*) The variability introduced by the axial ligand of the Mn atom (or its absence) proved to be one of the most difficult challenges for PCA and rPCA, not only because of the relatively low variance that remained in the data once the components associated with *SpinSt*, *OxSt*, and *EqLig* were extracted, but also because this categorical variable encompasses four values (instead of the two or three values seen in the other variables). As a result, poor separations between the different categories of *AxLig* were obtained, as shown in Figure 5.6. Although not being able to achieve complete separation between classes of *AxLig*, the PC4 of DB2 (Figure 5.6c) suggests that the four classes are organized as four overlapping quasi-normal populations around four different average values.

Using the PC4 of DB2 as the best possible discriminant that can be associated to *AxLig*, models without any axial ligand (**null**) and those coordinated with $CH_3CH_2NH^-$ (**amide**) appear to be the most extreme cases. This is in accordance to what would be

expected as the amide ligand is a strong donor ligand capable of transferring a significant amount of charge to the manganese atom. The **cl** and the **amide** classes lie close together, as well as those models belonging to the **amine** and **null** families. This results in a sorting between cationic and neutral systems.

The most prominent loadings in PC4 of DB2 are the charges of the oxygen atoms in the equatorial ligand, as well as the charges and spin densities in the carbon atoms of the outer aromatic rings of salen, all carrying a positive sign. This is in good accordance to the proposed model according to which the salen ligand serves as a charge reservoir for the metal center, which transfers charge to Mn in response to changes in the coordination sphere of the metal center, such as an exchange of the axial ligand [373]. In accordance to this model, axial coordination to a strong donor ligand (such as the case of **amide**) conceptually allows some charge density to be returned to the salen or acacen' moiety, thus reducing the magnitude of the positive effective atomic charges within it.

Diimine bridge (*bridge*) As shown in Table 5.1, this descriptor is best associated with PC7 and RC7 of DB1 and PC8 and DB8 of DB2. In all cases, the variability introduced by this categorical variable accounts for at most 6% of the total variance in each data matrix. As shown in Figure 5.7, the effect of the diimine bridge is relatively subtle and the rotation of the principal components helped achieving a good separation between entries representing models with EDA, and models with CEDA. Both RC7 of DB1 and RC8 of DB2 allowed excellent classification of the entries in each data set. The quest for a simpler expression for each discriminant lead to the choice of RC7 of DB1 as the best discriminant to be associated with the descriptor *Bridge*.

An inspection of the loadings of RC7 of DB1 reveals that the charges of $C_{(8)}$ and $C_{(9)}$ bear the most preponderant coefficients. This reflects the inductive effect exerted by the carbon atoms in CEDA. Other than that, considerable loadings are also observed for the chirality measurements and the bending angles, translating the asymmetry imparted by the CEDA bridge in the equilibrium geometry of the equatorial ligand.

Substitution at R_1 As shown in Figure 5.8a, PCA was unable to produce a meaningful separation among the different classes in this descriptor. Rotation of the principal components allowed the models without an alkyl group at their 5,5' position to be segregated from those with either methyl (Me) or *tert*-butyl (tBu), as depicted in Figure 5.8b. Thus, RC10 of DB2 was chosen as the descriptor for R_1. The loadings associated with RC10 are dominated by the charges and spin densities of $C_{(22)}$, $C_{(23)}$ and their immediate neighbors. These results show the limited effect this source of variance has upon the overall geometry and electronic structure of the Mn(salen) complexes, which can be mostly explained by the inductive effect of the alkyl groups.

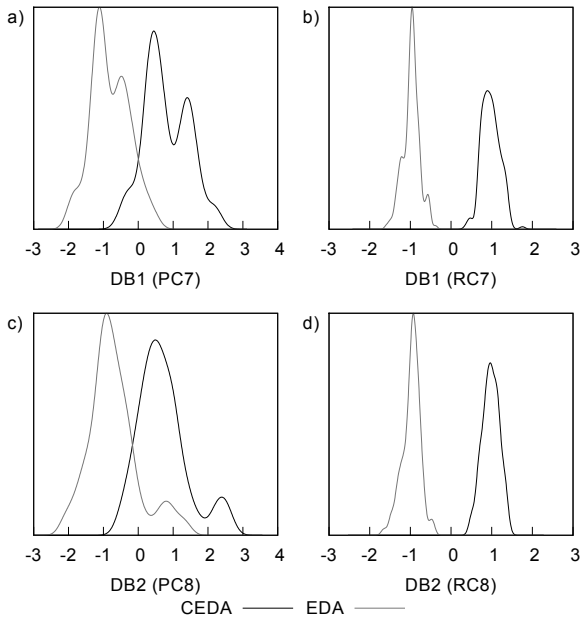

Figure 5.7: Distribution of the scores of the principal and rotated components of DB1 and DB2 best associated with variations in the diimine bridge: cycloexildiimine (DEDA) *versus* etildiimine (EDA).

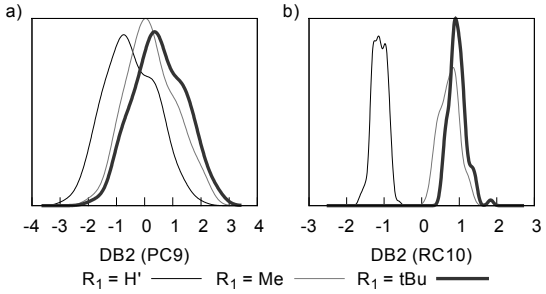

Figure 5.8: Distribution of the scores of the principal and rotated components of DB2 best associated with the variance introduced by the substitution patterns in R_1.

Substitution at R_2 Finding a PC or RC that would account for the variance introduced by the substitution pattern at R_2 was only accomplished in the analysis of DB2. Like in the case of R_1, this effect was better understood upon rotation of the principal components. RC5 accounts for about 8% of the total variance in DB2, and clearly distinguishes the R_2=H variants (negative scores), from those with bulkier substituents at R_2 (two populations distinct with positive scores), as shown in Figure 5.9b.

Upon inspection of the loadings, one finds the substitution pattern at R_2 to have an important effect on the charges and spin densities of $C_{(26)}$, $C_{(27)}$ and the atoms in their immediate vicinities, in accordance to the inductive effect of the alkyl groups. The analysis of the loadings further reveals that the presence of alkyl groups at R_2 also alters the conformation of the salen moiety, changing the bond lengths connecting $C_{(18)}$ and $C_{(19)}$

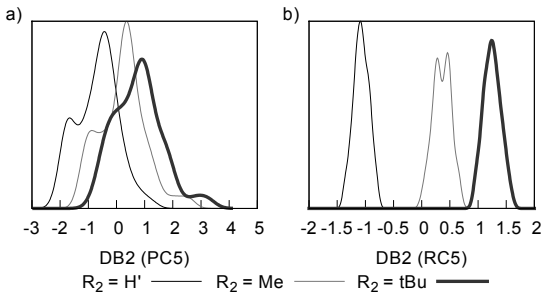

Figure 5.9: Distribution of the scores of the principal and rotated components of DB2 best associated with the variance introduced by the substitution patterns in R_2.

to their immediate neighbors, and also increasing the chirality measurements. Furthermore, the presence of bulky groups at R_2 can also be associated with an increase (in magnitude) of the charge in the oxygen atoms of the salen ligand.

In the face of these results, it would seem reasonable to use either model **3** or model **4** as models for the reactivity of the larger Mn(salen) complexes. It is therefore plausible to hypothesize that the effect of these bulky substituents may be properly treated using a QM/MM strategy, although not with the same truncation scheme used by Cavallo and Jacobsen. The present discussion, however, refers only to the effect of alkyl groups in the periphery of the salen scaffold and further work must be developed in order to access the effects of groups capable of greater interaction with the aromatic system of the salen ligand, such as OH or NO_2.

5.3.2 Linear Models

Having been able to provide some answers as to the importance and consequences of the use of truncated models in the study of the structure and reactivity of Mn(salen) catalysts, we tested whether the information collected from the factor analysis procedure is capable of shedding some light on the way these factors influence important properties of Mn(salen) complexes, such as the energy involved in the formation of their oxo-complexes, the energy gaps between the *S0*, *S2* and *S4* states, and the oxo-radical of oxo-Mn(salen) species. For this purpose, a composite discriminant matrix $\mathbf{M}_{CD}$ was created, having the loadings associated with he best discriminants for each categorical variable (chosen earlier in this work) as columns. Application of $\mathbf{M}_{CD}$ to the data matrix in DB0 determined the discriminant scores, a_X, where X represents each of the categorical variables mentioned earlier.

The distribution of these scores is similar to what was observed previously, during the selection of the discriminants. The major exception to this rule is a_{AxLig}, which inverts the sorting shown in Figure 5.6c, giving negative scores to compounds of the **null** family, followed by the **amine** family, while the **cl** and the **amide** families obtain positive scores (the latter scoring higher than the former, on average). The distribution of a_{R1} is similar to

the one found in Figure 5.8b, with the acacen' entries being concentrated on the positive half of the axis, together with the entries bearing Me or tBu at R_1. The distribution of a_{R2} is also similar to the one depicted in Figure 5.9b, despite not bearing such a clear distinction between the presence of Me and tBu groups in R_2. Furthermore the scores a_{R2} of the acacen' compounds form a bimodal distribution with one mode close to -2.0 (the same value as the mode for salen complexes with R_2 = H) and the other at approximately +1.5 (about the average value of the modes forR_2 = Me and R_2 = tBu). A graphical representation of the different scores a_X is available in the supplementary information.

These scores were used as independent variables in the development of linear models for $\Delta E_{0,4}$, ΔE_{ox} and $s(O_{(2)})$. For each linear model the significance of its coefficients was asserted using Anscombe's probabilistic permutation test, as implemented in the lmPerm package [374]. Each permutation test was allowed to run for a maximum of 10^6 iterations with a complete random permutation at each 10^4 iterations; the test for each coefficient was allowed to stop when the estimated standard error for the coefficient was less than 0.1% of its magnitude. Furthermore, an iterative protocol was devised in order to retain only the most significant coefficients: in the first iteration, the dependent variable was fitted against all independent variables and their products (second-order interactions). In the following steps, the dependent variable was fitted against the variables for which a significance level above 99% was obtained in the previous iteration. The procedure stopped when only independent variables with a significance level above 99% were observed. Moreover, in devising a linear model for $s(O_{(2)})$, only the data regarding oxo-complexes at their *S2* or *S4* state were considered.

The expressions for each of the three linear models mentioned can be constructed from the data in Table 5.2, which lists the coefficients obtained in each linear model, as well as their associated uncertainties. The results from the fitting procedure can also be appreciated in Figure 5.10. The linear models gave fair predictions of the calculated values of $\Delta E_{0,4}$, ΔE_{ox} and $s(O_{(2)})$ yielding adjusted-r^2 coefficients of 0.7796, 0.6729 and 0.8844, respectively.

The most peculiar feature of the results in Table 5.2 is the non-existence of any terms associated to a_{R2}. Although the presence of alkyl groups in R_2 has an important effect on the structure of the salen ligand and plays a vital effect on the stereoselectivity of the catalyst developed around the salen framework, our results suggest that this does no bear any significant effect on the three properties studied. Moreover, the small coefficients attributed to the interaction between the scores of different discriminants suggests that these discriminants are mostly orthogonal, despite their distinct origins.

The linear model for $\Delta E_{0,4}$ is dominated by a_{OxSt} and a_{AxLig}. Since the scores a_{OxSt} are distributed in the same manner as that depicted in Figure 5.4a, the results suggest that the energy gap between *S0* and *S0* is greater in the case of oxo-complexes. The model further predicts large contributions from a_{AxLig}, suggesting that a strong donor ligand may stabilize the *S4* state relative to *S0*.

Table 5.2: Coefficients for the linear models describing $\Delta E_{0,4}$, ΔE_{ox} and $s(O_{(2)})$, as well as their respective uncertainties determined by probabilistic permutation testing.

	$\Delta E_{0,4}$			ΔE_{ox}			$s(O_{(2)})$		
a_{SpinSt}	-0.040	$\pm$	0.003	0.073	$\pm$	0.004	0.173	$\pm$	0.011
a_{OxSt}	0.164	$\pm$	0.006	0.053	$\pm$	0.006		$-$	
a_{EqLig}		$-$			$-$		-0.26	$\pm$	0.03
a_{AxLig}	0.112	$\pm$	0.009	-0.0747	$\pm$	0.0101		$-$	
a_{Bridge}	0.030	$\pm$	0.012		$-$			$-$	
a_{R1}	0.045	$\pm$	0.017	0.070	$\pm$	0.019		$-$	
$a_{SpinSt} \cdot a_{OxSt}$	0.0029	$\pm$	0.0007	0.0031	$\pm$	0.0008		$-$	
$a_{SpinSt} \cdot a_{R1}$		$-$		0.0038	$\pm$	0.0016		$-$	
$a_{OxSt} \cdot a_{EqLig}$		$-$			$-$		0.041	$\pm$	0.004
$a_{OxSt} \cdot a_{AxLig}$	0.0081	$\pm$	0.0012		$-$			$-$	
$a_{OxSt} \cdot a_{R1}$	-0.006	$\pm$	0.002		$-$			$-$	
$a_{EqLig} \cdot a_{AxLig}$	-0.010	$\pm$	0.002		$-$		0.023	$\pm$	0.008
$a_{EqLig} \cdot a_{Bridge}$		$-$			$-$		0.012	$\pm$	0.005
$a_{EqLig} \cdot a_{R1}$	-0.024	$\pm$	0.007	-0.026	$\pm$	0.006	-0.020	$\pm$	0.009
$a_{EqLig} \cdot a_{R2}$	-0.007	$\pm$	0.004		$-$			$-$	

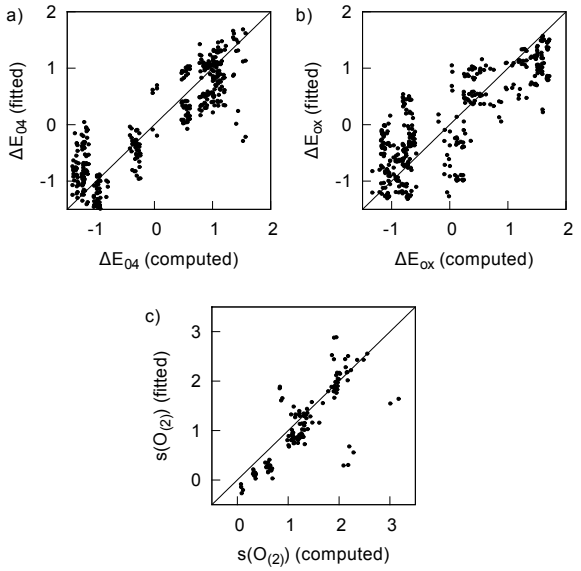

Figure 5.10: Plots of the computed *versus* fitted values for the linear regressions of $\Delta E_{0,2}$ (a),ΔE_{ox} (b) and $s(O_{(2)})$ (c). In each plot the identity function is plotted for comparison.

According to Table 5.2, the most influential contributions to ΔE_{ox} are a_{SpinSt}, a_{AxLig} and a_{R1}. The relatively large coefficient associated to a_{SpinSt} is likely due to the fact that this reaction in the *S4* state is much less exoenergetic than at either *S2* or *S0*. At the same time, the dependence on a_{AxLig} suggests that a strong donor group at the axial position of Mn reduces the magnitude of ΔE_{ox} (this quantity having always negative values in the range -600 to -300 kJ.mol^{-1}). Conversely a strong donor axial group would make the epoxidation energetically more favorable, which is in accordance with the known experimental evidence [137]. Furthermore, taking into consideration the distribution of a_{R1}, the results suggest that the oxidation of the metal center by H_2O_2 is more exoenergetic in the case of compound families **3**, **4**, **7**, **8**, **13** and **14**.

Further attempts to model $\Delta E_{0,2}$ and $q(O_{(2)})$ were made, but unsuccessful. The near-degeneracy of the S0 and S2 states may lead to an inaccurate estimation of $\Delta E_{0,2}$ within the framework of DFT, thus invalidating any model that could be drawn from these results. On the other hand, the ordinary linear regression of $q(O_{(2)})$ was hindered by the low relative variance of this variable (less than 2%).

Despite these problems, a third linear model was devised for $s(O_{(2)})$. Since the mechanism of oxygen transfer from the oxo-Mn(salen) complex to the olefin substrate during epoxidation is believed to be radical in nature, the spin density at $O_{(2)}$ would probably be a useful descriptor for modeling the activity of such compounds. Furthermore, recent work on metalloporphyrins has revealed some correlation between the oxo-radical character of their oxo-complexes and their degradation rate [80]. While the models for $\Delta E_{0,4}$ and ΔE_{ox} are essentially independent with respect to a_{EqLig}, this predictor is clearly the most prominent coefficient in the linear model for $s(O_{(2)})$, as shown in Table 5.2. Moreover, the second most prominent contributor to $s(O_{(2)})$ is a_{SpinSt}, which can be trivially explained by the fact that some of the spin density of Mn(salen) complexes at their *S4* state is spread throughout the the ligands of Mn [373]. It should be further noted that the outliers in Figure 5.10c belong to the **1-amide-S4**, **1-cl-S4**, **2-amide-S4** or **2-cl-S4** families.

The results from the three linear models are important as they allow us to link the results of Cavallo and Jacobsen, who concluded the general equivalence between salen and acacen' complexes [122, 123], to the apparent contradictions found in latter works which were attributed to the use of different models [112, 126]. Most of the validation of acacen' as a surrogate of the salen ligand was based on the ordering of the energies of the different spin states. Within the framework of DFT, this is an error prone procedure for $\Delta E_{0,2}$ (*S0* and *S2* being quasi-degenerate), and the results shown earlier show that $\Delta E_{0,4}$ is plausibly independent of the combination of atomic and molecular properties that best describe the differences between salen and acacen' complexes (a_{EqLig}). The same could be said for the energies involved either in the formation of the active oxo-complexes (ΔE_{ox}), or for the energy involved in the oxygen transfer from the oxo-complex to the substrate. It is therefore plausible that comparisons of Mn(salen) and Mn(acacen')

complexes (and their respective oxo- derivatives) based on energy differences would not account for any significant difference between these two families of complexes.

On the other hand, charge and spin distributions are significantly different when comparing acacen' and salen complexes, as seen in the loadings that best segregate the two classes of compounds. This observation was further confirmed by the very high dependence of $s(O_{(2)})$ with respect to a_{EqLig}. Because properties such as effective atomic charges and spin densities play an important role in the way a reaction path develops, our results confirm the assertion that the use of acacen' as a surrogate for the salen ligand is likely one of the major sources of discrepancies in the different theoretical models for the reactivity of Mn(salen) catalysts.

5.4 Conclusions

In this work, PCA was used to successfully associate structural features of different Mn(salen) and Mn(acacen') compounds to the major sources of variation in the data describing their geometrical features, as well as the charge and spin distribution across the metal-salen or metal-acacen' system.

With respect to the adequacy of using acacen' as a truncated model for salen in the study of Mn(salen) complexes, the results from factor analysis point that this variation in the data set accounted for about 11% of the total variance, being surpassed only by the spin state of the complexes (*S0*, *S2* or *S4*) and by their oxidation state. The results also show that the use of acacen' as a surrogate model for salen bears a strong effect on the charge and spin distribution among the molecule, as well as in a possible misrepresentation of the local geometry around the metal center.

The results also suggest that the nature of the diimine bridge and the presence of methyl or *tert*-butyl groups at the 3,3' and 5,5' positions of the salen scaffold, despite being important for the reactivity and enantioselectivity of the larger Mn(salen) catalysts, bear only some limited influence on the electronic structure of the salen ligand.

The results further allowed to shed some light on the effect of using APTES as the axial ligand when anchoring Mn(salen) complexes onto a supporting material. The structural features of compounds coordinated to a model for the neutral form of APTES are similar to those of the chloride-coordinated compounds usually found in homogeneous media, bearing no clear distinction under factor analysis. On the other hand, coordination to a model for the anionic form of APTES yields some alterations in the overall structure of the metal-salen system, specially with respect to the charge distribution and chiral content of the ligand. Furthermore, results suggest that this feature strongly affects the energetic balance of the oxidation of Mn(salen) and Mn(acacen') compounds to their oxo-derivatives.

The discriminants for the most prominent features of the compounds tested were selected and the scores obtained from this technique were used as predictors for measuring

the energy split between the singlet and quintuplet states, as well as the oxidation of the metal center assuming spin conservation. The results from these linear models were satisfactory, and suggest that this may be a valid approach for the development of predictive models of Mn(salen) catalyzed epoxidations.

Chapter 6

Effects of Axial Coordination on Immobilized Mn(salen) Catalysts[1]

Abstract

The consequences of anchoring Mn(salen) catalysts onto a supporting material using one of the vacant positions of the metal center are tackled by studying several Mn(salen) complexes with different axial ligands attached. This is accomplished using Density Functional Theory at the X3LYP/Triple-ζ level of theory and the Atom In Molecules formalism. The results suggest that both Mn(salen) complexes and their oxo derivatives should lie in a triplet ground state. Also, the choice of the axial ligand bears a moderate effect on the energy involved in the oxidation of the former to oxo-Mn(salen) complexes, as well as in the stability of such complexes towards ligand removal by HCl. AIM analysis further suggests that the salen ligand acts as a "charge reservoir" for the metal center, with strong correlations being obtained between the charge of salen and the electron population donated by the axial ligand to the metal center. Moreover, the results suggest that the Mn atom in Mn(salen) complexes holds different hybridization of its valence orbitals depending on the type of axial ligand present in the system.

6.1 Introduction

Manganese-salen complexes, hereafter Mn(salen), have long been known to efficiently catalyze the epoxidation of unfunctionalized alkenes. Chiral variations on this scaffold attain remarkable enantioselectivity upon the epoxidation of olefins [36, 62, 112]. Being so, the immobilization of Mn(salen) complexes onto a supporting material has yielded an assortment of novel materials with interesting catalytic properties [48, 50]. Among the different immobilization strategies that have came to light in recent years, one of the

[1] Adapted from F. Teixeira, R. Mosquera, A. Melo, C. Freire and M. Natália D. S. Cordeiro, *J. Phys. Chem. A* **2014**, (submited)
The contributions of F. Teixeira to this work were the following: Running the first principle computations, performing the linear regression analysis and writing the first draft of the manuscript.

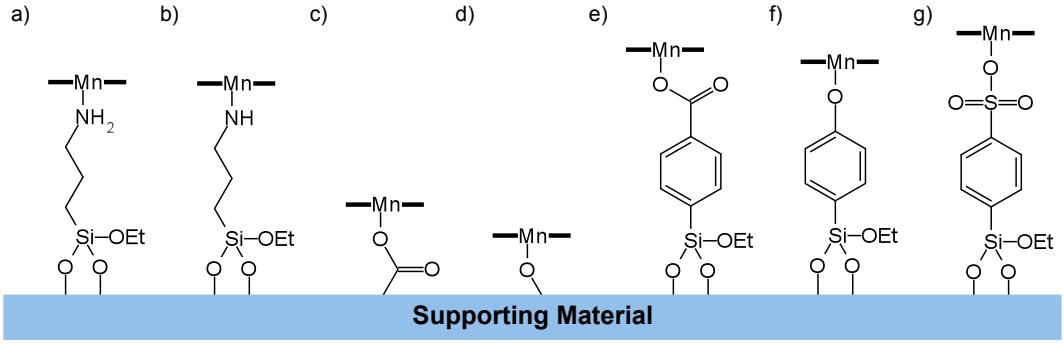

Figure 6.1: Examples of covalent attachment of Mn(salen) complexes onto a supporting material: a) and b) using ATPES as a linker molecule; c) and d) covalent attachment to hydroxyl and carboxyl functionalized carbon materials; e) f) and g) using phenoxy, phenylcarboxyl or phenylsulfonate linkers. The salen ligand in these schemes is represented in a simplified manner by the two bold lines around the manganese atom.

most common is covalent attachment of the metal center onto a functionalized supporting material (see Figure 6.1). The functional group at the surface of the supporting material acts as a donor ligand to the manganese atom. Such donor ligands usually occupy one of the axial positions of the coordination sphere of manganese, with the salen ligand lying in a quasi-planar conformation and binding to the four equatorial sites of the metal center [112, 124]. The use of axial coordination as an immobilization strategy raises interesting questions on how it may affect the electronic structure of the catalyst and moreover, whether it is responsible for altering its catalytic efficiency or chemoselectivity.

Early experimental studies in homogeneous media show that the presence of nitrogen heterocycle additives such as pyridine *N*-oxides, pyridines or imidazoles bear a strong influence over the rate, yield and selectivity of Mn(salen) catalysts. It was postulated by Kochi that such bases act as donor ligands at the axial position. This would stabilize the active oxo-Mn(salen) species formed in the course of the catalytic cycle, thus increasing the rate and yield of the reaction [36, 83, 112].

This subject has also been tackled from the theoretical point of view, with early studies showing that the omission of chloride from the axial position of the Mn(salen) model would make it conform poorly to the experimental evidence [115, 123]. Moreover, Cavallo and Jacobsen reported that a hypochloride anion coordinated to the axial position of the manganese atom would facilitate the regeneration of the active oxo-Mn(salen) species in a biphasic H_2O/CH_2Cl_2 system [135]. However, a general theoretical model for explaining the effect of axial donor ligands on the catalytic properties of Mn(salen) complexes has eluded later efforts by Cavallo and Jacobsen [137]. The development of novel hybrid nanocatalysts though axial immobilization and the increasing demand of such materials in the pursue of novel synthetic strategies entices this question to be addressed once again.

Despite its limitations, Density Functional Theory (DFT) may be an useful tool for obtaining the electron density of these transition metal complexes. It is known that the electron density that results from DFT calculations is comparable to that of high level

wavefunction methods, given a basis set with enough flexibility. This is possible because the shape and spread of the Kohn-Sham orbitals is a function of the electron density, that includes the effect of electron correlation [131, 182]. The topology of the electron density may be analyzed under the formalism of Bader's theory of Atoms in Molecules (AIM). This analysis allows the establishment of effective atomic charges and spin densities which provide means to rationalize the properties and chemical reactivity of these compounds [250, 273]. Although AIM may exaggerate the charge separation between bonded atoms, these somewhat exaggerated charges provide a "high contrast" picture of the charge distribution along the system, when compared with more traditional population analysis methods, as recently reported by Teixeira *et al.* [373]. Moreover, the analysis of the Laplacian of the electron density provides an useful tool for the localization of regions in which the electron density is locally concentrated. Such regions are traditionally related to the presence of localized orbitals, non-bonding electron pairs and unpaired electrons [262].

In this work, the effect of immobilization of Mn(salen) complexes through axial coordination is studied. This is done using two complimentary points of view: in one hand, energy differences for some typical reactions are compared, these energies being obtained from first principles DFT calculations. On the other hand, the topology of the electron density of the complexes in question is surveyed under the AIM formalism. An assortment of possible axial ligands was selected, as shown in Figure 6.2. These ligands attempt to mimic the local chemical environment of the metal center in some successful anchoring strategies [89, 92, 94, 375, 376], with chloride-coordinated complexes **1-re** and **1-ox** being used as reference. The results are given in the hope of providing a model for the effect of axial coordination to Mn(salen) catalysts.

6.2 Computational Methods

Throughout this work, we use the nomenclature established in Figure 6.2, in which the number of the compound is determined by the axial ligand used and the oxidation state of the metal center is given by an appropriate suffix (**re** and **ox** for Mn^{III}(salen) and oxo-Mn^{V}(salen) complexes, respectively). Moreover, this work follows the nomenclature used by Cavallo and Jacobsen [136] in which the relevant electronic states are identified by a notation indicating the respective total spin density $S = |\rho_\alpha(\mathbf{r}) - \rho_\beta(\mathbf{r})|$. So that the symbols *S0*, *S2* and *S4* refer to total spin densities of zero (singlet), two (triplet) and four (quintuplet) unpaired electrons, respectively. When needed, these symbols will be used as suffixes when referring to a particular state of a given compound.

DFT calculations were performed using the X3LYP functional [213], as implemented in the Orca program package, version 2.8 [355]. A mixed basis set was used in this work, which is available in the software under the keyword DefBas-4. This corresponds to a

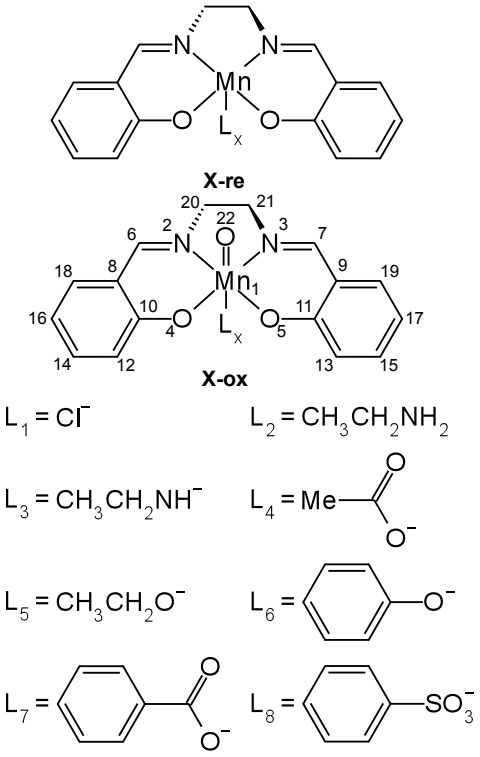

Figure 6.2: Generic structural formula of Mn(salen) (**X-re**) and oxo-Mn(salen) (**X-ox**) complexes, with different axial ligands.

triple-ζ valence (TZV) basis set with contraction pattern $\{311/1\}$ for hydrogen, $\{62111/411/11\}$ for other atoms in the main group and $\{842111/63111/411/1\}$ for manganese [360, 361].

The geometry of the sixteen Mn(salen) systems were optimized at their *S0*, *S2* and *S4* states. For the *S2* and *S4* states, all calculations were performed under an unrestricted Kohn-Sham scheme, with independent treatment of the electron densities $\rho_\alpha(\mathbf{r})$ and $\rho_\beta(\mathbf{r})$. In their turn, *S0* systems were treated under a restricted KS, following the results of preliminary calculations that validate the use of such formalism [373]. Following the method established by Cavallo and Jacobsen [134], the folding of the salen ligand was evaluated by means of the ligand bent angles, ϕ_e and ϕ_u, as well as the pyramidalization distance (d_P). A bent angle, ϕ, is defined as $\phi = 180^\circ - \angle(\mathrm{X_{NN}} - \mathrm{Mn} - \mathrm{X_{NO}})$ where $\mathrm{X_{NN}}$ and $\mathrm{X_{NO}}$ refer to the midpoint between the two nitrogen atoms and the midpoint between adjacent N,O atoms, respectively. Following the numbering scheme shown in Figure 6.2, the adjacent N,O atoms considered in ϕ_e are $\mathrm{N_{(2)}}$ and $\mathrm{O_{(4)}}$, whereas ϕ_u refers to atoms $\mathrm{N_{(3)}}$ and $\mathrm{O_{(5)}}$.

The nuclear Hessian of each system at the equilibrium geometry was calculated at the same level of theory as the geometry optimization, and the subsequent vibrational analysis allowed the confirmation of the equilibrium geometries as true minima in the potential energy surface. The results from these calculations further allowed for zero-point vibrational corrections and other thermochemistry parameters to be estimated for these systems.

A conversion utility (Molden2AIM, from Prof. Wenli Zou at the Southern Methodist University, Dallas [358]) was used to convert the output of Orca into a suitable format for the AIM analysis software. The topology of the electron density ($\rho(\mathbf{r})$) was surveyed using the AIMALL program package [377], which was also used for the integration of the atomic basins and determination of effective atomic charges, spin densities and related properties. The topology of the Laplacian of the electron density, $\nabla^2\rho(\mathbf{r})$, was surveyed using Bader's AIMPAC program suite [357]. Following the convention used by several authors, the $L(\mathbf{r})$ function will be defined as $-1/4\nabla^2\rho(\mathbf{r})$, for which a local maximum corresponds to a local concentration of the charge density, usually interpreted as the localization of a lone electron or non-bonding pair of electrons [261, 262].

All statistical analysis were carried out using the R language and software package [338]. In all cases, distances were expressed in angstroms, angles in degrees, and charges and charge densities in atomic units.

6.3 Results and Discussion

The geometry of the different complexes was successfully optimized. As expected, the salen ligand assumes a quasi-planar conformation at the equilibrium geometry. Despite this, the pyramidalization distance, d_P, varies significantly with respect to the choice of axial ligand, with average values of 0.32 ± 0.12 Å and 0.17 ± 0.05 Å for Mn(salen) and oxo-Mn(salen) species, respectively. On the other hand, ϕ_e and ϕ_u show limited variability, with average values of $169 \pm 4\,^\circ$ and $168 \pm 6\,^\circ$, respectively, in Mn(salen) complexes, and $160 \pm 8\,^\circ$ and $167 \pm 5\,^\circ$, respectively, in oxo-Mn(salen) complexes. These results show that the salen ligand sits in a slightly bent conformation, in good accordance to previous works [124, 137].

Relative Energies of *S0*, *S2* and *S4* states Three spin states (*S0*, *S2* and *S4*) are conceivable for Mn(salen) and oxo-Mn(salen) complexes. The relative energies of the *S2* and *S4* states of each complexes (taking *S0* as reference) are given in Table 6.1. The results suggest that the ground state of Mn(salen) species may be either *S0* or *S2*, depending on the axial ligand. In the homogeneous phase, **1-re** is likely to have an *S2* ground state, in accordance with the experimental evidence [113, 114, 378]. On the other hand, the *S0* and *S2* states of **2-re**, **3-re** and **5-re** are quasi-degenerate. Within the accuracy of DFT, it is difficult to predict which of *S0* or *S2* is the ground state for these complexes without further considerations. In their turn, oxo-Mn(salen) species show a clear tendency towards an *S2* ground state with a low lying *S0* excited state. In all cases, it is unlikely that any of the complexes would adopt *S4* as their ground state. Axial coordination with $PhCOO^-$ or $PhSO_3^-$ appears to have the least impact on the ordering and relative energies of the *S0*, *S2* and *S4* states. On the other hand, the most noticeable

Table 6.1: Energies of *S2* and *S4*, relative to *S0*, for the Mn(salen) and oxo-Mn(salen) complexes with different axial ligands. All values are given in $kJ \cdot mol^{-1}$ and include zero-point vibrational corrections.

X	Re		Ox	
	S2	*S4*	*S2*	*S4*
1	−14.1	26.9	−10.9	212.2
2	0.6	27.6	−12.8	212.8
3	1.9	67.3	−12.8	156.4
4	−7.7	37.2	−9.0	213.5
5	−2.6	44.9	−4.5	219.9
6	−21.8	26.3	−2.6	159.0
7	−14.7	32.1	−9.6	214.1
8	−12.8	23.7	−11.5	217.9

deviations to the overall behavior (in terms of ordering and energetic differences between spin states) are observed for species **3-re** and **3-ox**, as shown in Table 6.1.

To the best of our knowledge, this is the first time the results from vibrational analysis of Mn(salen) complexes are reported. The absolute energies, zero-point vibrational energy, and total entropy and Gibbs energy corrections at 298.15 K are given in the supplementary information[2]. The results show that zero-point corrections bear little effect on the overall ordering and energy differences between spin states. The same also applies to the enthalpic corrections at 298.15 K. On the other hand, an analysis of the relative Gibbs energies reveals a strong preference of the *S2* state for all complexes. This is mostly due to the electronic component of the entropy, S_{el} ,which is calculated assuming the states are orbitally non-degenerate and only accounts for spin degeneracy. At 298.15 K, the energetic contributions of S_{el} are -2.72 $kJ \cdot mol^{-1}$ and -3.99 $kJ \cdot mol^{-1}$ for complexes at the *S2* and *S4* state, respectively, thus pushing the *S2* state bellow *S0* for all cases under consideration. Despite the approximations involved in DFT, these results are significant, as they support the reaction models that predict the catalytic cycle of Mn(salen) complexes to occur exclusively in the *S2* state [124, 126, 135, 140].

Vibrational Analysis. Another important result obtained from the vibrational analysis calculations is the fact that very distinctive features are predicted for the infrared spectra of each compound at each spin state, as shown for **1-re** and **1-ox** in Figure 6.3. For both **1-re** and **1-ox**, the three different spin states are characterized by different intensities of the bands in the 1200–1400 cm^{-1}region. These wavenumbers correspond to an assortment of deformations in the salen framework, particularly wagging and rocking motions of the C−H groups in the salen ligand, as well as twisting of the CH_2 group in the diimine bridge. The spectra obtained for the three spin states of **1-ox** also differ in the 1500–1700 cm^{-1} region, where the normal modes associated to the stretching of the C−N bonds in the salen ligand are found. Moreover, the normal mode associated with

[2]The supplementary information is available in digital format in the CD-ROM that accompanies this work.

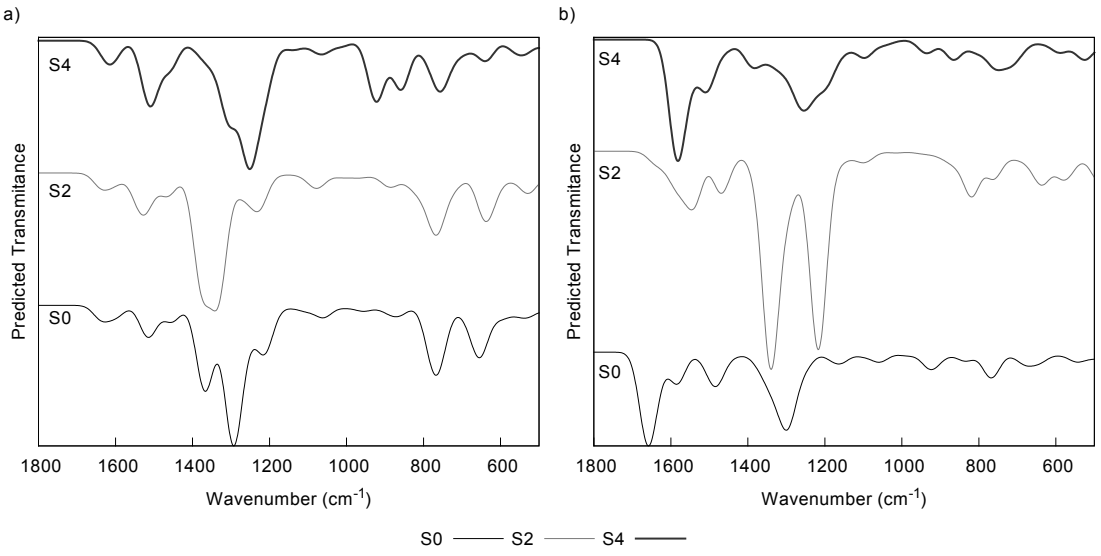

Figure 6.3: Predicted vibrational spectra for **1-re** (a) and **1-ox** (b) at their *S0*, *S2* and *S4* states, in the 500 cm^{-1}–1800 cm^{-1} region, at the X3LYP/DefBas-4 level of theory. The different spectra are shifted vertically, for clarity.

the Mn=$O_{(22)}$ stretching motion is found at 1293 cm^{-1}, 1212 cm^{-1} and 1197 cm^{-1} for the *S0*, *S2* and *S4* states, respectively, and is usually coupled with some distortion of the conformation of the salen ligand. In all cases, the most prominent bands of the spectra shown in Figure 6.3 correspond to normal modes which do not involve the movement of the chloride ligand. Moreover, similar features are also found in the predicted vibrational spectra of the other seven pairs of Mn(salen) complexes, although their interpretation is more involved, due to the overlapping of the normal modes associated with the motion of the axial ligand. The predicted spectra in Figure 6.3b may be of usefulness in the experimental identification of the elusive oxo-Mn(salen) intermediates, and the characterization of their ground state [106].

Reaction Energetics. An estimate of the energy involved in the oxidation of Mn(salen) complexes to their oxo-Mn(salen) analogues, ΔE_{ox}, was made by considering the energy balance of this reaction using H_2O_2 as oxidant and water as its by-product. This procedure further assumed spin conservation during the oxidation process, and the results are displayed in Table 6.2. The oxidation process is strongly exoenergetic and the value of ΔE_{ox} for the homogeneous catalyst appears to be close to the average of all other cases studied, at all spin states. Considering the *S2* case in more detail, ΔE_{ox} is greater (in absolute value) for the oxidation of **8-re**, and smaller for **3-re**, with a range of about 100 $kJ \cdot mol^{-1}$ between these two cases. The results suggest that coordination with $Et-NH^-$ yields the less stable oxo-derivative, relative to its parent complex.

A second type of energy balance, ΔE_{lx}, was considered in which the axial ligand is removed by HCl, yielding the conjugate acid of the original axial ligand and the corre-

Table 6.2: Energy balance for the oxidation of Mn(salen) to their oxo-Mn(salen) analogues, ΔE_{ox}, using H_2O_2 as oxidant, with different axial ligands, and at different spin states. All values are given in kJ · mol^{-1} and include zero-point vibrational corrections.

X	*S0*	*S2*	*S4*
1	−529.3	−526.1	−344.1
2	−539.0	−552.4	−353.7
3	−426.1	−440.9	−337.0
4	−522.9	−524.2	−346.7
5	−506.3	−508.2	−331.3
6	−536.4	−517.2	−403.7
7	−529.3	−524.2	−347.3
8	−549.9	−548.6	−355.6

Table 6.3: Energy balance for the removal of the axial ligand of Mn(salen) and oxo-Mn(salen) complexes using HCl, ΔE_{lx}, at different spin states. All values are given in kJ · mol^{-1} and include zero-point vibrational corrections.

X	Re			Ox		
	S0	*S2*	*S4*	*S0*	*S2*	*S4*
1	0.0	0.0	0.0	0.0	0.0	0.0
2	102.6	87.9	102.0	112.2	114.1	111.6
3	72.2	56.2	31.8	−31.0	−29.0	24.8
4	−7.3	−13.7	−17.5	−13.7	−15.6	−14.9
5	38.5	26.9	20.5	15.4	9.0	7.7
6	0.3	8.0	1.0	7.4	−1.0	60.6
7	−10.4	−9.8	−15.5	−10.4	−11.7	−12.3
8	−2.0	−3.3	1.2	18.5	19.2	12.7

sponding complex **1-re** or **1-ox**. This reaction is of some importance as it allows some sense on the spontaneousness of catalyst leaching processes. As shown in Table 6.3, compounds with different axial ligands behave rather differently. Focusing on the *S2* state, and assuming spin conservation, the ligand displacement reaction is always energetically unfavored for complexes coordinated with L_2 and L_5. By contrast, the displacement of a carboxilate group in the axial position of the manganese atom (L_4 and L_7) is energetically favored. However, the remaining cases shown in Table 6.3 not only reveal that the oxidation state of the metal center bears some influence on the energetic balance for this type of reaction, but also points towards the possibility that strong ligands are displaced from the oxo-complexes (**3-ox**) with a favorable energetic balance. Moreover, the results in Table 6.3 strongly suggest that the energetics of ligand exchange reactions within this set of compounds cannot be fully explained by the relative basicity of the axial ligand.

AIM Analysis. In order to further rationalize the observations described above, an AIM population analysis was made, the results of which are displayed in Figure 6.4. Our discussion of the AIM results will focus on the *S2* state, due to the likelihood of this being the ground state for all complexes. Moreover, the results from the AIM analysis for these

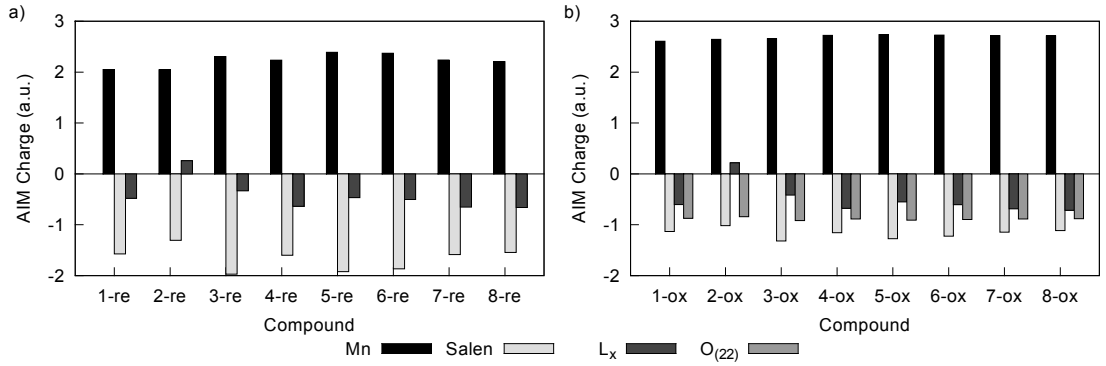

Figure 6.4: AIM charge distribution for the Mn(salen) (a) and oxo-Mn(salen) (b) complexes under study at their *S2* state at the X3LYP/DefBas-4 level of theory.

compounds at their *S0* state are very similar to those shown here for the *S2* state, in accordance to previous work [373].

As shown in Figure 6.4, the effective atomic charges of Mn and $O_{(22)}$ are very stable with respect to the different axial ligands tested, with average values of +2.69 $\pm$ 0.05 *e* and -0.89 ± 0.02 *e*, respectively in the oxo-Mn(salen) species. The effective charge of the metal center also shows little variation within the reduced Mn(salen) complexes, with an average value of +2.23 $\pm$ 0.13 *e*. On the other hand, the combined effective charges of the salen ligand, q_S, show significant variations with respect to the oxidation state of the metal center and also with respect to the choice of axial ligand. The coefficient of variation (CV) for q_S being 13.6% in the reduced Mn(salen) complexes and 8.1% in their oxo derivatives.

The combined effective charges of the of the the axial ligand, q_L, present huge variations, with CV of 69.6% and 60.7% for the reduced and oxidized manganese complexes, respectively. In order to better rationalize these results, we define the amount of electrons transferred from the axial ligand to the metal center, e_L, as $e_L = q_L^* - q_L$, in which q_L and q_L^* are the effective charge of the axial ligand and the charge of the free axial ligand, respectively. This measure is the symmetrical of the amount of charge transferred between the ligand and the metal center. Similar measures of the amount of electrons transferred from each ligand to the metal center where calculated, which are displayed in Table 6.4.

Table 6.4 allows the ordering of the different ligands by their donor capability, with L_2 being the weakest donor, and L_3 the strongest one. The chloride anion, L_1, which is the axial ligand usually found in homogeneous media, falls halfway between the two most extreme cases under consideration, although with some offset towards the strongest donors. The values of e_L for the Mn(salen) and oxo-Mn(salen) species are strongly correlated (r^2 = 0.9615) showing that e_L may be a good estimator for the donor power of the axial ligand in this collection of compounds, as shown in Figure 6.5a.

The amount of electron population transferred from the axial ligand to manganese is reduced to about 82% upon oxidation of the metal center, as shown in Figure 6.5a. This

Table 6.4: Transferred electrons from salen, e_S, the axial ligand, e_L, and $O_{(22)}$, e_O, to the manganese atom, at the *S2* state.

AxLig	e_S		e_L		e_O
	Re	Ox	Re	Ox	Ox
1	0.428	0.868	0.520	0.397	1.127
2	0.694	0.983	0.260	0.218	1.158
3	0.028	0.682	0.666	0.583	1.082
4	0.401	0.844	0.363	0.323	1.113
5	0.079	0.726	0.532	0.449	1.089
6	0.133	0.776	0.496	0.394	1.102
7	0.415	0.853	0.348	0.314	1.114
8	0.455	0.886	0.339	0.284	1.120

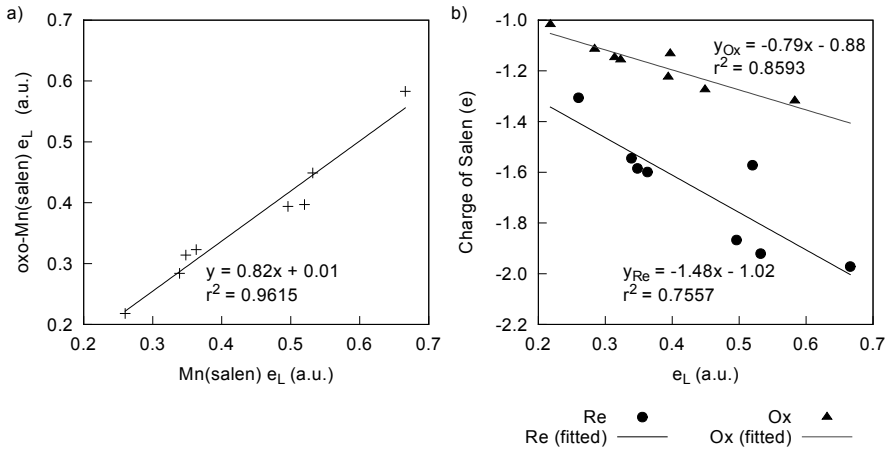

Figure 6.5: Relationship between the electronic population transferred from L_x to the metal center, e_L, in the reduced Mn(salen) complexes and their oxo derivatives (a) and charge of the salen ligand as a function of e_L (b).

is in apparent contradiction with the common sense perspective according to which the electron depleted Mn^V atom should be able to withdraw more electron density from the axial ligand. However, further analysis of the data in Table 6.4 shows that the salen ligand is the main responsible for the seemingly stable charge of the manganese atom. This is notorious upon oxidation of the metal center, which is accompanied by a large increase in the charge transferred from salen to Mn. As shown in Figure 6.5b, the overall charge of the salen ligand is strongly correlated to the amount of charge transferred between the axial ligand and the metal center, this effect being more noticeable in the reduced Mn(salen) complexes than in their oxo-analogues.

The picture emerging from Table 6.4 and Figure 6.5 points to the fact that strong donor ligands in the axial position of Mn(salen) complexes increase the electron population in the salen ligand. This is well illustrated by the case of the neutral ligand L_2: the small amount of electron density it donates (less that 0.27 *e*) implies that a greater amount of negative charge must be transferred from the salen ligand to the manganese atom in **2-re** and **2-ox**. This concept of salen as a "charge reservoir" was described in a recent work

that compares the charge distribution in $Mn(salen)^+$, Mn(salen)Cl and their respective oxo-analogues [373]. The results in this work further suggest that this concept may be an important factor for the rationalization of the role of the axial ligand.

Within the salen ligand, an analysis of the effective atomic charges of its constituent atoms revealed that the $N_{(2,3)}$ and $O_{(4,5)}$ bear most of the ligand's negative charge (about -1.1 *e* per atom). The excess negative charge in these atoms is partly counterbalanced by the prominent positive charges of $C_{6,7}$ and $C_{10,11}$, as mentioned in the recent work by Teixeira *et al.* [373]. The effective atomic charges of these four carbon atoms present the wider variation with respect to the different axial ligands. The combined charge of these four atoms (hereafter denoted q_C) behaves very differently according to the oxidation state of the metal center. In Mn(salen) complexes, q_C assumes a bimodal distribution, with values of about 1.60 *e* in **3-re**, **5-re** and **6-re**; and 1.79 e for the remaining complexes. In the oxo-Mn(salen) species, **2-ox** stands as an exception, with an extremely low q_C (+1.94 *e* against an average value of $+2.11 \pm 0.07$ *e*). Excluding **2-ox** reveals that q_C shows little variation in oxo-Mn(salen) complexes (with an average value of $+2.133 \pm 0.010$ e). Contrary to previous reports on the charge distribution on other conjugated systems [379, 380], the changes in q_S are mainly due to the effective atomic charge of the carbon atoms, while the hydrogen atoms retain their charges relatively unaffected by the choice of axial ligand or the oxidation state of the metal center. Such observations suggest that the charge transfer mechanism from salen to Mn should occur through the ligand's conjugated π system, leaving the σ skeleton of the ligand relatively unaffected.

Further exploration of the data also shows that q_S, e_L and the pyramidalization distance, d_P, are closely correlated in both reduced and oxidized species, as shown in Figure 6.6. The results in Figure 6.6a suggest that weak donor ligands may attach loosely to the manganese atom. For the reduced Mn(salen) complexes under such conditions, the coordination sphere of the metal center would resemble that of the four-coordinated $Mn(salen)^+$ species [373], in which the nitrogen and oxygen atoms of the salen ligands arrange in a nearly square planar geometry. With increased strengthening of the $Mn-L_x$ bond, the geometry around the manganese atom rearranges to a trigonal bipyramidal molecular arrangement, thus increasing d_P. A similar reasoning justifies the rearrangement of oxo-Mn(salen) complexes from the near trigonal bipyramidal geometry found in oxo-$Mn(salen)^+$ (which is only slightly distorted in the presence of weak donor ligands) to the near octahedral geometry attained around the metal center in the presence of strong donor ligands [124, 373]. Also, Figure 6.6 suggests that the charge of the salen ligand is strongly influenced not only by the oxidation state of the manganese atom, but also by the charge donating ability of the axial ligand and by the conformation assumed by the salen ligand itself, this last factor being also moderately correlated to e_L. This suggests that both electronic and steric effects play a role in defining the role of the axial ligand.

At this point, an analysis of $L(\mathbf{r})$ in the vicinity of the manganese atom may shed some light on the relationship between charge transfer and the conformation of the salen

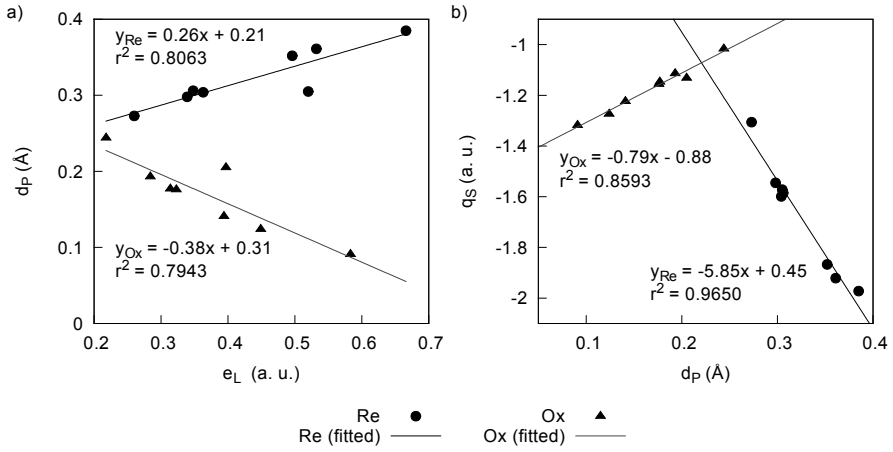

Figure 6.6: Pyramidalization distance, d_P, as a function of e_L (a), and the combined charge of the salen ligand, q_S, as a function of d_P (b) for Mn(salen), Re, and oxo-Mn(salen), Ox, complexes.

ligand. For the sake of simplicity, this discussion will be done by comparing Mn(salen) complexes with L_2 and L_3, as they are the weakest and strongest donor ligand in this study, respectively. Figure 6.7 shows the spin density of compounds **2-re**, **2-ox**, **3-re**, and **3-ox** and the local maxima, (3, −3) critical points, of $L(\mathbf{r})$ in overlay. The results show that there is a correspondence between the center of the lobes of the spin density and the maxima of $L(\mathbf{r})$. In turn, these maxima bisect the angles formed between the bonds of Mn to the nitrogen and oxygen atoms of salen. In the case of **2-re** (Figure 6.7a), such configuration implies a sp^2d^2 hybridization scheme for Mn in which the five hybrid orbitals are responsible for the square pyramidal arrangement of the bonds around the metal center, two 3*d* orbitals are occupied by one electron each and the remaining 3*d* orbital is empty. When using a stronger donor ligand (as in the case of **3-re**, Figure 6.7c), the localization of the maxima of $L(\mathbf{r})$ relative to the bonds around Mn is more compatible to what would be expected for a sp^3d hybridization of the metal center, which allows two of the remaining 3*d* orbitals to be occupied by one electron each, and the remaining 3*d* orbitals empty. In the oxo-Mn(salen) complexes, the sp^3d^2 hybridization is observed, warranting the near octahedral arrangement of the atoms bonded to the metal center and ensuring the $3d_{xz}$ and $3d_{yz}$ orbitals to be half filled. The fact that a change in the hybridization of Mn is observed in Mn(salen) complexes but not in their oxo derivatives conforms nicely with the less pronounced slope observed for the latter complexes in Figure 6.6b.

Finally, an interesting feature of the electronic structure of the oxo-Mn(salen) complexes under study was the dependence of the electron density at the bond critical point between the Mn and $O_{(22)}$ ($\rho_{BCP}(Mn{=}O_{(22)})$) and e_L, which is shown in 6.8a. Although $\rho_{BCP}(Mn{=}O_{(22)})$ varies little within the cases under study (CV = 2.14%), its variation appears to be strongly influenced by e_L, as shown in 6.8a. These results suggest a weaker $Mn{=}O_{(22)}$ bond for complexes with strong donors at their axial position. Such a fact may

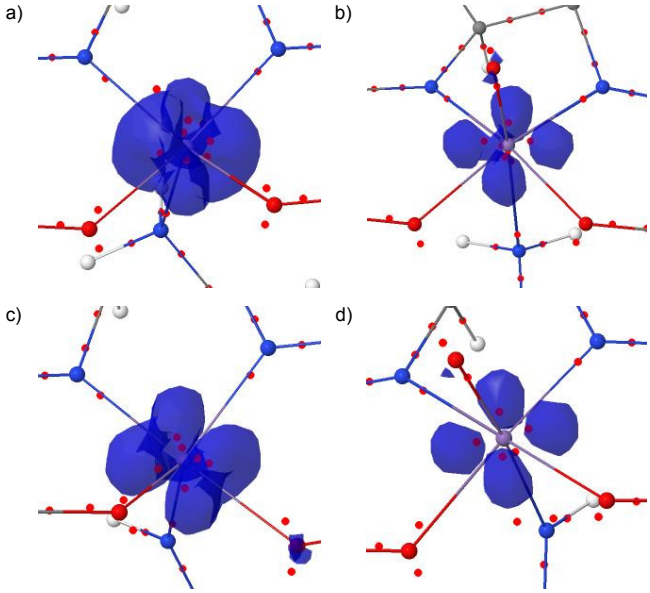

Figure 6.7: Depictions of the local maxima of $L(\mathbf{r})$ in the vicinity of the manganese atom, with the 0.05 isosurface of the spin density overlapped, for compounds: **2-re** (a), **2-ox** (b), **3-re** (c), and **3-ox** (d).

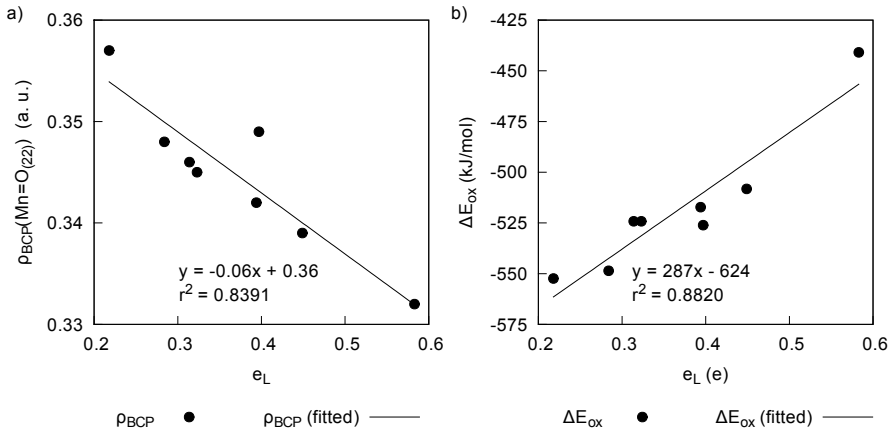

Figure 6.8: Electron density at the bond critical point between the Mn and $O_{(22)}$, $\rho_{BCP}(\mathrm{Mn}-\mathrm{O}_{(22)})$ as a function of e_L (a); and the energy involved in the formation of oxo-Mn(salen) complexes from Mn(salen) and H_2O_2, ΔE_{ox} as a function of e_L in the oxo-Mn(salen) species (b) .

be also related to the relationship between e_L and ΔE_{ox}, which is depicted in Figure 6.8b (cf. Table 6.2). Contrary to what was postulated by Kochi [36, 83, 112], strong donor ligands destabilize the oxo-Mn(salen) complexes, relative to their reduced parent compounds, as illustrated in Figure 6.8b. More importantly, the results show that a minute modification on the electron distribution on these systems may have a strong impact on the energy balance of the reactions in which these compounds take part.

6.4 Conclusions

In this work, several Mn(salen) and oxo-Mn(salen) complexes were studied in order to probe the effect that different axial ligands may have in the structure and reactivity of these complexes. The results show that the axial ligand influences the energy balance of the oxidation of Mn(salen) complexes to their oxo-Mn(salen) counterparts, with strong donor ligands yielding the less stable oxo-Mn(salen) complexes. Also, the charge of the salen ligand is strongly correlated to the donating power of the axial ligand, while the combined charge of Mn and of the oxo ligand (when present) remains stable. This constitutes further evidence that the salen ligand acts as a "charge reservoir" for the Mn atom (or the Mn=O group in oxo-Mn(salen) complexes). In general, the reduced Mn(salen) complexes are more sensitive to the choice of axial ligand than their oxo derivatives. In both cases weak donor ligands result in a diminished electron population of the salen ligand, and vice versa. In the case of Mn(salen) complexes, AIM analysis shows that the axial ligand also affects the hybridization of the metal center.

The results presented here show that a broad range of chemical properties are affected by changing the axial ligand in Mn(salen) complexes and their derivatives. Such variations suggest that, when dealing with immobilization of Mn(salen)-type catalysts, the issue of choosing the linker molecule strongly affects the chemical properties of the immobilized catalyst.

Chapter 7

Energetics of Vanadyl (IV) Acetylacetonate/TBHP Epoxidations[1]

Abstract

The study of vanadyl (IV) acetylacetonate, $VO(acac)_2$, catalyzed epoxidations has long been hindered by the large amount of possible chemical reactions that may take place, due to the labile nature of the acetylacetonate ligands. This question becomes ever more important when considering the epoxidation of allylic alcohols or the use of immobilized versions of this catalyst though Schiff base condensation. In this work, the energetics of over 2500 possible reactions are surveyed using Density Functional Theory (DFT). The results suggest that the mechanism develops in two stages. In the first stage, a series of slightly endoenergetic reactions takes place, converting $VO(acac)_2$ to a series of different oxo-vanadium (V) complexes. In the second stage, epoxidation of the substrate takes place upon conversion between two families of oxo-vanadium(V) complexes. Further insights on the regioselective epoxidation of allylic alcohols and the possible leaching of vanadium from the immobilized analogues of $VO(acac)_2$ are also given, based on the energetic balance of ligand-exchange reactions.

7.1 Introduction

Vanadyl (IV) acetylacetonate, $VO(acac)_2$, is a well known catalyst precursor with known applications in a large variety of oxidation reactions [31,381]. It has long been targeted as a desirable catalyst for the epoxidation of unsaturated organic compounds, since it offers

[1] Adapted from F. Teixeira, A. Melo, C. Freire and M. Natália D. S. Cordeiro, *J. Mol. Catal. A: Chem.* **2014**, (submited)
The contributions of F. Teixeira to this work were the following: Running the first principle computations, performing the data mining analysis and writing the first draft of the manuscript.

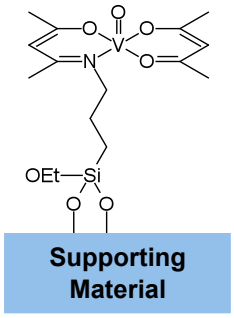

Figure 7.1: Example of $VO(acac)_2$ immobilized by Schiff base condensation.

an environmentally safer alternative to the use of traditional stoichiometric epoxidizing agents. This is usually accomplished using either hydrogen peroxide, H_2O_2, or *tert*-butylhydroperoxide, TBHP, as the terminal oxidant [50]. Moreover, the $VO(acac)_2$/TBHP system is well known for allowing the regioselective epoxidation of allylic alcohols, such as geraniol [31,152,381]. This property, in addition to its relatively low cost and low risk of hazard in its manipulation and use, has raised the interest in $VO(acac)_2$ as an interesting catalyst for the fragrance and flavoring industries [144, 154, 382].

More recently, the immobilization of $VO(acac)_2$ onto different supporting materials has been achieved, yielding novel materials with interesting catalytic activity [50, 161–163]. This has been accomplished by Schiff base condensation of the acetylacetonate (acac) moiety to an amine-functionalized supporting material, resulting in immobilized structures similar to the one depicted in Figure 7.1.

A detailed description of the catalytic cycle of $VO(acac)_2$ has eluded the efforts of several authors, due to the lability of the acac ligands [168, 171] and their tendency to be irreversibly oxidized into acetic acid (AcOH) and CO_2 [166, 167]. More recently, Vandichel *et al*. [165] published a comprehensive analysis of the catalytic cycle for the $VO(acac)_2$/TBHP catalyzed epoxidation of cyclohexene. The model proposed in Vandichel *et al*. [165] classifies the different vanadium species into active and inactive complexes, abbreviated as AC and IC, respectively. The criteria for considering a complex to be (potentially) active are the presence of an alkylperoxo or peroxo ligand in the complex. Activation reactions allow the formation of active complexes from inactive ones, as shown in Figure 7.2. The active complexes are inactivated upon the epoxidation of the substrate, the outcome of which depends on the possibilities offered by the set of ligands around the metal center. According to Vandichel *et al*. [165], these epoxidation steps may be further classified into five categories, schematically depicted in Figure 7.3.

Furthermore, the oxidation of vanadium (IV) to vanadium (V) is explained by means of radical decomposition of an active vanadium (IV) complex, with release of $^{t}BuO^{\cdot}$. In a similar manner, reduction from vanadium (IV) to vanadium (V) may occur via the homolytic cleavage of the O−O bond in an active vanadium (V) complex, as exemplified in Figure 7.4.

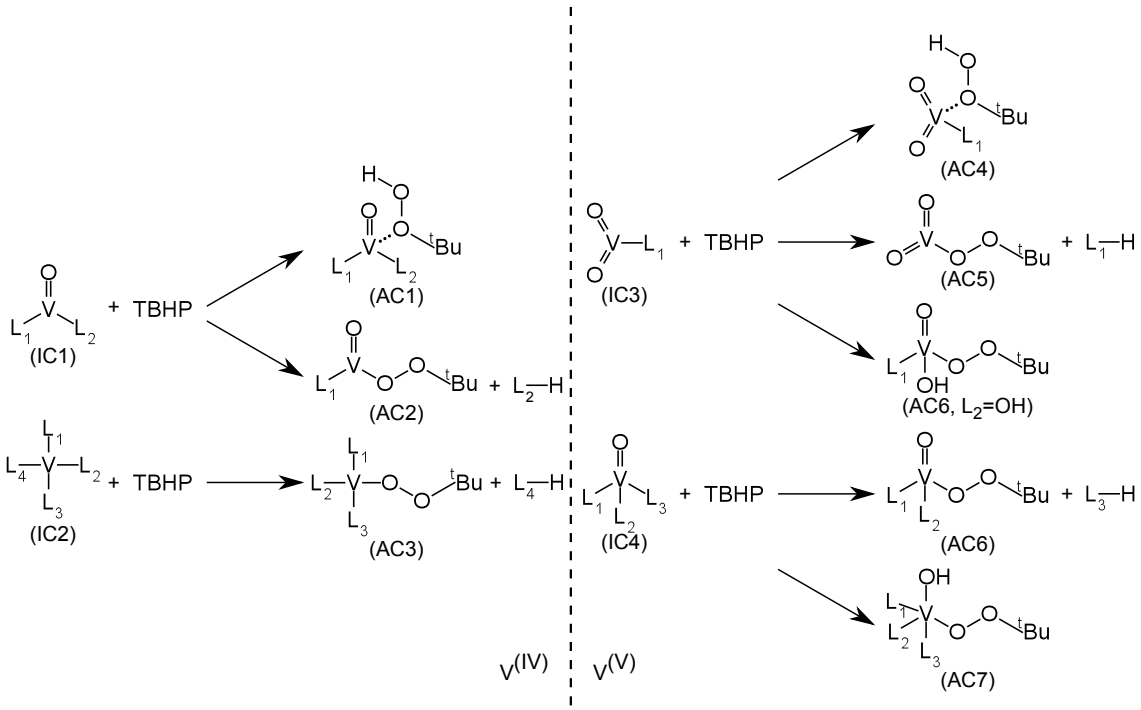

Figure 7.2: Generic structures for the inactive (IC) and active complexes (AC) in the catalytic cycle of the $VO(acac)_2$/TBHP system, and plausible activation reactions that link families of active and inactive complexes.

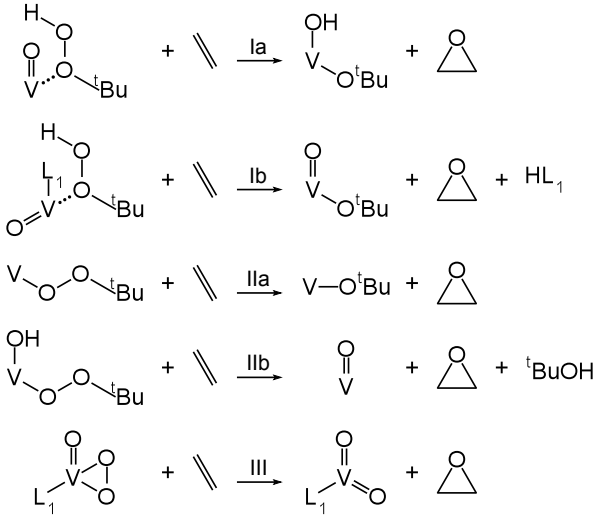

Figure 7.3: Possible reaction pathways for the epoxidation of an olefinic substrate.

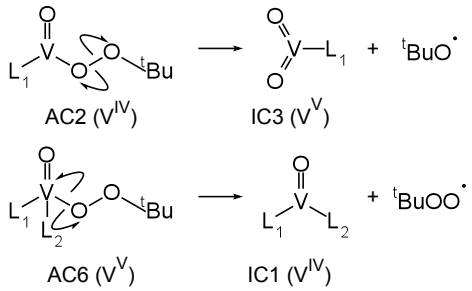

Figure 7.4: Examples of radical decomposition reactions allowing the formation of vanadium (V) species from vanadium (IV) ones, and vice-versa.

A key factor in the complexity of the reaction mechanism is the number of potential ligands in the reaction media. At the beginning of the $VO(acac)_2$ catalyzed epoxidation of an unfunctionalized alkene, the system is most likely to form adducts between $VO(acac)_2$ and TBHP [168–170]. Evidence has been collected supporting the fact that $VO(acac)_2$ looses at least one of its acetylacetonate ligands in the initial stages of the catalytic cycle, with formation of acetylacetone (Hacac) [166–168]. As the reaction develops, more potential ligands become available, such as $^tBuO^-$, AcO^- and OH^-. The origin of such ligands comes from the use of TBHP in the epoxidation reaction, the oxidation of acac, and from proton transfers to the oxo moiety of the vanadyl group, respectively [165]. This allows a multitude of ligand exchange reaction to occur for both active and inactive species. Moreover, such ligand exchange reactions may establish links between complexes of the same family, and also across different families of vanadium complexes, the latter case being depicted in Figure 7.5.

A few caveats need to be addressed when translating the model for the $VO(acac)_2$/TBHP epoxidation of alkenes to the epoxidation of allylic alcohols. Both allylic alcohols and their epoxides are possible ligands to vanadium, either forming alcohol-vanadium adducts or in the form of alkyloxo ligands. Also, the development of novel hybrid nanocatalysts derived from $VO(acac)_2$ by Schiff condensation raises new interesting questions [161–163]. For example, according to the model presented above, the acac ligands are promptly displaced and irreversibly oxidized to AcOH and CO_2. However, it is not clear if the ligand that links the metal atom to the supporting material either suffers a similar fate to that of acac, or if it is displaced from the coordination sphere of vanadium, but remains available to recapture the metal at a later stager, or even if the N−V and O−V bonds that hold the vanadium atom to its support are strong enough so that the whole catalytic cycle may develop with immobilized analogues of the complexes presented in this overview.

This work aims at answering the questions raised in the previous paragraph. To this purpose, the energetic balance of the reactions presented in Figures 7.2, 7.3, 7.4 and 7.5 is studied for a large range of possible ligands, which are depict in Figure 7.6a. Moreover, three different scenarios for the epoxidation of an olefinic substrate are considered and shown in Figure 7.6b: epoxidation of an unfunctionalized alkene (**S1**), epoxidation of an

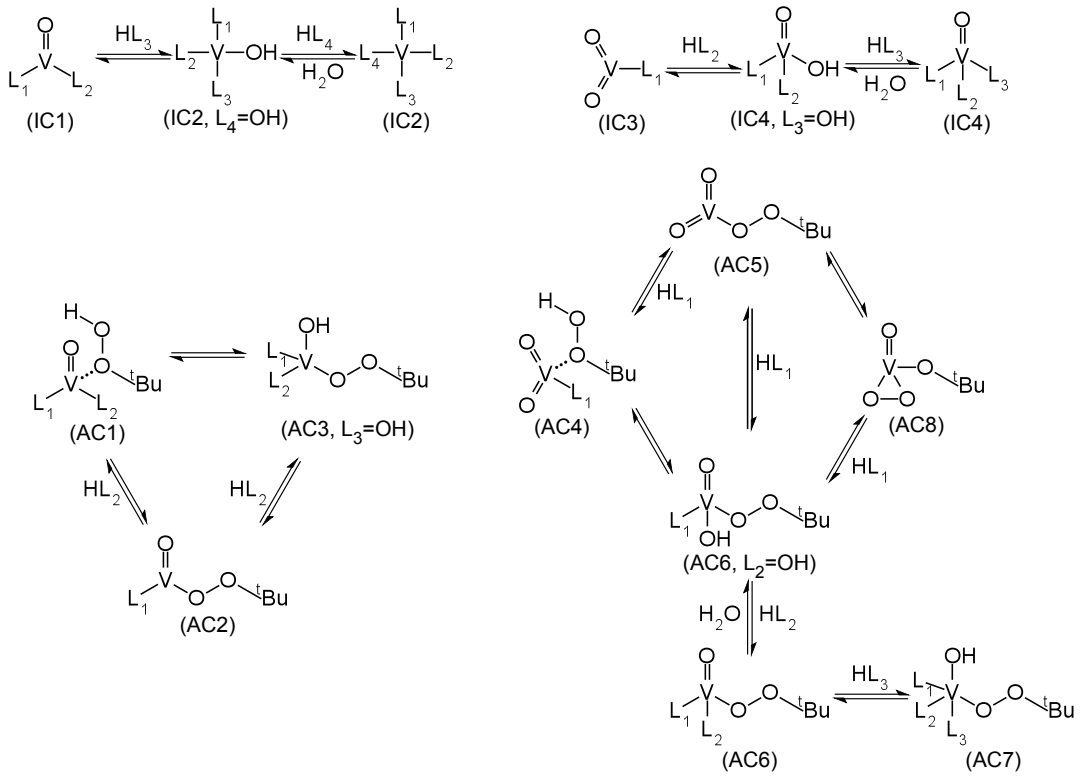

Figure 7.5: Possible equilibrium relationships between active (AC) and inactive (IC) complexes through ligand exchange reactions.

uncoordinated allylic alcohol (**S2**) and epoxidation of an allylic alcohol forming an alkyloxo complex with vanadium (**S3**). The main goal is to provide future experimental and theoretical studies within a framework of the most preponderant species in $VO(acac)_2$/TBHP epoxidations against which the results may be rationalized.

7.2 Computational Methods

Throughout this work, the following nomenclature is used: each compound is written in the form *XXn*-a*W*-b*X*-c*Y*-d*Z*, where *XXn* is the family name (as depicted in Figure 7.2) and *W*, *X*, *Y* and *Z* are the numbers corresponding to the different ligands given in Figure 7.6b, with unnecessary suffixes being omitted. Moreover, the scope of this work is limited to the following rules: compounds with a maximum of one Nacac ligand (**2**, in Figure 7.6b); the total number of either acac (**1**) or Nacac must be equal or less than two; only one peroxo or alkylperoxo group is allowed; only one allylic alkyloxo ligand (**6**) is permitted, and their epoxide derivatives (**7**) are only studied when connected to the inactive complexes that result from the epoxidation step, following the rationale proposed by Vandichel and co-workers [165].

DFT calculations where performed using the X3LYP functional [212, 213], as implemented in the Orca program package, version 2.8 [355]. A mixed basis set was used

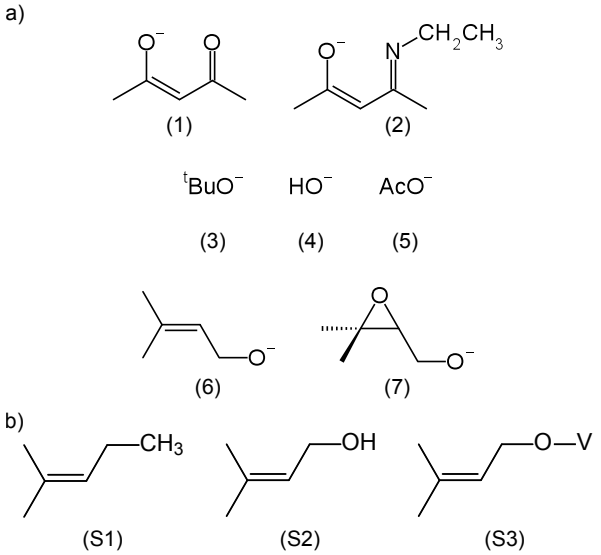

Figure 7.6: Possible ligands considered in this study (a), and the three different scenarios considered in this work for the olefinic substrate (b): alkene (S1), allylic alcohol (S2) and its alkyloxo derivative coordinated to vanadium in an active complex (S3).

in this work, which is available in the software under the keyword DefBas-4. This corresponds to a triple-ζ valence (TZV) basis set with contraction pattern $\{311/1\}$ for hydrogen, $\{62111/411/11\}$ for other atoms in the main group and $\{842111/63111/411/1\}$ for vanadium [360, 361].

Geometry optimizations were carried out using redundant internal coordinates, and under the unrestricted Kohn-Sham formalism. Moreover, when different isomers of the same complex were possible, all isomers were subjected to the optimization procedure, even though only the most stable isomer was subjected to further consideration. Vibrational analysis was carried out at the same level of theory, however, the restricted Kohn-Sham formalism was used for the singlet vanadium (V) species, in order to save some computational effort. Solvent effects were also evaluated, by performing single-point calculations on the equilibrium geometries using the conductor-like screening model (COSMO) [383, 384] with parameterization for dichloromethane (CH_2Cl_2, ϵ = 9.08, n = 1.4240) and the X3LYP/DefBas-4 level of theory.

Information about the thermochemistry of each system was gathered, including ground state energetics, zero point energy corrections as well as thermal contributions to the enthalpy, entropy and Gibbs energy at 298.15 K. A permutation script was designed for computing the thermodynamic properties of all possible reactions in this system, within the restrictions mentioned above. These reactions were further classified into five categories: ligand-exchange reactions within the same family of complexes; ligand exchange reactions across different families of complexes (Figure 7.5); activation of IC with TBHP (Figure 7.2); epoxidation (inactivation) reactions (Figure 7.3); and radical decomposition reactions (Figure 7.4).

7.3 Results

Despite the restrictions referred above, the strategy followed in this work originally contemplated about 2600 chemical reactions. The energy balance for these reactions ranges from $-849.2\ \text{kJ}\cdot\text{mol}^{-1}$ to $+821\ \text{kJ}\cdot\text{mol}^{-1}$, not considering zero-point corrections. Despite this wide range, 90% of the reaction considered have their energetic balance between $-198.9\ \text{kJ}\cdot\text{mol}^{-1}$ and $7.3\ \text{kJ}\cdot\text{mol}^{-1}$. The outliers from this distribution are mainly reactions that correspond to the formation or consumption of AC7 complexes, suggesting that these complexes are highly unstable. Indeed, obtaining optimized geometries for most of the AC7 complexes ligand **5** was a difficult process, since the acetate moiety would abstract the hydrogen from the hydroxyl group and form an adduct of AcOH and an AC6 complex. Because of this, AC7 complexes were not considered for further study.

Once all entries referencing the AC7 complexes were removed from the data set, a total of 2168 reaction remained under consideration. The energy balance, ΔE, for the remaining reactions ranged from $-313.9\ \text{kJ}\cdot\text{mol}^{-1}$ to $+233.5\ \text{kJ}\cdot\text{mol}^{-1}$, with 90% of its values reaching between $-184.5\ \text{kJ}\cdot\text{mol}^{-1}$ and $+6.5\ \text{kJ}\cdot\text{mol}^{-1}$.

The original energetic balances were only slightly affected by the application of zero-point vibrational energy (ZPVE) corrections, with deviations within$-10.7\ \text{kJ}\cdot\text{mol}^{-1}$ and $+14.0\ \text{kJ}\cdot\text{mol}^{-1}$. Further application of thermal corrections to the energy as well as enthalpic corrections at 298.15 K accounted for additional deviations within $-12.3\ \text{kJ}\cdot\text{mol}^{-1}$ and $+11.1\ \text{kJ}\cdot\text{mol}^{-1}$. Application of Gibbs energy corrections at 298.15 K accounted for larger deviations from the original values (between $-66.4\ \text{kJ}\cdot\text{mol}^{-1}$ and $+71.0\ \text{kJ}\cdot\text{mol}^{-1}$). To the best of our knowledge, the accuracy of the predicted vibrational frequencies for this type of compounds at the level of theory used remains untested. This fact, together with the exponential nature of the temperature-dependent vibrational components of the thermal energy, enthapy and entropy, lead us to report only the energy balance with ZPVE corrections. The application of implicit solvent corrections under the COSMO formalism accounted for additional deviations within $-88.1\ \text{kJ}\cdot\text{mol}^{-1}$ and $+63.5\ \text{kJ}\cdot\text{mol}^{-1}$ (including the effect from ZPVE corrections). In most cases, however, these corrections accounted only for a deviation of less than $10\ \text{kJ}\cdot\text{mol}^{-1}$ in either direction. A complete list of these reactions, as well as their corresponding calculated energetic balances is given in the supplementary information[2].

Ligand-exchange reactions in which both reactant and product are complexes of the same family are the most abundant type of reactions in this study, with 1547 entries in the data. A special loop in the permutation program allowed all reactions in this category to be evaluated in the exoenergetic direction (in the gas phase, prior to the application of zero-point energy corrections). In general, these reactions present very mild reaction energetics, with 75% of them presenting values for ΔE between $-172.65\ \text{kJ}\cdot\text{mol}^{-1}$ and $+7.852\ \text{kJ}\cdot\text{mol}^{-1}$, as shown in Figure 7.7a. Upon inclusion of solvent effects, the modal

[2]The supplementary information is available in digital format in the CD-ROM that accompanies this work.

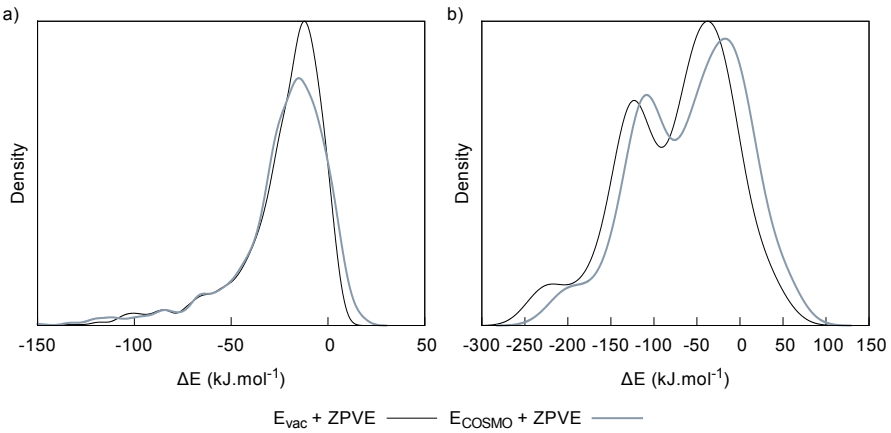

Figure 7.7: Distribution of the energy balance (ΔE) for the ligand-exchange reactions within the same family of complexes (a) and between complexes belonging to different families (b) in vacuum (E_{vac}) and including solvent corrections (E_{COSMO}).

peak in Figure 7.7a becomes slightly broader, without affecting the general order for these reactions. Being so, the most exoenergetic reactions within this class are those involving the inclusion of ligands **1** or **2** with removal of either H_2O, ^{t}BuOH or AcOH. On the other hand, all reactions involving the inclusion of water in IC2, IC4 and AC3 complexes show positive energetic balances, once ZPVE corrections are accounted for.

Ligand exchange reactions establishing equilibria between complexes belonging to different families account for 355 entries in the data. The energy involved in these reactions is distributed as portrayed in Figure 7.7b, suggesting a trimodal population. The most exoenergetic reactions in this class of reactions correspond to the addition of H_2O, AcOH, ^{t}BuOH, Hacac or HNacac to IC3 complexes, forming IC4-type complexes. On the other hand, the addition of alcohols or water to IC1 complexes is usually an endoenergetic process, with an average energetic balance of +16.7 $\text{kJ} \cdot \text{mol}^{-1}$, in vacuum. The modal peak at around -50 $\text{kJ} \cdot \text{mol}^{-1}$ (in vacuum) corresponds to the addition of an additional ligand to AC2 and IC1 complexes, yielding AC3 and IC2 complexes, respectively. As shown in Figure 7.7b, the energetic balances tend to be less exoenergetic when considering the effect of the solvent. Moreover, the degradation of AC5 and AC8 complexes is moderately exoenergetic (with typical ΔE_{vac} of -122 $\text{kJ} \cdot \text{mol}^{-1}$)

Activation reactions (such as those depicted in Figure 7.2) account for 402 processes. Their energetic balance in vacuum and in CH_2Cl_2 are depicted in Figure 7.8a. As a general trend, activation reactions without loss of a ligand are the most exoenergetics processes. These correspond to the formation of AC1 and AC4 complexes from their respective IC1 and IC3 precursors, as well as the formation of **AC6-a3** type complexes from IC4 ones. Overall, the energetic balance for these three reaction types is less than -70 $\text{kJ} \cdot \text{mol}^{-1}$ for the gas-phase reaction, and less than -50 $\text{kJ} \cdot \text{mol}^{-1}$ when accounting for solvent effects. Such processes are also the ones for which solvent corrections bear the most impact (+21 $\text{kJ} \cdot \text{mol}^{-1}$, on average). In all other cases, solvent effects impart

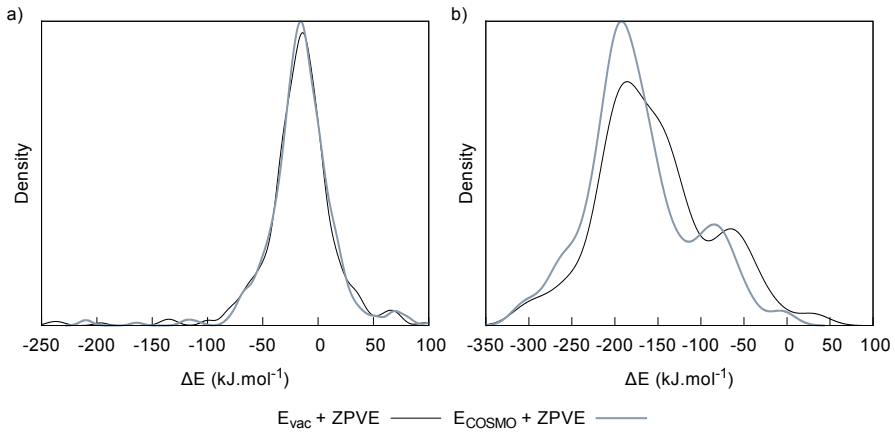

Figure 7.8: Distribution of the energy balance (ΔE) for the activation of inactive complexes with TBHP (a) and for the epoxidation reactions (b) in vacuum (E_{vac}) and including solvent corrections (E_{COSMO}).

only a negligible effect on the energetic balance of activation reactions (as shown in Figure 7.8a), with average differences between the energetic balance in vacuum and in CH_2Cl_2 of about +1.6 $kJ \cdot mol^{-1}$. Also, a general trend is observed in which the activation of vanadium (IV) inactive complexes is either endoenergetic, or only slightly exoenergetic. This observation is applicable to the activation of IC2 and IC3 complexes and also the activation of IC1 complexes with loss of one of the reactant's original ligands.

As shown in Figure 7.8b, most of the 263 epoxidation reactions considered in this work are exoenergetic. Despite this, the gas-phase epoxidation of either **S1** or **S2** by **AC6-a3-b4** and **AC6-a3-b3** with release of ^{t}BuOH are slightly endoenergetic (ΔE_{vac} = +30.6 $kJ \cdot mol^{-1}$, on average). Epoxidation reactions that do not involve the loss of one ligand during the oxygen-transfer step usually attain more favorable energetic balances than those where one of the ligands is lost (for the same substrate and active complex). The overall shape of the distribution in Figure 7.8b points towards two different types of epoxidation reactions. An analysis of the data show that the least exoenergetic reactions are usually observed for vanadium (IV) active complexes, whereas vanadium (V) active complexes usually attain the most favorable energetic balances, both in vacuum as in CH_2Cl_2. Figure 7.8b also suggests that the inclusion of solvent effects leads to a shift on the distribution of the energetic balances towards more negative values ($\Delta(\Delta E)$ = -17 $kJ \cdot mol^{-1}$, on average).

Radical decomposition reactions form a small group with only 25 cases being considered in this study. As can be seen in Figure 7.9, these reactions are enoenergetic processes. The six radical decomposition reactions of AC2 complexes to yield their IC3 relatives (*cf.* Figure 7.4) are much less endoenergetic than the processes involving the decomposition of AC6 complexes. This fact is well illustrated by the bimodal distribution depicted in Figure 7.9. Such results conform nicely with the experimental evidence that vanadium (V) species become dominant in the curse of the epoxidation

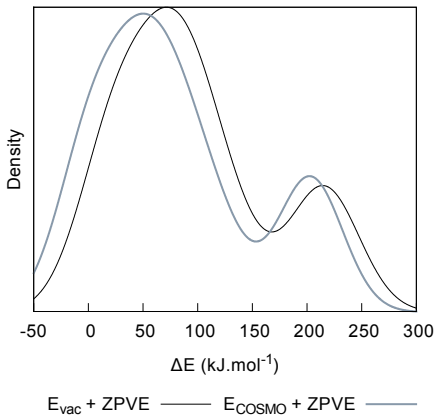

Figure 7.9: Distribution of the energy balance (ΔE) for the radical decomposition reactions of AC2 and AC6 complexes in vacuum (E_{vac}) and including solvent corrections (E_{COSMO}).

process [168, 169]. Despite this, there are three radical decomposition processes starting with AC6 complexes that are only slightly endoenergetic ($\Delta E_{vac} < 50$ kJ $\cdot$ mol^{-1}), corresponding to the decomposition of **AC6-a1**, **AC6-a2** and **AC6-a6** to their corresponding IC1 counterparts. Moreover, the inclusion of solvent effects, has a marginal effect on the energetic balance of these reactions ($\Delta(\Delta E) = -16$ kJ $\cdot$ mol^{-1}, on average).

7.4 Discussion

A reaction pathway can now be sketched from the data collected in this work, assuming negligible influence from kinetic factors. A mixture of VO(acac)$_2$ (**IC1-a1-b1**) and TBHP may form either **AC1-a1-b1** in a slightly exoenergetic process ($\Delta E_{vac} = -27.3$ kJ $\cdot$ mol^{-1}) or **AC2-a1**, with release of Hacac ($\Delta E_{vac} = +47.0$ kJ $\cdot$ mol^{-1}). The formation of **AC1-a1-b1** is energetically favorable and may account for the early epoxidation of the substrate reported by Talsi and co-workers [153,168–171]. However, radical decomposition of **AC2-a1** to **IC3-A1** ($\Delta E_{vac} = +18.2$ kJ $\cdot$ mol^{-1}) and the irreversible oxidation of Hacac to AcOH and CO_2 may eventually displace the equilibrium towards the formation of more **AC2-a1** [167]. Upon inclusion of solvent effects, the energetic balance for the formation of **AC1-a1-b1** increases to $\Delta E_{CH_2Cl_2} = -9.9$ kJ $\cdot$ mol^{-1}, while the formation of **AC2-a1** becomes energetically less favorable ($\Delta E_{CH_2Cl_2} = +50.1$ kJ $\cdot$ mol^{-1}). On the other hand, the energy balance for the radical decomposition of **AC2-a1** becomes almost null when considering the effect of CH_2Cl_2 ($\Delta E_{CH_2Cl_2} = +0.1$ kJ $\cdot$ mol^{-1}). Moreover, the capture of ^{t}BuOO$^\cdot$ by IC1 complexes is strongly exoenergetic, suggesting that for each IC3 complex formed by the radical decomposition of **AC2-a1**, an AC6 complex is formed by this process, thus pushing the population of vanadium atoms towards the +5 oxidation state.

Almost all reactions starting from **IC3-A1** (see Figures 7.2 and 7.5) are moderately exoenergetic, and this species may suffer activation to **AC6-a1-b3** ($\Delta E_{vac} = -73.1$ kJ $\cdot$ mol^{-1},

$\Delta E_{CH_2Cl_2} = -49.6$ kJ · mol^{-1}), activation to **AC4-a1** ($\Delta E_{vac} = -32.1$ kJ · mol^{-1}, $\Delta E_{CH_2Cl_2} = -11.8$ kJ · mol^{-1}) or participate in a number of ligand addition reactions to form different IC4 complexes. The three branches that depart from **IC3-A1** appear to converge towards the formation of AC6 complexes. This is done either by the already mentioned direct activation process or by re-arrangement of **AC4-a1** to **AC6-a1-b3** ($\Delta E_{vac} = -41.0$ kJ · mol^{-1}, $\Delta E_{CH_2Cl_2} = -37.8$ kJ · mol^{-1}). In the presence of an allylic alcohol (**S2**), the formation of **IC4-a1-b3-c6** from **IC3-A1** is strongly exoenergetic ($\Delta E_{vac} = -94.2$ kJ · mol^{-1}, $\Delta E_{CH_2Cl_2} = -71.2$ kJ · mol^{-1}). In turn, the activation of **IC4-a1-b3-c6** with possible loss of Hacac will yield **AC6-a3-b6** ($\Delta E_{vac} = -9.1$ kJ · mol^{-1}, $\Delta E_{CH_2Cl_2} = -6.3$ kJ · mol^{-1}). The latter being the most exoenergetic path for the activation of **IC4-a1-b3-c6**.

Taking into account the mechanistic pathways mentioned above, AC6 complexes play a pivotal role in the explanation of VO(acac)$_2$/TBHP epoxidations. A more detailed analysis of the reactions involving these complexes is therefore mandatory. As shown in Figure 7.5, AC6 species are in equilibrium with the other four active vanadium (V) complexes. As mentioned earlier, the formation of AC6 complexes from their AC4 analogues is always an exoenergetic process ($\Delta E_{vac} = -70.0$ kJ · mol^{-1} and $\Delta E_{CH_2Cl_2} = -64.0$ kJ · mol^{-1}, on average). AC5 complexes are also exoenergetically converted to AC6 complexes ($\Delta E_{vac} = -171.7$ kJ · mol^{-1} and $\Delta E_{CH_2Cl_2} = -151.0$ kJ · mol^{-1}, on average) and the same is also true for the conversion of AC8 complexes to their corresponding AC6 analogues, via ligand addition ($\Delta E_{vac} = -130.4$ kJ · mol^{-1} and $\Delta E_{CH_2Cl_2} = -117.8$ kJ · mol^{-1}, on average).

Upon epoxidation of either **S1** or **S2**, AC6 complexes may be converted to either IC3 or IC4 complexes, the latter case being preferred on energetic grounds, with average $\Delta E_{vac} = 51.4$ kJ · mol^{-1} and $\Delta E_{CH_2Cl_2} = -87.8$ kJ · mol^{-1} for the former case and $\Delta E_{vac} = -200.6$ kJ · mol^{-1} and $\Delta E_{CH_2Cl_2} = -206.9$ kJ · mol^{-1} for the latter. More interestingly, energetic considerations can not account for the preferential epoxidation of the double bond closer to the hydroxyl group of allylic alcohols, as the average values for the energy involved in the epoxidation of **S1**, **S2** and **S3** using AC6 complexes are -203.2, -197.8, and -192.9 kJ · mol^{-1}, respectively, for the gas-phase reaction; and -209.2, -204.7, and -193.7 kJ · mol^{-1}, respectively when accounting for the effect of CH_2Cl_2 as solvent. Although these values lie very close to each other, they suggest that the renown regioselectivity of VO(acac)$_2$/TBHP epoxidations is best explained by the fact that the $C_{(2)}$=$C_{(3)}$ bond in **S3** lies in close proximity to the distal oxygen of the alkylperoxo moiety, thus facilitating the epoxidation step.

Conversely, IC4 complexes are preferentially converted into AC6 complexes upon activation. This conversion may occur with loss of one ligand from IC4. The results show that the release of Hacac and HNacac is preferred to that of AcOH. On the other hand, the loss of hydoxo and alkyloxo ligands is energetically unfavored.

The results strongly suggest that IC4 and AC6 species function as “attractors” in the multitude of possible reactions for VO(acac)$_2$/TBHP epoxidations. This opens a new perspective on the reactions that take part in this system, and allows the proposal of a two

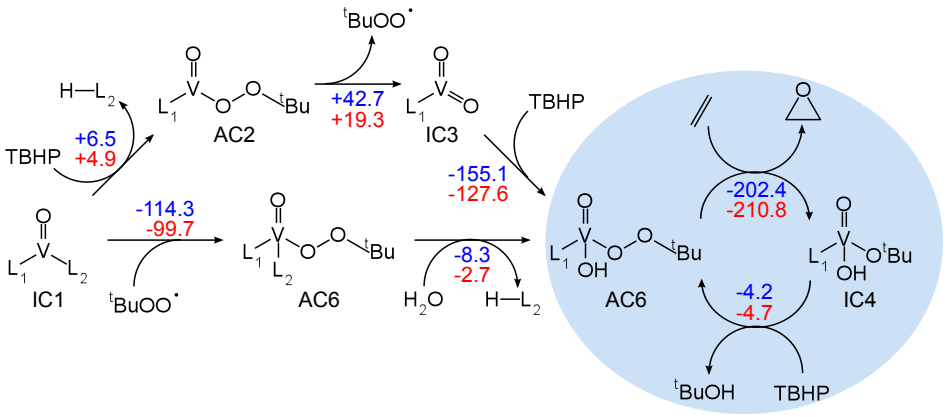

Figure 7.10: Proposal for the reaction mechanism of $VO(acac)_2$/TBHP epoxidations. As the reaction evolves, a closed catalytic cycle involving AC6 and IC4 complexes is established (shaded region). For each step, average values for ΔE_{vac} (blue) and $\Delta E_{CH_2Cl_2}$ (red) are given in $kJ \cdot mol^{-1}$, both values including the zero-point vibrational energy corrections calculated in the gas phase.

stage reaction mechanism (shown in Figure 7.10) as a viable model, complementary to the ones presented by previous authors [165, 169]. In the first stage of the reaction, the inactive catalyst precursor (IC1) is pre-activated to AC2. Because radical decomposition is an energetically unfavorable process, it is likely that AC2 complexes will promote the epoxidation of the substrate in the early stages of the reaction, specially if low concentrations of TBHP are present [153, 169, 171]. Eventually AC2 complexes will undergo radical decomposition into IC3. The resulting *tert*-buylperoxy radical may be scavenged by another molecule of IC1, yielding an AC6 complex. The activation of IC3 complexes by TBHP constitutes the beginning of the second stage of the reaction. In this second phase, AC6 species are the most preponderant active species in the epoxidation process, yielding IC4 complexes upon epoxidation of the substrate. In their turn IC4 complexes are favorably activated to AC6 complexes, with possible loss of ^{t}BuOH, restarting the catalytic cycle.

Despite the apparent simplicity of the reaction scheme depicted in Figure 7.10, a multitude of ligand exchange reactions are possible, as noted previously. Our concern is focused on ligands **2** and **6**, as the fate of the former may bring some insight on the problems associated with leaching of the metal from the supporting material, and the fate of the latter is undoubtedly connected to the regioselectivity of this reaction. According to Figure 7.10, only one degree of freedom for the composition of the coordination sphere of vanadium (L_1) is maintained throughout the catalytic cycle. This may bring the desire for stable (non-leaching) immobilized catalysts in conflict to that of high regioselectivity towards the epoxidation of allylic alcohols.

Displacement of HNacac is energetically unfavored in ligand exchange reaction between IC1 species, with an average ΔE_{vac} of +68.8 $kJ \cdot mol^{-1}$ and $\Delta E_{CH_2Cl_2}$ of +79.7 $kJ \cdot mol^{-1}$. Similar results are also observed for AC2 and IC3 complexes. On the other hand, ligand exchange reactions between AC6 or between IC4 complexes involving loss of HNacac

are not as energetically unfavorable, both in the gas phase (ΔE_{vac} = +2.2 kJ · mol^{-1} and ΔE_{vac} = +6.8 kJ · mol^{-1}, for AC6 and IC4 complexes respectively) as in solution ($\Delta E_{CH_2Cl_2}$ = +9.7 kJ · mol^{-1} and $\Delta E_{CH_2Cl_2}$ = +18.8 kJ · mol^{-1}, respectively). Although the results suggest that epoxidation reactions may take place while the vanadium atom is immobilized *via* ligand **2**, the increase in the number of available ligands such as ^{t}BuOH and AcOH may eventually displace the vanadium atoms from their anchoring ligand. Nevertheless, the process of recapturing vanadium into the functionalized supporting material appears to be energetically favored, assuming the uncoordinated linker molecule remains stable in the reaction medium.

Inclusion of an allylic alcohol (**S2**) as an alkyloxo ligand (**S3**) in the intermediate species of the catalytic cycle is of paramount importance for the regioselective epoxidation of allylic alcohols. In IC1 complexes, the results show that displacement of **1**, **2** and **5** by **S2** is energetically unfavored, with an average ΔE_{vac} of +64.1 kJ · mol^{-1} ($\Delta E_{CH_2Cl_2}$ = +69.5 kJ · mol^{-1}). The allylic alcohol may however, displace hydroxo or other alkyloxo ligands, including the epoxide of **S3** in a group of energetically favorable processes (ΔE_{vac} = −21.1 kJ · mol^{-1} and $\Delta E_{CH_2Cl_2}$ = −21.4 kJ · mol^{-1}, on average). The same observation, with similar values for the energy involved in these reactions is also observed for AC2 and IC3 complexes, although it should be noted that the displacement of the epoxide of **S3** by **S2** is not energetically favored in a ligand exchange equilibrium between two IC3 species. On the other hand, **S2** will favorably replace any ligand in an AC6 complex, with an average ΔE_{vac} of −26.6 kJ · mol^{-1} ($\Delta E_{CH_2Cl_2}$ = −28.2 kJ · mol^{-1}). The same behavior is also observed for IC4 complexes, with average ΔE_{vac} of −28.1 kJ · mol^{-1} and $\Delta E_{CH_2Cl_2}$ of −30.7 kJ · mol^{-1}.

These results allow us to propose a more detailed description of the catalytic cycle that may take place when dealing with the epoxidation of allylic alcohols. As shown in Figure 7.11, the **S3** scenario (Figure 7.6b) is made possible by displacement of L_1 from an AC6 complex by **S2**. A series of energetically favored reactions then allows the definition of a closed catalytic cycle for this scenario.

The hypothesis portrayed in Figure 7.11, together with the energetics for the **S1**, **S2** and **S3** scenarios discussed above, excludes the possibility of regioselective epoxidation of allylic alcohols while the complex is still anchored to the supporting material by its Schiff base ligand. Moreover, the inclusion of HNacac to either AC6 or IC4 species in Figure 7.11 is energetically unfavored, with average ΔE_{vac} of +21.7 kJ · mol^{-1} and +36.0 kJ · mol^{-1}, respectively; and $\Delta E_{CH_2Cl_2}$ of +18.5 kJ · mol^{-1} and +33.0 kJ · mol^{-1}, for the same AC6 and IC4 complexes, respectively.

7.5 Conclusions

The extensive survey on the different chemical reactions that may take place in $VO(acac)_2$ catalyzed epoxidations allowed the proposal of a reaction mechanism for these pro-

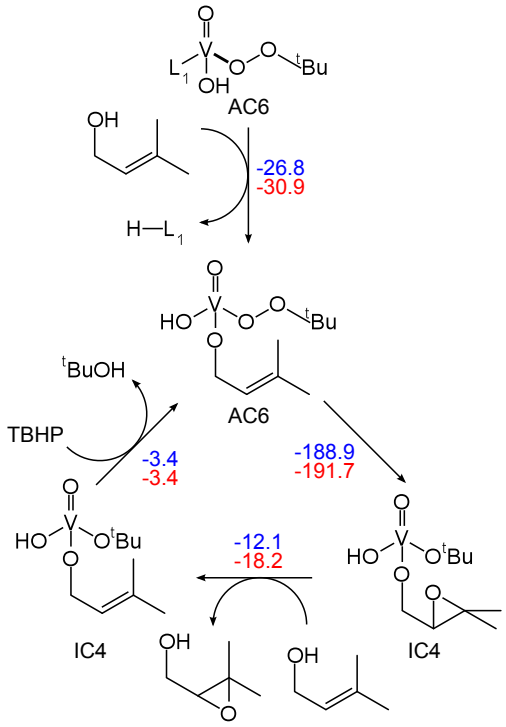

Figure 7.11: Alternative reaction pathway for the epoxidation of allylic alcohols by the $VO(acac)_2$/TBHP system, considering the possible coordination of the allylic alcohol to vanadium in the form of an alkyloxo ligand. For each step, average values for ΔE_{vac} (blue) and $\Delta E_{CH_2Cl_2}$ (red) are given in $kJ \cdot mol^{-1}$, both values including the zero-point vibrational energy corrections calculated in the gas phase.

cesses. The model proposed in this study postulates an initial stage where $VO(acac)_2$ is gradually converted into oxo-vanadium (V) complexes by radical decomposition reactions. In this stage, epoxidation of the substrate may occur in some reactions which are co-lateral to the main catalytic process. As the system evolves, the epoxidation process will be dominated by active $V^V(O)(OH)(OO^tBu)L_x$ and inactive $V^V(O)(OH)(O^tBu)L_x$ species, where L_x represents a generic ligand. This latter position may be occupied by an alkyloxo derivative of an allylic alcohol, in accordance to the model proposed by Sharpless [150].

With respect to the problem of leaching in vanadium catalyst immobilized using a Schiff base derivative of acetylacetonate, the model suggests that the linker is likely to be displaced as the reaction progresses towards the steady state part of the catalytic cycle.

The model presented in this work is both a simplification and an expansion of the model recently presented by Vandichel *et al.* [165]. In one hand, the impressive collection of possible reactions portrayed in the previous model is reduced to a more manageable number of reactions. This was achieved by excluding intermediate species whose formation is energetically unfavored. Also, the model presented here expands the previous one by considering alternative reaction paths for the epoxidation of allylic alcohols, as well as determining the fate of vanadium catalysts immobilized via Schiff base condensation.

Above all, the model presented here provides a framework for the rationalization of future experimental studies. It also allows further theoretical studies of $VO(acac)_2$/TBHP epoxidations to focus on the species which are most preponderant in the steady state phase of the reaction. This opens the door to novel insights on the oxygen-transfer process, and also to more complete simulations of immobilized vanadium catalysts.

Chapter 8

Reactivity of Alkylperoxo-vanadium Complexes Towards the Epoxidation of Alkenes and Allylic Alcohols: An Atoms in Molecules Approach

Abstract

Different vanadium-catalyzed epoxidation reactions of alkenes and allylic alcohols were studied with the aim of establishing relationships between the electronic structure of the reactants with the apparent energy barrier for this type of reactions. These reactions were studied using Density Functional Theory (DFT) at the X3LYP/Triple-ζ level of theory, and the electronic structure of the reactants was surveyed using Bader's theory of Atoms In Molecules (AIM). A set of vanadium (IV) and vanadium (V) complexes with *tert*-butylhydroperoxide (TBHP), *tert*-butylperoxide (TBP) and peroxide was chosen in order to reflect the diverse active species in $VO(acac)_2$/TBHP epoxidations. Typical values for the apparent activation energy of the reactions under study range from 20 $kJ \cdot mol^{-1}$ to 60 $kJ \cdot mol^{-1}$, although several vanadium (IV) complexes present activation energies over 100 $kJ \cdot mol^{-1}$ towards the epoxidation of alkenes and allylic alcohols. These results were rationalized by means of a linear model relating these results to the atomic effective charges, spin densities, and bond descriptors provided from AIM analysis of the reactants. This model satisfactorily reproduces the apparent barriers determined using DFT. The results show that large charge separations between vanadium and its ligands, as well as the presence of electron withdrawing groups in the olefinic substrate, result in an increase in the activation energy of these reactions.

8.1 Introduction

The advent of Green Chemistry, and the corresponding need for safer and environmentally friendlier industrial processes triggered an increase in interest for the development of novel catalysts [7]. In this context, vanadyl (IV) acetylacetonate ($VO(acac)_2$) catalyzed epoxidations have been foreseen as possible solutions for the synthesis of complex epoxides, using *tert*-butylhydroperoxide (TBHP) as oxidant. In their turn, these epoxides are useful intermediates in the production of medicines, fragrances and flavors [1, 2]. The potential applicability of the $VO(acac)_2$/TBHP system in industrial applications has been enhanced by the recent development of novel hybrid materials with interesting catalytic properties. The synthesis of such materials embodies the idea of immobilizing a transition metal catalyst onto a supporting material, in the hope of combining the advantages of homogeneous catalysts to the economy provided by heterogeneous catalysts [50]. In the case of $VO(acac)_2$, this has been accomplished by Schiff base condensation of the acetylacetonate (acac) moiety to an amine-functionalized supporting material [50, 161–163].

On the other hand, the study of vanadium peroxo and alkylperoxo complexes, such as those found in Figure 8.1a, has been carried on since the 1970's, when they were first identified as the active species in the epoxidation of alkenes and allylic alcohols in the $VO(acac)_2$/TBHP system [385, 386]. These complexes may be produced by the reaction of THBP with an inactive vanadium complex [152, 153, 171]. Upon oxidation of the substrate, the oxygen atom distal to the tert-butyl group (O_{dist}) is transferred to the substrate, forming the epoxide, and resulting in the inactivation of the vanadium complex [165]. Given the right conditions, TBHP may coordinate itself to vanadium (IV) or vanadium (V) atoms without the need for a ligand exchange reaction to occur. These adducts of THBP (AC1 and AC4, in Figure 8.1a) are closely related to the alkylperoxo complexes, being also active species towards epoxidation processes [153, 169, 170].

More recently, Vandichel and co-workers proposed a complete catalytic cycle for the epoxidation of alkenes using the $VO(acac)_2$/TBHP system [165]. Vandichel's model considers the compounds complexes depicted in Figure 8.1a to be the active species in $VO(acac)_2$/TBHP epoxidations. These compounds are further classified according to the oxidation state of the metal center: AC1, AC2 and AC3 corresponding to vanadium (IV) complexes, while the other compounds represented in Figure 8.1a are vanadium (V) species [165].

The labile nature of these vanadium complexes greatly increases the number of possible active complexes with each plausible ligand must be taken into account. This is well illustrated when attempting to consider the epoxidation of allylic alcohols and/or the immobilization of $VO(acac)_2$ by Schiff base condensation. Each of these situations involves considering one extra ligand, relative to the set of possible ligands considered by Vandichel and co-workers in their study of epoxidation of cyclohexene in the homogeneous phase [165]. As an example, the set of possible ligands that must be considered

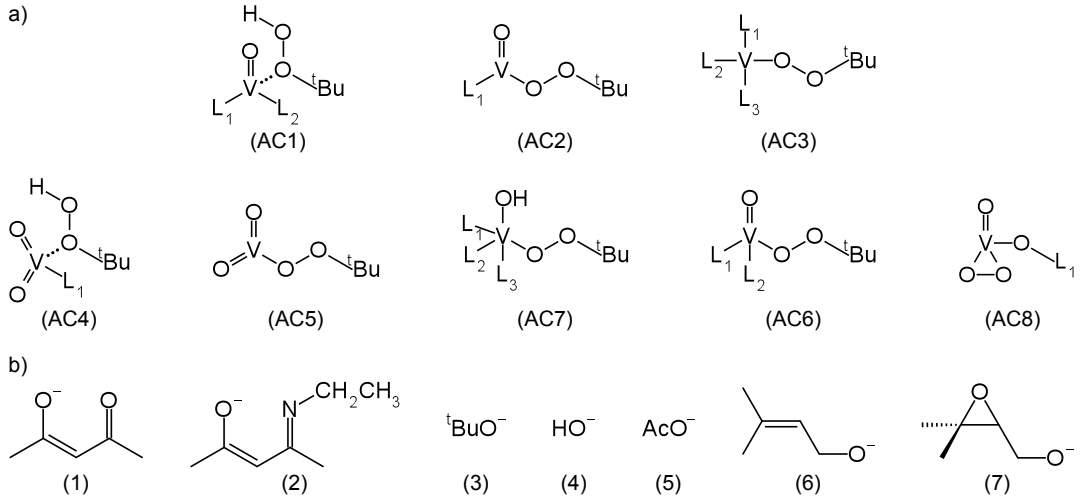

Figure 8.1: Generic structural formulas for active vanadium complexes in the $VO(acac)_2$/TBHP system (a); and the different possible ligands (b).

in order to address these questions is depicted in Figure 8.1b. This increase in complexity effectively hinders the study of the epoxidation of alkenes and allylic alcohols in more complex $VO(acac)_2$/TBHP systems.

Theoretical studies by Kuznetov, Aschi and respective co-workers have helped clarifying the oxygen transfer mechanism, confirming the original ideas by Sharpless and co-workers [42, 150, 151]. According to these authors, the oxygen transfer step takes place in a concerted manner, and the transition state resembles a three-membered ring structure [178, 387, 388]. Vandichel and co-workers further divided the possible epoxidation reactions which are conceivable by applying the Sharpless mechanism to the active complexes in Figure 8.1a into 5 categories, depicted in Figure 8.2. Vandichel and co-workers also noted that the activity of the different active complexes in Figure 8.1a depends of the other ligands coordinated to the metal center. In general, the coordination of alkyloxo ligands has a deactivating effect, whereas the coordination of acetylacetonate (acac) or acetate (AcO) translated into lower activation barriers to the epoxidation step [165].

Because the epoxidation step is usually strongly energetic (*see* Chapter 7), Hammond's rule postulates the transition state to lay close to the reactants. A hypothesis can therefore be made that information on the electronic structure of the reactants can be used to predict the energy of the transition state in these reactions. Information on the electronic structure of the reactants can be recovered from the electron density using Bader's theory of Atoms in Molecules (AIM). According to AIM, critical points of the electronic density give information on the position of the nuclei, and the connectivity of the atoms in a chemical system. The topological features of the electron density allow the establishment of atomic basins from which effective atomic charges and spin densities may be determined. Moreover, the topology of the Laplacian of the electron density allows the determination of regions in space where the electron density is locally concentrated,

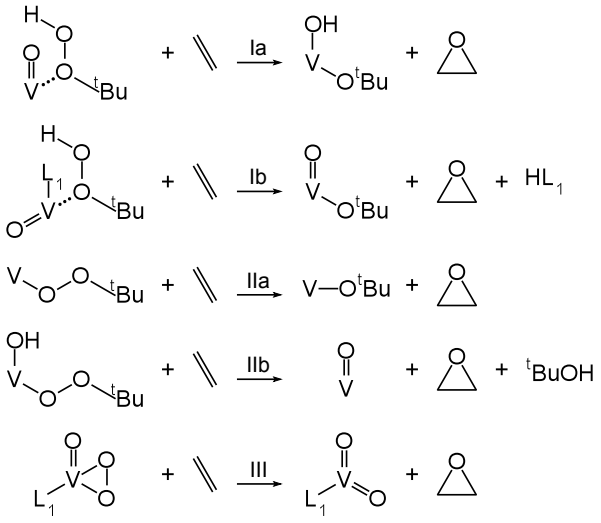

Figure 8.2: Sharpless type epoxidation reactions studied in this work. For simplicity, ligands not involved in the reaction are omitted, and only the epoxidation of an external alkene is depicted.

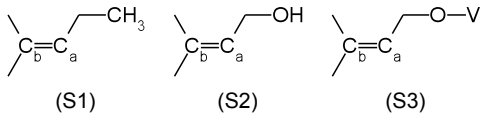

Figure 8.3: Different scenarios considered for the substrate of the Sharpless reaction: alkene (S1), allylic alcohol (S2) and its alkyloxo derivative coordinated to vanadium in an active complex (S3).

these features being usually associated to the localization of non-bonging electron pairs or even that of unpaired electrons [262].

In this work, the hypothesis mentioned above is is carefully tested. For that purpose, several epoxidation reactions of type Ia, IIa and III (Figure 8.2) were studied using DFT to determine the geometry and energy of their corresponding transition states. At the same time, the electronic structure of the eight families of active complexes was surveyed using AIM theory. Moreover, three different scenarios for the epoxidation of an olefinic substrate are considered and shown in Figure 8.3: epoxidation of an unfunctionalized alkene (S1), epoxidation of an uncoordinated allylic alcohol (S2) and epoxidation of an allylic alcohol forming an alkyloxo complex with vanadium (S3). The electronic structure of each of these substrates was also studied using AIM. The goal is to identify the main variables that govern the kinetics of $VO(acac)_2$/TBHP epoxidations, providing some insight on these reactions.

8.2 Methodology

Throughout this work, the following nomenclature is used: each compound is written in the form AC*n*-a*X*-b*Y*-c*Z*, where *n* is the family number (as depicted in Figure 8.1a) and *X*, *Y* and *Z* are the numbers corresponding to the different ligands given in Figure 8.1b, with unnecessary suffixes being omitted. Moreover, the scope of this work is limited to

the following rules: compounds with a maximum of one Nacac ligand (**2**, in Figure 8.1b); the total number of either acac (**1**) or Nacac (**2**) must be equal or less than two; only one allylic alkyloxo ligand (**6**) is permitted, following the rationale proposed by Vandichel and co-workers [165].

DFT calculations where performed using the X3LYP functional [213], as implemented in the Orca program package, version 2.8 [355]. A mixed basis set was used in this work, which is available in the software under the keyword DefBas-4 and corresponds to a triple-ζ valence (TZV) basis set with contraction pattern $\{311/1\}$ for hydrogen, $\{62111/411/11\}$ for other atoms in the main group and $\{842111/63111/411/1\}$ for vanadium [360, 361].

The Potential Energy Surface (PES) was surveyed using relaxed scans along the distances between the distal oxygen atom of the active alkylperoxo complexes and either carbon atom of the substrate. In order to save computational effort, these scans were performed using a simpler basis sets that omits the polarization functions of the hydrogen atoms. The geometry at the stationary points of the PES was optimized using redundant internal coordinates. The unrestricted Kohn-Sham formalism was used in these optimizations, allowing the independent treatment of the densities of α and β electrons. At the end of the geometry optimization procedure, a conversion utility (Molden2AIM) from Prof. Wenli Zou at the Southern Methodist University, Dallas [358] was used to generate the input files needed for AIM analysis from the output of Orca. Vibrational analysis was carried out at the same level of theory, but the restricted Kohn-Sham formalism was used for the singlet vanadium (V) species, in order to save some computational effort.

The topology of the electron density (ρ) was surveyed using the AIMALL program package [377], which was also used for the integration of the atomic basins and determination of effective atomic charges, spin densities and related properties. The topology of the Laplacian of the electron density was surveyed using Bader's AIMPAC program suite [357]. Following the convention used by several other authors, the $L(\mathbf{r})$ function will be defined as $-1/4\nabla\rho(\mathbf{r})$, for which a local maximum corresponds to a local concentration in ρ, usually related to the existence of a lone electron or non-bonding pair of electrons [261].

The relationship between activation barriers calculated using DFT and the electronic structure parameters obtained from AIM analysis of the reactants was studied using ordinary linear regression using the R language [338]. The significance of the coefficients was asserted using Anscombe's probabilistic permutation test, as implemented in the lmPerm package [374]. Each permutation test was allowed to run for a maximum of 10^6 iterations with a complete random permutation at each 10^3 iterations; the test for each coefficient was allowed to stop when the estimated standard error for the coefficient was less than 0.1% of its magnitude. Furthermore, an iterative protocol was devised in order to retain only the most significant coefficients: in the first iteration, the dependent variable was fitted against all independent variables. A standard stepwise regression with back-

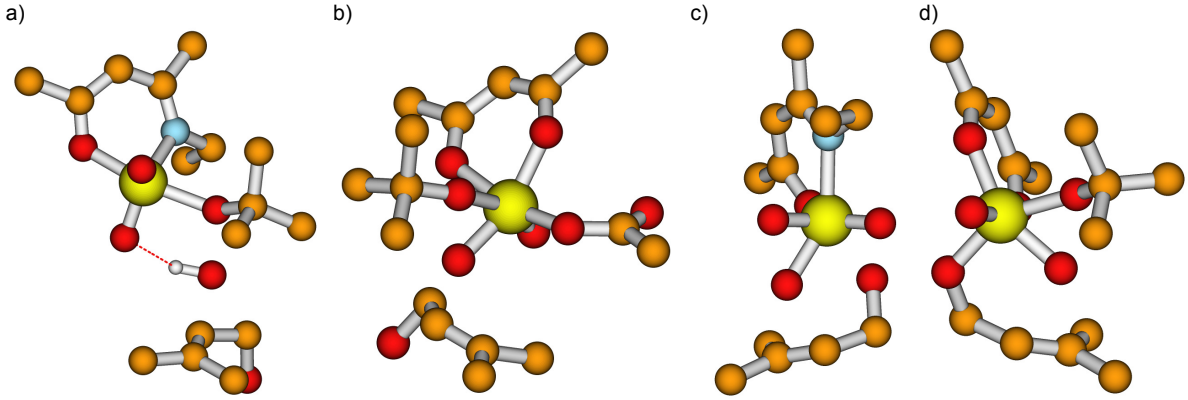

Figure 8.4: Examples of transition states for the epoxidation of S2 with AC4-a2 (a), AC6-a1-b5 (b), AC8-a2 (c); and epoxidation of AC3-a1-b3-c6 as an example of a S3 scenario. The hydrogen atoms not participating in a hydrogen bond were omitted, for clarity.

ward elimination procedure was then carried out until all independent variables attain a significance level above 99%.

8.3 Results and Discussion

DFT Calculations. Several transition states corresponding to the different epoxidation reactions depicted in Figure 8.2, with different ligands in the coordination sphere of the vanadium atom. Despite several attempts, no adequate transition state structure was found for AC7 complexes. Upon scanning of the PEs, these complexes were found to spontaneously convert into AC6 complexes via proton transfer between OH and any other ligand rather than interact with the substrate. All transition states found correspond to a concerted oxygen transfer mechanism involving the O_{dist} in the tert-butylperoxy (TBP), or in the TBHP residue (in AC1 and AC4 complexes). Also, no evidence of pre-coordination of the substrate to vanadium during the epoxidation step was witnessed. As shown in Figure 8.4, the transition states are well described by a triangular arrangement of the distal oxygen in the tert-butylperoxy moiety (or TBHP, in Figure 8.4a) and the carbon atoms in the $C_a{=}C_b$ bond of the substrate. This verifies the Sharpless model, and also confirms the theoretical calculations of previous authors who have studied this or similar systems [165, 177, 178, 387–391]. The geometry of the three atoms involved in the formation of the epoxide group moreover suggests that the formation of the two $C{-}O$ bonds occurs in an asynchronous fashion. Evidence supporting this claim can be found in the fact that, at the transition state, the distances $O{\cdots}C_b$ and $O{\cdots}C_a$ differ by about 0.3Å (on average) with the former being the largest. Information on the geometries, absolute energies and imaginary frequencies of the different transition states can be found in the supplementary information[1].

[1]The supplementary information is available in digital format in the CD-ROM that accompanies this work.

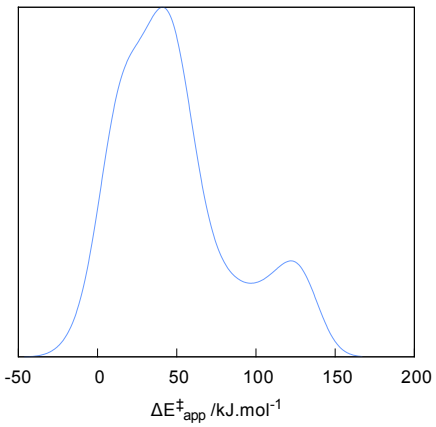

Figure 8.5: Density plot of the energy barriers for the reactions considered in this study.

The apparent energy barrier for each reaction, $\Delta E^{\ddagger}_{app}$, was defined as the energy difference between the transition state and the reactants, separated by an infinite distance. The decision to use this definition not only allows for a direct comparison to the results published by Vandichel and co-workers [165] but is also more sound, due to the lack of data on the accuracy of DFT when evaluating the energy of molecular complexes of this nature [131]. Our discussion will focus on the overall behavior of these values among different active complexes and substrates. A complete listing of the reactions studied and their respective activation barriers and energetic balances is also given in the supplementary information.

As shown in Figure 8.5, the energy barriers for the reactions considered form a bimodal population. The results show that the epoxidation processes promoted by AC1 and AC3 complexes with **1** and/or **2** (see Figure 8.1b) have the largest activation barriers (about 100 kJ $\cdot$ mol^{-1}). In most cases, however, the energy barrier is considerably lower, between 20 kJ $\cdot$ mol^{-1}and 60 kJ $\cdot$ mol^{-1}for about half of the determined values. AC2 and AC4 complexes with **3** or **4** in the coordination sphere of vanadium show particularly low activation energies (8.6 kJ $\cdot$ mol^{-1}, on average) and AC5 also stands out by presenting a negative apparent barrier (–9 kJ $\cdot$ mol^{-1}). The results obtained using S1 are in very good accordance with the results obtained by Vandichel and co-workers [165] for the epoxidation of cyclohexene. The small differences in the calculated energy barriers (usually less than 10 kJ $\cdot$ mol^{-1}) are perfectly justifiable by differences in the density functional and basis set used in each work.

Each active complex was tested with substrates S1 and S2, while complexes containing **6** were only tested for the epoxidation of a coordinated allylic alcohol (S3). The activation barriers for S2 were consistently 3 to 5 kJ $\cdot$ mol^{-1}higher than those calculated for S1. In turn, the apparent energy barriers determined for the S3 scenario are usually within 10 to 15 kJ $\cdot$ mol^{-1}of those determined for the S1 and S2 cases in similar active complexes of the same family. These results stand in defiance of the hypothesis for an ac-

tivation of the C=C bond closer to the oxygen atom by inductive effects, as advanced by Sharpless, Chong and Michaelson [44, 151]. By contrast, the geometries of the transition state for the S3 scenario (exemplified in Figure 8.4d) suggest that the preferential epoxidation of the double bond closer to the oxygen group is most likely due to an increase in the pre-exponential factor rather than a lowering of the activation energy, assuming an Arrhenius-like expression for the kinetics of these reactions.

AIM Analysis. The results presented so far suggest that the variance in the values of the apparent activation barriers shown in Figure 8.5 should depend mostly on the characteristics of the active complex involved in each reaction. In order to test such hypothesis, the topology of the electron density of all possible active complexes depicted in Figure 8.1 was examined using Bader's AIM theory, in an attempt to establish quantitative (or at least qualitative) relationships between the chemical structure of the different active complexes and the activation energy of the epoxidation reaction in which they are involved.

Before addressing the results from the AIM analysis of the active complexes, the claim of equivalence between the different scenarios for the substrate must be examined. For the purpose of this discussion, the labeling of the carbon atoms in the substrate follows the one depicted in Figure 8.3. The effective atomic charges of C_a in S1 and S2 are $-0.052\,e$ and $-0.043\,e$, respectively. These values are similar to the average atomic charge of $-0.035 \pm 0.005\,e$ found for the same carbon at S3. On the other hand, the effective atomic charges of C_b is about $-0.001\,e$ for the three cases. The electron density at the bond critical point (BCP) between C_a and C_b is 0.352, 0.353 and 0.349 a.u., for S1, S2 and S3, respectively. Also, the ellipticity of the electron density at the BCP is about 0.350 for the three scenarios. These values are typical of a slightly polarized C=C bond, and the results suggest that the alkene moiety is the same for the three situations considered (apart from the effective atomic charge of C_a.)

Figure 8.6 shows the distribution of the effective charge of vanadium, as well as those of its ligands, on the different complexes studied. As shown in Figure 8.6, a multimodal distribution was found for the effective atomic charges of vanadium. Vanadium (IV) complexes (AC1, AC2 and AC3) dominate the lower end of this distribution, with an average atomic charge of $2.09 \pm 0.07\,e$. On the other hand, AC7 complexes dominate the higher end of this distribution, with an average atomic charge of $2.31 \pm 0.02\,e$. However, most of the population is concentrated in the range $2.10 - 2.25\,e$. For doublet vanadium (IV) complexes, more than 90% of the spin density was concentrated at the vanadium atom, in good accordance with the experimental evidence [146, 169]. This result also allows for some simplification of the following discussion, as an analysis of the spin density at the ligands can be discarded.

The distribution of the collective charges for the TBHP moiety in AC1 and AC4 complexes shows a bimodal distribution (Figure 8.6b). A small positive charge is observed in all AC4 and some AC1 complexes ($0.03 \pm 0.02\,e$), while a small negative charge

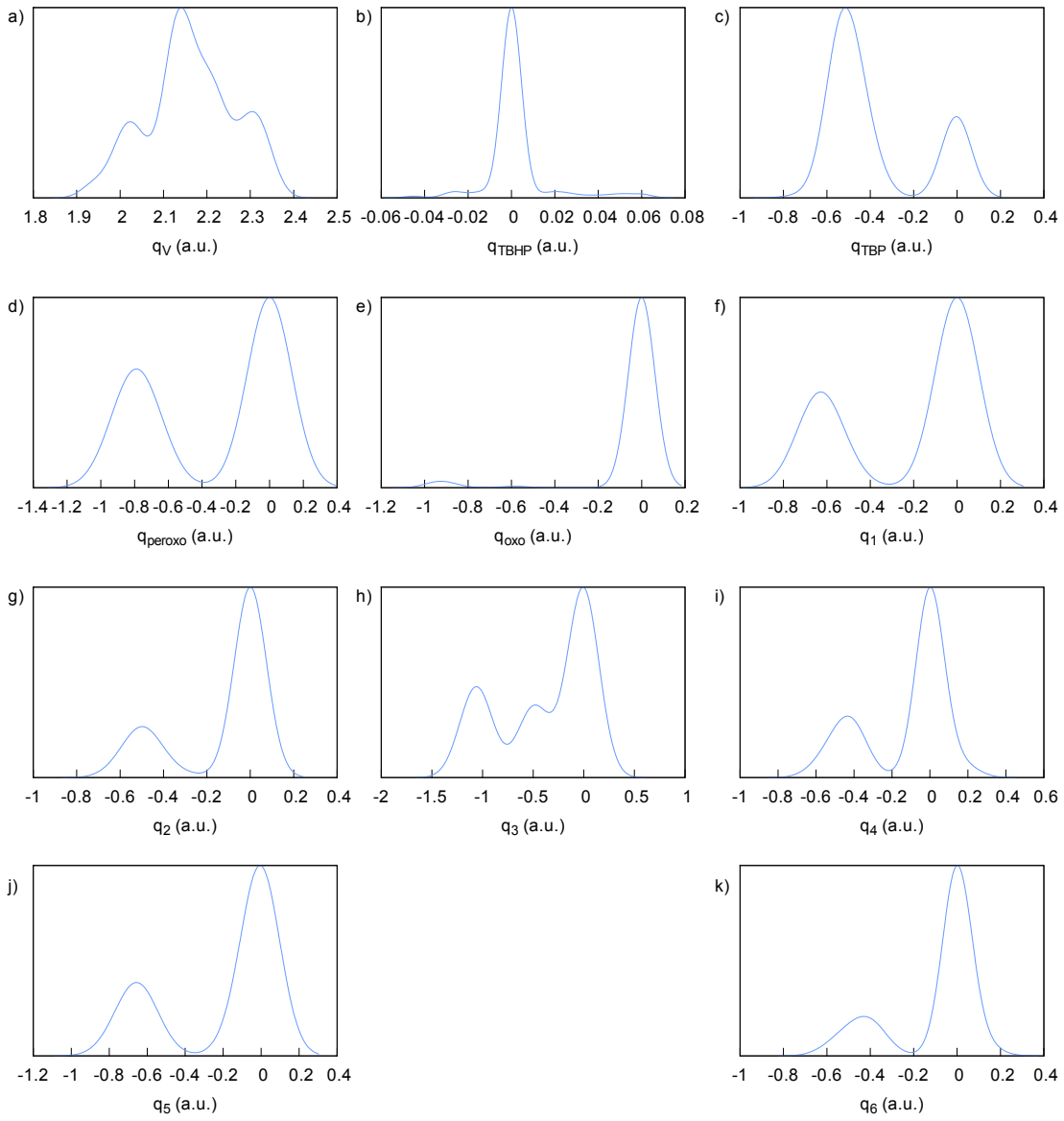

Figure 8.6: Distribution of the AIM charges of vanadium (a) and its ligands: b) TBHP (AC1 and AC4 complexes); c) TBP; d) peroxo (AC8 complexes only); e) oxo; f) acac (**1**); g) Nacac (**2**); h) hydroxo (**3**); i) tert-butyloxo (**4**); j) acetate (**5**), and; k) 3-methyl-but-2-en-1-oxo (**6**).

($-0.022 \pm 0.011\ e$) is observed for all AC1 complexes containing either **1** or **2**. , except AC1-a1-b5, for which a positive charge in the TBHP moiety (0.025 *e*) was calculated. Despite this exception, the fact that TBHP-vanadium (V) complexes present lower activation barriers towards epoxidation may be correlated to an overall positive charge in the TBHP moiety, as suggested by these results.

As shown in Figure 8.6c, the charge of TBP ranges from approximately $-0.6\ e$ to $-0.3\ e$. A few outliers were found, however: the TBP groups in **AC2-a2** and **AC7-a1-b2-c5** bear charges bellow $-0.6\ e$, while a small number of AC7 present charges between $-0.1\ e$ and zero. Although the peak in Figure 8.6c presents two shoulders, the inner structure of this distribution is not easily discernible. AC8 complexes present a peroxo group instead of alkylperoxo, and the distribution of the charges for this group is given in Figure 8.6d. The results show that, with the exception of AC8-a1, the AIM charge of the peroxo ligand is about $-0.92 \pm 0.04\ e$. Within the TBHP, TBP and peroxo moieties, the AIM charges of the two oxygen atoms may provide further information, which shall be discussed later in this work.

When present, the oxo ligand in these complexes attains an average charge of $-0.79 \pm 0.07\ e$, with the most negative charges being recorded for vanadium (IV) complexes. Following the distribution displayed in Figure 8.6e, the effective atomic charge of the oxo group is moderately correlated to that of the vanadium atom to which it is attached (r = 0.7031).

The average effective charge of the acac ligand (**1**, in Figure 8.1b) is $-0.62 \pm 0.04\ e$. This distribution could be narrowed by excluding the AC7 complexes were **1** behaves as a monodentate ligand due to sterical hindrances. The behavior observed in AC7 complexes yields less negative charges for this ligand, causing the shoulders shown in the right hand side of the distribution graph in Figure 8.6f. An interesting aspect concerning the immobilization of $VO(acac)_2$ via Schiff base condensation comes from comparing how the charges of **1** and **2** are distributed, the latter being depicted in Figure 8.6g. An average value of -0.47 ± 0.11 e was observed for the charge of **2**, and the results also show that **2** never attains charges as negative as those found for **1**. Moreover, the charges of **2** spread over a larger range of values, and present the same outliers associated with AC7 compounds.

The charges of the hydroxo ligands (**3**) are distributed in the manner depicted in Figure 8.6h, showing a bimodal distribution. The right hand side population depicted in Figure 8.6h is mostly composed by AC7 complexes (and also **AC8-a3**). Despite this, small negative charges for **3** can also be found in AC3 and AC6 complexes which do not present **1**, **2** or **5**. A similar case may be presented for the *tert*-butyloxo ligand (**4**), with the charge distribution shifted by about 0.4 e relative to that found in the case of ligand **3** as shown in Figure 8.6i. The same bimodal pattern is observed for the distribution of the charge in the acetate ligand (**5**) and 3-methyl-but-2-en-1-oxo (**6**), as shown in Figure 8.6j and Figure 8.6k, respectively. The most interesting aspects about the distribution of

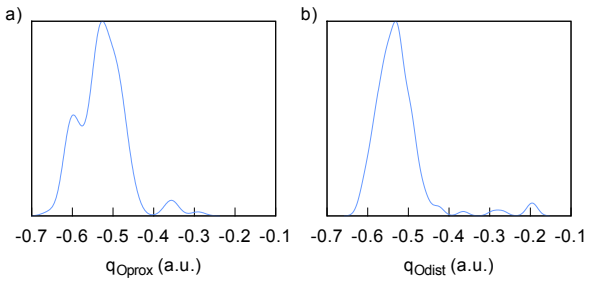

Figure 8.7: Distribution of the AIM charges of the proximal (a) and distal (b) oxygen atoms, relative to the tert-butyl group in TBHP and alkyperoxo complexes.

the effective charges of these four ligands is the fact that alkyloxo ligands **4** and **6** may present positive charges in AC3 and AC6 complexes were group **3** presents a strong negative charge (on average bellow $-0.88\,e$). The same condition is also observed for the cases were ligand **5** presents only a small negative charge. In general, the results suggest that the presence of **3** in the coordination sphere of vanadium has a noticeable impact on the charge distribution across the whole system.

As to the distribution of the charges in the oxygen atoms of TBHP, TBP and peroxo groups, the results for the former two are displayed in Figure 8.7. As for the case of the peroxo group in AC8 complexes, the charge of this group is equally distributed among the two oxygen atoms, each of which attains a distribution with the same characteristics as that found for the whole group (see Figure 8.6d). As shown in Figure 8.7, the charges of the two oxygen atoms in TBHP and TBP present similar distributions, and the two appear to be statistically correlated (r = 0.7540). Despite this, the distribution pattern for the charge of the distal oxygen atom (O_{dist}) appears to be almost featureless compared to that of the proximal oxygen (O_{prox}). These features are due to a small percentage of outliers, with AC7 and AC8 compounds dominating the right hand side of the distribution graphs in Figure 8.7a, while a group of AC1 complexes containing either **3**, **4** or **6** present larger charges for O_{prox}, in magnitude.

By confronting the results from the AIM analysis to those of the DFT calculations one may suggest that the energy barrier the epoxidation reactions may be correlated to some aspects of the electronic structure of the active complexes. A linear regression procedure allowed some light to be shed on this matter. At the beginning of the linear regression procedure, the following independent variables were selected: charge (q) and spin density (s) at the vanadium atom; charges of TBHP, TBP, peroxo, oxo, and ligands **1** to **6**; charge of the proximal and distal oxygen atom at TBHP, TBP or peroxo; electronic density (ρ) and its ellipticity (ϵ) at the BCP of the $V{-}O_{dist}$, $V{-}O_{prox}$ and $O_{dist}{-}O_{prox}$ bonds; and the charge of the C_a atom in the substrate. Atomic units are used to express all variables, save for energy barriers that are expressed in $\mathrm{kJ \cdot mol^{-1}}$. The coefficients obtained from the linear regression analysis and their associated uncertainties are displayed in Table 8.1. The results show a remarkable correlation between the activation energies calcu-

Table 8.1: Coefficients ($\hat{\beta}_X$) obtained from the linear regression procedure, and their respective uncertainties.

Descriptor[a]	$\hat{\beta}_X$		
(intercept)	49.108	±	1.078
q_V	129.551	±	18.315
q_1	–28.184	±	4.894
q_2	–85.296	±	8.475
q_3	–6.034	±	2.771
q_4	–17.543	±	6.634
q_5	–17.362	±	5.081
q_{ODist}	–198.323	±	57.355
q_{OProx}	251.404	±	30.863
$\epsilon(\mathrm{V-O_{Dist}})$	–400.446	±	32.781
$\rho(\mathrm{V-O_{Prox}})$	–270.174	±	49.127
$\epsilon(\mathrm{O_{Prox}-O_{Dist}})$	–1408.140	±	98.868
q_{Ca}	649.390	±	260.733

[a] See text for the definition of the used descriptors.

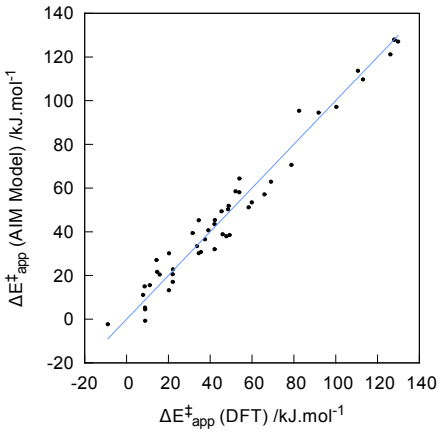

Figure 8.8: Plot of the energy barriers calculated using DFT and those predicted from the linear model, with the identity function plotted, for comparison.

lated using DFT and those predicted from the AIM data, as displayed in Figure 8.8, with an adjusted r^2 of 0.9578.

The remarkable success of the linear regression calls for a physical interpretation of the coefficients in Table 8.1. For the most part, the results suggest that larger charges (in magnitude) at either vanadium or any of its ligands results in a larger activation barrier for the epoxidation reaction, the exception being O_{dist}. At the same time, larger charges (also in magnitude) at C_a translate into smaller activation barriers. It is also important to notice the importance of different parameters concerning the bonding situation between vanadium and the two oxygen atoms in TBHP, TBP or peroxo groups. Deviations from a pure cylindrical symmetry of the $V-O_{dist}$, and $O_{dist}-O_{prox}$ bonds facilitates the epoxidation reaction, as does an increase in the density of the electron density at the BCP of the $V-O_{prox}$ bond. This latter effect is possibly related to the fact that activation energies

for AC1 and AC4 complexes is generally greater than what is observed in the other complexes. Moreover, the results also confirm that the putative inductive effect of coordination of an allylic alcohol to vanadium results in an inactivation, rather than the activation proposed in the past. With this in mind, the regioselective epoxidation of allylic alcohols like geraniol should be better explained by the improved orientation between the epoxidizing and substrate regions of an active complex with ligands similar to **6**.

8.4 Conclusions

In this work the electronic structure of several vanadium complexes was studied using Bader's AIM theory and the parameters retrieved from such calculations were successfully used for predicting the energy barriers involved in the epoxidation of olefins and allylic alcohols. A linear model with 12 descriptors sufficed for predicting the reactivity of the active complexes. The results show that lower energy barriers can be achieved by preventing large charges (in magnitude) at the metal center and on its ligands. Also, larger negative charges on the carbon atom of the substrate that is to from the first C−O bond are associated to lower activation energies in the epoxidation step.

The results in this work provide a new perspective on the reactivity of vanadium alkylperoxo complexes and some of its analogues, by associating properties of the active epoxidizing reagent with the activation energy of the reaction. Because of the rapid increase in the complexity of $VO(acac)_2$ catalyzed epoxidation, the methodology proposed in this work provides a simple framework that can be used for the study of different variants of $VO(acac)_2$/TBHP epoxidations.

Chapter 9

Concluding Remarks

> The known is finite, the unknown infinite; intellectually we stand on an islet in the midst of an illimitable ocean of inexplicability. Our business in every generation is to reclaim a little more land.
>
> T. H. Huxley

In this work different computational methods were used in order to gain some insight on the consequences of anchoring transition metal catalysts onto a supporting material. This was achieved using different models that mimic the chemical environment of the metal center in the immobilized transition metal complexes. Moreover, different computational methodologies (some of which used in previous studies) were examined, allowing the establishment of a solid ground on which further knowledge may be achieved.

The study of Mn(salen) catalysts reported here proved the need for a re-examination of the computational methods used to treat this system. As shown in this work, the use of simplified models for the salen ligand that misrepresent the conjugated π may bear a strong influence on the properties calculated for these compounds. Such differences may not reflect on the ordering of the different spin states, but may translate into different charge and spin distribution across the whole system, leading to erroneous conclusions on the reactivity of these compounds.

By using a proper Mn(salen) model, some insight on the effects of axial coordination to these complexes was gained. Clearly, two different situations emerged from the results. In one hand, axial ligands with an extensive conjugated π system bear similar results as that of the homogeneous-phase catalysts (using chlorine as counter ion). On the other hand, aliphatic amine, amide and alkyloxo ligands behave differently from the homogeneous catalyst. Moreover, the results in this work strongly suggest that the leaching of immobilized Mn(salen) catalysts occurs more favorably when they are in their oxidized form. This result may be of some importance for the development of novel catalysts.

Another important result that emerged from the study of Mn(salen) complexes is the relative stability of the effective atomic charge of the metal center with respect to changes in its coordination sphere, save for the inclusion of the oxo ligand that carries a change in the oxidation state of manganese. This is possible because the salen ligand behaves as a “charge reservoir”, as the results seem to suggest. In the presence of strong donor ligands, salen retains most of its electronic population, whereas the attachment of a weak donor ligand to the manganese atom increases the amount of charge transferred from salen to the metal center. These changes in the electronic population of the salen ligand are most noticeable at the oxygen atoms, as well as on four carbon atoms and may affect the electrostatic potential felt by an approaching substrate molecule. This model may explain at least part of the differences in chemoselectivity that are observed between immobilized Mn(salen) complexes and their homogeneous counterparts.

With respect to the study of the catalytic cycle of $VO(acac)_2$/TBHP epoxidations, the most relevant result is the possible competition between the allylic alcohol and the linker molecule (the result from Schiff base condensation between acetylacetone and APTES). The results in this work suggest that increasing concentrations of alcohol species in the system may increase the leaching of vanadium complexes. With this results in mind, perhaps better schemes for the epoxidation of allylic alcohols using immobilized derivatives of $VO(acac)_2$ may be designed. To that purpose, a model for the apparent energy barrier of the epoxidation step in this system was developed. Beside its possible predictive value, the model shows that the kinetic properties of systems as complex as $VO(acac)_2$/TBHP may be reasonably approximated by the electronic structure properties of the reactants in each elementary step. This may allow the survey of the reactions involved in further variations of this system, providing valuable insights prior to the use of more elaborate calculations.

Besides, this work does not provide a complete picture of the phenomena involved in the anchoring of transition metal catalysts onto a supporting material. For example, solvent effects are ignored for the most part of this work. Also long range interactions between the transition metal complex and the supporting material as well as the effects of confining the catalyst on the pores of meso, micro or nanostructured materials remain relatively unexplored. These questions may not be answered by DFT calculations, and hybrid QM/MM methods may be required to meet these aims. On the other hand, this work establishes the theoretical grounds on which such surveys should be conducted. In it, important information is ascertained on which parts of the system require a quantum mechanical treatment and which may be correctly approximated using molecular mechanics, for both Mn(salen) and $VO(acac)_2$ systems. Moreover, it provides a simplified reaction scheme for vanadium catalyzed epoxidations that can account for the immobilization of $VO(acac)_2$ *via* Schiff base condensation, the epoxidation of allylic alcohols and the concurrency between the two scenarios. These contributions on top of which novel insights can be gained are, above all else, the most important results reported here.

Bibliography

[1] Hughes, D. L. In *Comprehensive Chirality*; Carreira, E. M.; Yamamoto, H., Eds.; Elsevier: Amsterdam, 2012; pp 1–26.

[2] Song, J.; Frutos, R. P.; Tampone, T.; Senanayake, C. H.; Krishnamurthy, D. In *Comprehensive Chirality*; Carreira, E. M.; Yamamoto, H., Eds.; Elsevier: Amsterdam, 2012; pp 46–72.

[3] Clark, J. H. *Green Chem.* **1999**, *1*, 1–8.

[4] Anastas, P. T.; Zimmerman, J. B. *Environ. Sci. Technol.* **2003**, *37*, 94A–101A.

[5] Anastas, P. T.; Kirchhoff, M. M. *Acc. Chem. Res.* **2002**, *35*, 686–694.

[6] Poliakoff, M.; Fitzpatrick, J. M.; Farren, T. R.; Anastas, P. T. *Science* **2002**, *297*, 807–810.

[7] Horváth, I. T.; Anastas, P. T. *Chem. Rev.* **2007**, *107*, 2169–2173.

[8] Anastas, P. T.; Kirchhoff, M. M.; Williamson, T. C. *Appl. Catal., A* **2001**, *221*, 3–13.

[9] Choudary, B. M.; Kantam, M. L.; Santhi, P. L. *Catal. Today* **2000**, *57*, 17–32.

[10] Gron, L. U. In *Green Chemistry Education*, 1st ed.; Anastas, P. T.; et al., Eds.; ACS Symposium Series; American Chemical Society, 2009.

[11] Gunanathan, C.; Milstein, D. *Acc. Chem. Res.* **2011**, *44*, 588–602.

[12] Noyori, R. *Chem. Commun.* **2005**, *2005*, 1807–1811.

[13] Sheldon, R. A. *J. Mol. Catal. A: Chem.* **1996**, *107*, 75–83.

[14] Arnaud, P. *Curso de Química Orgânica*, 1st ed.; Dinalivro, 1978.

[15] Pine, S. H. *Organic Chemistry*, 5th ed.; McGraw-Hill, 1987.

[16] Molander, G. A.; Mautner, K. *Pure Appl. Chem.* **1990**, *62*, 707–712.

[17] Padwa, A.; Murphree, S. S. *ARKIVOC* **2006**, *3*, 6–33.

[18] Bach, R. D.; Canepa, C.; Winter, J. E.; Blanchette, P. E. *J. Org. Chem.* **1997**, *62*, 5191–5197.

[19] Kim, C.; Traylor, T. G.; Perrin, C. L. *J. Am. Chem. Soc.* **1998**, *120*, 9513–9516.

[20] Yang, D. *Acc. Chem. Res.* **2004**, *37*, 497–505.

[21] Miaskiewicz, K.; Smith, D. A. *J. Am. Chem. Soc.* **1998**, *120*, 1872–1875.

[22] Baumstark, A. L.; Franklin, P. J.; Vasquez, P. C.; Crow, B. S. *Molecules* **2004**, *9*, 117–124.

[23] Page, P. C. B.; Buckley, B. R.; Blacker, A. J. *Org. Lett.* **2004**, *6*, 1543–1546.

[24] Page, P. C. B.; Barros, D.; Buckley, B. R.; Ardakani, A.; Marples, B. A. *J. Org. Chem.* **2004**, *69*, 3595–3597.

[25] Murray, R. W.; Jeyaraman, R. *J. Org. Chem.* **1985**, *50*, 2847–2853.

[26] Curci, R.; Fiorentino, M.; Troisi, L.; Edwards, J. O.; Pater, R. H. *J. Org. Chem.* **1980**, *45*, 4758–4760.

[27] Denmark, S. E.; Wu, Z. *J. Org. Chem.* **1998**, *63*, 2810–2811.

[28] Bach, R. D.; Wolber, G. J. *J. Am. Chem. Soc.* **1984**, *106*, 1410–1415.

[29] Sobczak, J.; Ziółkowski, J. J. *J. Mol. Catal.* **1981**, *13*, 11–42.

[30] Lane, B. S.; Burgess, K. *Chem. Rev.* **2003**, *103*, 2457–2474.

[31] Ligtenbarg, A. G. J.; Hage, R.; Feringa, B. L. *Coord. Chem. Rev.* **2003**, *237*, 89–101.

[32] Mimoun, H. *J. Mol. Catal.* **1980**, *7*, 1–29.

[33] Mimoun, H.; de Roch, I. S.; Sajus, L. *Tetrahedron* **1970**, *26*, 37–50.

[34] Talsi, E. P.; Chinakov, V. D.; Babenko, V. P.; Sidelnikov, V. N.; Zamaraev, K. I. *J. Mol. Catal.* **1993**, *81*, 215–233.

[35] Liu, Y.; Murata, K.; Inaba, M. *Chem. Commun.* **2004**, *2004*, 582–583.

[36] McGarrigle, E. M.; Gilheany, D. G. *Chem. Rev.* **2005**, *105*, 1563–1602.

[37] Sono, M.; Roach, M. P.; Coulter, E. D.; Dawson, J. H. *Chem. Rev.* **1996**, *96*, 2841–2888.

[38] Nam, W.; Oh, S.; Sun, Y. J.; Kim, J.; Kim, W.; Woo, S. K.; Shin, W. *J. Org. Chem.* **2003**, *68*, 7903–7906.

[39] Paula, R. D.; Simões, M. M. Q.; Neves, M. G. P. M. S.; Cavaleiro, J. A. S. *Catal. Commun.* **2008**, *10*, 57–60.

[40] Zakavi, S.; Abasi, A.; Pourali, A. R.; Rayati, S. *Bull. Korean Chem. Soc.* **2008**, *29*, 866–868.

[41] Singh, A.; Agarwala, A.; Kamaraj, K.; Bandyopadhyay, D. *Inorg. Chim. Acta* **2011**, *372*, 295–303.

[42] Sharpless, K. B.; Townsend, J. M.; Williams, D. R. *J. Am. Chem. Soc.* **1972**, *94*, 295–296.

[43] Bradley, L. M.; Springer, J. W.; Delate, G. M.; Goodman, A. *J. Chem. Educ.* **1997**, *74*, 1336–1338.

[44] Chong, A. O.; Sharpless, K. B. *J. Org. Chem.* **1977**, *42*, 1587–1590.

[45] Clerici, M. G.; Bellussi, G.; Romano, U. *J. Catal.* **1991**, *129*, 159–167.

[46] Cativiela, C.; Figueras, F.; Fraile, J. M.; García, J.; Mayoral, J. A. *Tetrahedron Lett.* **1995**, *36*, 4125–4128.

[47] Gascon, J.; Corma, A.; Kapteijn, F.; Llabrés i Xamena, F. X. *ACS Catal.* **2014**, *4*, 361–378.

[48] Corma, A.; García, H.; Llabrés i Xamena, F. X. *Chem. Rev.* **2010**, *110*, 4606–4655.

[49] Choi, J. S.; Kim, D. J.; Chang, S. H.; Ahn, W. S. *Appl. Catal., A* **2003**, *254*, 225–237.

[50] Freire, C.; Pereira, C.; Rebelo, S. In *Catalysis: Volume 24*; The Royal Society of Chemistry, 2012; Vol. 24, pp 116–203.

[51] Astruc, D.; Lu, F.; Aranzaes, J. R. *Angew. Chem. Int. Ed.* **2005**, *44*, 7852–7872.

[52] Roy, S.; Pericas, M. A. *Org. Biomol. Chem.* **2009**, *7*, 2669–2677.

[53] Polshettiwar, V.; Varma, R. S. *Green Chem.* **2010**, *12*, 743–754.

[54] Schötz, A.; Reiser, O.; Stark, W. *Chem. Eur. J.* **2010**, *16*, 8950–8967.

[55] Chefson, A.; Auclair, K. *Mol. BioSyst.* **2006**, *2*, 462–469.

[56] Guilmet, E.; Meunier, B. *Tetrahedron Lett.* **1980**, *21*, 4449–4450.

[57] Groves, J. T.; Memo, T. E. *J. Am. Chem. Soc.* **1983**, *105*, 5786–5791.

[58] Meunier, B.; Guilmet, E.; Carvalho, M. E. D.; Poilblanc, R. *J. Am. Chem. Soc.* **1984**, *106*, 6668–6676.

[59] Groves, J. T.; Myers, R. S. *J. Am. Chem. Soc.* **1983**, *105*, 5791–5796.

[60] Adam, W.; Stegmann, V. R.; Saha-Möller, C. R. *J. Am. Chem. Soc.* **1999**, *121*, 1879–1882.

[61] Chan, W.; Liu, P.; Yu, W.; Wong, M.; Che, C. *Org. Lett.* **2004**, *6*, 1597–1599.

[62] Katsuki, T. *J. Mol. Catal. A: Chem.* **1996**, *113*, 87–107.

[63] Dalton, C. T.; Ryan, K. M.; Wall, V. M.; Bousquet, C.; Gilheany, D. G. *Top. Catal.* **1998**, *5*, 75–91.

[64] Samsel, E. G.; Srinivasan, K.; Kochi, J. K. *J. Am. Chem. Soc.* **1985**, *107*, 7606–7617.

[65] Srinivasan, K.; Michaud, P.; Kochi, J. K. *J. Am. Chem. Soc.* **1986**, *108*, 2309–2320.

[66] Yoon, H.; Burrows, C. J. *J. Am. Chem. Soc.* **1988**, *110*, 4087–4089.

[67] Pietikäinen, P.; Ph.D. thesis; University of Helsinki; 2001.

[68] Kim, G.; Kim, S. J.; Lee, H. S.; Park, D.; *Chiral polymeric salen catalyst, and a process for preparing chiral compounds from racemic epoxides by using them*; US6903043 B2; 2005; US Patent. `https://www.google.com/patents/US6903043B2`.

[69] Jacobsen, E. N.; Zhang, W.; *Chiral catalysts and epoxidation reactions catalyzed thereby*; EP0521099 B1; Dec 29, 1997; European Patent.

[70] Abashkin, Y. G.; Burt, S. K. *Inorg. Chem.* **2005**, *44*, 1425–1432.

[71] Bermejo, M. R.; Fernández, M. I.; González-Noya, A. M.; Manero, M.; Pedrido, R.; Rodríguez, M. J.; García-Monteagudo, J. C.; Donnadieu, B. *J. Inorg. Biochem.* **2006**, *100*, 1470–1478.

[72] Meftah, S.; Sajadimajd, S.; Yazdanparast, R. *Drug Chem. Toxicol.* **2013**, *36*, 9–18.

[73] Rosenthal, R. A.; Fish, B.; Hill, R. P.; Huffman, K. D.; Lazarova, Z.; Mahmood, J.; Medhora, M.; Molthen, R.; Moulder, J. E.; Sonis, S. T.; Tofilon, P. J.; Doctrow, S. R. *Anticancer Agents Med. Chem.* **2011**, *11*, 359–372.

[74] Zhang, W.; Loebach, J. L.; Wilson, S. R.; Jacobsen, E. N. *J. Am. Chem. Soc.* **1990**, *112*, 2801–2803.

[75] Zhang, W.; Jacobsen, E. N. *J. Org. Chem.* **1991**, *56*, 2296–2298.

[76] Deng, L.; Jacobsen, E. N. *J. Org. Chem.* **1992**, *57*, 4320–4323.

[77] Palucki, M.; Pospisil, P. J.; Zhang, W.; Jacobsen, E. N. *J. Am. Chem. Soc.* **1994**, *116*, 9333–9334.

[78] Sasaki, H.; Irie, R.; Hamada, T.; Suzuki, K.; Katsuki, T. *Tetrahedron* **1994**, *50*, 11827–11838.

[79] Guedes, D. F. C.; Leod, T. C. O. M.; Gotardo, M. C. A. F.; Schiavon, M. A.; Yoshida, I. V. P.; Ciuffi, K. J.; Assis, M. D. *Appl. Catal., A* **2005**, *296*, 120–127.

[80] Rebelo, S. L. H.; Pereira, M. M.; Simões, M. M. Q.; Neves, M. G. P. M. S.; Cavaleiro, J. A. S. *J. Catal.* **2005**, *234*, 76–87.

[81] Rocha, M.; Rebelo, S. L. H.; Freire, C. *Appl. Catal., A* **2013**, *460*, 116–123.

[82] Palucki, M.; Finney, N. S.; Pospisil, P. J.; Güler, M. L.; Ishida, T.; Jacobsen, E. N. *J. Am. Chem. Soc.* **1998**, *120*, 948–954.

[83] Adam, W.; Roschmann, K. J.; Saha-Möller, C. R. *Eur. J. Org. Chem.* **2000**, *2000*, 3519–3521.

[84] Miura, K.; Katsuki, T. *Synlett* **1999**, *6*, 783–785.

[85] Xia, Q.-H.; Ge, H.-Q.; Ye, C.-P.; Liu, Z.-M.; Su, K.-X. *Chem. Rev.* **2005**, *105*, 1603–1662.

[86] Baleizão, C.; Garcia, H. *Chem. Rev.* **2006**, *106*, 3987–4043; PMID: 16967927.

[87] Salavati-Niasari, M. *Microporous Mesoporous Mater.* **2006**, *95*, 248 – 256.

[88] Das, P.; Kuzniarska-Biernacka, I.; Silva, A. R.; Carvalho, A. P.; Pires, J.; Freire, C. *J. Mol. Catal. A: Chem.* **2006**, *248*, 135–143.

[89] Kuzniarska-Biernacka, I.; Silva, A. R.; Carvalho, A. P.; Pires, J.; Freire, C. *J. Mol. Catal. A: Chem.* **2007**, *278*, 82–91.

[90] Silva, A. R.; Wilson, K.; Clark, J. H.; Freire, C. *Microporous Mesoporous Mater.* **2006**, *91*, 128–138.

[91] Leod, T. C. O. M.; Kirillova, M. V.; Pombeiro, A. J. L.; Schiavon, M. A.; Assis, M. D. *Appl. Catal., A* **2010**, *372*, 191–198.

[92] Gaspar, H.; Andrade, M.; Pereira, C.; Pereira, A. M.; Rebelo, S. L. H.; Araujo, J. P.; Pires, J.; Carvalho, A. P.; Freire, C. *Catal. Today* **2013**, *203*, 103–110.

[93] Maia, F.; Silva, R.; Jarrais, B.; Silva, A. R.; Freire, C.; Pereira, M. F. R.; Figueiredo, J. L. *J. Colloid Interface Sci.* **2008**, *328*, 314–323.

[94] Das, P.; Silva, A. R.; Carvalho, A. P.; Pires, J.; Freire, C. *Catal. Lett.* **2009**, *129*, 367–375.

[95] Jia, Z.; Fu, X.; Lu, Y.; Zhang, H.; Huang, X.; Wu, H. *J. Inorg. Organomet. Polym.* **2012**, *22*, 415–422.

[96] Wei, S.; Tang, Y.; Xu, X.; Xu, G.; Yu, Y.; Sun, Y.; Zheng, Y. *Appl. Organometal. Chem.* **2010**, *25*, 146–153.

[97] Climent, M. J.; Corma, A.; Iborra, S. *Chem. Rev.* **2011**, *111*, 1072–1133.

[98] Corma, A.; Iborra, S.; Velty, A. *Chem. Rev.* **2007**, *107*, 2411–2502.

[99] von Lilienfeld, O. A. *Int. J. Quantum Chem.* **2013**, *113*, 1676–1689.

[100] Collman, J. P.; Brauman, J. I.; Hampton, P. D.; Tanaka, H.; Bohle, D. S.; Hembre, R. T. *J. Am. Chem. Soc.* **1990**, *112*, 7980–7984.

[101] Collman, J. P.; Brauman, J. I.; Meunier, B.; Raybuck, S. A.; Kodadek, T. *Proc. Natl. Acad. Sci. U.S.A.* **1984**, *81*, 3245–3248.

[102] Collman, J. P.; Kodadek, T.; Raybuck, S. A.; Meunier, B. *Proc. Natl. Acad. Sci. U.S.A.* **1983**, *80*, 7039–7041.

[103] Collman, J. P.; Zhang, X.; Lee, V. J.; Uffelman, E. S.; Brauman, J. I. *Science* **1993**, *261*, 1404–1411.

[104] Groves, J. T.; Memo, T. E.; Myers, R. S. *J. Am. Chem. Soc.* **1979**, *101*, 1032–1033.

[105] de Visser, S. P.; Ogliaro, F.; Sharma, P. K.; Shaik, S. *J. Am. Chem. Soc.* **2002**, *124*, 11809–11826.

[106] Feichtinger, D.; Plattner, D. A. *Angew. Chem. Int. Ed. Engl.* **1997**, *36*, 1718–1719.

[107] Finney, N. S.; Pospisil, P. J.; Chang, S.; Palucki, M.; Konsler, R. G.; Hansen, K. B.; Jacobsen, E. N. *Angew. Chem. Int. Ed. Engl.* **1997**, *36*, 1720–1723.

[108] Pospisil, P. J.; Carsten, D. H.; Jacobsen, E. N. *Chem. Eur. J.* **1996**, *2*, 974–980.

[109] Sejr Jepsen, A.; Roberson, M.; G. Hazell, R. *Chem. Commun.* **1998**, *1998*, 1599–1600.

[110] Norrby, P.-O.; Linde, C.; Aakermark, B. *J. Am. Chem. Soc.* **1995**, *117*, 11035–11036.

[111] Linde, C.; Arnold, M.; Åkermark, B.; Norrby, P.-O. *Angew. Chem. Int. Ed. Engl.* **1997**, *36*, 1723–1725.

[112] Kürti, L.; Blewett, M. M.; Corey, E. J. *Org. Lett.* **2009**, *11*, 4592–4595.

[113] Bryliakov, K. P.; Babushkin, D. E.; Talsi, E. P. *Mendeleev Commun.* **1999**, *9*, 29 – 31.

[114] Campbell, K. A.; Lashley, M. R.; Wyatt, J. K.; Nantz, M. H.; Britt, R. D. *J. Amer. Chem. Soc.* **2001**, *123*, 5710–5719; PMID: 11403603.

[115] Abashkin, Y. G.; Collins, J. R.; Burt, S. K. *Inorg. Chem.* **2001**, *40*, 4040–4048.

[116] Ivanic, J.; Collins, J. R.; Burt, S. K. *J. Phys. Chem. A* **2004**, *108*, 2314–2323.

[117] Sears, J. S.; Sherrill, C. D. *J. Chem. Phys.* **2006**, *124*, 144314.

[118] Sears, J. S.; Sherrill, C. D. *J. Phys. Chem. A* **2008**, *112*, 6741–6752.

[119] Takatani, T.; Sears, J. S.; Sherrill, C. D. *J. Phys. Chem. A* **2009**, *113*, 9231–9236.

[120] Takatani, T.; Sears, J. S.; Sherrill, C. D. *J. Phys. Chem. A* **2010**, *114*, 11714–11718.

[121] Linde, C.; Akermark, B.; Norrby, P.; Svensson, M. *J. Am. Chem. Soc.* **1999**, *121*, 5083–5084.

[122] Jacobsen, H.; Cavallo, L. *Chem. Eur. J.* **2001**, *8*, 800–807.

[123] Cavallo, L.; Jacobsen, H. *J. Org. Chem.* **2003**, *68*, 6202–6207.

[124] Khavrutskii, I. V.; Musaev, D. G.; Morokuma, K. *Proc. Natl. Acad. Sci. U.S.A.* **2004**, *101*, 5743–5748.

[125] Abashkin, Y. G.; Burt, S. K. *Org. Lett.* **2004**, *6*, 59–62.

[126] Malek, K.; Jansen, A. P. J.; Li, C.; van Santen, R. A. *J. Catal.* **2007**, *246*, 127–135.

[127] Khavrutskii, I. V.; Musaev, D. G.; Morokuma, K. *Inorg. Chem.* **2003**, *42*, 2606–2621.

[128] Becke, A. D. *Phys. Rev. A* **1988**, *38*, 3098–3100.

[129] Perdew, J. P.; Yue, W. *Phys. Rev. B* **1986**, *33*, 8800–8802.

[130] Becke, A. D. *J. Chem. Phys.* **1993**, *98*, 1372–1377.

[131] Neese, F. *Coord. Chem. Rev.* **2009**, *253*, 526–563.

[132] Cavallo, L.; Jacobsen, H. *J. Phys. Chem. A* **2003**, *107*, 5466–5471.

[133] Cavallo, L.; Jacobsen, H. *Angew. Chem. Int. Ed.* **2000**, *39*, 589–592.

[134] Cavallo, L.; Jacobsen, H. *Eur. J. Inorg. Chem.* **2003**, *2003*, 892–902.

[135] Cavallo, L.; Jacobsen, H. *Inorg. Chem.* **2004**, *43*, 2175–2182.

[136] Jacobsen, H.; Cavallo, L. *Phys. Chem. Chem. Phys.* **2004**, *6*, 3747–3753.

[137] Jacobsen, H.; Cavallo, L. *Organometalics* **2006**, *25*, 177–183.

[138] Reiher, M.; Salomon, O.; Artur Hess, B. *Theor. Chem. Acc.* **2001**, *107*, 48–55.

[139] Salomon, O.; Reiher, M.; Hess, B. A. *J. Chem. Phys.* **2002**, *117*, 4729–4737.

[140] Malek, K.; Li, C.; van Santen, R. A. *J. Mol. Catal. A: Chem.* **2007**, *271*, 98–104.

[141] Zabrodsky, H.; Peleg, S.; Avnir, D. *J. Am. Chem. Soc.* **1992**, *114*, 7843–7851.

[142] Zabrodsky, H.; Peleg, S.; Avnir, D. *J. Am. Chem. Soc.* **1993**, *115*, 8278–8289.

[143] Zabrodsky, H.; Avnir, D. *J. Am. Chem. Soc.* **1995**, *117*, 462–473.

[144] Chen, W.; Viljjoen, A. M. *S. Afr. J. Bot.* **2010**, *76*, 643–651.

[145] Kollar, J.; *Epoxidation process*; US3351635 A; 1967; US Patent. `https://www.google.com/patents/US3351635`.

[146] Amin, S. S.; Cryer, K.; Zhang, B.; Dutta, S. K.; Eaton, S. S.; Anderson, O. P.; Miller, S. M.; Reul, B. A.; Brichard, S. M.; Crans, D. C. *Inorg. Chem.* **2000**, *39*, 406–416.

[147] Raj, N. K. K.; Ramaswamy, A. V.; Manikandan, P. *J. Mol. Catal. A: Chem.* **2005**, *227*, 37–45.

[148] Éll, A. H.; Jonsson, S. Y.; Borje, A.; Adolfsson, H.; Backvall, J.-E. *Tetrahedron Lett.* **2001**, *42*, 2569–2571.

[149] Raghavan, S.; Rajender, A.; Joseph, S. C.; Rasheed, M. A. *Synth. Commun.* **2001**, *31*, 1477–1480.

[150] Sharpless, K. B.; Michaelson, R. C. *J. Am. Chem. Soc.* **1973**, *95*, 6136–6137.

[151] Michaelson, R. C.; Palermo, R. E.; Sharpless, K. B. *J. Am. Chem. Soc.* **1977**, *99*, 1990–1992.

[152] Bryliakov, K. P.; Talsi, E. P.; Stasko, S. N.; Kholdeeva, O. A.; Popov, S. A.; Tkachev, A. V. *J. Mol. Catal. A: Chem.* **2003**, *194*, 79–88.

[153] Bryliakov, K. P.; Talsi, E. P.; Kühn, T.; Bolm, C. *New J. Chem.* **2003**, *27*, 609–614.

[154] Leus, K.; Muylaert, I.; Vandichel, M.; Marin, G. B.; Waroquier, M.; Van Speybroeck, V.; Van Der Voort, P. *Chem. Commun.* **2010**, *46*, 5085–5087.

[155] der Voort, P. V.; Possemiers, K.; Vansant, E. F. *J. Chem. Soc., Faraday Trans.* **1996**, *92*, 845–848.

[156] Baltes, M.; der Voort, P. V.; Weckhuysen, B. M.; Rao, R. R.; Catana, G.; Schoonheydt, R. A.; Vansant, E. F. *Phys. Chem. Chem. Phys.* **2000**, *2*, 2673–2680.

[157] Baltes, M.; Cassiers, K.; der Voort, P. V.; Weckhuysen, B. M.; Schoonheydt, R. A.; Vansant, E. F. *J. Catal.* **2001**, *197*, 160–171.

[158] Kumar, A., Jr; Das, S. K.; Kumar, A. *J. Catal.* **1997**, *166*, 108–110.

[159] Maurya, M. R.; Arya, A.; Kumar, A.; Pessoa, J. C. *J. Chem. Soc., Dalton Trans.* **2009**, *2009*, 2185–2195.

[160] Maurya, M. R.; Kumar, M.; Kumar, A.; Pessoa, J. C. *J. Chem. Soc., Dalton Trans.* **2008**, *2008*, 4220–4232.

[161] Jarrais, B.; Pereira, C.; Silva, A. R.; Carvalhal, A. P.; Pires, J.; Freire, C. *Polyhedron* **2009**, *28*, 994–1000.

[162] Jarrais, B.; Silva, A. R.; Freire, C. *Eur. J. Inorg. Chem.* **2005**, *2005*, 4582–4589.

[163] Pereira, C.; Silva, A. R.; Carvalho, A. P.; Pires, J.; Freire, C. *J. Mol. Catal. A: Chem.* **2008**, *283*, 5–14.

[164] Anand, N.; Reddy, K. H. P.; Rao, K. S. R.; Burri, D. R. *Catal. Lett.* **2011**, *141*, 1355–1363.

[165] Vandichel, M.; Leus, K.; der Voort, P. V.; Waroquier, M.; Speybroeck, V. V. *J. Catal.* **2012**, *294*, 1–18.

[166] Stepovik, L. P.; Gulenova, M. V. *Russ. J. Gen. Chem.* **2009**, *79*, 1663–1670.

[167] Stepovik, L. P.; Gulenova, M. V.; Kalacheva, I. A.; Potkina, A. Y. *Russ. J. Gen. Chem.* **2011**, *81*, 550–558.

[168] Talsi, E. P.; Chinakov, V. D.; Babenko, V. P.; Zamaraev, K. I. *React. Kinet. Catal. Lett.* **1991**, *44*, 257–263.

[169] Talsi, E. P.; Chinakov, V. D.; Babenko, V. P.; Zamaraev, K. I. *J. Mol. Catal.* **1993**, *81*, 235–254.

[170] Babushkin, D. E.; Talsi, E. P. *React. Kinet. Catal. Lett.* **2000**, *71*, 115–120.

[171] Bryliakov, K. P.; Talsi, E. P. *Kinet. Catal.* **2003**, *44*, 334–346.

[172] Itoh, T.; Jitsukawa, K.; Kaneda, K.; Teranoshi, S. *J. Am. Chem. Soc.* **1979**, *101*, 159–169.

[173] Butler, A.; Clague, M. J.; Meister, G. E. *Chem. Rev.* **1994**, *94*, 625–638.

[174] Awasthy, A. K.; Rocek, J. *J. Am. Chem. Soc.* **1969**, *91*, 991–996.

[175] Correia, I.; Pessoa, J. C.; Duarte, M. T.; Henriques, R. T.; Piedade, M. F. M.; Veiros, L. F.; Jakusch, T.; Kiss, T.; Dörnyei, A.; Castro, M. M. C. A.; Geraldes, C. F. G. C.; Avecilla, F. *Chem. Eur. J.* **2004**, *10*, 2301–2317.

[176] Pessoa, J. C.; Marcão, S.; Correia, I.; Gonçalves, G.; Dörnyei, A.; Kiss, T.; Jakusch, T.; Tomaz, I.; Castro, M. M. C. A.; Geraldes, C. F. G. C.; Avecilla, F. *Eur. J. Inorg. Chem.* **2006**, *2006*, 3595–3606.

[177] Adão, P.; Pessoa, J. C.; Henriques, R. T.; Kuznetov, M. L.; Avecilla, F.; Maurya, M. R.; Kumar, U.; Correia, I. *Inorg. Chem.* **2009**, *48*, 3542–3561.

[178] Kuznetov, M. L.; Pessoa, J. C. *J. Chem. Soc., Dalton Trans.* **2009**, *2009*, 5460–5468.

[179] Feynman, R. P. *Six Not-So-Easy Pieces*, 1st ed.; Penguin Books, 1999.

[180] Bohr, N. *Sobre a Constituíção de Átomos e Moléculas*, 3rd ed.; Textos Fundamentais da Física Moderna; Fundação Calouste Gulbenkian, 1989.

[181] Schrödinger, E. *Phys. Rev.* **1926**, *28*, 1049–1070.

[182] Jensen, F. *Introduction to Computational Chemistry*, 2nd ed.; John Wiley & Sons Ltd: Chichester, England, 2007.

[183] Cramer, C. J. *Essentials of Computational Chemistry*, 2nd ed.; John Wiley & Sons Ltd: Chichester, UK, 2002.

[184] Slater, J. C. *Phys. Rev.* **1929**, *35*, 210–211.

[185] Dias, J. J. C. T. *Química Quântica: Princípios e Aplicações*, 1st ed.; Fundação Calouste Gulbenkian, 1982.

[186] Szabo, A.; Ostlund, N. S. *Modern Quantum Chemistry Introduction to Advanced Electronic Structure Theory*; Dover Publications, Inc.: New York, 1996.

[187] Davidson, E. R.; Feller, D. *Chem. Rev.* **1986**, *86*, 681–696.

[188] Jolly, W. L. *Modern Inorganic Chemistry*, 2nd ed.; McGraw-Hill, 1991.

[189] Simons, J. *An Introduction to Theoretical Chemistry*, 2nd ed.; Cambridge University Press: Cambridge, UK, 2003.

[190] Simons, J.; Nichols, J. *Quantum Mechanics in Chemistry*, 1st ed.; Oxford University Press, 1997.

[191] Hartree, D. R. *Proc. Cambridge Philos. Soc.* **1928**, *24*, 89–110.

[192] Hartree, D. R. *Proc. Cambridge Philos. Soc.* **1928**, *24*, 111–132.

[193] Slater, J. C. *Phys. Rev.* **1951**, *81*, 385–390.

[194] Roothaan, C. C. J. *Rev. Mod. Phys.* **1960**, *32*, 172–185.

[195] Page, T. R.; Boots, C. A.; Freitag, M. A. *J. Chem. Educ.* **2008**, *85*, 159.

[196] Young, D. C. *Computational Chemistry: A Practical Guide for Applying Techniques to Real-World Problems*; John Wiley and Sons, Inc.: New York, 2001.

[197] Tsuchimochi, T.; Scuseria, G. E. *J. Chem. Phys.* **2010**, *133*, 141102.

[198] Davidson, E. R.; Plakhutin, B. N. *J. Chem. Phys.* **2010**, *132*, 184110.

[199] Pople, J. A.; Nesbet, R. K. *J. Chem. Phys.* **1954**, *22*, 571–572.

[200] Schmidt, M. W.; Gordon, M. S. *Ann. Rev. Phys. Chem.* **1998**, *49*, 233–266.

[201] Hill, J. G. *Int. J. Quantum Chem.* **2013**, *113*, 21–34.

[202] Argaman, N.; Makov, G.; *Density Functional Theory — an introduction*; http://arXiv.org/abs/physics/9806013v2; 1999.

[203] Hohenberg, P.; Kohn, W. *Phys. Rev.* **1964**, *136*, B864–B871.

[204] Kohn, W.; Sham, L. J. *Phys. Rev.* **1965**, *140*, A1133.

[205] von Barth, U.; Hedin, L. *J. Phys. C: Solid State Phys.* **1972**, *5*, 1629–1642.

[206] Vosko, S. H.; Wilk, L.; Nusair, M. *Can. J. Phys.* **1980**, *58*, 1200–1211.

[207] Ceperley, D. M.; Alder, B. J. *Phys. Rev. Lett.* **1980**, *45*, 566–569.

[208] Perdew, J. P.; Wang, Y. *Phys. Rev. B* **1992**, *45*, 13244–13249.

[209] Lee, C.; Yang, W.; Parr, R. G. *Phys. Rev. B* **1988**, *37*, 785–789.

[210] Tao, J.; Perdew, J. P.; Staroverov, V. N.; Scuseria, G. E. *Phys. Rev. Lett.* **2003**, *91*, 146401–146405.

[211] Zhao, Y.; Truhlar, D. G. *Theor. Chem. Acc.* **2008**, *120*, 215–241.

[212] Xu, X.; Goddard III, W. A. *Proc. Natl. Acad. Sci. U.S.A.* **2004**, *101*, 2673–2677.

[213] Xu, X.; Zhang, Q.; Muller, R. P.; Goddard III, W. A. *J. Chem. Phys.* **2005**, *122*, 014105.

[214] Gritsenko, O.; Schippen, P. R. T.; Baerends, E. J. *J. Chem. Phys.* **1997**, *107*, 5007–5015.

[215] Su, J. T.; Xu, X.; Goddard III, W. A. *J. Phys. Chem. A* **2004**, *108*, 10518–10526.

[216] Grimme, S. *J. Chem. Phys.* **2006**, *124*, 034108.

[217] Jacob, C. R.; Reiher, M. *Int. J. Quantum Chem.* **2012**, *112*, 3661–3684.

[218] Scherlis, D. A.; Estrin, D. A. *Int. J. Quantum Chem.* **2002**, *87*, 158–166.

[219] Kannemann, F. O.; Becke, A. D. *J. Chem. Theory Comput.* **2009**, *5*, 719–727.

[220] Minenkov, Y.; Occhipinti, G.; Jensen, V. R. *J. Phys. Chem. A* **2009**, *113*, 11833–11844.

[221] Kohn, W. *Rev. Mod. Phys.* **1999**, *71*, 1253–1266.

[222] Pulay, P.; Fogarasi, G.; Pang, F.; Boggs, J. E. *J. Am. Chem. Soc.* **1979**, *101*, 2550–2560.

[223] Schlegel, H. B. *Theor. Chim. Acta* **1984**, *66*, 333–340.

[224] Head-Gordon, M.; Pople, J. A. *J. Phys. Chem.* **1988**, *92*, 3063–3069.

[225] Fischer, T. H.; Almlof, J. *J. Phys. Chem.* **1992**, *96*, 9768–9774.

[226] Fogarasi, G.; Zhou, X.; Taylor, P. W.; Pulay, P. *J. Am. Chem. Soc.* **1992**, *114*, 8191–8201.

[227] Alsberg, B. K.; Jensen, V. R.; Borve, K. J. *J. Comput. Chem.* **1996**, *17*, 1197–1216.

[228] Burger, S. K.; Ayers, P. W. *J. Chem. Theory Comput.* **2010**, *6*, 1490–1497.

[229] Culot, P.; Dive, G.; Nguyen, V. H.; Ghuysen, J. M. *Theor. Chim. Acta* **1992**, *82*, 189–205.

[230] Lindh, R.; Bernhardson, A.; Schutz, M. *Chem. Phys. Lett.* **1999**, *303*, 567–575.

[231] Nye, M. J. *J. Comput. Chem.* **2007**, *28*, 98–108.

[232] Ishida, K.; Morokuma, K.; Komornicki, A. *J. Chem. Phys.* **1977**, *66*, 2153–2156.

[233] Nagase, S.; Morokuma, K. *J. Am. Chem. Soc.* **1978**, *100*, 1666–1672.

[234] Gonzalez, C.; Schlegel, H. B. *J. Chem. Phys.* **1989**, *90*, 2154–2161.

[235] Gonzalez, C.; Schlegel, H. B. *J. Phys. Chem.* **1990**, *94*, 5523–5527.

[236] Gonzalez, C.; Schlegel, H. B. *J. Chem. Phys.* **1991**, *95*, 5853–5860.

[237] Levine, I. N. *Physical Chemistry*, 4th ed.; McGraw-Hill, 1995.

[238] McClurg, R. B.; Flagan, R. C.; Goddard III, W. A. *J. Chem. Phys.* **1997**, *106*, 6675–6680.

[239] Pfaendtner, J.; Yu, X.; Broadbelt, L. J. *Theor. Chem. Acc.* **2007**, *118*, 881–898.

[240] Silva, G. D.; Bozzelli, J. W. *J. Phys. Chem. A* **2007**, *111*, 12026–12036.

[241] Strekalov, M. L. *Chem. Phys.* **2009**, *362*, 75–81.

[242] Scott, A. P.; Radom, L. *J. Phys. Chem.* **1996**, *100*, 16502–16513.

[243] Grev, R. S.; Janssen, C. L.; III, H. F. S. *J. Chem. Phys.* **1991**, *95*, 5128–5132.

[244] McQuarrie, D. A.; Simon, J. D. *Molecular Thermodynamics.*, 1st ed.; University Science Books: Sausalito, Califórnia, 1999.

[245] DeFrees, D. J.; McLean, A. D. *J. Chem. Phys.* **1985**, *82*, 333–341.

[246] Wong, M. W. *Chem. Phys. Lett.* **1996**, *256*, 391–399.

[247] Tantirungrotechai, Y.; Phanasant, K.; Roddecha, S.; Surawatanawong, P.; Sutthikhum, V.; Limtrakul, J. *J. Mol. Struct. THEOCHEM* **2006**, *760*, 189–192.

[248] Irikura, K. K.; III, R. D. J.; Kacker, R. N. *J. Phys. Chem. A* **2005**, *109*, 8430–8437.

[249] Irikura, K. K.; III, R. D. J.; Kacker, R. N.; Kessel, R. *J. Chem. Phys.* **2009**, *130*, 114102.

[250] Martin, F.; Zipse, H. *J. Comput. Chem.* **2005**, *26*, 97–105.

[251] Löwdin, P. *Phys. Rev.* **1955**, *97*, 1474–1489.

[252] Löwdin, P. *Phys. Rev.* **1955**, *97*, 1490–1508.

[253] Davidson, E. R. *Rev. Mod. Phys.* **1972**, *44*, 451–464.

[254] Löwdin, P. *Phys. Rev.* **1955**, *97*, 1509–1520.

[255] Foster, J. P.; Weinhold, F. *J. Amer. Chem. Soc.* **1980**, *102*, 7211–7218.

[256] Reed, A. E.; Curtiss, L. A.; Weinhold, F. *Chem. Rev.* **1988**, *88*, 899–926.

[257] Carpenter, J.; Weinhold, F. *J. Mol. Struct. THEOCHEM* **1988**, *169*, 41–62.

[258] Reed, A. E.; Weinstock, R. B.; Weinhold, F. *J. Chem. Phys.* **1985**, *83*, 735–746.

[259] Weinhold, F.; Landis, C. R. *Chem. Educ. Res. Pract.* **2001**, *2*, 91–104.

[260] Matta, C. F.; Boyd, R. J. *The Quantum Theory of Atoms in Molecules: From Solid State to DNA and Drug Design*; Wiley-VCH, 2007.

[261] Matta, C. F.; Boyd, R. J. In *The Quantum Theory of Atoms in Molecules: From Solid State to DNA and Drug Design*; Matta, C. F.; Boyd, R. J., Eds.; Wiley-VCH, 2007; pp 1–30.

[262] Bader, R. F. W. *Atoms in Molecules: A Quantum Theory*; Oxford University Press: New York, 1990.

[263] Bader, R. F. W. *J. Am. Chem. Soc.* **1979**, *101*, 1389–1395.

[264] Bader, R. F. W.; Nguyen-Dang, T. T.; Tal, Y. *J. Chem. Phys.* **1979**, *70*, 4316–4329.

[265] Bader, R. F. W.; Hernández-Trujillo, J.; Cortés-Guzmán, F. *J. Comput. Chem.* **2007**, *28*, 4–14.

[266] Cremer, D.; Kraka, E. *Croatica Chem. Acta* **1984**, *57*, 1259–1281.

[267] Kraka, E.; Cremer, D. In *Theoretical Models of Chemical Bonding. The Concept of the Chemical Bond*; Maksic, Z. B., Ed.; Springer Verlag: Heidelberg, 1990; Vol. 2, p 453.

[268] Bader, R. F. W. *J. Chem. Phys.* **1980**, *73*, 2871–2883.

[269] Biegler-König, F. W.; Bader, R. F. W.; Tang, T. *J. Comput. Chem.* **1982**, *3*, 317–328.

[270] Meister, J.; Schwarz, W. H. E. *J. Phys. Chem.* **1994**, *98*, 8245–8252.

[271] Lorenzo, L.; Mosquera, R. A. *Chem. Phys. Lett.* **2002**, *356*, 305–312.

[272] Vila, A.; Mosquera, R. A. *J. Phys. Chem. A* **2006**, *110*, 11752–11759.

[273] Cortés-Guzmán, F.; Bader, R. F. W. *Coord. Chem. Rev.* **2005**, *249*, 633–662.

[274] Tiana, D.; Francisco, E.; Blanco, M. A.; Macchi, P.; Sironi, A.; Pendás, A. M. *J. Chem. Theory Comput.* **2010**, *6*, 1064–1074.

[275] Tiana, D.; Francisco, E.; Blanco, M. A.; Macchi, P.; Sironi, A.; Pendás, A. M. *Phys. Chem. Chem. Phys.* **2011**, *13*, 5068–5077.

[276] Karelson, M.; Lobanov, V. S.; Katritzky, A. R. *Chem. Rev.* **1996**, *96*, 1027–1044.

[277] Pinsky, M.; Avnir, D. *Inorg. Chem.* **1998**, *37*, 5575–5582.

[278] Pinsky, M.; Lipkowitz, K. B.; Avnir, D. *J. Math. Chem.* **2001**, *30*, 109–120.

[279] Solomon, Y.; Avnir, D. *J. Comput. Chem.* **1999**, *20*, 772–780.

[280] Alvarez, S. *J. Am. Chem. Soc.* **2003**, *125*, 6795–6802.

[281] Alvarez, S.; Alemany, P.; Avnir, D. *Chem. Soc. Rev.* **2005**, *34*, 313–326.

[282] Ok, K. M.; Halasyamani, P. S.; Casanova, D.; Llunell, M.; Alemany, P.; Alvarez, S. *Chem. Mater.* **2006**, *18*, 3176–3183.

[283] Joanes, D. N.; Gill, C. A. *J. Roy. Stat. Soc. D – Sta.* **1998**, *47*, 183–189.

[284] Kim, T.; White, H.; *On More Robust Estimation of Skewness and Kurtosis: Simulation and Application to the SP500 Index*; Tech. Rep.; Department of Economics, University of California, San Diego; 2003.

[285] Janert, P. K. *Gnuplot in Action: Understanding Data with Graphs*, 1st ed.; Mannig: Shelter Island, 2010.

[286] Kabacoff, R. I. *R in Action: Data Analysis and Graphics with R*, 1st ed.; Mannig: Shelter Island, 2011.

[287] Pinto, J. C. C.; Curto, J. J. D. *Estatística para Economia e Gestão*, 1st ed.; Edições Sílabo, 1999.

[288] Reis, E. *Estatística Multivariada*, 2nd ed.; Edições Sílabo, 2001.

[289] Wold, S.; Esbensen, K.; Geladi, P. *Chemometr. Intell. Lab.* **1987**, *2*, 37–52.

[290] Hotelling, H. *J. Educ. Psycol.* **1933**, *24*, 417–441.

[291] Hotelling, H. *J. Educ. Psycol.* **1933**, *24*, 498–520.

[292] Katritzky, A. R.; Fara, D. C.; Kuanar, M.; Hur, E.; Karelson, M. *J. Phys. Chem. A* **2005**, *109*, 10323–10341.

[293] Heberger, K.; Lopata, A. *J. Org. Chem.* **1998**, *63*, 8646–8653.

[294] Tackley, D. R.; Dentb, G.; Smith, W. E. *Phys. Chem. Chem. Phys.* **2000**, *2*, 3949–3955.

[295] Faget, G.; Felcman, J.; Giannerini, T.; Téllez, C. A. *Spectrochim. Acta, Part A* **2005**, *61*, 2121–2129.

[296] Bu, Y.; Han, K. *J. Phys. Chem. A* **2002**, *106*, 11897–11910.

[297] Illien, B.; Evain, K.; Berthelot, M.; Laurence, C. *J. Phys. Org. Chem.* **2003**, *16*, 608–614.

[298] Pitzer, K. S.; Gwinn, W. D. *J. Chem. Phys.* **1942**, *10*, 428–440.

[299] Pople, J. A.; Schlegel, H. B.; Krishman, R.; DeFress, D. J.; Frisch, J. S.; Whiteside, R. A.; Hout, R. F.; Hehre, W. J. *Int. J. Quantum Chem., Quantum Chem. Symp.* **1981**, *20*, 269–278.

[300] Harris, N. J. *J. Phys. Chem.* **1995**, *99*, 14689–14699.

[301] Finley, J. W.; Stephens, P. J. *J. Mol. Struct. THEOCHEM* **1995**, *357*, 225–235.

[302] Rahut, G.; Pulay, P. *J. Phys. Chem.* **1995**, *99*, 3093–3100.

[303] Peterson, P. E.; Abu-Omar, M.; Johnson, T. W.; Parham, R.; Goldin, D.; III, C. H.; Cook, A.; Dunn, K. M. *J. Phys. Chem.* **1995**, *99*, 5927–5933.

[304] Sinha, P.; Boesch, S. E.; Gu, C.; Wheeler, R. A.; Wilson, A. K. *J. Phys. Chem. A* **2004**, *108*, 9213–9217.

[305] Andersson, M. P.; Uvdal, P. *J. Phys. Chem. A* **2005**, *109*, 2937–2941.

[306] Halls, M. D.; Velkovski, J.; Schlegel, H. B. *Theor. Chem. Acc.* **2001**, *105*, 413–421.

[307] Berezin, K. V.; Nechaev, V. V.; Krivokhizhina, T. V. *Opt. Spectrosc.* **2003**, *94*, 357–360.

[308] Joint Committee for Guides in Metrology; *JCGM 100: Evaluation of Measurement Data - Guide to the Expression of Uncertainty in Measurement*; Tech. Rep.; JCGM; Geneva; 2008.

[309] Linstrom, P.; Mallard, W. *NIST Chemistry WebBook, NIST Standard Reference Database Number 69*; National Institute of Standards and Technology: Gaithersburg MD, 20899, 2009.

[310] Shimanouchi, T. *Tables of Molecular Vibrational Frequencies Consolidated VolumeI*; National Bureau of Standars, 1972.

[311] Kawaguchi, K. *J. Chem. Phys.* **1992**, *96*, 3411–3415.

[312] Kawaguchi, K.; Butler, J. E.; Yamada, C.; Bauer, S. H.; Minowa, T.; Kanamori, H.; Hirota, E. *J. Chem. Phys.* **1987**, *87*, 2438–2441.

[313] Petek, H.; Nesbitt, D. J.; Darwin, D. C.; Ogilby, P. R.; Moore, C. B.; Ramsay, D. A. *J. Chem. Phys.* **1989**, *91*, 6566–6578.

[314] Butenhoff, T. J.; Rdhlfing, E. A. *J. Chem. Phys.* **1993**, *98*, 5469–5476.

[315] Stancu, G. D.; Röpcke, J. *J. Chem. Phys.* **2005**, *122*, 014306.

[316] Häidrich, S.; Hefter, S.; Pfelzer, B.; Doerk, T.; Jauemik, P.; Uhlenbusch, J. *Chem. Phys. Lett.* **1996**, *256*, 83–86.

[317] Tam, S.; Macler, M.; Fajardo, M. E. *J. Chem. Phys.* **1997**, *106*, 8955–8963.

[318] Flaud, J. M.; Camy-Peyret, C.; Johns, J. W. C.; Carli, B. *J. Chem. Phys.* **1989**, *91*, 1504–1510.

[319] Klee, S.; Winnewisser, M.; Perrin, A.; Flaud, J.-M. *J. Mol. Spectrosc.* **1999**, *195*, 154–161.

[320] Isoniemi, E.; Khriachtchev, L.; Pettersson, M.; Räsänen, M. *Chem. Phys. Lett.* **1999**, *311*, 47–54.

[321] Junttila, M. L.; Lafferty, W. J.; Burkholder, J. B. *J. Mol. Spectrosc.* **1994**, *164*, 583–585.

[322] Lafferty, W. J.; Olson, W. B. *J. Mol. Spectrosc.* **1986**, *120*, 359–373.

[323] Rumbles, G.; Lee, E. K. C.; Valentini, J. J. *J. Chem. Soc., Faraday Trans.* **1990**, *86*, 3837–3841.

[324] Sappey, A. D.; Crosley, D. R. *J. Chem. Phys.* **1990**, *93*, 7601–7608.

[325] Brown, S. S.; Berghout, H. L.; Crim, F. F. *J. Chem. Phys.* **1996**, *106*, 5805–5815.

[326] Brown, S. S.; Berghout, H. L.; Crim, F. F. *J. Chem. Phys.* **1997**, *107*, 9764–9770.

[327] Reid, C. *J. Chem. Phys.* **1950**, *18*, 1544–1550.

[328] Pettersson, M.; Khriachtchev, L.; Jolkkonen, S.; Räsänen, M. *J. Phys. Chem. A* **1999**, *103*, 9154–9162.

[329] Jacox, M. E.; Milligan, D. E. *J. Chem. Phys.* **1964**, *40*, 2457–2460.

[330] Bürger, H.; Pawelke, G.; Rahner, A.; Appelman, E. H.; Halonen, L. *J. Mol. Spectrosc.* **1989**, *138*, 346–354.

[331] Bürger, H.; Pawelke, G.; Rahner, A.; Appelman, E. H.; Mills, I. M. *J. Mol. Spectrosc.* **1988**, *128*, 278–287.

[332] Irikura, K. K. *J. Phys. Chem. Ref. Data* **2007**, *36*, 389–397.

[333] Becke, A. D. *J. Chem. Phys.* **1993**, *97*, 9173–9177.

[334] Schmidt, M. W.; Baldridge, K. K.; Boatz, J. A.; Elbert, S. T.; Gordon, M. S.; Jensen, J. H.; Koseki, S.; Matsunaga, N.; Nguyen, K. A.; Su, S. J.; Windus, T. L.; Dupuis, M.; Montgomery, J. A. *J. Comput. Chem.* **1993**, *14*, 1347–1363.

[335] Feller, D. J. *J. Comp. Chem.* **1996**, *17*, 1571–1586.

[336] Schuchardt, K. L.; Didier, B. T.; Elsethagen, T.; Sun, L.; Gurumoorthi, V.; Chase, J.; Li, J.; Windus, T. L. *J. Chem. Inf. Model.* **2007**, *47*, 1045–1052.

[337] Bode, B. M.; Gordon, M. S. *J. Mol. Graphics Modell.* **1998**, *16*, 133–138.

[338] R Core Team; *R: A Language and Environment for Statistical Computing*; R Foundation for Statistical Computing; Vienna, Austria; 2013. http://www.R-project.org.

[339] Mevik, B. H.; Wehrens, R. *J. Stat. Softw.* **2007**, *18*, 1–24.

[340] Durig, J. R.; Wertz, D. W. *J. Chem. Phys.* **1968**, *49*, 2118–2121.

[341] Lewis, J. D.; Laane, J.; Malloy, T. B. *J. Chem. Phys.* **1974**, *61*, 2342–2345.

[342] Little, T. S.; Zhu, X.; Wang, A. Y.; Durig, J. R.; Dakkouri, M.; Hermann, T.; Sala, O. *Spectrochim. Acta, Part A* **1993**, *49*, 1913–1933.

[343] Kim, G.; Park, D. *Catal. Today* **2000**, *63*, 537–547.

[344] Zhang, Y.; Zhao, J.; He, L.; Zhao, D.; Zhang, S. *Microporous Mesoporous Mater.* **2006**, *94*, 159–165.

[345] Yu, K.; Gu, Z.; Ji, R.; Lou, L.; Liu, S. *Tetrahedron* **2009**, *65*, 305–311.

[346] Sun, C.; Hu, B.; Zhao, D.; Liu, Z. *J. Appl. Polym. Sci.* **2012**, *125*, E79–E87.

[347] Svobodová Vareková, R.; Geidl, S.; Ionescu, C.-M.; Skrehota, O.; Kudera, M.; Sehnal, D.; Bouchal, T.; Abagyan, R.; Huber, H. J.; Koca, J. *J. Chem. Inf. Model.* **2011**, *51*, 1795–1806.

[348] Breneman, C. M.; Wiberg, K. B. *J. Comput. Chem.* **1990**, *11*, 361–373.

[349] Szefczyk, B.; Sokalski, W. A.; Leszczynski, J. *J. Chem. Phys.* **2002**, *117*, 6952–6958.

[350] Rigby, J.; Izgorodina, E. I. *Phys. Chem. Chem. Phys.* **2013**, *15*, 1632–1646.

[351] Oxford, G. A. E.; Snurr, R. Q.; Broadbelt, L. J. *Ind. Eng. Chem. Res.* **2010**, *49*, 10965–10973.

[352] Rutkowska-Zbik, D.; Witko, M.; Serwicka, E. M. *Catal. Today* **2011**, *169*, 10–15.

[353] Zhou, T.; Lin, X.; Zheng, X. *J. Chem. Theory Comput.* **2013**, *9*, 1073–1080.

[354] Perdew, J. P.; Schmidt, K. In *Density Functional Theory and its Application to Materials*; American Institute of Physics; pp 1–20.

[355] Neese, F. *WIREs Comput. Mol. Sci.* **2012**, *2*, 73–78.

[356] Glendening, E. D.; Badenhoop, J. K.; Reed, A. E.; Carpenter, J. E.; Bohmann, J. A.; Morales, C. M.; Weinhold, F.; *NBO 5.9*; Theoretical Chemistry Institute, University of Wisconsin, Madison, WI, 2009; http://www.chem.wisc.edu/ nbo5.

[357] Bader, R. F. W.; *AIMPAC: A suite of programs for the AIM theory*; www.chemistry.mcmaster.ca/aimpac; Retrieved from: https://github.com/ecbrown/aimpac.

[358] Zou, W.; *Molden2AIM, version 2.0.6*; http://people.smu.edu/wzou/program/index.html.

[359] Perdew, J. P. *Electronic Structure of Solids*; Ziesche, P.; Eschrig, H., Eds.; Akademie Verlag: Berlin, 1991; p 11.

[360] Schaefer, A.; Horn, H.; Ahlrichs, R. *J. Chem. Phys.* **1992**, *97*, 2571–2577.

[361] *The Ahlrichs (2d,2p) polarization functions were obtained from the TurboMole basis set library*; ftp.chemie.uni-karlsruhe.de/pub/basen.

[362] Rodrigues, E. F. F.; Sá, E. L.; Haiduke, R. L. A. *Int. J. Quantum Chem.* **2008**, *108*, 2417–2427.

[363] Bader, R. F. W. *Chem. Rev.* **1991**, *91*, 893–928.

[364] Oxford, G. A. E.; Dubbeldam, D.; Broadbelt, L. J.; Snurr, R. *J. Mol. Catal. A: Chem.* **2011**, *334*, 89–97.

[365] Teodoro, T. Q.; Haiduke, R. L. A. *Comput. Theor. Chem.* **2013**, *1005*, 58 – 67.

[366] Lou, L.; Jiang, S.; Yu, K.; Gu, Z.; Ji, R.; Dong, Y.; Liu, S. *Microporous Mesoporous Mater.* **2011**, *142*, 214–220.

[367] Ma, L.; Su, F.; Guo, W.; Zhang, S.; Guo, Y.; Hu, J. *Microporous Mesoporous Mater.* **2013**, *169*, 16–24.

[368] Linde, C.; Koliaï, N.; Norrby, P.; Akermark, B. *Chem. Eur. J.* **2002**, *8*, 2568–2573.

[369] Jolliffe, I. *Principal Component Analysis*, 2nd ed.; Springer Series in Statistics; Springer: New York, 2002.

[370] Weigend, F.; Ahlrichs, R. *Phys. Chem. Chem. Phys.* **2005**, *7*, 3297–3305.

[371] Revelle, W.; *psych: Procedures for Psychological, Psychometric, and Personality Research*; Northwestern University; Evanston, Illinois; 2013; R package version 1.3.10. `http://CRAN.R-project.org/package=psych`.

[372] Attias, H. *Neural Comput.* **1999**, *11*, 803–851.

[373] Teixeira, F.; Mosquera, R. A.; Melo, A.; Freire, C.; Cordeiro, M. N. D. S. *Int. J. Quantum Chem.* **2014**, *114*, 525–533.

[374] Anscombe, F. J. *J. Roy. Stat. Soc. B Met.* **1953**, *15*, 1–29.

[375] Xiang, S.; Zhang, Y.; Xin, Q.; Li, C. *Chem. Commun.* **2002**, *2002*, 2696–2697.

[376] Zhang, H.; Xiang, S.; Li, C. *Chem. Commun.* **2005**, *2005*, 1209–1211.

[377] Keith, T. A.; *AIMAll (Version 13.11.04)*; 2013. `http://aim.tkgristmill.com/`.

[378] Krzystek, J.; Telser, J. *J. Magn. Reson.* **2003**, *162*, 454–465.

[379] Estévez, L.; Mosquera, R. A. *Chem. Phys. Lett.* **2008**, *451*, 121–126.

[380] Stutchbury, N. C. J.; Cooper, D. L. *J. Chem. Phys.* **1983**, *79*, 4967–4972.

[381] C.Bolm *Coord. Chem. Rev.* **2003**, *237*, 245–256.

[382] van Putten, R.-J.; van der Waal, J. C.; de Jong, E.; Rasrendra, C. B.; Heeres, H. J.; de Vries, J. G. *Chem. Rev.* **2013**, *113*, 1499–1597.

[383] Klamt, A.; Schuurmann, G. *J. Chem. Soc., Perkin Trans. 2* **1993**, *1993*, 799–805.

[384] Sinnecker, S.; Rajendran, A.; Klamt, A.; Diedenhofen, M.; Neese, F. *J. Phys. Chem. A* **2006**, *110*, 2235–2245.

[385] Crans, D. C. *Pure Appl. Chem.* **2005**, *77*, 1497–1527.

[386] Bortolini, O.; Conte, V. *J. Inorg. Biochem.* **2005**, *99*, 1549–1557.

[387] Kirillova, M. V.; Kuznetov, M. L.; Romakh, V. B.; Shul'pina, L. S.; Silva, J. D.; Pombeiro, A. J. L.; Shul'pin, G. B. *J. Catal.* **2009**, *267*, 140–157.

[388] Aschi, M.; Crucianelli, M.; Giuseppe, A. D.; Nicola, C. D.; Marchetti, F. *Catal. Today* **2012**, *192*, 56–62.

[389] Gracia, L.; Polo, V.; Sambrano, J. R.; Andrés, J. *J. Phys. Chem. A* **2008**, *112*, 1808–1816.

[390] Yudanov, I. V. *J. Struct. Chem.* **2007**, *48*, S111–S124.

[391] Gracia, L.; Sambrano, J. R.; Safont, V. S.; Calatayud, M.; Beltrán, A.; Andrés, J. *J. Phys. Chem. A* **2003**, *107*, 3107–3120.

Index